# Coherence and high fidelity control of two-electron spin qubits in GaAs quantum dots

Von der Fakultät für Mathematik, Informatik und Naturwissenschaften der RWTH Aachen University zur Erlangung des akademischen Grades eines Doktors der Naturwissenschaften genehmigte Dissertation

vorgelegt von

Diplom-Physiker

Tim Botzem

aus Siegburg

Berichter: Universitätsprofessor Prof. Dr. Hendrik Bluhm

Universitätsprofessor Prof. Dr. Ferdinand Kuemmeth

Tag der mündlichen Prüfung: 27.01.2017

Diese Dissertation ist auf den Internetseiten der Hochschulbibliothek online verfügbar.

## Coherence and high fidelity control of two-electron spin qubits in GaAs quantum dots

#### Abstract

Electron spin qubits confined in GaAs quantum dots are among the most established and well understood qubit systems. Long coherence times due to their weak interaction with the environment and the electrical tunability of the semiconductor quantum dot have allowed GaAs-based spin qubits to play a central role in demonstrating the key operations of semiconductor spin qubits, such as initialization, read-out, universal control and two-qubit gates. Furthermore, spins confined in semiconductor nanostructures provide a solid-state approach to quantum computation which leverages current, well established semiconductor production technology for device fabrication and potential scalability.

However, the interaction with nuclear spins in the GaAs host material complicates not only the preservation of qubit coherence, but also the precise control of the electron spins. As both these properties, the coherence time and the fidelity of gate operations, play a crucial role as prerequisites for quantum computing, the focus of this thesis are experiments addressing these challenges on the basis of two-electron spin qubits.

Interesting effects arise from the quadrupolar interaction of nuclear spins with electric field gradients. We show experimentally that quadrupolar broadening of the nuclear Larmor precession reduces electron spin coherence via faster decorrelation of transverse nuclear fields. However, this effect disappears for appropriate field directions. Furthermore, we observe an additional modulation of coherence attributed to an anisotropic electronic *g*-tensor. These results complete our understanding of dephasing in gated quantum dots and point to mitigation strategies.

A key requirement for quantum computation are high-fidelity single qubit operations, which so far have not been demonstrated for encoded qubits in GaAs. Here, we realize such accurate operations by iteratively tuning of the all-electrical control pulses. Using randomized benchmarking, a well established characterization method, we find an average gate fidelity of  $\mathcal{F}=(98.5\pm0.1)\,\%$  and determine the sum of gate leakage out of and back into the computational subspace to be  $\mathcal{L}=(0.4\pm0.1)\,\%$ . These results demonstrate that high fidelity gates can be realized even in the presence of nuclear spins as existent in all III-V semiconductors.

The potential of a feedback mechanism based on electric dipole spin resonance for narrowing the nuclear hyperfine field and its effectiveness for extending qubit coherence time is investigated in a last experiment. Compared to a previously developed feedback mechanism, this polarization scheme promises higher and more stable pump rates and the ability to set local magnetic fields in each quantum dot individually.

## Coherence and high fidelity control of two-electron spin qubits in GaAs quantum dots

#### Kurzfassung

Elektronen-Spinqubits in GaAs-Quantenpunkten sind eine der etabliertesten und am besten verstandenen Qubitsysteme. Lange Kohärenzzeiten aufgrund der geringen Wechselwirkung mit der Umgebung, und gute elektrische Kontrolle der Halbleiterstruktur haben dafür gesorgt, dass viele der Schlüsselkonzepte und -operationen für Qubits erfolgreich im Experiment gezeigt werden konnten. Darunter fallen die Initialisierung und Auslese des Elektronenspins, die universelle Kontrolle des Spinzustands und Zwei-Qubit-Operationen. Weiterhin bieten Halbleiter-Spinqubits einen Ansatz für Quanten-Computing im Festkörper an, dessen Skalierbarkeit von der aktuellen Halbleiterproduktionstechnologie profitiert. Obwohl gering, verkompliziert die Wechselwirkung mit den Kernspins der GaAs-Halbleiterstruktur nicht nur die Lebensdauer des Qubits, sondern auch die präzise Kontrolle des Elektronenspins. Da lange Kohärenzzeiten und hohe Kontrollfidelitäten wichtige Voraussetzungen für Quantum-Computing sind, stehen Experimente, die diese Parameter für das Zweielektronen-Spinqubit in GaAs untersuchen und optimieren, im Fokus dieser Promotionsarbeit.

Interessante Effekte entstehen durch die Quadrupol-Wechselwirkung zwischen Kernspins und elektrischen Feldgradienten in der Probe. In dieser Arbeit zeigen wir experimentell, dass eine Quadrupolverbreiterung der Kernspin-Larmorfrequenzen die elektronische Kohärenzzeit reduziert. Dieser Effekt kann durch eine geeignete Wahl des externen Magnetfeldes unterdrückt werden, allerdings wird eine zusätzliche Modulation des Kohärenzverlaufs entlang dieser Feldrichtung beobachtet, die wir mit einer Anisotropie des *g*-Faktors erklären. Diese Ergebnisse vervollständigen unser Verständnis über die Dephasierungsmechanismen des Elektronenspins in GaAs und weisen auf Möglichkeiten hin, beide Effekte gleichzeitig zu minimieren.

Hochpräzise Einzelqubitoperationen sind eine wichtige Voraussetzung für Quanten Computing, die bisher noch nicht experimentell realisiert wurde. Wir realisieren solche präzise Operationen, indem wir die elektrischen Kontrollpulse in einer iterativen Regelschleife am Experiment optimieren. Wir zeigen mit *Randomized Benchmarking* Kontrollfidelitäten von  $\mathcal{F}=(98.5\pm0.1)\%$  und bestimmen die Leckrate aus der und in die Qubit-Basis zu  $\mathcal{L}=(0.4\pm0.1)\%$ . Dieses Ergebnis demonstriert, dass hochpräzise Einzelqubitoperationen auch in Anwesenheit von Kernspins möglich sind.

Das Potenzial und die Effizienz eines Polarisationschemas, welches auf der elektrischen Dipolspinresonanz basiert und das Kernspinmagnetfeld kontrollieren soll, wird in einem weiteren Teil der Arbeit experimentell untersucht. Wir finden und identifizieren die beiden Kernspinresonanzen der zwei Elektronen im Doppelquantenpunkt und analysieren den Einfluss auf das Kernmagnetfeld durch bewusstes Treiben dieser Übergänge.

#### Preface and acknowledgment

Before I start with my actual thesis, I want to take a moment and reflect on the time of my PhD thesis <sup>1</sup>. Starting my PhD only a couple of weeks after Hendrik arrived at the RWTH University gave me the unique opportunity to witness and more importantly be part of establishing experimental quantum information in Aachen. It has been a very exciting, fun and educational journey that I could not have done by my own. Therefore I would like to use this chapter to thank and mention defining memories of people who have supported me for the last years.

I thank my advisor Hendrik for having me in his group from the very beginning, for all the trust he put in me handling the cryogenics<sup>2</sup> and all the support and guidance especially in the beginning of my thesis. I still recall the very frequent late night discussions in the lab and the occasional cell phone calls from our (back then) girlfriends. He really is an excellent physicist with an open door policy and always takes his time to discuss nearly any subject. I learned a lot about high frequency electronics, about intuitively accessible quantum theory and about the fine art of taking visually nice data.

I would also like to thank Prof. Ferdinand Kuemmeth for taking the position as second assessor of my thesis.

I thank Rob for teaching and helping me a lot with the handling of the cryogenics and neat everyday tricks. He also taught me how to perform first quantum dot measurements and encouraged me to save data, even if it might not look too interesting; which is easier said then done as measurements are really fast to do.

Together with our most senior group member Michi, I survived the early ages of special measure and I am very thankful for your first driver for the Alazar card; although it still took some time to get it working reliably. I wish you all the best raising your SQUIDS in your dark, stinky hell;).

For roughly one year I shared the experiment with Rob, Pascal and Steffi. I hope I wasn't too overcautious with you, but I spent quite some time setting it up;). It was a fun and informative atmosphere working with you. Pascal and I worked on the same project and I really enjoyed the time. One of us was measuring while the other one was writing pulses or analyzing data. But I will probably never understand your bs<sup>3</sup> struct completely.

<sup>&</sup>lt;sup>1</sup> and save a lot of people the time flipping through all my thesis, because let's be honest, this is the only part most of you came by to read

<sup>&</sup>lt;sup>2</sup>even though it resulted in my first all-nighter in the lab

<sup>&</sup>lt;sup>3</sup>stands for bootstrap

The last six month I worked with Patrick on new GaAs samples; with a smile in one eye and a tear in the other I am handing over the wet fridge to him. Good luck to you and I hope you can top the two year cooldown.

Furthermore, I would like to thank my bachelor students Jonathan and Simon for their nice work.

Especially in the beginning I did some fabrication together with Kilian and I always enjoyed working with him. I guess, it came to us (you) as a shock, but sometimes asking more qualified staff for help instead of trying to fix everything ourselves can be safer;).

I also want to thank all members of "AG Bluhm" for the incredible atmosphere during and outside of work. You really get to know each other and it is never boring, especially in a 12 man office. Although, sometimes I felt I was fighting in an open arena with you guys and I had to call the shots.

A big thanks goes to our electrical workshop, namely Lars and Uwe (I still have some good jokes for our next institute party). With you is always good cherry eating! I also liked working with Guido; thanks for all the help fixing the ebeam machine. I am also very thankful for all the great work provided from the mechanical workshop. My experiments wouldn't have been possible without the incredible work from our (n)ice guys, Sascha (the early inventor of the ice bucket challenge) and Jörg (Jörg was here: A4. XD). I am still amazed that you managed to get us trough all helium and nitrogen crises. Thank you.

I would also like to thank KSV Helios and the Aachener Kraftsport e.V. for providing a place where I could blow of steam when things wouldn't go as planned.

Last but not least I want to give a special thanks to my parents, my sister and Maike for their unconditional and continuous support and love whatever I decide to do.

### **Contents**

Pr	eface	and acknowledgment	iii	
1.	Introduction			
	1.1.	Motivation and physical implementation	1	
	1.2.	1 • 1	3	
2.	Spin	qubits in semiconductor quantum dots	5	
	2.1.	Qubit 101 and the Bloch sphere	6	
	2.2.	GaAs/AlGaAs heterostructure, ohmic contacts and depletion gates	7	
	2.3.	Gate defined quantum dots	8	
	2.4.	Two-electron spin qubit	9	
		2.4.1. ST <sub>0</sub> basis	10	
		2.4.2. Qubit basics in the basis of a $ST_0$ spin qubit	12	
		2.4.3. Basic control operations	15	
	2.5.	Spin flips due to the spin-orbit interaction	16	
	2.6.	Interaction with the surrounding nuclear spin bath	17	
		2.6.1. Hyperfine interaction	18	
		2.6.2. Implication on electron coherence	20	
		2.6.3. Dynamic nuclear polarization	22	
	2.7.	Current state of the art: Semiconductor spin qubits	23	
		2.7.1. Scalable well-defined qubit	23	
		2.7.2. Initialization	24	
		2.7.3. Universal set of quantum gates	24	
		2.7.4. Qubit specific measurement	24	
		2.7.5. Long coherence times	24	
3.	Devi	ice fabrication	27	
	3.1.	Mesa	28	
	3.2.	Ohmic contacts to the 2DEG	29	
	3.3.	Electrostatic Gates	29	
		3.3.1. Optical Gates	30	
		3.3.2. Quantum dot design	30	
	3.4.	Sample testing	30	
		3.4.1. Room temperature checks	31	

		3.4.2. Gate testing at 4K	32
4.	Expe	erimental setup	33
	4.1.	Ice Oxford dilution refrigerator	33
	4.2.		33
			34
			35
	4.3.	$\epsilon$	38
			39
	4.4.	1	39
	4.5.		40
	4.6.		41
	7.0.	Ocherar data acquisition	71
5.		8	43
	5.1.	Abstract	43
	5.2.		43
	5.3.	Device layout and experimental setup	45
	5.4.	Coarse tuning of the quantum dots	47
		5.4.1. Tuning of the RF-read-out circuit	47
		5.4.2. Tuning of the sensing dot	49
		5.4.3. Locating the $(2,0)$ - $(1,1)$ or $(0,2)$ - $(1,1)$ charge transition	50
	5.5.	Fine tuning of the qubit	53
		5.5.1. Setting up virtual gates	53
		5.5.2. Tunnel coupling to the leads	54
		5.5.3. Inter-dot tunnel coupling	55
		5.5.4. Locating the measurement point	55
			57
			58
			59
			60
			60
			62
			63
	5.6.		63
_	_		
6.	_	drupolar effects and anisotropy on dephasing in two-electron spin	<b>6</b> 5
	-		65
			65
			65
	0.3.		67 67
		6.3.1 S.T. aubit	67

		6.3.2. Quadrupolar interaction
		6.3.3. g-factor anisotropy
		6.3.4. Semiclassical fit model
	6.4.	Discussion
	6.5.	Methods
		6.5.1. Qubit system and experimental setup
		6.5.2. Echo sequence
	6.6.	Supplementary information
		6.6.1. Experimental setup
		6.6.2. Data normalization and stitching
		6.6.3. g-factor anisotropy in asymmetric GaAs heterostructure 7'
		6.6.4. Quadrupolar interaction
		6.6.5. Semiclassical fit model
7.	Depl	nasing of electron spins in InAs nanowires
	7.1.	Abstract
	7.2.	Introduction
	7.3.	Qubit system
	7.4.	Echo envelope modulation due to a <i>g</i> -factor anisotropy 92
		7.4.1. Fit to experimental data
	7.5.	Mitigation strategies
	7.6.	Summary
	7.7.	Appendix
		7.7.1. <i>g</i> -factor anisotropy
		7.7.2. Semiclassical fit model
8.	Feed	back-tuned high-fidelity gates for encoded spin qubits 10
	8.1.	Abstract
	8.2.	Introduction
	8.3.	Results
		8.3.1. S-T <sub>0</sub> Qubit
		8.3.2. GAMBIT
		8.3.3. Tomography and randomized benchmarking
	8.4.	Discussion
	8.5.	Methods
		8.5.1. Qubit system
		8.5.2. Readout calibration
	8.6.	Supplementary Information
		8.6.1. Experimental setup
		8.6.2. System characterization
		8 6 3 Ontimal pulses 11'

#### Contents

		8.6.4. 8.6.5. 8.6.6. 8.6.7.	Readout and initialization	122 124
9.	Dyna	amical r	nuclear polarization by hyperfine mediated electric dipole spi	n
	resor	nance		135
	9.1.	Introdu	ction	135
		9.1.1.	Experimental setup	136
	9.2.	Results		136
		9.2.1.	Locating the EDSR transitions	137
		9.2.2.	Pumping the nuclear bath	142
		9.2.3.	IQ mixer measurements	147
	9.3.	Discuss	sion	147
10.	Sum	mary aı	nd outlook	149
	Sum	·	nd outlook	149 155
	Appo	endix		155
	<b>Appe</b> A.1.	e <b>ndix</b> Double	quantum dot fabrication recipe	<b>155</b> 155
	<b>Appe</b> A.1. A.2.	e <b>ndix</b> Double Bondin	quantum dot fabrication recipe	<b>155</b> 155 157
	Appe A.1. A.2. A.3.	e <b>ndix</b> Double Bondin Sample	quantum dot fabrication recipe	155 155 157 159
	Appe A.1. A.2. A.3. A.4.	endix Double Bondin Sample Circuit	e quantum dot fabrication recipe	155 155 157 159 160
	Appe A.1. A.2. A.3. A.4. A.5.	endix Double Bondin Sample Circuit Circuit	quantum dot fabrication recipe	155 155 157 159 160 160
<b>A.</b>	Appe A.1. A.2. A.3. A.4. A.5. A.6.	endix Double Bondin Sample Circuit Circuit	quantum dot fabrication recipe	155 155 157 159 160 160
A. B.	Appe A.1. A.2. A.3. A.4. A.5. A.6.	endix Double Bondin Sample Circuit Circuit Tuning	quantum dot fabrication recipe	155 155 157 159 160 160

#### 1. Introduction

Today, our ability to use previously untapped quantum effects in customised systems and materials is paving the way for a second [quantum] revolution. With quantum theory now fully established, we are required to look at the world in a fundamentally new way: objects can be in different states at the same time (superposition) and can be deeply connected without any direct physical interaction (entanglement). [1]

#### 1.1. Motivation and physical implementation

In the last couple of years, interest in quantum computing, or more general quantum information processing, has increased significantly, not only in the physics community but also in the more public media. Furthermore, governments and corporations, such as Google, Microsoft, Intel and IBM, are investing millions of dollars in this research field and even work in close collaborations with several universities.

It is said that we are currently taking the first steps towards a *Second Quantum Revolution*<sup>[2]</sup>, as already stated in the quote mentioned above. The *First Quantum Revolution*, taking place nearly a century ago, provided a new understanding of physics and laid out new rules to describe physical reality. In the *Second Quantum Revolution*, these new rules will be used and the key physical concepts, such as superposition, entanglement and tunneling, will be employed to man-made, artificial quantum states, solely designed for our purposes. For instance, we are nowadays able to fabricate quantum dots in semiconductor heterostructures<sup>[3]</sup> or superconducting loops<sup>[4]</sup> that behave like artificial atoms with electric properties that can be engineered as demanded.

These man-made quantum states, possessing novel quantum-mechanical properties, have created new research fields, such as quantum information processing, quantum secure communication, and quantum metrology (in analogy to their classical counterparts).

Especially quantum information processing is thought to have the potential of revolutionizing our way of computing by employing fundamentally different quantum mechanical principles. Quantum entanglement and superposition lead to an intrinsic computational parallelism that allows an exponential speed-up of solving certain problems, like prime factorization<sup>[5]</sup>, using quantum algorithms. Another application for a quantum computer lies in the field of quantum simulation and quantum chemistry. For exam-

ple, quantum computers<sup>1</sup> promise novel computer-aided designs of catalysts for the nitrogen fixation problem<sup>[6,7]</sup>, carrying along a great economic value. Furthermore, quantum computers may allow the understanding of strongly correlated many-body physics problems, a complex or even practically impossible task for a classical computer<sup>[8]</sup>.

However, the experimental realization of most of these possible application lies far ahead in the future as they possibly require millions of quantum bits (qubits), the basic building blocks of a quantum computer. Experimentally, we are at an exciting stage where first initial steps have been taken in realizing several of these qubits in the laboratory. As of now, there is quite a variety of promising qubit realizations, including superconducting qubits, trapped atoms and ions, semiconductor electron spin qubits and nuclear spins. Each of them have their own advantages and disadvantages. So far, none of the physical implementations clearly stands out and all are part of active research.

In 2011, our group started to work on two-electron spin qubits in gate-defined quantum dots in GaAs, a platform that historically played a central role in demonstrating the key operations of semiconductor spin qubits <sup>[9,10,11,12]</sup>. Although being a experimentally and theoretically well understood qubit system, the presence of nuclear spins in the GaAs host material complicates not only preserving qubit coherence, but also the precise control of the electron spins. As both these properties, the coherence time and the fidelity of gate operations, play a crucial role as prerequisites for quantum computing, the research field split into two camps. Whereas one camp pursues the idea to leverage spinless material for the heterostructure, creating a semiconductor vacuum for the electron spin and thus avoid nuclear spins, the other camp tries to mitigate and even control the effect of nuclear spins employing more complex and advanced control methods<sup>2</sup>. Indeed, it is experimentally possible to harness these nuclear spins and use them to our advantage for controlling the electron spin by polarizing the nuclear magnetic field using the electron spin as a hardware feedback loop<sup>[13]</sup>.

Nevertheless, qubit performance including coherence times and control fidelities are not yet at the level needed for quantum computation. The striking advantage of qubits, namely the superposition principle, leaves the qubit very prone to not only bit-flip errors, as they occur as well on the classical counterpart, but also to phase errors, which come in a much higher variety. To our current understanding, the largest tolerable error rate per qubit gate is set to about 1%, using state of the art surface error correction code [14], although for any practical use the error rate should be at least an order of magnitude smaller.

A decrease in gate error rate can be achieved in two ways. On the one hand, enhancing the spin coherence time while keeping the time for gate operations constant, reduces the error per gate. In 2011, *Bluhm et al.* [15] concluded from a measured coherence time of more than  $200 \,\mu s$  an error rate per average gate below  $10^{-4}$ . As the limiting factors of

<sup>&</sup>lt;sup>1</sup>At least millions of qubits are needed for this application.

<sup>&</sup>lt;sup>2</sup>Our group actually pursues both possibilities, but my work was exclusively done in GaAs.

this coherence were not completely understood, I continue this line of work in Ch. 6, discovering the limiting factor and pointing to mitigation strategies which will lead to longer coherence times for electron spin qubits in GaAs. On the other hand, increasing qubit control fidelities directly translates into lower error rates. But so far the figure of merit, the gate fidelity, has not been experimentally investigated for electron spins in GaAs or even for encoded spin qubits in general. In this work, we experimentally show in Ch. 8 gate fidelities approaching the above mentioned error correction threshold for an encoded spin qubit, even in the presence of nuclear spins.

Experiments performed in my thesis show how to enhance coherence times and how to implement accurate single qubit gate operation and thus brings the system of encoded spin qubits in GaAs one step closer to be a viable option as semiconductor spin qubits. Furthermore, the findings allow a staple of interesting new experiments including investigations of spin dynamic using correlation measurements and state and process tomography using high-fidelity gates.

#### **1.2.** Organization of this thesis

All experiments presented in this thesis aim to improve and understand the performance of a two-electron spin qubit in GaAs. I will provide experiments and theory investigating the coherence time of the electron spin, present a method to tune up high fidelity gate operations using an experimental feedback and finally I will discuss a novel method to polarize the nuclear bath using high frequency manipulation.

In order to understand the following chapters, I will introduce this type of qubit in Chapter 2 and address the most basic theoretical concepts of gated heterostructures, quantum dots and electrons interacting with a nuclear spin bath. Detailed theoretical background is presented elsewhere.

A summary of the different processing steps for sample fabrication is given in Chapter 3. The cryogenic, high frequency setup, built-up in the beginning of my thesis, and its functionality is explained in Chapter 4. All experiments presented here were performed in this setup.

In Chapter 5 I address different tuning methods that have been established over the last few years, to tune-up a two-electron spin qubit in GaAs. The overall aim of these tuning methods is that they should be completely automated in the near future, once the multiqubit stage is reached.

Experiments investigating electron decoherence due to a surrounding nuclear bath are presented in Chapter 6. We demonstrate experimentally that quadrupolar broadening of the nuclear Larmor precession reduces electron spin coherence via faster decorrelation of transverse nuclear fields. However, this effect disappears along appropriate external magnetic field directions, but an additional modulation of coherence attributed to an anisotropic electronic *g*-tensor arises. We use this study to propose a new sample layout

which allows for mitigating both these decoherence effects.

In Chapter 7 I adapt the theory of an Hahn echo envelope modulation due to a *g*-factor anisotropy from Chapter 6 to an InAs nanowire system. I show that this theory can explain the surprisingly short coherence times measured in this system from Ref. 16.

In Chapter 8, a tune-up procedure resulting in high-fidelity gate operation using experimental feedback, named GAMBIT (Gate AdjustMent By Iteratively Tune-up), is introduced. We show that even in a noisy environment, such as GaAs, gate fidelities of 98.5% are feasible using randomized benchmarking as an independent measure. Furthermore, we find that gate operation fidelity is currently limited by decoherence, whereas gate leakage and systematic errors only play an inferior role.

Experiments for establishing a novel polarizing method exploiting electric dipole spin resonance to manipulate and set a magnetic field gradient are discussed in Chapter 9. Continuing the experimental efforts from Ref.17, we find the single electron resonances and probe their potential to influence the surrounding nuclear spins. A brief conclusion and an outlook of future experiments and implications will be given in Chapter 10.

For the really interested readers (probably only my direct successor), I have summarized use- and helpful peripheral material in the Appendix.

## 2. Spin qubits in semiconductor quantum dots

The spin degree of freedom of a spin-1/2 particle as an intrinsic two-level system weakly coupled to its environment presents itself as a natural representation of a qubit. Beginning with theoretical proposals and first experiments to isolate single electron spins in bulk semiconductor samples in the 1990s, the field of semiconductor spin qubits has steadily advanced, and nowadays we have full control and a profound understanding of the electron spin. Using the same technology as today's modern transistor architecture further promises excellent prospects of scalability for semiconductor spin qubit devices.

This chapter is intended to cover the basic theoretical background of the physical phenomena examined in this thesis. I do not intend to motivate the use of quantum computers again, as this is already provided in the introduction, but I will focus on the basic physical properties of its building blocks, the qubits. First, I will give a very brief introduction to quantum two-level systems and how to visualize them using the Bloch sphere representation. Detailed properties of qubits will be given later in this chapter on the basis of the ST<sub>0</sub> qubit with the intent for the reader to accept them as real qubits instead of mesoscopic quantum dots and to better understand the challenges associated with this interpretation. Nevertheless, especially for the first grad student who has to set-up, build, fabricate, program, tune-up and interpret everything from the ground up, it is absolutely crucial to understand not only the quantum information point of view but also the mesoscopic semiconductor side of the picture. I will therefore introduce the realization of gated semiconductor spin qubits in this chapter as well. After understanding how single electrons can be confined in a gated semiconductor heterostructure, I will explain how the spin of two electrons can be used to define the ST<sub>0</sub> electron spin qubit. The basic properties of qubits will be addressed using the example of the twoelectron spin qubit. In a last step, I will address different dephasing mechanism due to the interaction of one single spin with an whole ensemble of nuclear spins. As this chapter focuses only on the basic principles, detailed theoretical information is provided throughout the document if needed.

#### 2.1. Qubit 101 and the Bloch sphere

The quantum mechanical analogon of the classical bit, which can either be on (1) or off (0), is a quantum bit or short qubit, represented by any two-state quantum system that can be written as [18]

$$|\psi\rangle = \alpha |0\rangle + \beta |1\rangle,$$
 (2.1)

where  $\alpha$  and  $\beta$  are complex numbers satisfying  $|\alpha|^2 + |\beta|^2 = 1$ . The orthogonal basis of the qubit subspace is formed by the computational states  $|0\rangle$  and  $|1\rangle$ . Often, it is useful to represent the pure qubit state on the surface of a sphere. We therefore write

$$|\psi\rangle = \cos\left(\frac{\theta}{2}\right)|0\rangle + e^{i\phi}\sin\left(\frac{\theta}{2}\right)|1\rangle,$$
 (2.2)

where  $\theta$  and  $\phi$  represent latitude and longitude, respectively. This representation, depicted in Fig. 2.1, is called Bloch sphere [18] and allows a visualization of the qubit state independent from its physical implementation. We will later see in this chapter that this representation is furthermore suited to visualize qubit evolution and mixed states. For

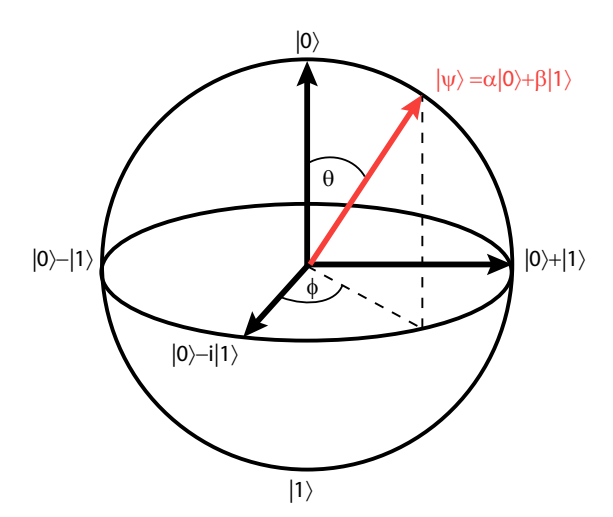


**Figure 2.1.: Bloch Sphere.** The Bloch sphere is a graphical representation of the quantum state of a two-level system, with orthogonal states  $|0\rangle$  and  $|1\rangle$ . Pure qubit states are available on the surface of the sphere.

now, this information will be sufficient to understand how to physically realize an electron spin qubit in a GaAs heterostructure. Further properties will follow in section 2.4.2.

## 2.2. GaAs/AlGaAs heterostructure, ohmic contacts and depletion gates

For the last couple of decades the pristine two-dimensional electron gas (2DEG) in a GaAs/AlGaAs heterostructure has truly enabled a lot of interesting experiments in mesoscopic low-temperature physics and has been used as a pioneering platform for the field of semiconductor spin qubits. The GaAs substrate can be grown extremely clean and defect free by means of molecular beam epitaxy (MBE) and possesses truly remarkable properties. Its band structure allows to confine single electrons providing a smooth quantum well potential that grants enough tunability to construct the desired qubit Hamiltonian. Furthermore, standard, well-established lithography can be applied allowing, in principle, scalable device architectures of almost arbitrary complexity and size.

The different band gaps of the two semiconducting materials GaAs and  $Al_{0.3}Ga_{0.7}As$  result in a conduction band discontinuity, as can be seen schematically in Fig  $2.2^{[19]}$ . An intentional doping layer, in our case realized by a  $\delta$ -doping layer of Silicon, provides an electric field in growth direction and bends the conduction band into a triangular quantum well shape at the interface between GaAs and AlGaAs. Electrons in this so-called 2DEG region, originating from the doping layer, are confined in growth direction. Ohmic contacts, fabricated by annealing a gold/germanium eutectic, provide an electrical connection to the well and allow for control of the electro-chemical potential.

Lateral electron confinement is obtained by biasing lithographically defined electrodes forming Schottky barriers on the surface. These metallic electrodes, referred to as gate electrodes or simply gates, perform two important tasks. On the one hand, by applying a negative voltage relative to the 2DEG potential they locally deplete the population of the 2DEG underneath the gate pattern. This feature is used to isolate and confine single electrons in quantum dots. On the other hand, as the gates couple capacitively to the confined electrons, they can be used to shift the energy of the electrons, as we will see in the next section.

A very important property of the heterostructure, in order to be successfully used as a host material for electron spin

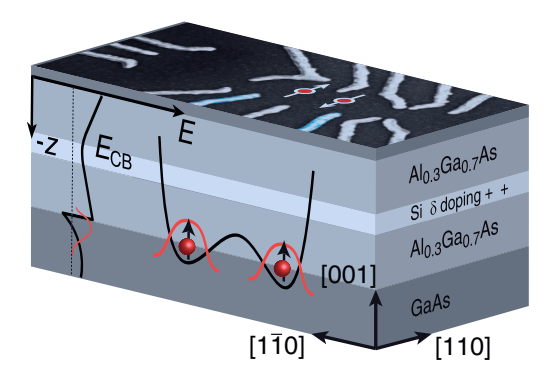


Figure 2.2.: Device layout. Applying negative voltages to electrostatic gates on top of a GaAs 2DEG defines the two-electron spin qubit in a double quantum dot potential.

qubits, is electrical stability or the absence of charge noise. Although the actual origin of charge noise is not completely understood, a good candidate would be the doping layer  $^{[20,21]}$ . Populating charge traps, in form of so-called DX-center in the AlGaAs layers, from leaky gates and charge rearrangements in the doping layer itself were found to play an important role. The obvious solution to simply abandon the doping layer and populate the 2DEG using a global top gate turns out to be difficult from a fabrication point of view, with ohmic contacts to the 2DEG creating the bottleneck. To minimize the influence of a noisy doping layer, the doping atoms should be spread out over a large range, best far away from the region of the electron spin of interest. Instead of  $\delta$ -doping, that has a high concentration of dopants in a thin layer, one should strive for so-called modulation doping, spreading out the doping layer over a larger region.

If tunnelling from the gates to proximal charge traps is the limiting factor, an additional layer of dielectric between wafer surface and electrode might solve the problem. The sample stability of different devices throughout my thesis is given in Ch. A.3.

#### 2.3. Gate defined quantum dots

The extraordinary advances in semiconductor technology allow a PhD student to fabricate a device known from his first class in quantum mechanics: the electron in a box, or as we call it here, a quantum dot. Quantum dots are nanostructures confining a discrete number of electrons in all three dimensions within the spatial extent of their Fermi wave length ( $\approx 50\,\mathrm{nm}$  in GaAs), revealing their true quantum mechanical nature. They are realized by an appropriate pattern of depletion gates. Quantum dots can be thought of as artificial atoms as the confinement reveals discrete energy levels, similar to orbital states of a free atom.

Contrary to the simple electron in the box problem, the experimental quantum dot is tunnel-coupled to two ohmic contacts (leads), acting as source and drain, and capacitively coupled to its surroundings, including ohmic contacts, metallic gates and even other quantum dots. Simple transport phenomena are best described by the so-called *constant interaction model* [3], assuming that the Coulomb interaction between individual electrons can be parameterized by a single, constant capacitance C and that the energy spectrum is independent of the number of electrons. If the chemical potential of the quantum dot is equal or below the chemical potential of a lead, an electron can tunnel onto the dot. If it even lies between the chemical potential of the source and drain lead, the so-called bias window, transport through the quantum dot takes place. If  $\mu$  is outside this window, the quantum dot is in Coulomb blockade. This effect results in the characteristic pinch-off-curve [3] of a single quantum dot, depicted in Fig.2.3c, and is used for charge sensing in the experiments, which will be explained later in this thesis.

The constant interaction model can easily be extended to include an additional quantum dot in series and can be used to explain the characteristic hexagonal or *honeycomb* 

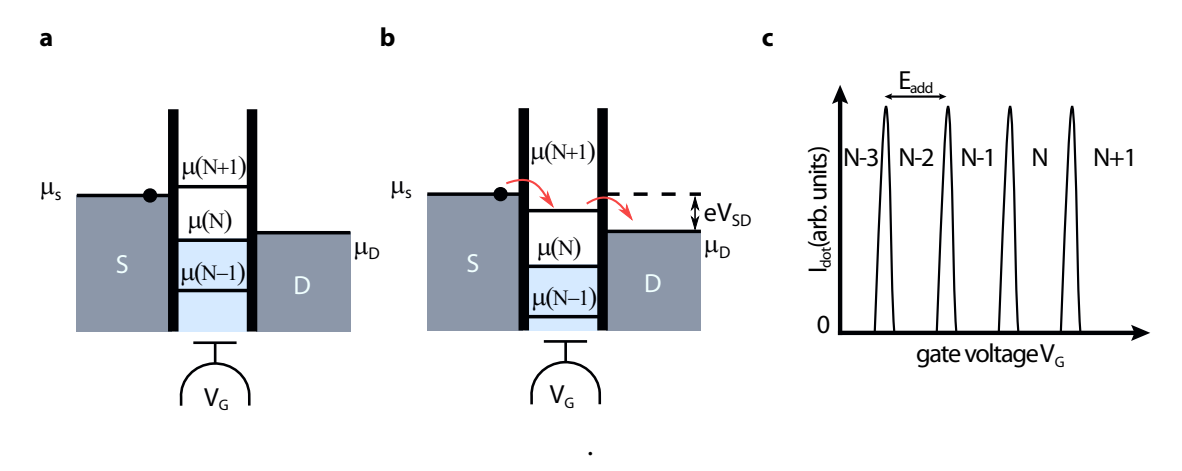


Figure 2.3.: Single quantum dot in the low bias regime. a, b Schematic diagram of the electro-chemical potential of a single quantum dot with a low source-drain bias. Due to Coulomb blockade, no electron can hop onto the dot if the levels lie outside the bias window (a). The  $\mu(N+1)$  potential lies within the window and tunnelling transport through the dot occurs in b. c, Schematic IV-characteristic through the quantum dot showing Coulomb blockade (a) unless the chemical potential of the dot lies within the bias window (b). Adapted from Refs. 19,22

pattern of a double quantum  $dot^{[3,23]}$ . The main results of this model are summarized in Fig. 2.4 and treated in more detail in Ch. 5.

#### 2.4. Two-electron spin qubit

Being able to confine single electrons in individual tunnel coupled quantum dots allows the definition of various qubit systems, ranging from the historical charge qubit to several variations of spin qubits, differing in the number of spins used to encode the actual qubit. The original spin qubit proposal<sup>[24]</sup>, the so-called Loss-DiVincenzo qubit, uses a single electron spin as a natural realization of a two-level system. Using only the ST<sub>0</sub>-subspace of two electron spins<sup>[25]</sup> defines the so-called ST<sub>0</sub> qubit, used throughout this thesis. Lastly, the exchange-only qubit<sup>[26]</sup> is defined by a two-level-subspace of three electron spins. Generally, it is said that the more electrons participate in defining the qubit, the easier it is to control them. An exchange-only qubit, for example, can be manipulated using only electrical control, which is far easier to realize in the lab (and especially in the cryostat) compared to the need of local magnetic fields for Loss-DiVincenzo qubits. So far it is unclear, what kind of semiconductor spin qubit is superior and one can easily imagine an architecture utilizing of all types simultaneously, exploiting their individual advantages.

In this work, I focus on the two-electron ST<sub>0</sub> spin qubit mainly for the following rea-

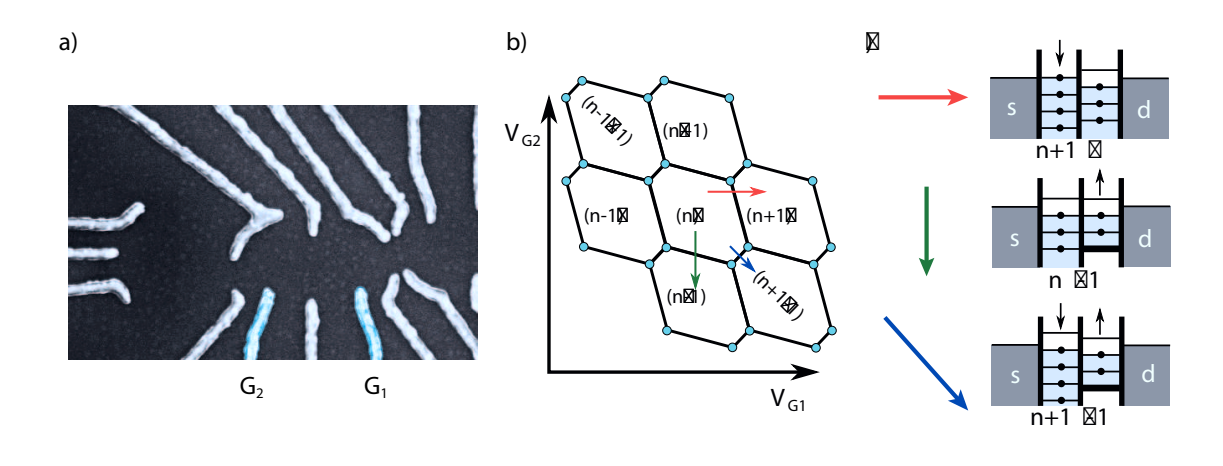


**Figure 2.4.: Double quantum dot. a** Double quantum dot device including a proximal sensing quantum dot. **b, c** Schematic drawing of the charge stability diagram showing the characteristic honeycomb structure. Due to cross-capacitance of the gates to the opposite dot, lines separating different charge configurations are tilted. At intermediate inter-dot tunnel couplings the crossing between lines splits and the charge state domains become hexagonal, leading to the so-called *honeycomb* structure. The label (n, m) depicts the number of electrons in the left and right quantum dot, adjusted by the voltage on G<sub>1</sub> and G<sub>2</sub>, respectively. The corresponding transitions in direction of the colored arrows are illustrated in c). At the triple points (depicted in light blue) the energy levels in both dots are aligned with the chemical potentials of source and drain. Figures adapted from Refs. 19,22

sons: Realizing microwave fields to address single spin qubits is not only experimentally challenging but also will most likely not result in high control fidelities as the qubit's precession frequency varies over time due to the interaction with the surrounding nuclear spins in GaAs (for details see Ch. 9). Using the electrically controllable exchange interaction qubit control is easier to implement and yields higher control fidelities (see Ch. 8). For single qubit universal control, a second axis of rotation is required. This rotation axis is realized by using a dynamical nuclear polarization (DNP) scheme to polarize the surrounding nuclei and create a stable magnetic field gradient between the two dots. Fabricating tunnel-coupled triple quantum dots to form the exchange-only qubit was quite a challenge, hence it was not a serious alternative at the beginning of my thesis.

#### **2.4.1.** $ST_0$ basis

By adding the spin degree of freedom, the  $ST_0$  qubit emerges from a tunnel-coupled charge qubit, operated at either the (2,0)-(1,1) or (0,2)-(1,1) charge state transition, where (n,m) denotes the charge state with n electrons in the left and m electrons in

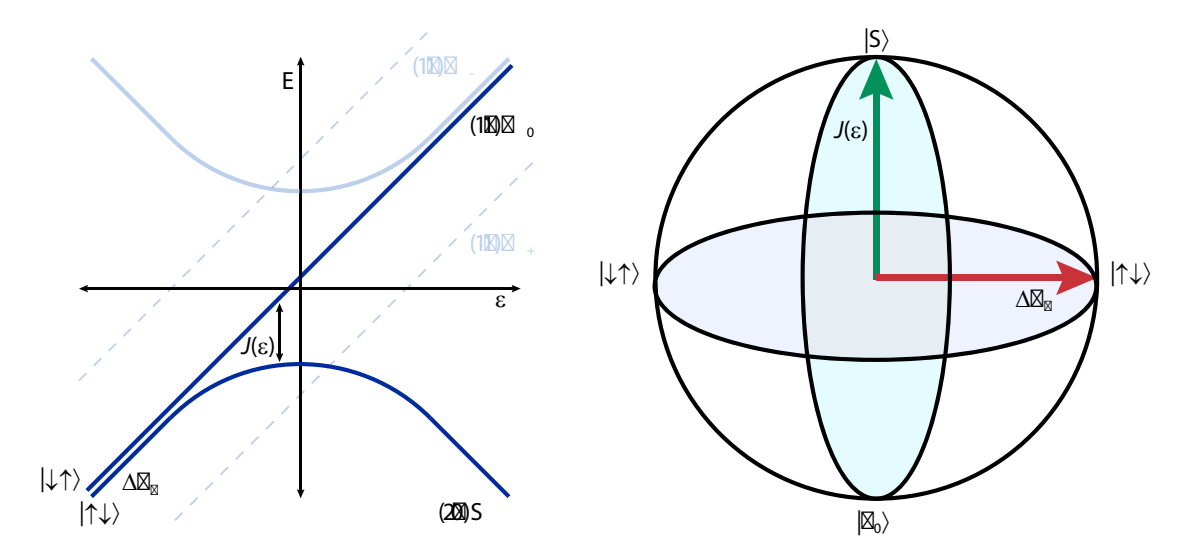


Figure 2.5.: Energy diagram and Bloch sphere of the  $ST_0$  qubit. a Energy diagram of two tunnel-coupled electrons in the double quantum dot. Described in more detail in the main text. **b** The Bloch sphere representation of the  $ST_0$  qubit shows the two orthogonal control axes for qubit manipulation,  $J(\varepsilon)$  and  $\Delta B_z$ .

the right quantum dot. We control the number of electrons by the detuning parameter  $\varepsilon$  that changes the electric potential between the quantum dots<sup>[3]</sup>.

In total, the  $ST_0$  qubit comprises two electron spins and the four possible two-electron spin states are

$$|S\rangle = \frac{1}{\sqrt{2}} (|\uparrow\downarrow\rangle - |\downarrow\uparrow\rangle)$$

$$|T_0\rangle = \frac{1}{\sqrt{2}} (|\uparrow\downarrow\rangle + |\downarrow\uparrow\rangle)$$

$$|T_+\rangle = |\uparrow\uparrow\rangle$$

$$|T_-\rangle = |\downarrow\downarrow\rangle,$$
(2.3)

where  $|\uparrow\downarrow\rangle$  denotes the spin of the electron. In order to identify the spin states in the energy diagram (see Fig. 2.5a), we consider the Pauli exclusion principle. In the absence of magnetic fields, the two-electron ground state in the (2,0) charge configuration must be a spin singlet, as the total fermionic wavefunction must be antisymmetric. The triplet states from equation 2.3 occupy the first excited states and are neglected for conceptual simplicity as they usually are only populated during initial charge scans (see Ch. 5.5.4 for more details). The same argument applies for the (1,1) charge configuration, but this time the singlet and triplet state are almost degenerate as the overlap of the separated electron wavefunctions is smaller. Recapitulating, the spin singlet states can occupy

both the (2,0) and the (1,1) charge states, whereas the triplet states are spin blockaded in the (1,1) configuration (an effect later used to efficiently determine the qubit state).

Applying an external magnetic field  $B_{\rm ext}$  lifts the triplet degeneracy, splitting the  $T_{\pm}$ -states energetically and leaves a two-level system consisting of S and  $T_0$ , with an energy splitting whose strength is determined by the exchange interaction  $J(\varepsilon)$ .

In a last step, a magnetic field gradient  $\Delta B_z$  between the two separated electrons lifts the degeneracy between  $|\uparrow\downarrow\rangle = 1/\sqrt{2}(|S\rangle + |T_0\rangle)$  and  $|\downarrow\uparrow\rangle = 1/\sqrt{2}(|S\rangle - |T_0\rangle)$  in (1,1).

In the end, we we have formed tunable, well-defined two-level system, as depicted in Fig. 2.5a, whose Hamiltonian can simply be written as

$$H = \frac{J(\varepsilon)}{2}\sigma_z + \frac{\Delta B_z}{2}\sigma_x,\tag{2.4}$$

with  $\sigma_i$  being the *i*th Pauli matrix, driving rotations around the *i*-axis, i = x, y, z (see next section for further details). By DC-biasing the detuning, we have fast control of the exchange splitting  $J(\varepsilon)$ , ranging from a few MHz to a couple GHz. We phenomenologically find that  $J = J_0 \exp(-\varepsilon/\varepsilon_0)$  with  $\varepsilon_0 \approx 0.3$  mV, is nearly independent of the inter-dot tunnel coupling. Using DNP to build up and stabilize a non-zero magnetic field gradient across the dots, we are also able to statically set the precession frequency of  $\Delta B_z$ , typically around 60 MHz. Note, I will refer to coupling strength mostly in units of frequency, as this is the natural unit in the experiments. Please also note that for the ease of understanding, the Bloch sphere might also sometimes be rotated by 90° with the  $|\uparrow\downarrow\rangle$ - and  $|\downarrow\uparrow\rangle$ -states on the north and south pole, respectively.

#### **2.4.2.** Qubit basics in the basis of a $ST_0$ spin qubit

Now that we have learned how to realize a semiconductor spin qubit, it is time to forget about the physical implementation and focus on the quantum mechanical treatment of such a qubit. A very neat side effect of the current interest in quantum information is that it can be used to nicely teach basic and advanced quantum mechanical phenomena on the example of qubits instead of an abstract, purely theoretical construction. Furthermore, treating the ST<sub>0</sub> qubit as just a qubit brings certain advantages in the theoretical understanding, especially for later chapters.

#### Time evolution

In the last chapter we have derived the Hamiltonian for the ST<sub>0</sub>-qubit and have stated that the individual terms drive rotation around the x- and z-axis. Let's take a step back and see the actions of the  $\frac{\Delta B_z}{2}\sigma_x$ -term. For this purpose we will have to solve the Schrödinger equation

$$i\hbar \frac{\partial}{\partial t} |\psi\rangle = H |\psi\rangle.$$
 (2.5)

Assuming the qubit is initialized in the ground state  $|S\rangle$  we find the solution by plugging in the  $\sigma_x$ -term of the Hamiltonian from Eq. 2.4

$$|\Psi\rangle = \sin(\Delta B_z t) |S\rangle + \cos(\Delta B_z t) |T_0\rangle.$$
 (2.6)

The state  $|\psi\rangle$  evolves between  $|S\rangle$  and  $|T_0\rangle$  with frequency  $\Delta B_z$ . Looking at the Bloch sphere representation, we can identify the time evolution as rotations around the *x*-axis, the axis connecting the eigenstates  $|\uparrow\downarrow\rangle$  and  $|\downarrow\uparrow\rangle$  of the Hamiltonian. This holds as a general rule and hence the  $\sigma_z$  term in Eq. 2.4 performs rotations about the ST<sub>0</sub>-axis. As discussed earlier, pure quantum states and their time evolution can be represented by states on the surface of the Bloch sphere and by rotations around various axes.

#### **Determining the qubit state**

As learned in every quantum mechanical class, measuring a qubit will ultimately alter its state, as the qubit state will be projected onto one of two orthogonal states, though not necessarily the computational states. As one individual measurement is basically meaningless since it does not reveal anything about the initial qubit state, the measurement process has to be repeated several times on identically prepared qubits. Given that the read-out axis comprises the computational basis states, this ensemble measurement determines the probabilities  $P_S = |\langle S | \psi \rangle|^2$  and  $P_{\Gamma_0} = |\langle T_0 | \psi \rangle|^2$  and hence the prefactors  $\alpha$  and  $\beta$  from Eq. 2.1, albeit leaving the phase between them unknown.

In order to retrieve the full quantum mechanical state, the projection on three orthogonal axes has to be measured. This method, called quantum state tomography [18], reproduces the state vector  $\mathbf{r} = (\langle \sigma_x \rangle, \langle \sigma_y \rangle, \langle \sigma_z \rangle)$  by measuring the expectation values of the different  $\sigma_i$ -operators. This is a non-trivial task for the ST<sub>0</sub>-qubit as we natively can only distinguish, if the qubit is in the singlet or triplet state. To perform state tomography, we have to apply certain gate operations before read-out to map the qubit state on the respective read-out axis. For example, if we want to determine  $\langle \sigma_y \rangle$ , we would have to apply a  $\pi/2_x$ -pulse (a 90° rotation around  $\Delta B_z$ ) right before the measurement, mapping the y-component onto the z-axis.

As this naive realization of state and process tomography requires perfect pulses, it presents itself as a bootstrap problem: We do not have perfect pulses to begin with and in order to tune-up accurate pulses we would need quantum process tomography, a method to identify quantum dynamical processes to characterize them. This method however requires quantum state tomography of an ensemble of quantum states which in return relies on accurate pulses. This dilemma and the task to reliably determine a qubit state or even a gate operation is subject to ongoing theoretical and experimental work in the community, and will be addressed and (partly) solved in Ch. 8.

Note, there are various other methods to determine a quantum process, such as randomized benchmarking<sup>[27]</sup>, gate set tomography<sup>[28]</sup> and self-consistent tomography<sup>[29]</sup>.

There are even non-demolishing read-out<sup>[30]</sup> schemes that do not collapse the qubit state onto any eigenstate.

#### Relaxation and decoherence

Just as the classical bit, the qubit is prone to errors that alter its state. In more detail, the scenario is even worse for the quantum mechanical version, as the qubit is not only susceptible to bit-flip errors (transitions between S and T<sub>0</sub>) but also to phase errors. In general, we distinguish between energy relaxation, causing, for example, bit flip errors, and decoherence, causing loss of phase information. Both mechanisms are caused by unintended and uncontrollable interactions with the environment of the qubit composed i.e. of the three spin carrying isotopes <sup>69</sup>Ga, <sup>71</sup>Ga and <sup>75</sup>As of the host material or phonons. In the following, I will summarize the key parameters for each individual error type <sup>[31]</sup>.

#### • Energy relaxation

The qubit exchanges energy with the environment and consequently the population of  $|S\rangle$  and  $|T_0\rangle$  changes. Possible relaxation or excitation can be caused by phonon interaction initiated by measuring the sensor dot. This process takes place on a timescale called  $T_1$ , which can generally be different for relaxation and excitation.

#### Decoherence

Loss of phase coherence occurs for an individual qubit. Decoherence does not change the relative state population, only the longitudinal component is altered. This process happens on a timescale  $T_2$ .

#### Inhomogeneous broadening

Phase noise that was initially introduced to measure how fast an ensemble of qubits dephases (looses its phase coherence) due to inhomogeneities in for example the control field or the environment of different qubits. The characteristic timescale is called  $T_2^{\star}$ . For a single qubit dephasing becomes noticeable by repeatedly measuring identically prepared 'copies' of the qubit, which experience slightly different values of  $J(\varepsilon)$  and  $\Delta B_z$ . This dephasing however, unlike relaxation and decoherence, can be mitigated by thoughtful qubit manipulation that dynamically decouples the qubit evolution from interaction with its environment. The most popular decoupling technique is the Hahn Echo and is extensively studied in Ch. 6.

Even though these three types of interactions differ fundamentally from each other, they are connected by the following relationship: The upper bound for the dephasing time is  $T_2 \ge T_2^*$ , while the relaxation rate limits the coherence time at  $T_2 \le 2T_1^{-1}$ . All these

<sup>&</sup>lt;sup>1</sup>wherever that factor 2 comes from...

timescales are figures of merit of how well isolated the qubit is from its surroundings, and are probably the most interesting and important properties of a qubit system. These timescales, relative to the time it takes to manipulate a qubit, can be taken as a metric to determine the error rate of certain qubit operations and should be below the current error threshold required for quantum computation. All work presented here (and probably most qubit work in general at this moment) aims to either prolong (Ch. 9), measure and understand (Ch. 6) or exploit (Ch. 8) relaxation and decoherence for quantum gate operations.

The interaction of the electron with its environment leads to loss of information about its original state and creates a so-called mixed state, a probabilistic mixture of pure states. In order to describe such a mixed state, we define the density matrix:

$$\rho = \sum_{i} p_{i} |\psi_{i}\rangle \langle \psi_{i}|, \qquad (2.7)$$

with the probability  $p_i$  to find the qubit in state  $|\psi_i\rangle$ . In the Bloch sphere representation pure single qubit states are located on the surface of the sphere, whereas mixed states lie in the interior. The worst case, a completely mixed or dephased state, occupies the center of the Bloch sphere<sup>[18]</sup>.

#### **2.4.3.** Basic control operations

This section is intended to make the reader familiar with some of the basic operation procedures of a ST<sub>0</sub>-qubit and provide first information in helping to understand the greater picture. A far more detailed version of more involved aspects will be given in later Chapters 5 and 8.

#### **Initialization**

Typically, the qubit is initialized in the S(2,0) state by pulsing it close to the (2,0)-(1,0) transition far in the (2,0) charge configuration where the exchange interaction is the dominating energy scale compared to the electron temperature,  $J(\varepsilon) \gg T_{\rm e}$ . At this point, the chemical potential of the dot approaches the Fermi energy of the lead and an electron will be exchanged. Staying energetically below the singlet-triplet splitting ensures an initialization of a singlet state (see Ch. 5 for further details). By controlling the tunnel barrier with the lead, this exchange can be realized to be within a few nanoseconds (typically 20 ns). The fidelity of this initialization is limited by excitation into the triplet states due to thermal activation, i.e. originating from the RF-read-out signal.

#### Manipulation

The  $ST_0$  qubit is manipulated by changing the detuning  $\varepsilon$  using nanosecond voltage pulses of a few mV applied to the control gates. Natively two (nearly) orthogonal control

axis for rotations exist. Pulsing the detuning into a region of the energy diagram where the exchange interaction dominates the hyperfine gradient,  $J(\varepsilon) \gg \Delta B_z$  drives rotations about the x- (or singlet-triplet)-axis in the Bloch sphere, exchanging the electrons in the double dot. Separating the electrons by pulsing far into the (1,1) region switches off  $J(\varepsilon)$  and  $\Delta B_z$  becomes the largest splitting. Rotations about the z- (or  $\Delta B_z$ )-axis between S and  $T_0$  are performed. Rotations around the combined axis of  $J(\varepsilon)$  and  $\Delta B_z$  are realized at intermediate detunings<sup>[11]</sup>.

Although it is also possible to manipulate the  $ST_0$  qubit using AC-control, as shown in Ref.32, this thesis mainly explores the potential of base-band control. While theoretically this DC-control should allow for a precise manipulation of the qubit, experimental constraints, such as non-linearities in the control function, finite pulse rise-times and noise, hinder the realization of native high fidelity gates (simple rotation about either the  $J(\varepsilon)$ - or  $\Delta B_z$ -axis) in the experiment. A far more sophisticated way to manipulate the  $ST_0$  qubit with fidelities above 98.5 %, by iteratively tuning up the all-electrical control pulses on the experiment, is given in Ch. 8.

#### Measurement

Inherently, measuring the spin state of the two electrons would be a very difficult task. Fortunately, we can use Pauli spin blockade [33,34] to map the spin information onto a charge information that can reliably be measured by a proximal charge sensor, realized by an additional quantum dot in our case. For this scheme, the detuning  $\varepsilon$  is set to a value in the energy diagram where the singlet state occupies the (2,0) charge configuration and the triplet stays in the (1,1) state, see Fig. 2.5.

In order to achieve single-shot read-out, reliably determining the projection of the qubit state onto the singlet-triplet-axis within the qubit's relaxation time, we use RF-reflectometry<sup>[35]</sup> to measure the conductance change of a proximal charge sensor. This read-out method has advanced to a standard measurement technique in the field of semi-conductor spin qubits and is described in more detail in Chapters 4.3 and 5.

#### 2.5. Spin flips due to the spin-orbit interaction

A moving electron in an electric field E experiences its own magnetic field  $B = E \times p$  which leads to spin-orbit interaction (SOI), well known for example from the fine structure splitting of atoms.

For our purpose, it also provides a mechanism to flip the electron spin and might thus lead to decoherence, quenching of dynamical nuclear polarization and *g*-factor anisotropies which all play a crucial role in the remainder of this thesis. Hence, I will provide a short introduction to SOI in confined semiconductor nanostructures.

In general, there are two possibilities to create an electric field for a confined electron in GaAs. First, we have electric fields from the heterostructure as the zinc-blende structure of GaAs breaks inversion symmetry. This so-called Dresselhaus term leads to an effective two-dimensional spin-orbit field<sup>[3]</sup>

$$H_{\rm D} = \beta \left( -p_x \sigma_x + p_v \sigma_v \right), \tag{2.8}$$

where  $p_i$  is the momentum operator and  $\sigma_i$  the spin operator in i = x, y-direction (with z pointing along the growth direction of the GaAs heterostructure). As depicted in Fig. 2.6a, the Dresselhaus contribution is parallel to  $\mathbf{p}$  when moving along [100] and perpendicular when moving along the [010] crystal axis.

A second effective spin-orbit field arises from the confinement of the electron in *z*-direction (growth direction of the crystal or [001]) and the associated electric field of the conduction band. The so-called Rashba contribution is given by

$$H_{\rm R} = \alpha \left( -p_{\rm y} \sigma_{\rm x} + p_{\rm x} \sigma_{\rm y} \right), \tag{2.9}$$

with Rashba constant  $\alpha$ . Contrary to the Dresselhaus-term, the Rashba spin orbit field is always perpendicular to the direction of movement, cf. Fig. 2.6b.

The characteristic length scale it takes for an electron in GaAs to flip its spin is typically  $l_{\rm SO}\approx 1-10\,\mu{\rm m}$ , usually much larger than the typical dot size of 100 nm. For this reason spin-orbit interaction only has a small contribution to the electron coherence time, but it plays an important role in the effectiveness of dynamic nuclear polarization (see Ch. 9). Furthermore, for the right alignment between dot connection axis, crystallographic axis and direction of the external magnetic field, the effective spin-orbit field provides a perpendicular component that can be used to resonantly drive spin transitions (see Ch. 9).

#### 2.6. Interaction with the surrounding nuclear spin bath

The wavefunction of a single electron overlaps with on the order of one million nuclear spins<sup>[3]</sup> from the host material GaAs. Even though the magnetic moment of the electron is tiny, this overlap leads to a variety of possible interactions with the nuclear environment, most of which are well known from first lectures of quantum mechanics or atom physics. In analogy to the hydrogen atom, the qubit in a GaAs heterostructure experiences contact hyperfine interaction with the nuclei as well as interaction via the Larmor precession and dipole-dipole interaction of the nuclear spins. The study of the various couplings between one single spin and an ensemble of spins, is called *the central spin problem* and is still an active field of theoretical and experimental research.

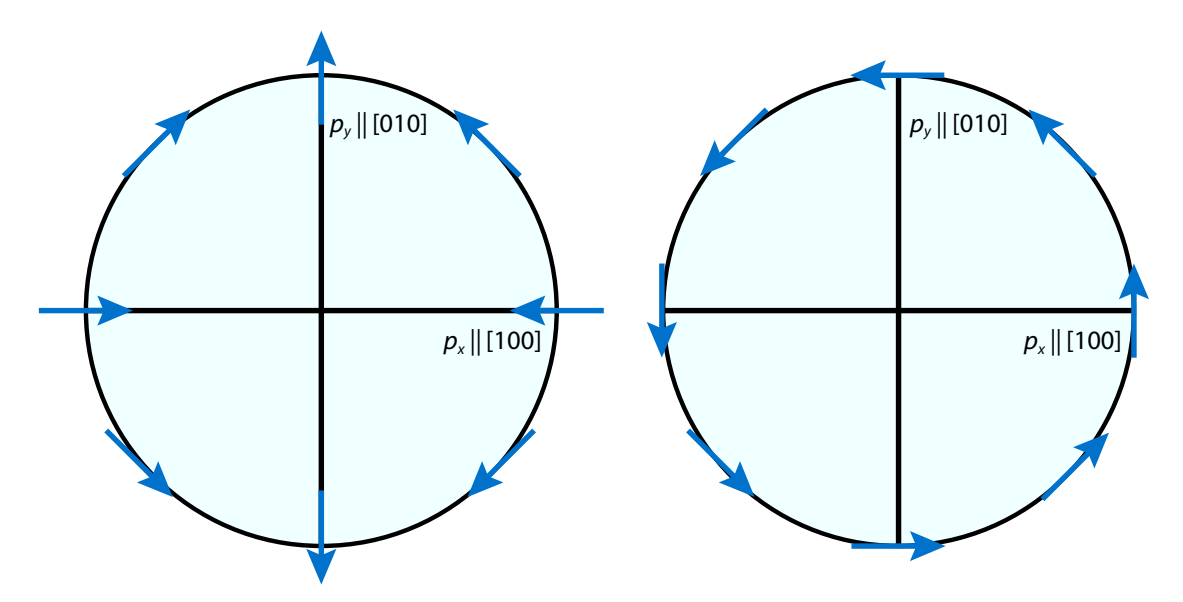


**Figure 2.6.: Spin-orbit interaction.** Direction of the effective spin-orbit field (blue arrows) depending on the alignment of momentum und crystallographic axes for the Dresselhaus (a) and Rashba (b) term.

In the following sections I will address the main theoretical parts of the nuclear interaction, discuss how they alter the nuclear magnetic field and derive their implication on qubit dephasing and decoherence.

#### 2.6.1. Hyperfine interaction

Not only is an electron spin affected by its own orbital momentum but also by surrounding nuclear spins, that for example give rise to the hyperfine structure in atomic physics. The s-type wavefunction of a confined electron in a GaAs quantum dot typically overlaps with about one million nuclear spins and they interact via the Fermi contact hyperfine interaction<sup>[3]</sup>

$$H_{\mathrm{HF}} = \sum_{i=1}^{N} A_i \mathbf{I}_i \cdot \mathbf{S},\tag{2.10}$$

where  $I_i$  and S are the spin operators for nucleus i and the electron, respectively. The hyperfine coupling strength  $A_i$  is weighted with the electron wavefunction overlap  $\psi(r_i)$  at position  $r_i$  for a volume of the crystal unit cell  $v_0$ 

$$A_i = v_0 A |\psi(r_i)|^2. \tag{2.11}$$

The hyperfine interaction can lead to very complex dynamics as both the electron and the nuclei are quantum mechanical objects. This may lead to entanglement between the qubit and the nuclear bath and to back-action effects from the qubit to the nuclei and vice versa. But in all cases in this thesis, it is sufficient to make use of the large number of nuclear spins which make quantum fluctuations elusive and of the different time scales of qubit and nuclear dynamics. This allows us to treat the surrounding nuclear spins as a random classical field, called the Overhauser field  $B_{\text{nuc}}$ . We can substitute

$$H_{\mathrm{HF}} = \sum_{i=1}^{N} A_{i} \mathbf{I}_{i} \cdot \mathbf{S} = g^{*} \mu_{\mathrm{B}} \mathbf{B}_{\mathrm{nuc}} \cdot \mathbf{S}. \tag{2.12}$$

In this approximation, the electron spin experiences an additional classic field added vectorially to  $B_{\rm ext}$  that is taken constant during qubit evolution but shows statistical fluctuation on longer time scales. In the case of large N these fluctuation can be modeled as Gaussian distributed, hence showing a spread of  $\sigma_N \approx A/\sqrt{N} \approx 1-5\,\mathrm{mT}$  in all three dimensions, parallel and perpendicular to  $B_{\rm ext}$ . These fluctuations have various different physical origins, depending on the strength of  $B_{\rm ext}$ , and will be discussed in the following.

#### Virtual spin flip-flops

Taking one step back and exploiting the fact that hyperfine interaction conserves total angular momentum, we can rewrite Eq. 2.10

$$H_{\rm HF} = \sum_{i=1}^{N} A_i \left( I_z^i S_z + I_+^i S_- + I_-^i S_+ \right), \tag{2.13}$$

using the lowering and raising spin operators for the nuclei  $I^{\pm} = (I_x \pm I_y)/\sqrt{2}$  and  $S^{\pm} = (S_x \pm S_y)/\sqrt{2}$ . It can be directly seen that an electron spin flip is accompanied by a nuclear spin flop. For increasing magnetic field (and distance from the ST<sub>+</sub>-transition) the mismatch in Zeeman energy between electron and nuclei prohibits direct spin flip-flops, but virtual processes still take place. In this case a spin flip-flop between electron and nucleus i is accompanied by a simultaneous spin flip-flop with nucleus j. For different coupling strengths  $A_i$  and  $A_j$  of the nuclear configuration the electron experiences a different Overhauser field. The flip probability in these virtual processes scales with  $1/B_{\rm ext}$ , compared to  $1/B_{\rm ext}^2$  for the direct flip-flops [36].

#### Spin diffusion

Another possibility to change the nuclear field are nuclear spin flips caused by dipole-dipole interaction. For high magnetic fields the secular part of the dipole-dipole interaction Hamiltonian states<sup>[37]</sup>

$$H_{i,j} = D\left(I_{+}^{i}I_{-}^{j} + I_{-}^{i}I_{+}^{j} - 4I_{z}^{i}I_{z}^{j}\right), \tag{2.14}$$

where  $D=\hbar/100\,\mu s$  is an interaction constant. The first two terms in this equation describe nuclear spin flip-flops that change the local magnetic field experienced by the electron. Theoretical predictions on the time scale of this Overhauser drift are difficult to calculate [38,39,40] and highly depend on the actual dot dimension, but typically prediction for electron coherence times are in the range of  $10-100\,\mu s$ .

#### **Nuclear Larmor precession**

For external fields on the order of  $B_{\rm nuc} \leq 500\,{\rm mT}$  the individual nuclei precess around the combined magnetic field with their respective Larmor frequency. Although only to second order, at these low fields the dynamics of the transverse Overhauser field  $B_{\rm nuc}^{\perp}$  determines electron coherence and leads to collapses and revivals of the Hahn echo<sup>[41]</sup> amplitude with a periodicity given by the relative Larmor periods of the nuclear spins. The effective field seen by the electron states<sup>[15,42]</sup>

$$B_{\text{eff}} = \sqrt{(B_{\text{ext}} + B_{\text{nuc}}^{z})^{2} + B_{\text{nuc}}^{\perp}(t)^{2}}$$

$$\approx B_{\text{ext}} + B_{\text{nuc}}^{z} + \frac{1}{2B_{\text{ext}}} B_{\text{nuc}}^{\perp}(t)^{2}, \qquad (2.15)$$

where the nomenclature can be taken from Fig. 2.7. Usually, the dynamics of the transverse field only contribute to electron dephasing at low magnetic field as it only couples quadratically. But

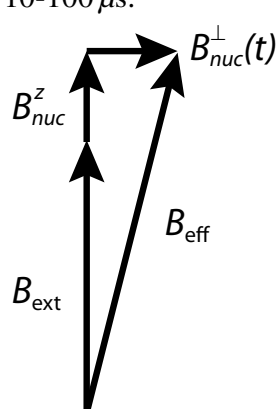


Figure 2.7.: Effective magnetic field.. For small external magnetic fields the transverse component of the Overhauser field  $B_{\rm nuc}^{\perp}(t)$  contributes in second order to the Zeeman splitting.

we will see in Ch. 6 that an electron g-factor anisotropy leads to a linear coupling of  $B_{\text{nuc}}^{\perp}(t)$  to the effective Zeeman-splitting, resulting in a complex pattern of the echo envelope following the time evolution of  $B_{\text{nuc}}^{\perp}(t)$ .

While the Larmor precession of nuclear spins leads to an Echo envelope modulation, a spectral broadening of their frequencies results in loss of electron coherence and allows to link the nuclear dephasing  $T_2^*$  to the electronic  $T_2$  time. We will see in Ch. 6 that dipolar interaction between nuclei as well as quadrupolar interaction with electric field gradients from the heterostructure contribute to the broadening of nuclear Larmor frequencies.

#### **2.6.2.** Implication on electron coherence

As we have seen in the last section, the local nuclear magnetic field slowly fluctuates in time. This will lead to dephasing of the electron spin and will effect the ensemble coherence time  $T_2^*$ . Methods that decouple the electron spin from the fluctuating bath will be discussed in greater detail in Ch. 6.

#### **Ensemble coherence time**

To easily see the influence of a fluctuating nuclear bath on qubit dephasing we consider the simple Hamiltonian

$$H = \frac{B_{\text{nuc}} + \delta B_{\text{nuc}}(t)}{2} \sigma_x, \tag{2.16}$$

where  $\delta B_{\rm nuc}(t)$  describes a random time-dependent offset on the local magnetic field  $B_{\rm nuc}$ . When performing free Larmor precession around  $B_{\rm nuc}$ , this offset will lead to an additional, unknown phase pick up  $\Delta \phi = \int_0^\tau \delta B_z(t) dt$  during time  $\tau$  and results in a loss of phase information. The exact form of the resulting decay law strongly depends on the noise distribution of  $\delta B_z$ . In the quasi-static approximation it can be shown [43] that for Gaussian distributed values of  $B_{\rm nuc}$  with rms-values along all three directions

$$B_{\rm rms} = \sqrt{\frac{\langle |B_{\rm nuc}^z|^2 \rangle}{3}} \approx \frac{A}{g^* \mu_{\rm B} \sqrt{N}}$$
 (2.17)

the resulting decay curve takes a Gaussian decay of the form  $e^{-(t/T_2^{\star})^2/2}$ . The characteristic time scale  $T_2^{\star}$ 

$$T_2^{\star} = \frac{\sqrt{2}\hbar}{g^{\star}\mu_{\rm B}\sqrt{\langle |B_{\rm nuc}^z|^2\rangle}}$$
 (2.18)

strongly depends on the fluctuations and on the number of overlapping nuclei and is typically of the order of 10 ns in GaAs<sup>[9]</sup>.

#### Coherence time T<sub>2</sub>

In general, extracting the real decoherence time  $T_2$  experimentally and theoretically is a complicated undertaking. But the fact that nuclear dynamics happen on a much longer time scale compared to electronic dynamics, allows the application of various decoupling techniques. The most basic of these decoupling pulse sequences is the Hahn echo<sup>[41]</sup>, which will be used in Ch. 6 to study nuclear dynamics and their contribution to electronic dephasing. Here, after half the evolution time  $\tau/2$ , a  $\pi$ -pulse is applied that reverses the interaction with the environment for the remainder of the evolution, removing fluctuations happening on a time scale  $\tau$ .

An established procedure to determine and characterize how fluctuation and noise sources in general affect qubit dephasing is to study their noise spectral density [44]

$$S(\omega) = \frac{1}{2\pi} \int_{-\infty}^{+\infty} e^{i\omega\tau} \langle \delta \Delta B_z(t) \cdot \delta \Delta B_z(t+\tau) \rangle d\tau, \qquad (2.19)$$

the Fourier transformation of the correlator  $\langle \delta \Delta B_z(t) \cdot \delta \Delta B_z(t+\tau) \rangle$ . In the so-called filter-function-formalism<sup>[44]</sup> it can be shown that coherence of the system follows a form  $\exp(-i\Phi)$ , where the decoherence function or phase pick-up is given by

$$\Phi(\tau) = \int_{0}^{\infty} \frac{d\omega}{\pi} S(\omega) \frac{F(\omega \tau)}{\omega^{2}}.$$
 (2.20)

Here the filter function  $F(\omega)$  is a characteristic function describing the frequency sensitivity of a certain decoupling pulse scheme. The calculation of  $\Phi$  for the Hahn echo including quadrupolar broadening of Larmor frequencies and an electronic g-factor anisotropy will be presented in great detail in Ch. 6.

#### 2.6.3. Dynamic nuclear polarization

So far we have discussed several types of interaction with the nuclear environment and concluded that they mainly lead to dephasing and loss of coherence of the electron spin. An obvious but hasty decision would be to abandon nuclear spin by using different, nuclear-free heterostructures to confine the electrons in a so-called semiconductor vacuum. On the contrary, nuclear spins, once controllable, offer great potential for spin qubit manipulation, especially for the  $ST_0$  qubit as the hyperfine field gradient  $\Delta B_z$  is part of the Hamiltonian. The controlled and intended build-up of local magnetic fields and hence a gradient between the two quantum dots is called dynamic nuclear polarization (DNP). Several schemes using the electron spin to polarize the surrounding nuclei exist and in Ref. 13 a DNP scheme that employs the electron as a hardware feedback was experimentally realized that even stabilizes the gradient at a given value for  $\Delta B_z$ .

This scheme exploits the contact hyperfine interaction to flop a nuclear spin once an electron spin is flipped in a controlled manner. Contrary to what Fig. 2.5 conveys, the  $ST_+$  is actually an avoided crossing and performing adiabatic Landau-Zener sweeps across it can drive transitions between S and  $T_+$ . This transition flips an electron spin, as the magnetic quantum number changes from m=0 to m=-1, and is associated with a nuclear flop, if the hyperfine interaction is the driving force. Repeatedly driving this transition from either side within the spin diffusion time constant increases or decreases the local nuclear polarization. Using the electron to probe the actual magnetic field gradient  $\Delta B_z$  by free induction decay measurements, this scheme can be extended to

build up and stabilize a desired value for  $\Delta B_z$ . The efficiency of nuclear pumping mostly depends on three aspects.

First, the sweep speed across the transition determines the flip probability  $p_{LZ}$  via

$$p_{\rm LZ} = 1 - e^{\frac{2\pi\Delta}{\hbar\alpha}},\tag{2.21}$$

where  $\Delta$  denotes the hyperfine matrix element driving the transition and the parameter  $\alpha = \varepsilon/t$  describes the sweep speed of the detuning  $\varepsilon$ . The slower and more adiabatic the sweep is performed, the higher the flip probability.

Secondly, in order to flop nuclear spins, the force driving the transition must be the hyperfine interaction. For confined electrons in GaAs a competing spin flip mechanism is provided by spin orbit interaction. A spin flip mediated by spin orbit can only occur, if the effective spin orbit field linked to the electron displacement is perpendicular to the external magnetic field. Therefore its contribution to flipping the spin strongly depends on the alignment of the quantum dots relative to the crystal axes and the external magnetic field. For example, a slight misalignment with the [110] crystallographic axis of  $\approx 5^{\circ}$  completely quenches the pulsed DNP scheme. Further details on how spin orbit effects nuclear pumping efficiency can be found in Ref. 45 and in Ch. 9.

The detailed mechanism of nuclear pumping is currently not completely understood, especially the reason behind a gradient build-up remains unclear. Hence, for the maximum pump efficiency the experimenter also needs some luck, as sometimes nuclear pumping just does not work as efficiently as seen in the publication. Up to this day, it is unclear how it exactly depends on dot tuning and on dot sizes. I do not mean to say that this DNP scheme does not reliably work, because it does and one can always create a stabilized  $\Delta B_z$ , but reaching  $T_2^* \geq 150$  ns may not happen every day.

How to actually set up this pulsed-based DNP scheme is explained in more detail in Ch. 5. A novel polarization scheme promising  $T_2^{\star} \approx 6 \mu s$  will be introduced in Ch. 9 and is accompanied by preliminary experimental results.

#### 2.7. Current state of the art: Semiconductor spin qubits

Having it made through most of the theory part<sup>2</sup>, I would like to present the obligatory five criteria for viable qubits originally proposed by David DiVincenzo<sup>[46]</sup>. As this is done in every thesis I read, I would like to mix things up and address these criteria with discussing the current state of the art of spin qubits in GaAs.

#### 2.7.1. Scalable well-defined qubit

As a pioneering platform, spin qubits in GaAs are amongst the most established and most understood semiconductor spin qubit realization to date. The interaction with the

<sup>&</sup>lt;sup>2</sup>trust me, there is more to come

nuclear environment is well known, even though not completely, and can even be used as a control knob for manipulation. Semiconductor spin qubits, being compatible with standard semiconductor processing technology, in general promise good prospects of scalability and devices with up to five quantum dots have been realized so far.

#### 2.7.2. Initialization

As discussed in more detail in Ch. 5, the ST<sub>0</sub>-qubit can be reliably initialized in the ground state S within a few nanoseconds. The fidelity of initialization only depends on the S-T energy splitting and electron temperature.

#### 2.7.3. Universal set of quantum gates

Although in theory the two orthogonal control axes  $J(\varepsilon)$  and  $\Delta B_z$  offer universal single-qubit control, in reality naive rotations around two axes are not feasible due to experimental constraints in the control parameters. We provide a possibility to experimentally realize high-fidelity gates close to the error correction threshold in Ch. 8. This is a remarkable achievement as it was long thought to be impossible to accurately manipulate electron spins in the presence of the nuclear bath.

Entaglement between two ST<sub>0</sub>-qubits has been experimentally realized in Ref.12 although only realizing a low fidelity due to low capacitive coupling. There are currently various schemes to increase this coupling, i.e. by adding a floating gate between the qubits <sup>[47]</sup> or moving to the exchange-mediated coupling region <sup>[48]</sup>. The latter has the advantage to directly benefit from the gate-tuning-protocol discussed in Ch. 8. In my opinion the maximum two-qubit gate fidelity will decide the future fate of GaAs based spin qubits, as surpassing the surface error correction threshold will be a definite ultimatum.

#### 2.7.4. Qubit specific measurement

Exploiting the extraordinary electrical properties of a single electron transistor as a proximal charge detector and using Pauli spin blockade for spin-to-charge conversion, high fidelity single-shot read-out of the qubit's state projected on the  $ST_0$ -axis is possible. Adiabatically mapping the qubit state on the  $|\uparrow\downarrow\rangle-|\downarrow\uparrow\rangle$ -axis further allows accurate read-out of the *x*-axis.

#### 2.7.5. Long coherence times

Long coherence times compared to manipulation time scales allow for high qubit gate fidelities and are a prerequesite for fault-tolerant quantum computing. Tremendous enhancement of both  $T_2^*$  and  $T_2$  has been achieved by either programming the nuclear bath

by means of DNP or by dynamically decoupling the electron spins from nuclear fluctuations. Using the qubit as a hardware feed-back loop increased the ensemble coherence time from  $T_2^{\star} \approx 10\,\mathrm{ns}^{[9]}$  to  $T_2^{\star} \geq 150\,\mathrm{ns}^{[13]}$ . Recent advances in faster determination of the hyperfine gradient using fast FPGA-based electronics and Bayesian Hamiltonian estimation showed  $T_2^{\star} \geq 2\,\mu\mathrm{s}^{[32]}$ . Even longer coherence times can be achieved by applying decoupling pulse schemes and for years the number to beat was  $T_2 \approx 200\,\mu\mathrm{s}^{[15]}$  using a CPMG pulse sequence. Recently it was shown that by applying a nuclear notch filter (a pulse sequence whose filter function is insensitive to the relative nuclear Larmor frequencies) coherence times of 0.8 ms [49] are achievable in GaAs.

Charge noise affecting qubit dephasing via fluctuations in the exchange interaction strength (and possibly via hyperfine fluctuation due to changes in the electrostatic confinement) is another serious challenge (not only in GaAs spin qubits). Although the exact origin is still not completely known, the extrinsic doping layer of the heterostructure is suspected to play an important role and there is recent effort to abandon it in the device architecture, motivated by recent advances in the Si/SiGe community [50].

# 3. Device fabrication

This chapter addresses the different fabrication steps needed in order to produce the quantum dot devices examined Most of the fabricain this thesis. tion process took place in the cleanroom of the 2nd Institute of Physics at RWTH Aachen University, which honestly at this time (early 2012) was actually more of a room with yellow lights and it was jokingly called 'Reinraum, weil nicht jeder 'rein'-kommt'. With the lack of an own evaporator, metal deposition was done at various nearby institutes, i.e. Taubner lab, Institute for Semiconductor Technology and Research Center Jülich. The doped GaAs/AlGaAsheterostructures, grown by molecular beam epitaxy, were provided by either the

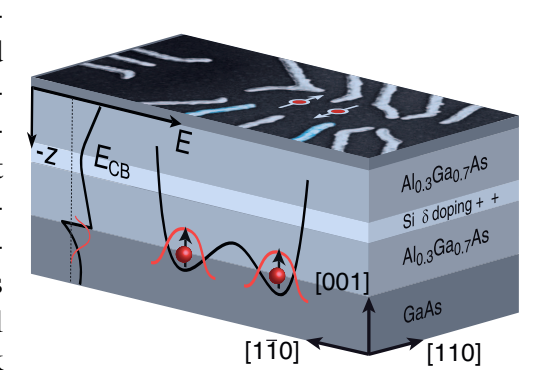


**Figure 3.1.: Device layout.** Applying negative voltages to electrostatic gates on top of a GaAs 2DEG defines the two-electron spin qubit in a double quantum dot potential.

Bougeard lab in Regensburg or the Wieck lab in Bochum.

Although the fabrication of the quantum dots follows a standard recipe for lithography on a GaAs two-dimensional electron gas (2DEG), some obstacles needed to be overcome in order to establish the process in Aachen. Especially the high-resolution e-beam-lithography, to be addressed later in this chapter, took longer than expected.

Before starting this chapter I would like to give some advice for successfully working in the cleanroom. Not all physicists enjoy working in the cleanroom. If you fall in this category, I advise you to fully commit to the fact that you may be staying a long time in the cleanroom, be it during or after working-hours. As the finished device, your time and expertise is more valuable than lab consumables, like acetone, isopropanol or gloves, there is no need to unnecessarily save them; of course don't waste them as well. Always use your own tweezers and clean them regularly. The same applies to your resist. Always use your own private bottle and under no circumstances let other people 'borrow' it (especially not me).

In order to define a lateral quantum dot in a GaAs/AlGaAs heterostructure, electrostatical gates on top of the substrate are used to confine the 2DEG, which typically lies

approximately 100 nm below the surface (see Fig. 3.1). The 2DEG is then contacted by an Au/Ge-alloy, so-called Ohmic contacts. Fabrication includes the following steps (detailed recipe of the individual fabrication steps is given in the Appendix A.1).

# **3.1.** Mesa

Doped heterostructures provide a 2DEG across the whole wafer, hence it is necessary to confine only a local conductive area. Standard positive optical lithography and a subsequent 80 nm etch using diluted piranha acid (see Appendix A.1) is used to produce a  $300 \, \mu \text{m} \times 300 \, \mu \text{m}$  mesa, as depicted in Fig. 3.2. Removing the donor layer outside of this island ensures that the 2DEG underneath cannot be populated and leaves only the mesa conductive.

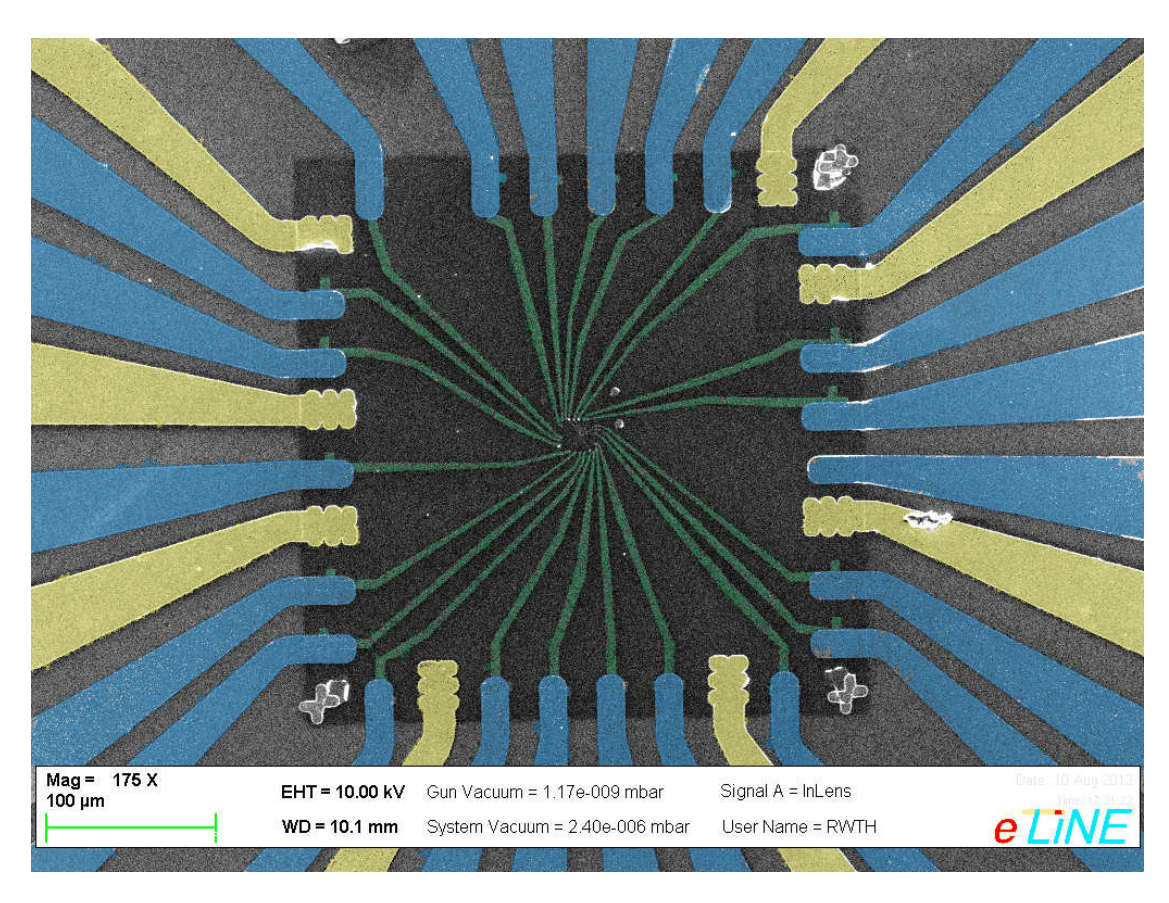


Figure 3.2.: Coarse sample pattern. False color SEM picture of the coarse sample region. Optical gates (blue) connect to the finer e-beam-defined gates (green) on top of the mesa (dark square region). Ohmic contacts (yellow), formed by annealing a gold/germanium alloy, are used to contact the 2DEG beneath the surface.

# 3.2. Ohmic contacts to the 2DEG

The 2DEG, located approximately 100 nm beneath the GaAs surface, needs to be contacted in order to perform transport measurements and define the electrical potential of the 2DEG <sup>1</sup>. For contacting the 2DEG a standard gold/germanium alloy is used. This material has proven to be stable over time and under temperature changes. Furthermore, it shows a linear I-V characteristic and hence these contacts are called Ohmic contacts. To define these contacts, standard negative optical lithography, ensuring a profile undercut, is used for easier lift off. Process parameters for the image reversal resist AR-U 4040 can be taken from Appendix A.1. Different layers of metal, namely 5 nm Ni, 200 nm Au, 100 nm Ge and 75 nm Ni, are then deposited on the sample. A standard lift-off process removes the metal deposited on the resist afterwards. The layout of the Ohmic contacts can be seen in Fig. 3.2 (in yellow).

By annealing the samples at temperatures above 450 °C in a forming gas atmosphere for approximately 50 s the Ge/Au alloy diffuses into the GaAs contacting the 2DEG. Nickel is mainly used as a wetting layer which prevents the gold from balling up on the GaAs surface once heated <sup>[51]</sup>.

A two-terminal resistance of a few  $k\Omega$  at room temperature without illumination is a good indicator for working Ohmic contacts. Once cooled down to 4 K the resistance should drop to a few hundred  $\Omega$  as phonons freeze out.

## 3.3. Electrostatic Gates

Local metal electrodes on top of the GaAs surface are used in order to define a quantum dot. Applying a negative bias to these gates depletes the 2DEG beneath. A double well potential for the electrons can be created by using a suitable pattern for these gates. As quantization of the electron energy inside is a crucial requirement for the quantum dot to act as a two level system, the dimension of those gate structures needs to be on the order of the Fermi wavelength, approximately 50 nm for GaAs.

Patterns at this nanometer-scale can be reliable realized by standard electron

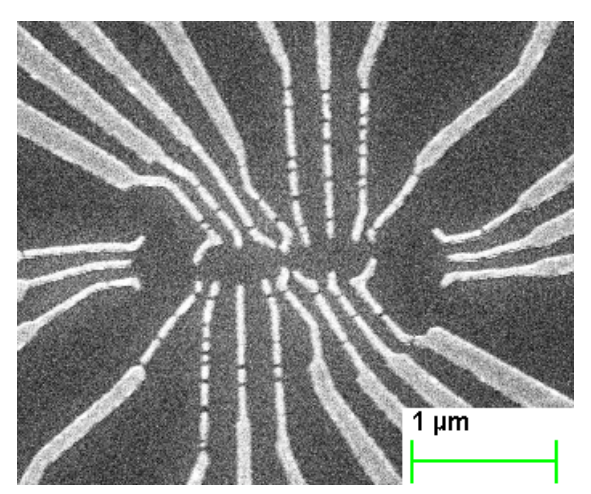


Figure 3.3.: Faulty e-beam-lithography.

Residual resist due to faulty development results in a broken pattern of fine e-beam gates.

<sup>&</sup>lt;sup>1</sup>trust me, you do not want to measure a quantum dot with floating leads

beam lithography (EBL). A focused electron beam is used to expose a PMMA resist and break molecular chains inside, which can subsequently be removed by a suitable developer. To ensure a reliable lift-off process, a two layer resist structure is used. On top of a PMMA layer with a low solid content another layer of PMMA with a higher solid content is spun. The bottom layer, being slightly over-exposed, leads to a profile undercut. This undercut prevents metal deposition on the sides of the pattern and provides a bigger target for the aceton during lift-off. A more detailed description of this process can be found in Appendix A.1.

In order to reach the full potential of EBL, a cold development of the resist in addition to an ultrasonic irradiation has been tested. Standard e-beam developer (MIBK:IPA 1:3) is cooled to 0° C and then used to develop the sample. This cold development will lead to a higher resist contrast, leading to a minimum pattern width of approximately 20 nm. The use of ultrasound during the last five seconds of development helps to remove residual resist that would lead to broken metallic gates otherwise (see Fig. 3.3).

### 3.3.1. Optical Gates

As a last step of sample fabrication, standard negative optical lithography is used to contact the small e-beam pattern with the bond pads by 200 nm thick gold gates (shown as blue gates in Fig. 3.2). A more detailed version of this fabrication step can be found in the Appendix A.1.

# 3.3.2. Quantum dot design

The gate pattern design of the sample layout chosen in this thesis for the double quantum dot is adapted from the Marcus group at Harvard University where it was first used in Ref. 52 and shown in Fig. 3.4. It consists of two adjacent double quantum dots, both connected to a nearby sensing dot. Each double quantum dot is formed by six DC-gates which confine the electrons. Two RF-gates are used exclusively to manipulate the double dot potential using voltage pulses on the nanosecond time scale. Typically, these gates do not contribute in forming the dots, although they may be used as additional DC-gates when using the 2DEG as a global gate to open the barriers to the leads. This method was only used in the very first cooldown when I was forced to use transport measurements through the dot for tuning due to a broken coaxial cable in the read-out circuit.

# 3.4. Sample testing

This section explains the methods I used for sample testing. After checking all electrical connections on the PCB and experimental setup, a very fast and crude room tempera-

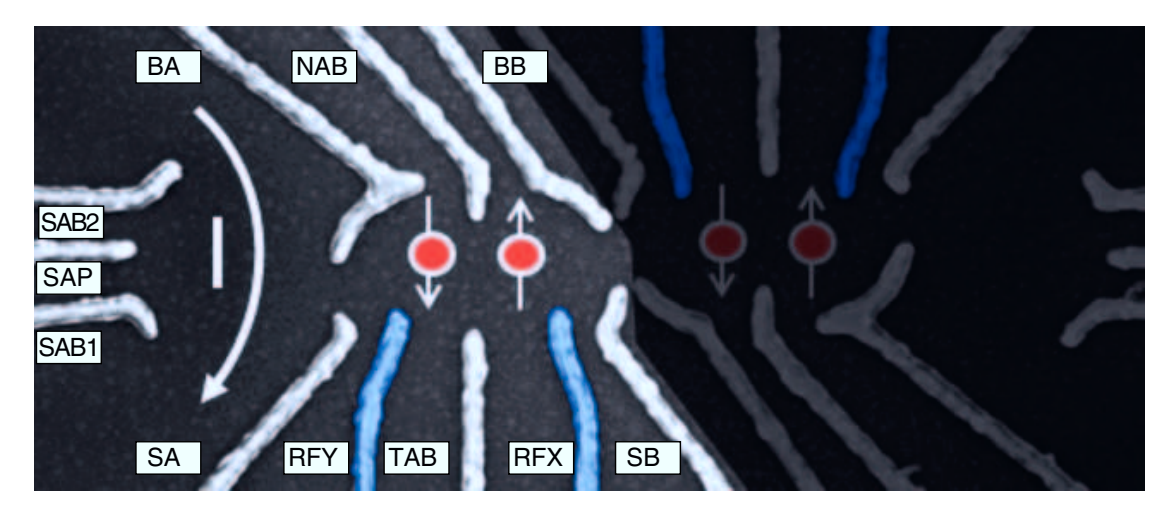


**Figure 3.4.:** Fine e-beam gates. High resolution SEM picture of the double dot region, showing the nomenclature of the gates used to define the double quantum dot and the nearby sensing dot. Applying static voltages on the white gates confines two electrons inside a double-well potential. Manipulation of the electrons is done exclusively by applying fast voltage pulses on the RF-gates, depicted in blue.

ture test is performed deciding wether or not to cool the sample to 4 K. During this 4 K measurement, which was always performed in a test setup, the functionality of all gates and Ohmic contacts is checked prior to a full cooldown in the dilution refrigerator. Furthermore, the resonance frequency of the tank circuit was adjusted to fit the bandwidth of the read-out circuit (see chapters 4 and 5 for further details).

### 3.4.1. Room temperature checks

In order to decide if a particular sample is worth dipping in liquid helium, the device is mounted onto the 4K dipstick and the IV-characteristic of each gate or Ohmic contact is measured individually with a source-measure-unit. A working gate contact typically shows very low leakage current of a few nA for negative voltages which increases when illuminating the sample. Providing a Schottky barrier, this behavior changes when a positive applied voltage surpasses the work function of GaAs at approximately 0.7 V and a sudden leakage current to ground sets in. To protect the sample it is advisable to set a compliance of  $1\,\mu\text{A}$ . Working Ohmic contacts show a linear, polarity independent IV-curve (as expected from their name). Typically a bias voltage of a few mV was used to measure the two-point resistance between two Ohmics of  $2\,\text{k}\Omega$ .

### 3.4.2. Gate testing at 4K

It is not advisable (at least I was told so) to check the gates with a SEM as the electrons may damage the 2DEG, hence the easiest way to verify working gates is by determining the pinch-off voltage of the gates. At this voltage the gates suppress conductivity between two Ohmic terminals and its value can be seen as an indicator for the distance between the gates. For a usual distance of a few tens of nanometers a typical pinch-off voltage would range from -0.6 to -1.2 V. An incomplete pinch-off or a more negative voltage would therefore indicate missing e-beam patterns. Furthermore, the shape of the pinch-off characteristics usually contains useful information. A typical pinch-off curve for the double quantum dot samples used here comprises three different characteristic kinks, originating from different gate regions as shown in Fig. 3.5. Broader gate structures far way from the small region depicted in Fig.3.4

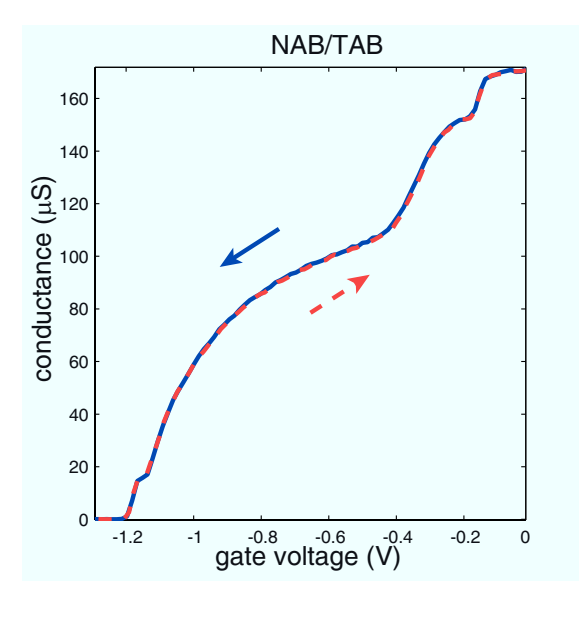


**Figure 3.5.: 4K gate test.** Characteristic pinch-off curve for a working, tunable gate pair NAB/TAB showing three distinct kinks.

lead to the first two kinks. As a certain negative voltage threshold is reached, the area underneath these gate structures becomes insulating all at once, resulting in a steep drop of conductance that is nearly untunable. Once these voltages are surpassed, the fine ebeam patterns ideally show a nearly linear response, pinching off the remaining 2DEG. The flatter this final kink is, the more control for fine tuning of later tunnel rates is provided (see Ch. 5). The pinch-off characteristic should ideally show no sign of hysteresis when sweeping the gates back and forth. Ideally, the pinch-off curves of the left and right quantum dot of one double quantum dot should be identical. In reality however, we have to apply negative voltages to the adjacent double quantum dot in order to measure conductance through the device as some of the Ohmic contacts are shorted due to a lack of available DC connections (see Ch. A.2 for details). Therefore, the pinch-off of the BB and SB gates occurs at a slightly more positive voltage ( $\approx 10~\%$ ). Furthermore, some of the gate combination (especially the ones including SAP/SDP) may not completely pinch off at -1.5 V. But as long as they show an onset of the final kink we assume a working gate pattern.

# 4. Experimental setup

This chapter addresses the set-up of the cryogenic experiment which mostly took place during my first year at the institute. I will provide detailed information about the modifications we performed on the Ice Oxford dilution refrigerator that allow us to perform high frequency measurements at the mK-temperature scale. Apart from wiring and filtering, I will further explain the installation of a partly cryogenic RF-read-out circuit.

# 4.1. Ice Oxford dilution refrigerator

All measurements performed in my thesis were carried out in an Ice Oxford dilution refrigerator with a base temperature of  $20 \,\mathrm{mK}$  and  $200 \,\mu\mathrm{W}$  cooling power specified at  $100 \,\mathrm{mK}$ . The system arrived equipped with 96 DC-lines down to the mixing chamber, 8 AC-lines mounted down to the 1 K stage and a 7-3-1 T 3D vector magnet. The insert was further modified to match our demands by adding filters to the DC-lines, extending the coaxial lines to the sample, and by installing a sample holder and the high frequency equipment for the RF-readout (see Fig. 4.1).

# 4.2. Wiring

In order to probe the quantum mechanical properties of our quantum dot device, the temperature should be well below 1 K. To reach these kind of temperatures, we use the above-mentioned dilution refrigerator to cool down the heterostructure to  $\approx 25\,\text{mK}$ . Although phonons of the host material will reside at a similar temperature, the confined electrons are typically hotter at  $\approx 100\,\text{mK}$  as they are connected to a high frequency read-out and control circuit. Operating at high frequencies in an ultra-cold environment is an experimentally challenging undertaking and requires thoughtful design of thermal anchoring, filtering of electrical connections and choosing the right material. I guess every group has their own standards and relies on setups that have worked for them. In the beginning of my thesis I built (and of course added modifications to) a setup similar to one previously established in the Yacoby lab at Harvard University (see Ref. 37 for further details). I will address the main technical aspects in the following. A nearly complete overview of the electrical wiring and filtering of the setup is depicted in Fig. 4.2.

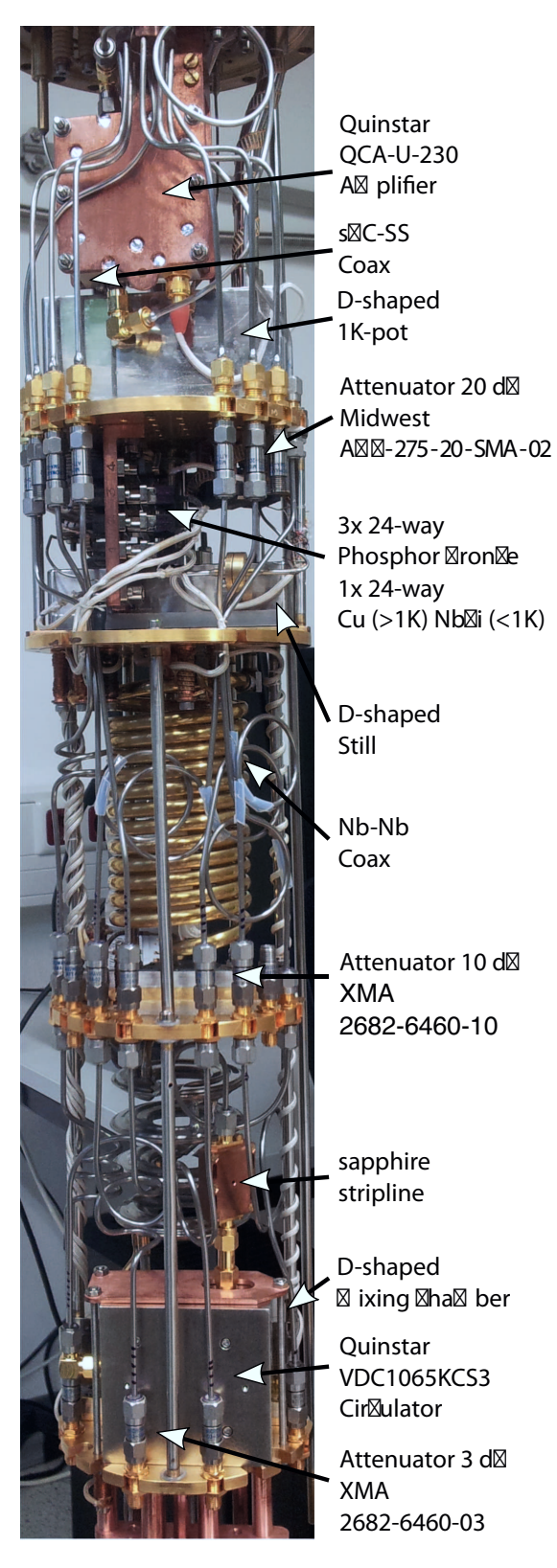


**Figure 4.1.: ICE Oxford dilution refrigerator.** Installation of the RF-equipment including a cryogenic circulator at the mixing chamber and a cryogenic amplifier at the 1 K stage, and various semi-rigid coaxial lines.

## 4.2.1. DC wiring and filtering

The insert of the dilution refrigerator arrived in Aachen with 4 DC looms (3 phosphorbronze, 1 copper), each containing 12 twisted pair wires for a total of 96 DC-lines from room temperature to the mixing chamber. In order to thermalize the wires (and eventually the sample), the looms are anchored at various temperature stages by wrapping them around and gluing them to copper bobbins. As electron temperature and coherence times are sensitive to electric noise, heavy filtering of the DC-lines is essential for qubit performance.

### Room temperature filtering

At room temperature, we employed low-pass filters (MiniCircuit BLP-1.9) with a cut-off frequency of 1.9 MHz to minimize coupling of room temperature radiation from our home-built voltage sources (DecaDAC) to the break-out-boxes, which provide the link between the cold woven looms and coaxial cables at room temperature. We further added an optional two-stage low-pass filter with capacitances  $0.47\,\mu\text{F}$  and  $22\,\mu\text{F}$  on a printed circuit board (PCB) inside the break-out boxes. In order to exploit the maximum voltage resolution (16 bit for a 10 V range), an optional 1:11 voltage divider can be added. Note that some of the voltage dividers were changed to a ratio of 1:6 later, as some of the gates required a more negative bias. All electrical components were situated inside an RF-sealed aluminum box to ensure good grounding. A circuit diagram of all components can be found in Ch. A.4.

### 48-pin filter box

At the mixing chamber stage, a 48-pin filter box comprising another two-stage RC-filter was installed. The filter box consists of three RF-sealed chambers, each connected by either feed-through resistors or feed-through capacitors, to minimize stray capacitance from the circuit elements. As feed-through resistors are commercially not available, I glued the bodies of regular  $1 \, \mathrm{k} \Omega$  metal film resistors into a thin copper plate. Making the hole in the copper as tight as possible and using conductive epoxy hinders the propagation of electrical field lines from one chamber to the other and hence reduces spurious resonances in the RC-filter. A room temperature transmission measurement<sup>2</sup>, depicted in Fig. 4.3, shows a high attenuation of order -80 dB with the absence of high frequency resonances. A commercial capacitative filter plate was used with capacitances of 4 nF at room temperature. A schematic wiring of the filter box can be found in the in Ch. A.5

<sup>&</sup>lt;sup>1</sup>and ensure sample safety

<sup>&</sup>lt;sup>2</sup>although it is difficult to test a high impedance filter at high frequencies

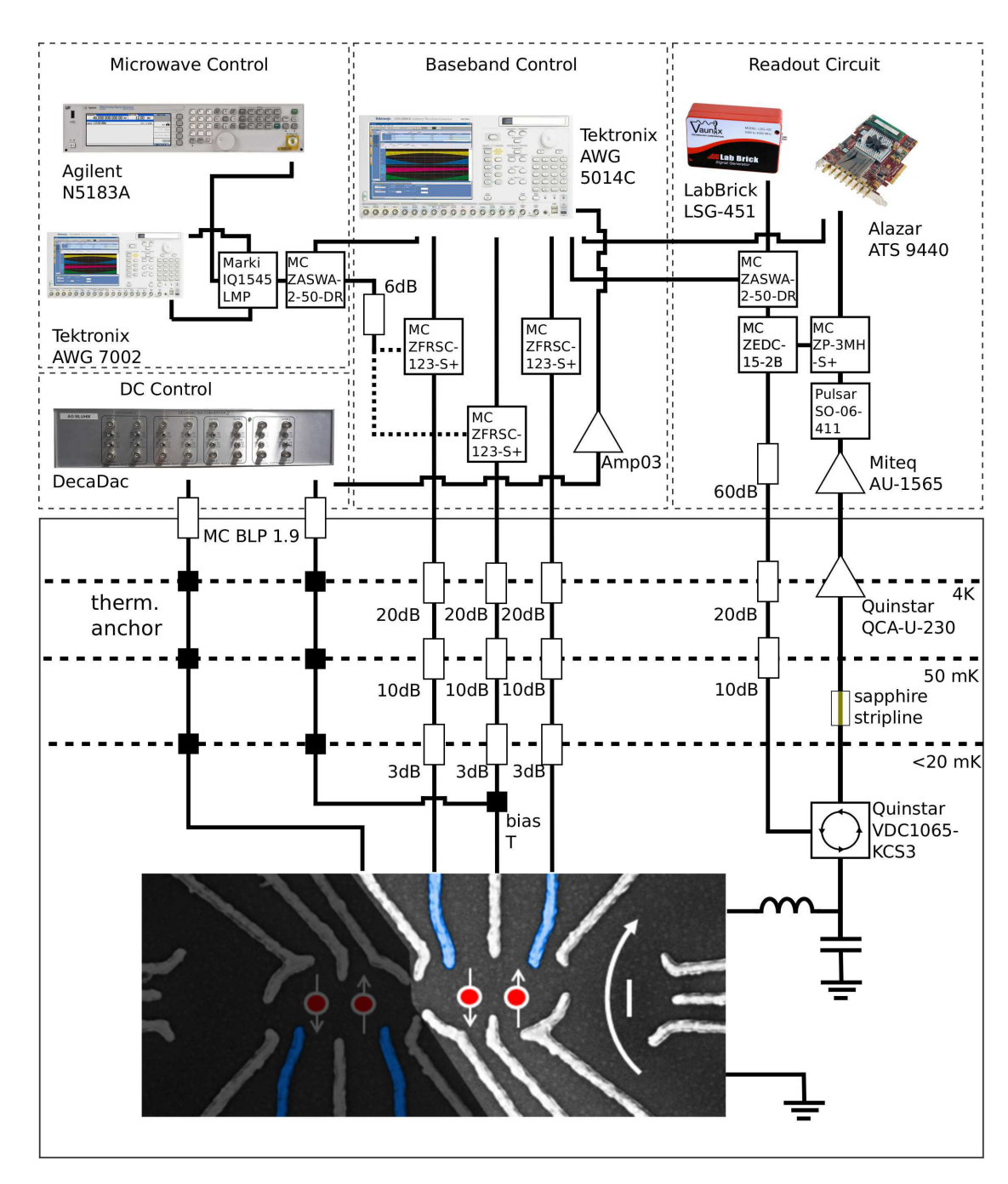


**Figure 4.2.: Schematic setup.** Wiring scheme and electrical equipment used for the ICE Oxford dilution refrigerator. Details concerning the DC control part are given in Ch. 4.2.1. Ch. 4.2.2 discusses the AC-control part and the RF-read-out circuit is addressed in Ch. 4.3.

### Filtering on the PCB

The second capacitor of 10 nF for the two-stage filter mentioned above is soldered onto the sample PCB, as depicted in Fig. 4.5. It is brought as close to the device as possible to filter out noise, thus preventing coupling of noise into the DC-lines. Note, in order to guarantee low temperature functionality, temperature stable ceramic capacitors should be used, usually referred to as NPO (negative positive 0) capacitors.

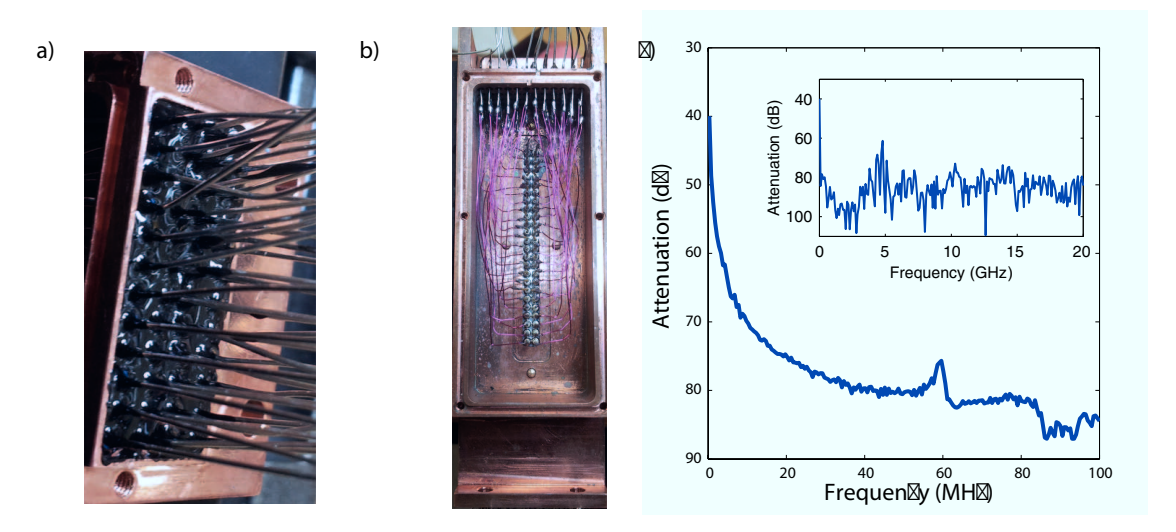


**Figure 4.3.:** Cryogenic filterbox. **a** A homebuilt feed-through resistor plate minimizes stray capacitance of the lumped elements. **b** A capacitive filter plate connects the two resistor plates. **c** Transmission through the filterbox employing a two-stage RC filter of  $2 \times 1 \text{ k}\Omega$  and 4 nF (an additional 10 nF are directly soldered onto the sample PCB). The inset shows a wider frequency range.

# **4.2.2. AC** wiring

Compared to the DC-wiring, installation of the semi-rigid coaxial cable is straightforward once the materials of the inner and outer connector are chosen. Unfortunately, choosing the right material is quite a dilemma, as good thermal isolation, needed to reach ultra cold temperatures, usually contradicts good electrical conductivity, which is required for high bandwidth high frequency lines. There is no real ideal solution at hand and different groups use different materials. For our fridge, we settled with the following choices.

From room temperature to the 1 K-pot, we used coaxial cables with a stainless steel outer conductor and a silver-coated beryllium-copper inner conductor. Stainless steel and beryllium-copper are bad conductors and hence bad thermal conductors as well (electrons contribute significantly to thermal conductivity). As high frequencies mostly

travel inside the dielectric and only penetrate the metal conductors superficially (the skin depth is inversely proportional to the square root of the frequency), coating the outer side of the inner conductor with a good electrical conductor, silver in our case, increases the bandwidth of the cable without adding an unnecessary heat load. From the 1 K-pot to the mixing chamber, we chose to use niobium semi-rigid cables. At these temperatures niobium becomes superconducting, resulting in very good electrical conductivity and a high thermal resistivity as low energy electronic excitations are absent and only cold phonons contribute. Once we reach base temperature at the mixing chamber, we swapped to pure copper semi-rigid cables which are good thermal and electrical conductors. At this stage we do not apply additional heat loads and are mostly interested in thermally anchoring the sample.

Some of the AC-control lines are combined with the DC-lines via simple bias-Tees, soldered onto the PCB, as can be seen in Fig. 4.5. In order to minimize resonance effects, we abandon inductors and only use a  $10 \, \text{nF}$  capacitor (directly soldered between coaxial cable and the PCB) and a  $1 \, \text{k}\Omega$  SMD-resistor.

At room temperature, the control AC-lines are connected to a Tektronix AWG5014C via resistive splitters (MiniCircuit ZFRSC-123-S+), providing an additional 10 dB attenuation. Optionally, an additional RF-source (Agilent N5183A) can be installed into the control pathway using a 6 dB attenuator to ensure impedance matching. Using another AWG (Tektronix AWG7002) and an IQ-mixer allows for rapid vector control of the RF-output.

#### **AC** filtering

We do not install any direct filters<sup>3</sup> in the ac-control lines coming from the Tektronix AWG 5014c but attenuate the room temperature noise at different temperature stages. As thermal noise is proportional to  $k_BT$ , we introduce a 20 dB attenuator into the AC pathway at the 1 K stage to account for the temperature change (20 dB is a factor 100 which equals the temperature ratio). For a similar reason, we further install 10 dB attenuation at 100 mK and 3 dB at base temperature. We distribute attenuation over various cooling stages according to their cooling power.

# 4.3. RF-readout

In the last couple of years the technique of RF-reflectometry has become the standard way of measuring qubits [53,35,54]. In our case, we employ a proximal sensor quantum dot as the resistive part of an impedance matching LC-tank circuit and measure the reflected amplitude of a carrier signal that is proportional to the actual resistance of the quantum dot. There already is a vast variety of excellent work explaining the very

<sup>&</sup>lt;sup>3</sup>badly conducting coaxial cables are very effective at filtering high frequencies

details of this method and I doubt I can provide a better job. Hence, in this section I will only present the basics of this readout technique and motivate the interested reader to look at Ch. 5 and Refs.37,35 for further information.

In this work, we use a setup based on the designs discussed in Refs.35 with the addition of a cold circulator at the mixing chamber stage. In order to rapidly<sup>4</sup> measure the qubit's state, the nearby charge sensor is integrated into a LC-tank-circuit (see Fig. 4.5) to match its impedance of typically  $50 \, \mathrm{k}\Omega$  to the attached  $50 \, \Omega$  impedance of the semirigid coaxial cable. We then sense the impedance of the charge sensor by measuring the reflected RF-power of this tank circuit, using a home-built high frequency, high bandwidth lock-in amplifier, that is realized in the following way.

The carrier frequency, usually between 220 and 240 MHz, is generated by a LabBrick LSG-451 signal generator and set to the resonance frequency of the tank circuit. The signal passes a Minicircuit ZASWA-2-50-DR switch and is then divided into two pathways (sample and local oscillator) using a Minicircuit ZEDC-15-2B directional coupler. The attenuated signal is then further attenuated by 60 dB at room temperature and 33 dB inside the fridge and sent to the tank-circuit via a Quinstar VDC1065KCS3 circulator at a power of approximately -100 dBm. The reflected signal is proportional to the resistance of the quantum dot and is sent to a cryogenic amplifier (Quinstar QCA-U-230) via the circulator and a sapphire stripline, used to thermalize the inner conductor of the output readout line. Both components are not quite impedance matched, hence it is important to have a circulator that redirects direct reflection away from the sample pathway. At room temperature the signal is further amplified using a low-noise Miteq AU-1565 amplifier. After the phase of the signal has been corrected for the coaxial lines using a Pulsar SO-05-411 phase shifter, the signal is down-converted to DC in a Minicircuit ZP-3MH-S+ mixer with the original local oscillator signal. In a final step, the signal is recorded using an Alazar ATS9440 digitizer. We also added filters for the input and output signals (Minicircuit SHP-50+ and SHP-450+) and a low-pass filter BBLP-39+ after the mixer to filter out the frequency-doubled signal and other unwanted signals.

## 4.3.1. Choice of components

The choice of the inductance of the combined RLC-tank circuit defines not only the resonance frequency  $\omega_{res} = 1/\sqrt{LC_{stray}}$ , but also the impedance at  $\omega_{res}$ 

$$Z_{\rm RLC} = \frac{L}{R_{\rm SD}C_{\rm stray}},\tag{4.1}$$

where L is the inductance,  $R_{\rm SD}$  the sensor dot resistance and  $C_{\rm stray}$  the stray capacitance. On the one hand, we have to match the frequency range of the experimental setup which is determined by the cryogenic circulator to 220-240 MHz. On the other hand we want

<sup>&</sup>lt;sup>4</sup>sampling frequency is 100 MHz typically down-sampled to 250 kHz

 $Z_{RLC} \approx 50\,\Omega$ , close to the impedance of the RF-equipment. We typically use inductors from 680-820 nH, depending on the stray capacitance of the PCB and the sample. The first PCB had higher stray capacitance, hence the 680 nH inductor was used. Stray capacitances were 0.4 pF from the coil and the PCB and 0.3 pF from wire bonding and sample design. After removing some parts of the soldering mask for the inductor, I managed to reduce the stray capacitance and use the 820 nH inductor.

# 4.4. Cold finger design

To place the sample at the center of the vector magnet a sample holder was constructed, in the following referred to as cold finger and depicted in Fig. 4.4. It was designed to be RF-sealed and to prevent infrared radiation from the inner vacuum chamber reaching the actual sample. For that purpose, I designed a screwable brass can that can be easily attached to the copper plate which holds the connection to the 48-pin filter box and the four AC-lines (SMPM connectors). The copper rods mounting the adapter plate to the mixing chamber are slitted to minimize heating effects due to eddy currents in a magnetic field.

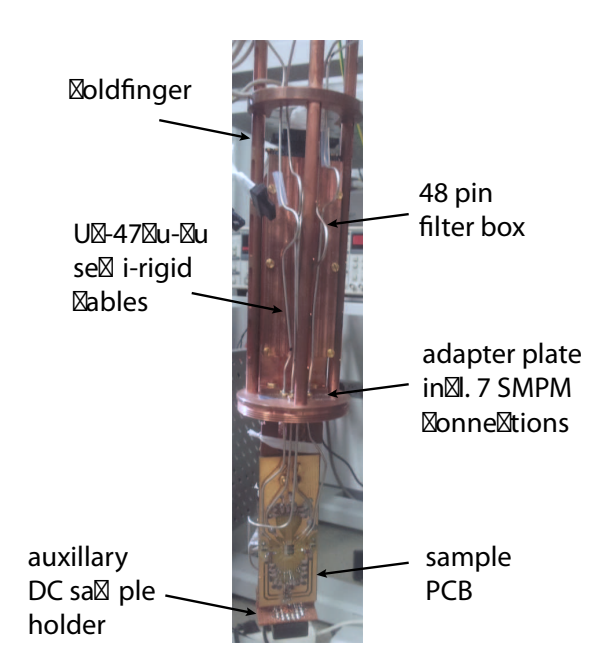


**Figure 4.4.:** Cold finger. The cold finger designed to hold the sample (and an auxiliary sample) in the center of the magnet. A brass can can be screwed to the adapter plate that holds the DC- and AC-connectors in order to shield the sample from radiation.

<sup>&</sup>lt;sup>5</sup>after loosening roughly 100 screws to reach the sample holder it is actually also nice to just untwist the cold finger

# 4.5. Sample printed circuit board

The actual device is glued onto a PCB using temperature resistant GE varnish. The sample board I used in my thesis was originally designed by David Reilly at Harvard University. The layout and functionality is not optimal for our double quantum dot design including 4 AC control lines and demands some experimental dexterity in wirebonding and placing the electrical components for filtering and manipulation (see Fig. 4.5).

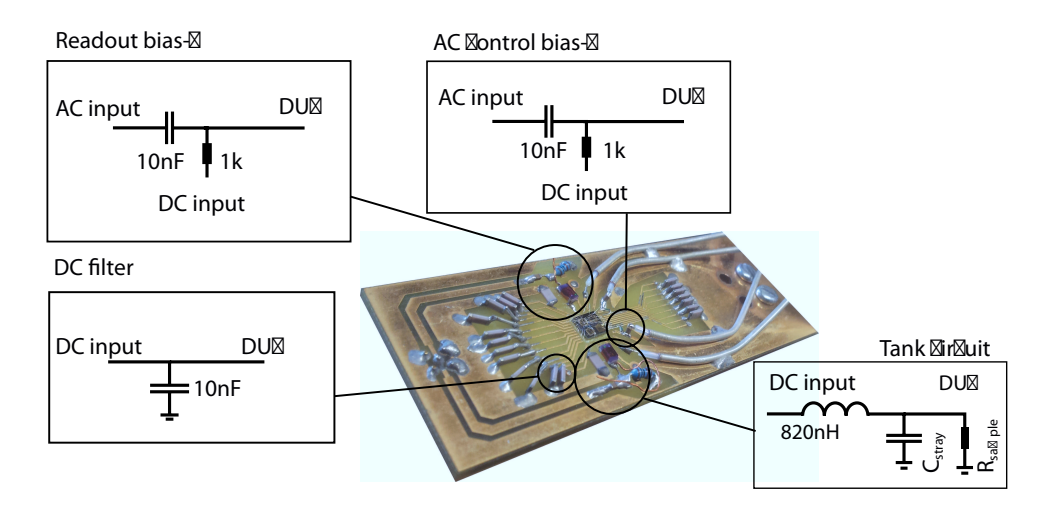


**Figure 4.5.: PCB control and filter wiring scheme.** The legacy PCB for the final electrical connection to the sample designed by David Reilly at Harvard University. Using SMD components, low pass filters and bias-T's were realized on the PCB in proximity of the sample.

With the lack of a solder mask envisioned for the 10 nF capacitors used for filtering, the SMD components<sup>6</sup> were simply soldered to the PCB DC-lines using pieces of copper wire, as can be seen in Fig. 4.5. The capacitors needed for the bias-Tees were also soldered directly between the inner conductor of the coaxial cable and the AC bond pad. In order to fine-tune the resonance frequency of the tank circuit, a small copper wire is soldered next to the inductor and adds a certain amount of stray capacitance depending on its proximity to the other components. Furthermore, bonding the sample is challenging as especially the AC control lines are quite far away from the PCB connections and needed to be bonded all across the sample (see Ch. A.2 for further details).

A simple micro D-sub-connector is soldered to the DC-pins using a copper woven loom. The readout line is connected using a SMPM connector. Having done extensive research for the best ultra-miniature RF-connectors, we settled for SMPM connectors as

<sup>&</sup>lt;sup>6</sup>The 1 k SMD resistor used in the first cool-down was replaced by a mini-MELf version to ensure better temperature stability.

they provide excellent impedance matching and offer all connection types and genders needed for our purposes.

# 4.6. General data acquisition

Data acquisition for all measurements performed in this work has been done using special measure, a command line based package for Matlab developed by Hendrik Bluhm. This acquisition software on the one hand allows to perform fast two-dimensional gate voltage sweeps by exploiting hardware ramps and synchronized buffered readout of instruments. These types of measurement are predominantly used while tuning up a quantum dot device. On the other hand, in combination with the software package pulsecontrol, that provides its own programming language for defining waveforms on the Tektronix AWG, special measure allows for combining rapid pulse-based control and fast, high bandwidth data acquisition, as schematically explained in Fig. 4.6. Being command line based, special measure offers fast prototyping of novel experiments.

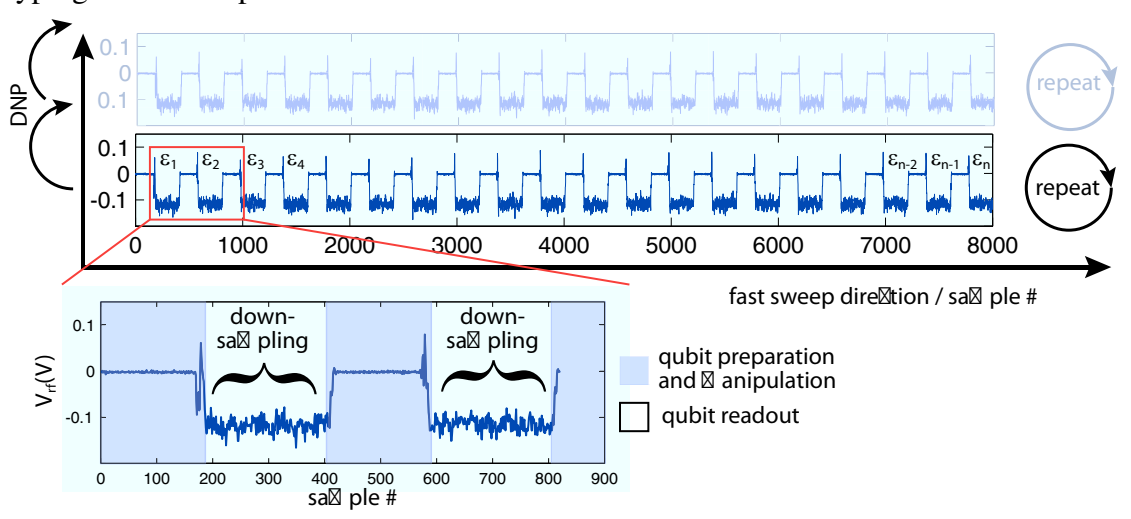


**Figure 4.6.: Schematic flow of typical data acquisition.** Typically, a scanline consists of one or more pulse groups, each comprising several pulses with different parameters, i.e.  $\varepsilon_i$ , repeated to match a certain buffer size of the Alazar digitizer. Between repetitions of scanlines, DNP pulses are applied to the qubit without measuring. We always sample with a constant hardware sample rate of 100 MHz and average over the duration of the readout window, indicated by the white areas; we only apply readout power during that time. Eventually each  $2.5 \,\mu s$  measurement window is downsampled to one measurement point. For a typical pulse length of  $4 \,\mu s$  the downsampling frequency is  $250 \, kHz$ .

<sup>&</sup>lt;sup>7</sup>once the driver works properly

# 5. Tuning methods for semiconductor spin qubits

Parts of this chapter are in preparation for publication<sup>1</sup>.

### 5.1. Abstract

We present methods and measurements to reliably characterize and tune-up gate-defined semiconductor spin qubits. Our methods are designed to target the tuning procedures of semiconductor double quantum dot in GaAs heterostructures and are applicable to ST<sub>0</sub>- and Loss-DiVincenzo-qubits, but can easily be adapted to other quantum-dot-like qubit systems. These tuning procedures include characterization of the inter-dot tunnel coupling, the tunnel coupling to the surrounding leads and finding the locations of various fast initialization points for the qubit. As these semiconductor based spin qubits, being compatible with standard semiconductor processing technology, promise good prospects of scalability, this challenge will only grow in the near future once the multi-qubit stage is reached. With the anticipation to be used as the basis for future automated tuning protocols, all measurements presented here are fast to execute and easy to analyse characterization methods. They result in quantitative measures of the relevant qubit parameters within a couple of seconds of measurement time and require almost no human interference.

### 5.2. Introduction

The recent development in semiconductor based spin qubits [55,56,57,58,59,60,61,62,63] shows their great potential as building blocks of a quantum computer and demonstrates their promise for scalable architectures. With increasing number of physical qubits, challenges like device architecture [64,65,66], long-range coupling [67,68,69], error correction [14,70], decoherence due to charge noise [71,72] and scalable implementation [73,74] of

<sup>&</sup>lt;sup>1</sup>Molecular-beam-epitaxy growth of the sample was carried out by D. Schuh and D. Bougeard. T.Botzem fabricated the sample, set-up and conducted the experiment. T. Botzem, M. Shulman, S. Foletti, S. Harvey, O. Dial and H. Bluhm developed the various tuning methods and fit models, T. Botzem and H. Bluhm wrote the paper with input from all co-authors.

the control electronics<sup>[75,76]</sup> play an increasingly important role. One obstacle that has not received much attention so far is the tuning of the qubit devices. Especially in the case of gate-defined quantum dots, this procedure itself presents a non-trivial task even in the case of just two electron spins, as each quantum dot comprises at least three electrostatic gate electrodes, all capacitively coupled, which all influence the number of electrons, the tunnel coupling to the adjacent lead, and the inter-dot tunnel coupling. The current practice of manually tuning the qubits is a time-consuming and non-scalable procedure.

In this work we present tuning and characterization methods used to realize two-electron spin qubits in GaAs that have evolved over the course of the experiments in Refs. 15,13,12,77,32,45,78,55. Complementary to Ref. 79 that showed a computer automation to coarse-tune quantum dots into the single-electron regime, we focus on the fine-tuning of the spin qubit once this regime has been reached. We exploit the high-bandwidth readout by radiofrequency (RF)-reflectometry [53,35] of semiconductor spin qubits and present fast, easy analyzed and quantitative measurements to characterize these devices. Contrary to the relatively slow tuning using DC-transport [11], all necessary scans can be performed within a few seconds of measurement time. Furthermore, as the tuning parameters of interest are obtained directly as fit parameters and require no human intervention, these methods are well suited as a basis for full automation of the complete tuning procedure. Note that all measurements presented here were performed on two-electron spin qubits in GaAs quantum dots, but the basic tuning principles can easily be adapted to other quantum-dot-like qubit systems.

The outline of this paper is as follows: In Sec. 5.3 we first introduce the device layout of the two-electron spin qubit in GaAs and explain the basics of the experimental setup including the RF-reflectometry circuit.

The first step of tuning the device to either the (2,0)-(1,1) or the (1,1)-(0,2)-charge-transition (the numbers indicate the occupancy in each dot) will be covered in Sec. 5.4. Furthermore, the formation of the adjacent quantum dot for readout via charge sensing is described. These methods have hardly changed compared to legacy quantum transport measurements<sup>[11]</sup> and will need further refinement<sup>[79]</sup> for automation. They are included here for completeness.

In Sec. 5.5 we present our methods to quantitatively characterize and fine-tune the resulting qubit. We first motivate the use of virtual gates, a linear combination of several gates that allows changing specific junction parameters individually. We continue by describing the characterization of the inter-dot tunnel coupling  $t_c$  and the tunnel couplings to the left and right electron reservoirs,  $t_l$  and  $t_r$ , which must be tunable to certain values. Although these three properties already define the qubit, the gate voltages at which various qubit operations can be carried out have to be determined. Hence, we additionally provide routines for locating fast reload points, used to initialize the qubit in different states, and the  $ST_+$  anti-crossing, allowing us to set up a hardware feed-

back loop to polarize and stabilize the surrounding nuclear spin bath in the GaAs host material.

In the last sections, we provide information on how to set-up the pulsed hardware feedback to stabilize the hyperfine gradient  $\Delta B_z$  from Ref. 13. Furthermore, we outline an experiment to measure the detuning dependent energy splitting  $J(\varepsilon)$  of the qubit. At last, the setup of an automated detection of charge rearrangements is provided.

# 5.3. Device layout and experimental setup

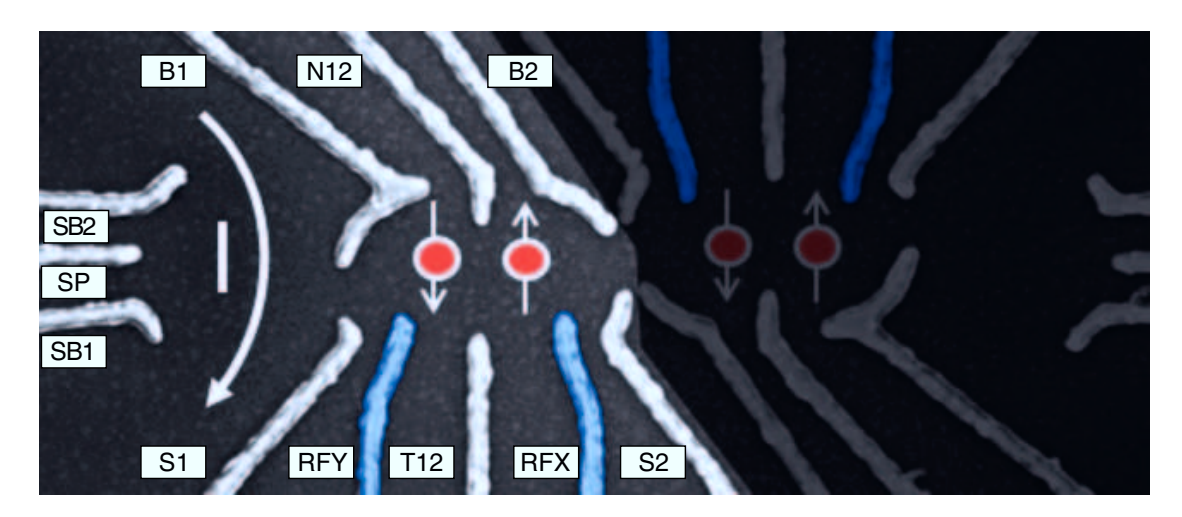


**Figure 5.1.: Device Layout.** The figure depicts the device and nomenclature of the gates used to form the two-electron spin qubit in this work (only left side is used, but same procedure can be applied to the right double quantum dot, as shown in Ref. 12). Applying static voltages to the grey gates confines two electrons in a double dot potential in the 2DEG of a GaAs/Al<sub>0.69</sub>Ga<sub>0.31</sub>As heterostructure. The blue gates, RFX and RFY, are used exclusively for fast manipulation and are DC-coupled to a Tektronix AWG5014C. A charge sensing dot can be seen next to each qubit.

While very similar tuning methods were employed in Refs. 12,77,32,45, the particular data shown in this paper is obtained from the qubit in Refs. 78,55. The two-electron ST<sub>0</sub> spin qubit is defined by the  $m_z = 0$  subspace  $S = (|\uparrow\downarrow\rangle - |\downarrow\uparrow\rangle)/\sqrt{2}$  and  $T_0 = (|\uparrow\downarrow\rangle + |\downarrow\uparrow\rangle)/\sqrt{2}$  of two electron spins [25], where  $\uparrow$  or  $\downarrow$  describes the spin state of the electrons. These electrons are confined in a GaAs double quantum dot formed by electrostatic gates on top of a two-dimensional electron gas (2DEG), shown in Fig. 5.1.

The legacy quantum dot layout, for example from Refs. 9,80, uses a single gate for high and low frequency control combined with a (home-built or commercial) bias tee. Home built, on-chip bias tee's, as used in Refs. 13,11 have the advantage of avoiding difficult-to-model additional inductances in the DC-arm, but still show pulse distortion

that need to be corrected for in order to achieve optimal fidelity between intended and actual pulses. [13]. To avoid this complication and the resulting pulse imperfections, we exploit dedicated all DC-coupled static and high frequency control gates. Static voltages of order 1 V, provided by a home-built voltage source, are applied to the heavily filtered static gates (depicted in grey in Fig. 5.1) and are used to define and tune the quantum dots into the single-electron regime. The control gates (depicted in blue in Fig. 5.1), used for qubit manipulation by applying mV-scale signals, are DC-coupled to an arbitrary waveform generator Tektronix AWG5014C, operated at 1 GS/s. Using separated static and control gates eliminates the need for bias tee's and results in a nearly flat frequency response of the control gates from DC to a few hundred MHz at a cost of one additional gate electrode. The control gates are attenuated by 33 dB to reduce thermal noise from room temperature.

To directly measure the conductance through the double dot and the sensing dot, a voltage bias of typically  $100~\mu V$  is applied across the device. The current through the sample, converted to a voltage  $V_{\rm SD}$  or  $V_{\rm D}$  for the sensing dot and double dot, respectively, using a home-built IV-converter, is measured with a Standford Research SR830 lock-in amplifier. This measurement technique is only used in the initial coarse tuning of the quantum dots and later omitted.

To enable readout via spin-to-charge conversion due to Pauli-spin-blockade, a sensing dot is placed next to the qubit. It is embedded as the resistive component in an impedance matching circuit so that the conductance through the dot can also be monitored using RF-reflectometry<sup>[53,35,54]</sup>. A similar setup to Ref. 35 is used, with the addition of a cryogenic circulator at base temperature. The demodulated signal  $V_{\rm rf}$  is recorded using an Alazar ATS9440 digitizer board. We typically use a hardware sample rate of 100 MS/s which we downsample on the fly at full data rate to typically 250 kHz using a multithreaded, high throughput C++-based driver for the Alazar card. This downsampled rate arises from a typical length of 4 µs for experiments which usually comprises a  $2.5 \mu s$  long measurement window during which we power the RF-circuit. A standard probe cycle, used in the tuning protocol but also the actual qubit experiments, consist of initialization, manipulation at different voltages or for different times, and measurement of the final state of the qubit. The triplet return probability P(T) is proportional to  $V_{\rm rf}$  and the readout circuit is tuned such that a low value of the signal corresponds to the singlet and a higher value to the triplet states. Effects of 1/f-like noise are eliminated from the data by changing the swept pulse parameter after each single cycle and then averaging over many repetitions of the parameter sweep to elude slow drifts in the sensor or gate voltage configuration. For a typical tuning dataset, the sweep comprises 100 values and is repeated 1536 times for a total measurement time of  $1536 \times 4 \mu s \approx 600 \,\mathrm{ms}$  and then averaged again over 5-10 repetitions, if necessary. Note that these acquisition parameters are not optimized for speed and we expect that a speed-up of at least a factor 10 is possible while still maintaining an adequate accuracy of the parameters to be extracted.

# 5.4. Coarse tuning of the quantum dots

### 5.4.1. Tuning of the RF-read-out circuit

In order to exploit the remarkable properties concerning response time and charge sensitivity of the sensing dot, the single electron transistor is embedded in an impedance matching circuit [53,35,54] that transforms its high resistance of approximately 50 k $\Omega$  to match the 50  $\Omega$  transmission line impedance. Otherwise, most of the RF probing signal would be completely reflected independently of the actual resistance of the quantum dot. The two tuning parameters of the read-out circuit are the frequency, set to resonance with the LC-tank circuit, and the phase of the carrier signal. To ensure that the carrier frequency lies in the relatively narrow frequency window of the RF-components, mostly determined by the 20 MHz bandwidth of the cryogenic amplifier and circulator (Quinstar QCA-U-230 and VDC1065K3), a newly assembled sample holder PCB including the tank circuit components is usually first tested at room temperature without the sample by measuring the reflected power using a vector network analyzer. Typically, the resonance frequency without a bonded sample is 40 to 60 MHz higher than the resonance frequency with the sample, due to lower stray capacitance. After bonding, the sample is cooled to 4 K and the resonance frequency is measured again to determine if it fits into the frequency window. Adding or removing stray capacitance by bending a small copper wire soldered next to the inductor, allows for fine tuning of the resonance condition in a limited range of approximately  $\pm 20 \,\mathrm{MHz}$ . Once the resonance frequency is known, the phase of the carrier, controlled by a voltage  $V_{\text{phase}}$  of a phase shifter, can be coarsely adjusted by comparing two-dimensional phase-frequency scans of the read-out circuit output with an open and a closed sensing quantum dot, as shown in Fig 5.2a, b, respectively. The resonance of the non-linear output which is predominantly given by the frequency response of the phase shifter (Pulsar SO-06-411) can be seen in the indicated region in Figs. 5.2b. Typically, the phase is set to a value close to the zero-crossing allowing maximum sensitivity.

Optimization of these parameters is usually done simultaneously with the tuning of the actual quantum dots which will be described in the next two sections. For convenience, we report here how to fine-tune the readout circuit and assume working quantum dots. Finding the optimal values is done by measuring Coulomb oscillations of the sensing dot (Figs. 5.2c,d) and sweeps across a lead transition of the double-quantum dot (Figs. 5.2e,f) as a function of phase and frequency. Typically, values that yield maximum contrast are chosen (see indicated areas in Figs. 5.2c-f). Note that this is an iterative process and usually needs a couple of iteration to find the optimum phase and frequency combination.

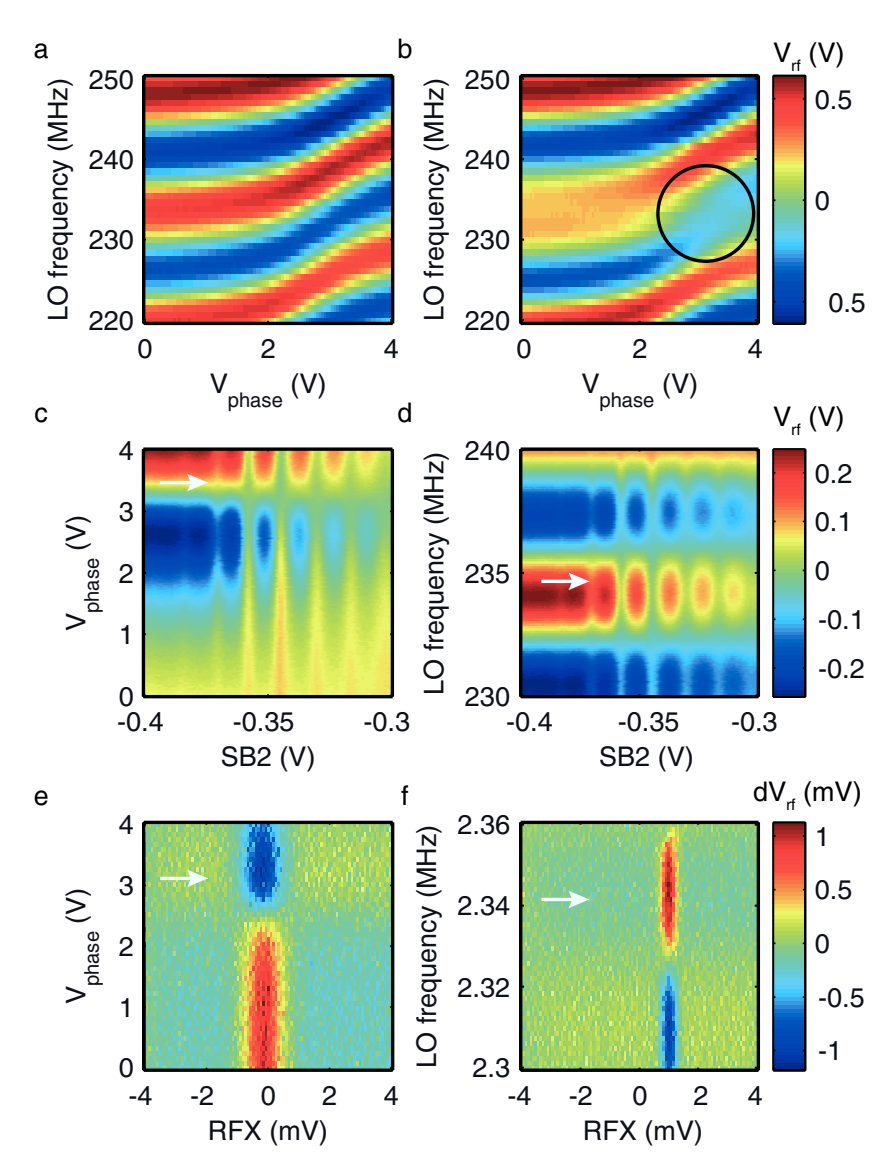


**Figure 5.2.: Tuning of the RF-read-out circuit.** Output of the RF-reflectrometry circuit as a function of the phase and frequency of the local oscillator. **a** An open sensing dot shows the inherent, non-linear response of the read-out circuit. **b** Pinching off the quantum dot shows the resonance of the tank circuit attached, indicated by the black circle. Coarse tuning of the read-out circuit is done by measuring Coulomb oscillations through the sensing dot as a function of phase (**c**) and frequency (**d**). Sweeps across one of the lead transitions of the double quantum dot as a function phase (**e**) and frequency (**f**) determine the final values for maximum sensitivity of the read-out tuning.

In a last step the power of the local oscillator needs to be set. We usually strive for a power of -90 to -100 dBm at the sensing dot. We set the power to a value that maximizes signal while still maintaining a decent temperature broadening of the Coulomb peaks of the sensing dot. In the beginning of the tune-up procedure it might be advantageous to go to higher RF-power and exploit the higher dynamic range of slightly temperature broadened sensing dot peaks. For very high local oscillator powers we found that a ringing of the tank circuit is visible in the readout of the qubit probably mediated by phonons. Such high excitations should be avoided. Although not ideal as the mixer might work sub-optimally, it is convenient to first adjust the power of the RF-source and test the effect on the Coulomb peaks. The manual attenuators on the RF input line can be adjusted afterwards.

### 5.4.2. Tuning of the sensing dot

The next two sections describe how to tune the sensing dot and the actual qubit double dot and do not include novel methods<sup>[79]</sup> but are included for completeness. A nearby

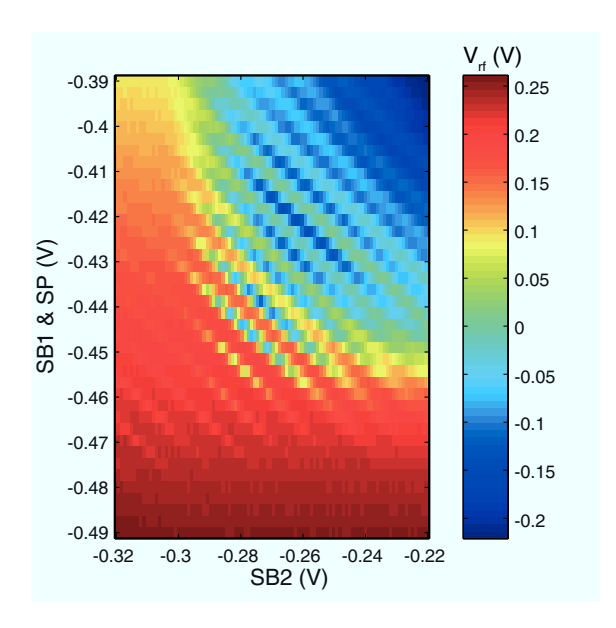


**Figure 5.3.: Charge sensor tuning.** The characteristic charge stability diagram of the sensing dot shows Coulomb oscillations once tunnelling to the source and drain is slowed down at negative gate voltages, but not too slow. Tuning the sensor to a sensitive position allows for charge sensing of the nearby double quantum dot.

quantum dot is used to sense the charge distribution in the double quantum dot and allows to monitor its occupancy once transport through the qubit dot is limited by opaque tunnel contacts<sup>[52]</sup>. We perform a two-dimensional scan with the sensing dot gates SB2 vs. SB1 and SP (gate names are defined in Fig. 5.1), measuring the conductance through

the dot. Upon making the gates more negative, Coulomb oscillations show up once the barriers to the source and the drain are opaque enough. Fig. 5.3 shows a region in gate voltage space that shows the typical pattern of a single quantum dot<sup>[3]</sup>. Note, in this particular sample SP and SB1 were shorted and thus had to be kept on the same potential. Usually, SP can be used to fine tune the dot and shift it closer to the double quantum dot, but is not very relevant. Typically, the charge sensor is tuned to a position where the slope of the Coulomb peak is steepest to maximize sensor sensitivity.

# **5.4.3.** Locating the (2,0)-(1,1) or (0,2)-(1,1) charge transition

As a first step to tune the double quantum dot, the depletion and pinch-off voltages of the different dot-defining gates have to be determined. The conductance through the dot is measured while applying a negative voltage on the gates pairwise (i.e. N12 and T12, S1 and B1, S2 and B2, see Fig. 5.1 for gate nomenclature). Knowing the depletion

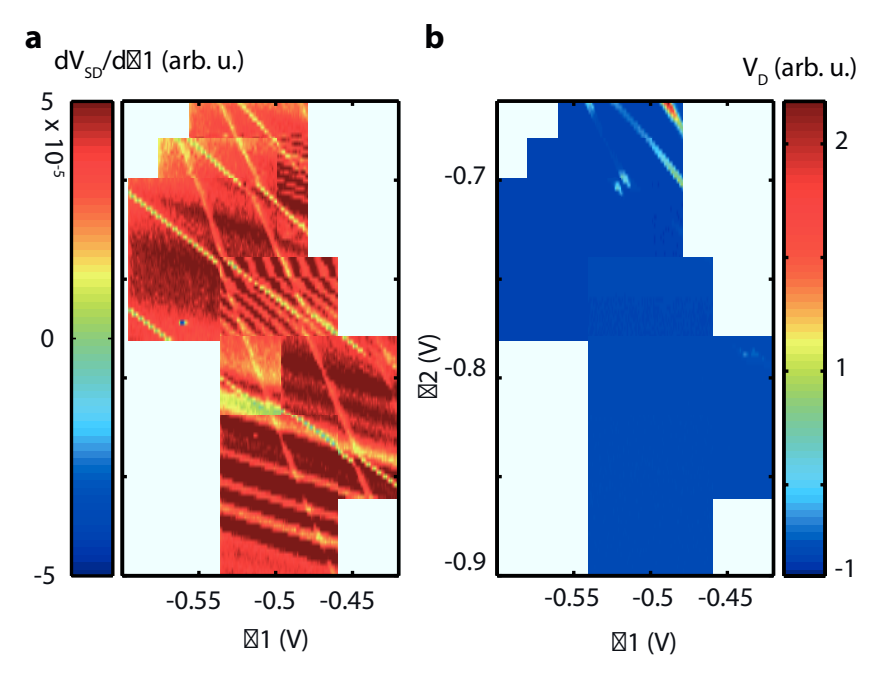


**Figure 5.4.:** Charge sensing and transport through a double dot. a Monitoring the differential conductance through a nearby sensing dot tuned to a sensitive position shows the electron occupancy of the double dot in a typical honeycomb pattern. Background oscillations are caused by an imperfect compensation of the sensing dot gates relative to B1 and B2. **b** When measuring transport through the lateral quantum dots, conduction only occurs at the triple-points. Since B1 and B2 also influence the coupling to source and drain, Coulomb peaks become only faintly visible for negative voltages.

voltages, the device is tuned close to complete pinch-off. We initially perform a two-dimensional scan over a couple of tens of mV with the barrier gates B1 and B2, which have less influence on the tunnel barriers to the leads located beneath the RF-gates (see Fig. 5.4). Usually we start by forming one, big quantum dot and continue by separating it by applying more negative voltage on the T12 and N12 gates. Once the tunnel barriers between the dot and the source and the dot and the drain are almost pinched off and have similar transmission probabilities, Coulomb blockade peaks should appear, showing the characteristic honeycomb pattern of a lateral double quantum dot [3], as shown in Fig. 5.4b.

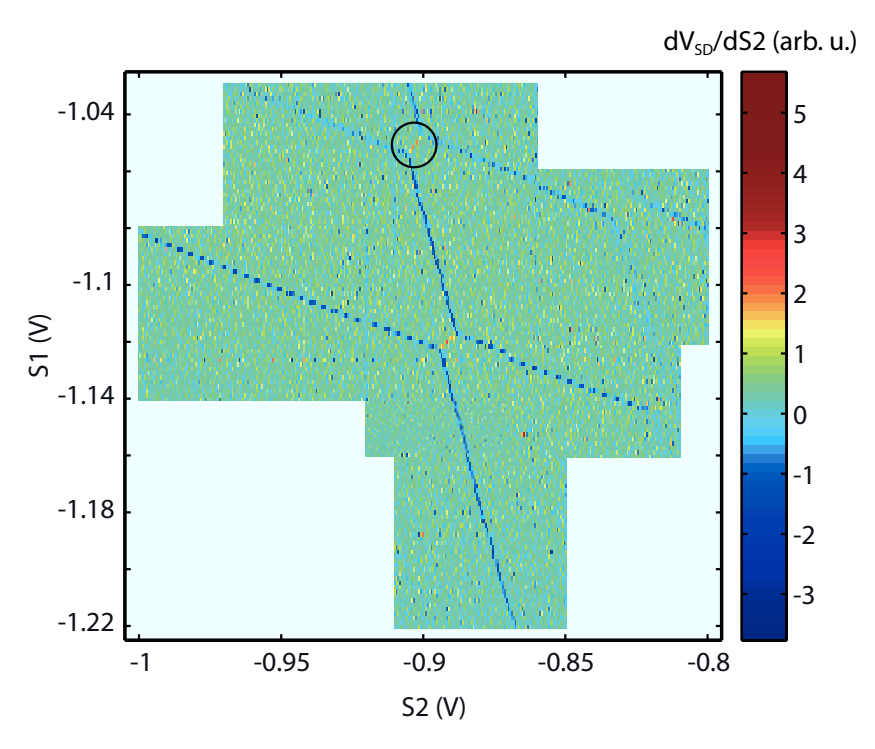


**Figure 5.5.:** Charge sensing with QPC compensation. Electron occupancy of the double dot detected by a nearby charge sensor. A linear interpolation was used to adjust the voltage on the sensing dot gate SB2 to compensate any influence of the stepping gate S1. Notice how the side-gates S1 and S2 influence the width of the tunnel barriers to the leads at different charge transition.

Even though applying more negative voltages on the barrier gates (B1 and B2) primarily empties the dot, they will eventually close the tunnel barriers to the reservoirs resulting in hardly detectable Coulomb peaks unless other gates are carefully tuned. When this region in gate space is approached, it is useful to tune the sensing dot to a sensitive position (see section 5.4.2 and Fig. 5.3) and simultaneously monitor its conductance as a function of gate voltages, as depicted in Fig. 5.4. A change in electron

occupancy in the double dot changes the potential in the sensing dot due to their capacitive coupling and results in a step in the sensing dot conductance. To compensate the unintentional influence of the stepping gate B2 on the sensing dot potential, the voltage on SB2 is adjusted accordingly when performing a two-dimensional scan. As the barrier gates in general have a stronger influence on the sensing dot, using the side gates S1 and S2 reduces the background oscillation, as seen in Fig. 5.5. Shifting the field of view towards more negative voltages eventually locates either the (2,0)-(1,1) or the (0,2)-(1,1) charge transition. Once a suitable transition has been found, S1 and S2 are centered around this junction and a charge stability diagram using the RF-gates, RFX and RFY, with higher resolution is recorded (see Fig. 5.6). Tuning of the qubit can now begin.

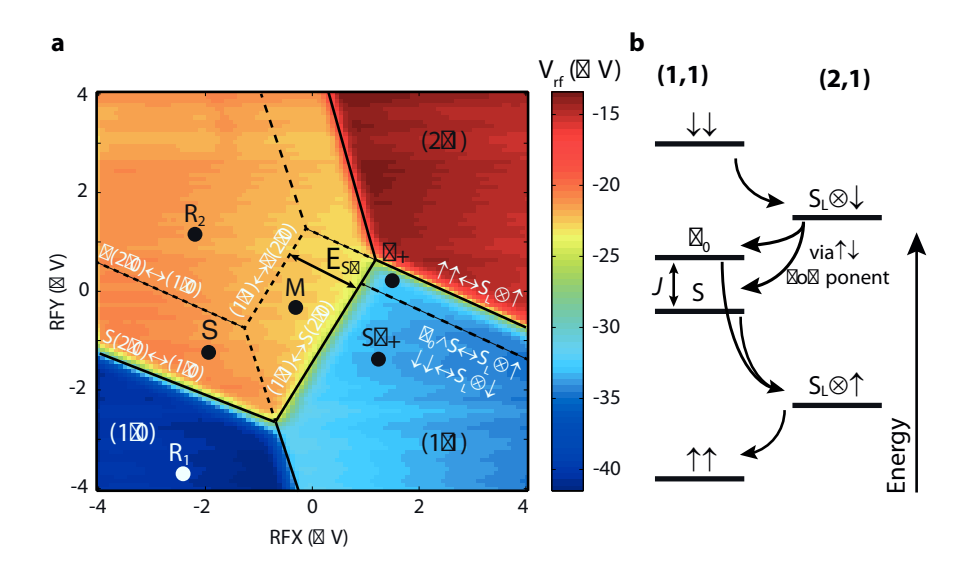


Figure 5.6.: Charge stability diagram. (a) High resolution charge stability diagram of the important gate space of the (2,0)-(1,1)-junction used to define the two-electron spin qubit. Important points in gate-space near this transition, which is used to initialize the qubit in different states and for measurement, are marked by dots and further explained in the main text. Ground state and excited state transitions are labeled in white. (b) This diagram shows the energy relaxation cascade used to initialize the (1,1) ground state  $|\uparrow\uparrow\rangle$  at point  $T_+$  in (a).  $S_L\otimes\downarrow(\uparrow)$  denotes the state of a singlet state in the left quantum dot and an down (up)-state in the right dot.

# 5.5. Fine tuning of the qubit

### 5.5.1. Setting up virtual gates

Once the (2,0)-(1,1) (or (0,2)-(1,1)) charge transition has been located and the gate voltages have been adjusted to center the charge stability scan using the RF-gates, it is advisable to switch to virtual gates, a linear combination of three actual gates (see Tab. 5.1). These virtual gates allow tuning of dot parameters while leaving the RF-gate voltages at which charge transitions occur unaffected. They are chosen such that each virtual gate primarily affects one specific dot parameter. In addition to changing the gate which most strongly influences the desired parameter, a compensating voltage is applied to the B1 and B2 gates to cancel out any cross-capacitance. LeadY and LeadX primarily change the tunnel coupling to the respective lead. The tunnel coupling between the dot is manipulated by the T and N virtual gates. X and Y only change B1 and B2 to shift the features of the charge stability diagram.

In order to obtain the virtual gate coefficients, the effect of all gates on the position of the charge stability diagram is measured by successively stepping the individual gate voltages between two different values, typically differing by 2-6 mV. The dot's response with respect to these gate changes is measured by sweeping across both lead transitions as exemplarily shown in Fig. 5.7d for the Y-lead. By fitting the different traces using a phenomenological fit model corresponding to a Fermi distribution,

$$V_{\rm rf}(v) = V_{\rm rf,0} + \delta V_{\rm rf} v - \frac{1}{2} A \left( 1 + \tanh \left( \frac{v - v_{\rm lead}}{w} \right) \right), \tag{5.1}$$

the exact influence of the stepping gate on the location of the transition can be extracted. Here, v is the voltage on either the RFX or RFY sweeping gate. The first term  $V_{\rm rf,0}$  in Eq. 5.1 represents the background value of the charge sensing signal  $V_{\rm rf}$ . The linear term  $\delta V_{\rm rf} v$  accounts for the direct influence of the sweeping gate on the conductance through the sensor. The third term accounts for the excess charge once an electron tunnels into or out of the quantum dot and includes a finite electron temperature via w. The location of the lead transition is given by  $v_{\rm lead}$ . We use  $V_{\rm rf,0}$ ,  $\delta V_{\rm rf}$ ,  $v_{\rm lead}$ , A and w as fit parameters.

The shift of the transition in RFX and RFY direction due to different voltages on the surrounding gates is extracted from the fits and the values are used to construct the cross-capacitance matrix. Inverting appropriate sub-matrices of this  $2 \times n$  matrix leads to the virtual gate coefficients, with typical values shown in Tab. 5.1, that compensates any changes in S1, T12, N12 or S2 by applying an additional voltage on the B1 and B2 gate.

A similar concept is used in Ref. 56 to perform orthogonal charge stability diagrams in a three-electron quantum dot and in Refs. 12,81.

Virtual gate							
		LeadY	LeadX	T	N	X	Y
Physical gate	S1	1	0	0	0	0	0
	B1	-0.76	0.5	-0.52	-0.5	1.5	-2.1
	T12	0	0	1	0	0	0
	N12	0	0	0	1	0	0
	S2	0	1	0	0	0	0
	B2	0.26	-1.1	-1.25	-0.5	-3.68	1.03

**Table 5.1.: Virtual gates.** Typical values for the coefficients of the virtual gates that either leave certain dot parameters or the dot position unaffected. Changes in S1, T12, N12 or S2 are compensated by simultaneously adjusting the voltages on B1 and B2. The values correspond to the ratio of change in physical gate voltages to that of the virtual gate.

### 5.5.2. Tunnel coupling to the leads

The double quantum dot is tunnel coupled to two grounded leads (Ohmic contacts next to the RF-gates) acting as electron reservoirs. On the one hand, the tunnel rates, mostly controlled by the virtual gates LeadY and LeadX, should be slow to prevent excess  $T_1$  relaxation due to cotunneling or thermal activation. On the other hand, at least the lead to the (1,0) charge configuration should be transparent enough to allow fast qubit initialization within tens of nanoseconds. In order to reliably measure the two tunnelling rates  $t_1$  and  $t_r$  of the left and right leads, we apply 25 MHz square wave pulses across both lead transitions. This forces an electron to tunnel to and from the dot, and the charge sensor signal is measured. To measure the time dependent charge occupation we exploit repetitive signal averaging over approximately 1500 periods recorded at a hardware sampling rate of 100 MS/s. Typical time traces are shown in Fig. 5.7a, b. Applying the square wave pulses to regions without a lead transition allows for a subtraction of the background due to direct sensor coupling. The tunnelling time through the leads can be extracted from the rise times of the recorded square pulses, with a lower sensitivity bound of about 25 ns determined by the bandwidth of the tank circuit attached to the sensing dot. The fit model used in Fig. 5.7a, b is given by

$$V_{\rm rf}(t,t_0) = \begin{cases} V_{\rm rf,0} + \frac{1}{2} A \frac{\cosh\left(\frac{t_0}{2t_{1,1}}\right) - \exp\left(\frac{t_0 - 2t}{2t_{1,1}}\right)}{\sinh\left(\frac{t_0}{2t_{1,1}}\right)} & \text{for } t < t_0 \\ V_{\rm rf,0} - \frac{1}{2} A \frac{\cosh\left(\frac{t_0}{2t_{1,2}}\right) - \exp\left(\frac{t_0 - 2t}{2t_{1,2}}\right)}{\sinh\left(\frac{t_0}{2t_{1,2}}\right)} & \text{for } t \ge t_0, \end{cases}$$

$$(5.2)$$

where  $t_0 = 2\mu$ s is the half-period. The prefactors and offsets of the exponential rise and decay are chosen such that the curve is continuous. Typical target values for  $t_1$  range from 25 ns to 50 ns. Note that faster tunneling times can be resolved with the reload sweep discussed in Sec. 5.5.5. All initialization methods addressed here (see Sec. 5.5.4 for more detail) only require one lead to be tuned, hence the other lead transition can be made less transparent to avoid excess relaxation.

### 5.5.3. Inter-dot tunnel coupling

Tunnel coupling  $t_c$  between the two dots is mostly controlled by the N and T virtual gates and determines the strength of the exchange interaction  $J(\varepsilon)$  between the two electrons. In order to characterize the tunnel coupling, we measure the broadening of the interdot transition between the (2,0)-(1,1) charge configuration by sweeping the (2,0)-(1,1)detuning  $\varepsilon$  orthogonally across the junction and recording the average charge state [82], as shown in Fig. 5.7c. Using pulses from the AWG we typically measure each detuning step for 1 µs and average over 4000 scans for a total measurement time of 0.4 s. For simplicity we extract the broadening of the transition by fitting Eq. 5.1 to the data rather than using the physically correct model of an avoided crossing as we find the difference between these models to be marginal. Typical values for  $t_c$  range from 18  $\mu$ eV to 24  $\mu$ eV, using an estimated lever arm of 9.8 V/eV. A smaller value for the tunnel coupling leads to Zener-tunnelling when separating the electrons and should be avoided. Temperature broadening provides a lower limit of around 9  $\mu$ eV for this characterization method in our setup. An alternative approach for determining the inter-dot tunnel coupling based on time-resolved charge sensing is given in Ref. 83. Furthermore, the tunnel coupling can also by extracted by photon assisted tunneling spectroscopy<sup>[84]</sup>. Compared to the presented method, both alternatives are time-consuming and thus less attractive for our purpose.

# 5.5.4. Locating the measurement point

The operation of a qubit heavily relies on the ability to reliably initialize the qubit in a well known state and to accurately measure the qubit's final state [46]. These procedures should be readily available with high fidelity. Here, we present our methods to load the qubit in the ground state S(2,0) using only the lead to the (1,0) charge configuration and our method to set-up the measurement readout area of the qubit via Pauli spin blockade. Historically motivated, the standard approach for singlet initialization uses spin blockade [33]. Via the transition cycle  $T(1,1) \rightarrow (0,1) \rightarrow S(0,2)$  both electrons relax in the ground state by electron exchange with both lead transitions. We present a modified version which only relies on one open lead transition. This procedure requires less tuning and enables simpler future device layouts. Closing one lead transition also allows

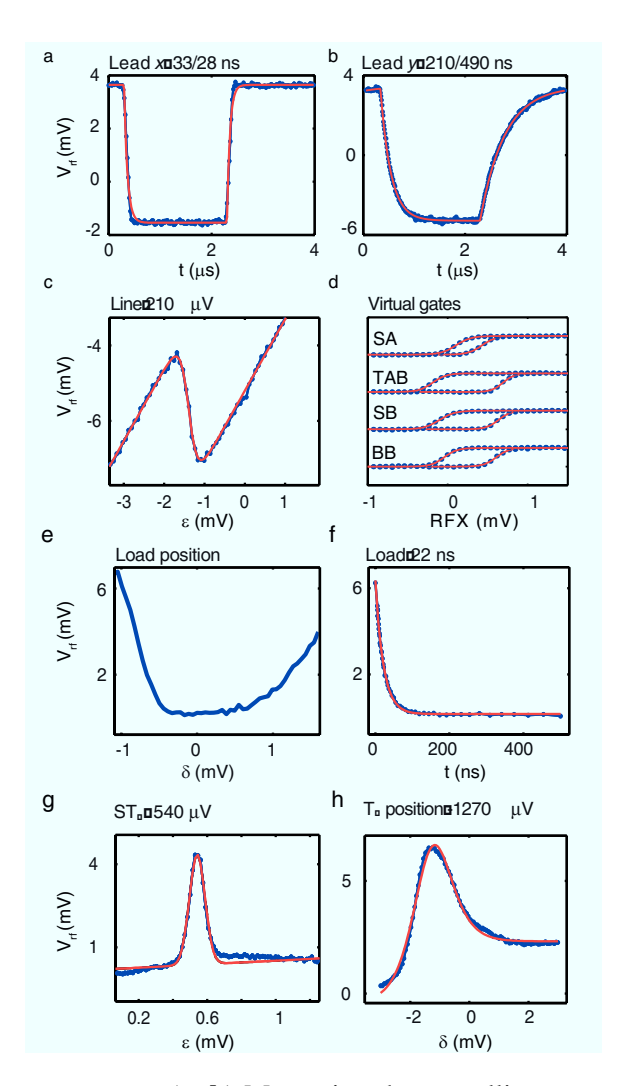


Figure 5.7.: Tuning parameters. (a, b) Measuring the tunnelling rates to the leads by applying MHz voltage pulses across the respective lead transition, forcing an electron exchange with the respective reservoir. The tunnelling time can be extracted by the rise time of the response. (c) The inter-dot tunnelling rate can be extracted by sweeping along the detuning ε, recording the average charge occupancy and measuring the broadening of the transition. (d) Measuring the influence of various gates on the location of the vertical lead transition by stepping each channel between two voltages and sweeping across the transition. (e) Shifting point S along the detuning δ locates the optimum singlet reload position located between the (2,0)-singlet and -triplet transition. f Varying the wait time at point S (see Fig. 5.6) shows a singlet reload time of 22 ns. (g) Sweeping along the detuning ε locates the ST<sub>+</sub> transition. (h) Sweeping along the detuning δ around point T<sub>+</sub> locates the triplet T<sub>+</sub> reload point.

for an enhanced charge detection<sup>[85]</sup> readout scheme to counter visibility loss at high magnetic field gradients<sup>[86]</sup>.

In order to set-up the Pauli spin blockade-technique to distinguish between spin singlet and triplet states [10,33], we first need to locate the region of metastable (1,1) triplets within the (2,0) ground state charge configuration (highlighted area in Fig. 5.6). We perform a regular charge scan by sweeping the DC-offset on the RF-gate voltages while simultaneously applying a pulse scheme M-R<sub>1</sub>-R<sub>2</sub>-M repeatedly. By stepping to point R<sub>1</sub>, deep into (1,0), one electron is discarded. We initialize a random (2,0) spin configuration within a couple of 100 ns when we step back into (2,0), to point R<sub>2</sub>, far away from the anticipated read-out area and well above the singlet-triplet energy splitting. As the transition into the (1,1) charge configuration occurs earlier for the triplet (2,0) states, stepping back to M maps out the region of the metastable triplet states (see Fig. 5.8). During the manipulation of the electrons acquisition is masked out and we only apply RF-power at point M. The resulting charge signal contains a mixture of singlet (2,0) and triplet (1,1) states and the so-called measurement triangle (or trapezoid for a singlet-triplet splitting smaller than the inter-dot charge coupling) becomes visible.

By extending the pulse scheme to M-R<sub>1</sub>-R<sub>2</sub>-M-S-M, including an additional 100 ns wait at point S, we are able to roughly determine the singlet reload point S. Having initialized a random (2,0) spin configuration at point R<sub>2</sub>, we pulse to point S, close to the (2,0)-(1,0)-transition. Staying energetically below the singlet-triplet-splitting and above the (1,1)-T(2,0) transition (see Fig. 5.6), one electron is exchanged with the lead and we initialize a (2,0) singlet state. In regions where this sequence is possible, the signal is set back to the (2,0) level instead of the mixture seen in Fig. 5.8. Performing scans with both pulse sequences and subtracting them maps out a region within the measurement triangle that allows for Pauli spin blockade and singlet initialization. This initialization procedure requires only one lead to be tuned and the initialization time is given by the tunnel coupling to this lead (see section 5.5.2) and can be as fast as a few nanoseconds. Note that exchanging an electron with the (1,0) lead allows for a much faster initialization compared to the  $T_1$  relaxation time at the operating point for qubit manipulation.

# 5.5.5. Locating the singlet reload point

To further tune the voltages for singlet initialization, we sweep the position of point S in the M-R<sub>1</sub>-R<sub>2</sub>-M-S-M pulse sequence introduced above perpendicular to the (2,0)-(1,0) lead transition while keeping point M fixed. For an optimal point S, the (2,0)-triplet states must be energetically inaccessible while exchanging one electron with the lead is still allowed. We measure the triplet return probability which is proportional to  $V_{\rm rf}$ , by pulsing back to point M. Ideally point S should lie symmetrically in the middle between the (2,0)-singlet and -triplet transitions to (1,0) (see Figs. 5.7(e) and 5.6).

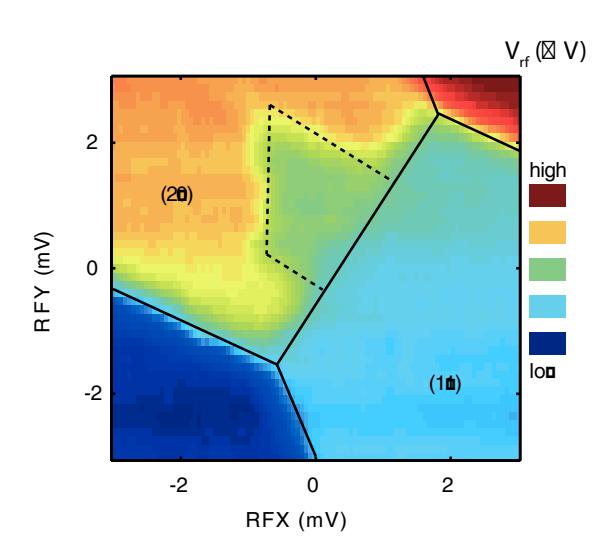


**Figure 5.8.:** Measurement triangle. Recording a regular charge stability diagram while simultaneously reloading a random (2,0)-spin configuration maps out the region of metastable triplet states within the (2,0)-charge-configuration due to Pauli spin blockade. The visible boundaries of the readout triangle reflect a failure of the random load pulse sequence rather than instabilities.

In a last characterization scan we vary the wait time t at the optimal point S and again measure the triplet probability P(T). Fitting a simple exponential decay

$$V_{\rm rf}(t) = V_{\rm rf,0} + Ae^{-\frac{t}{t_{\rm load}}}$$
 (5.3)

to the data provides the singlet reload time  $t_{\text{load}}$ , which typically lies in the range of 10 to 50 ns for a well-tuned dot, as can be seen in Fig. 5.7f. Again,  $V_{\text{rf},0}$ , A and  $t_{\text{load}}$  are fit parameters. This characterization scan is complementary to determining the lead tunnel time from Sec. 5.5.2 but allows the usage of the full time resolution of 1 ns of the AWG as it is not limited by the bandwidth of the readout tank circuit.

# **5.5.6.** Locating the triplet $T_+$ reload point

The pulsed dynamical nuclear polarization (DNP) scheme from Ref.13 which is used to stabilize the surrounding nuclear spins of the host material GaAs, relies on the ability to additionally initialize the (1,1) ground state  $T_+$ . This is done at point  $T_+$  in the charge stability diagram (Fig. 5.6), using only the transition to the (2,1) charge configuration, i.e., tunneling through the left lead. For a large  $B_{\rm ext}$  this transition is spin split and the left quantum dot will always occupy a singlet state in (2,1). The transition between (2,1) and the excited (1,1) states, S,  $T_0$  and  $T_-$ , occurs at a more negative voltage compared to the transition to the (1,1) ground state  $T_+$  (see Fig. 5.6a). Ideally, point  $T_+$  should lie

between these two transitions. For sufficiently open tunnel barriers, the excited  $T_-$  state rapidly relaxes to the S or  $T_0$  state by exchanging the left electron with the reservoir. Repeatedly exchanging the two electrons in the (1,1) configuration using an exchange interaction  $J(\varepsilon) > \Delta B_z$ , while still maintaining  $J(\varepsilon) - B_{\rm ext} < k_{\rm B}T$ , further ensures mixing of  $|\uparrow\downarrow\rangle$  and  $|\downarrow\uparrow\rangle$ , so that the system will subsequently relax into the desired  $T_+$  by another exchange with the left reservoir. This relaxation cascade into the ground state is schematically depicted in Fig. 5.6b. Alternatively, the  $T_+$  could be initialized using both the (2,1)-(1,1) and the (1,0)-(1,1) leads, relaxing both electrons individually, as originally introduced in Ref.11. In this case, both tunnel barriers need to be open.

In order to find the optimal  $T_+$  reload point in the charge stability diagram, the following sweep is performed. The qubit is first initialized in a S(2,0) state and subsequently voltages are set to point  $T_+$  without crossing the upper triple point to avoid measurement artefacts. After a wait time of 100 ns to allow energy relaxation we switch back to the measurement point M and measure the triplet return probability. The location of point  $T_+$  is shifted perpendicular to the y-lead by a voltage  $\delta$ . To fulfill the energy requirement  $B_{\rm ext} > J(\epsilon) > \Delta B_z$ , the distance from the upper triple point in Fig. 5.6 is set by hand, depending on the actual value of the inter-dot tunnel coupling. Once this point is set correctly, a maximum can be seen in the triplet return probability which indicates the  $T_+$  reload point, as shown in Fig. 5.7h. We use a phenomenological model motivated by Eq. 5.1 and given by

$$V_{\rm rf}(\delta) = V_{\rm rf,0} + \frac{1}{2} A_1 \left( 1 + \tanh\left(\frac{\delta - \delta_{\rm tl,1}}{w}\right) \right)$$
$$-\frac{1}{2} A_2 \left( 1 + \tanh\left(\frac{\delta - \delta_{\rm tl,2}}{w}\right) \right) \tag{5.4}$$

to fit the data to extract the exact reload point. Here, the position of the  $T_+$  point is given by  $(\delta_{tl,1} + \delta_{tl,2})/2$ .

# 5.5.7. Locating the $ST_+$ -transition

For locating the S-T<sub>+</sub>-anti-crossing, we follow Ref. 9 and initialize the qubit in the singlet state at point S, change the detuning  $\varepsilon$ , followed by a 100 ns wait time at a given detuning and read out the final qubit state at point M. Due to hyperfine and spin-orbit interaction, the S state can evolve to a T<sub>+</sub> state once the detuning hits the S-T<sub>+</sub> transition and its location becomes visible as a peak in the measured triplet return probability  $P(T)(\varepsilon)$ . As the exact location of this transition strongly depends on the local magnetic field that splits the T<sub>±</sub> states, any unintentional polarization, for example due to hyperfine mediated spin flips at the ST<sub>+</sub> transition, shifts the precise position of the anti-crossing. To avoid excessive polarization, we perform fast  $\varepsilon$ -sweeps and

include pauses of a few milliseconds between averaging steps to allow any unintentional polarization to relax. We fit a Gaussian model

$$V_{\rm rf}(\varepsilon) = V_{\rm rf,0} + \delta V_{\rm rf} \varepsilon + A e^{-\frac{(\varepsilon - \varepsilon_{\rm stp})^2}{2w^2}}$$
 (5.5)

to the data (see Fig. 5.6e) and extract the position  $\varepsilon_{stp}$  of the  $ST_+$  transition.

Not only is this position crucial for the pulsed DNP scheme (see next section) but in combination with the  $T_+$  reload point it is also used as an anchor point in the charge stability diagram. Shifting the dot using the X and Y virtual gates to obtain the same values for the  $ST_+$  and  $T_+$  scan after a small charge switching event usually restores all junction parameters, and results in the same  $J(\varepsilon)$  relation. Furthermore, the position of the  $ST_+$  crossing is used to automatically determine switching events [21,71,20] that shift the whole transition by several mV.

### 5.5.8. Tuning workflow

The typical fine-tuning workflow of the (2,0)-(1,1) charge transition starts by defining the virtual gates. The next step is to bring the tunnel couplings to the leads in the right regime. As initialization and readout is part of any further pulse sequence (and any experiment in general), tuning the singlet reload point S and the measurement triangle is done in a next step, once the tunnel barriers to the (1,0) lead is set. The energy splitting of the qubit is subsequently tuned by adjusting the inter-dot tunnel coupling. A working scan of the S-T+ transition as described in Sec. 5.5.7 is a good indicator for a suitable tunnel coupling. Usually, this is an iterative procedure as adjusting the T and N virtual gates also affects the lead tunneling rates a little. Finally, the position of the  $T_+$  reload point is tuned. Generally, manual retuning to restore previous junction parameters once a charge rearrangement in the heterostructure has occurred takes a few iterations of performing the various characterization scans and adjusting the gate voltages. It can usually be completed in about one hour.

# **5.5.9.** Setting up the pulsed $\Delta B_z$ feedback scheme

Universal control of a qubit generally requires two orthogonal control axes. For  $ST_0$ -qubits in GaAs, these are the exchange interaction  $J(\epsilon)$  and a gradient in local magnetic fields  $\Delta B_z$  between the two dots<sup>[11]</sup>. While  $J(\epsilon)$  can be electrically controlled by applying voltage pulses on the ns-timescale that change the detuning  $\epsilon$ , controlling  $\Delta B_z$  is more challenging. There are various approaches to provide different magnetic fields in the dots that include using micro- or nanomagnets<sup>[87,60,88,89]</sup> on top of the heterostructure. Here, we exclusively use the pulsed dynamical nuclear polarization scheme from Ref. 13 that relies on bidirectional Landau-Zener sweeps across the  $ST_+$ -anticrossing.

Sweeping adiabatically over this transition allows the controlled flipping of the electron spin between spin singlet S and triplet  $T_+$ , mediated by either hyperfine or spin-orbit interaction. Electron spin flips due to the hyperfine interaction are accompanied by a nuclear spin flop, thus changing the local magnetic field gradient. Controlled electron spin flips from  $S \rightarrow T_+$  and  $T_+ \rightarrow S$  in a feedback loop allows a stabilization of  $\Delta B_z$ .

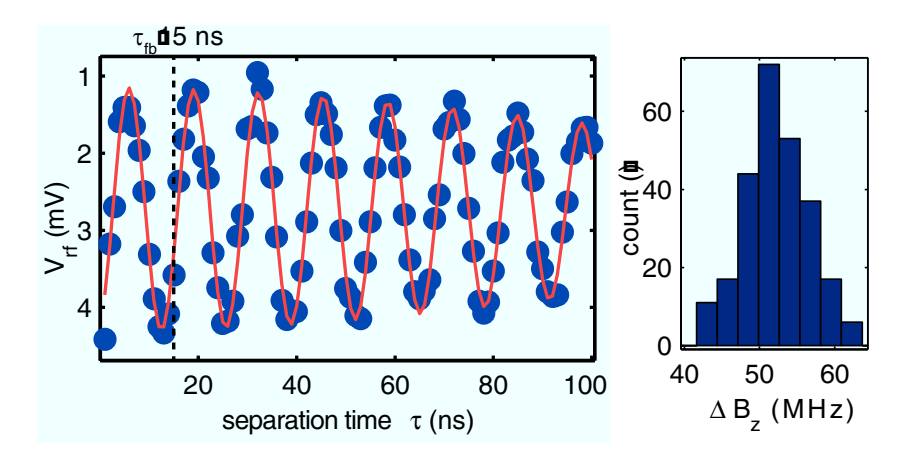


**Figure 5.9.:** Averaged  $\Delta B_z$  oscillations. a Using the qubit as a hardware feedback loop, DNP between different scanlines is used to stabilize the hyperfine gradient  $\Delta B_z$ . A feedback time of 15 ns results in  $\Delta B_z \approx 54$  MHz. The coherence time for this specific measurement is  $T_2^{\star} \approx 165$  ns. **b** A histogram of the instantaneous values of  $\Delta B_z$  of each scanline before ensemble averaging shows the distribution with standard deviation of a few MHz.

Once the position of the ST<sub>+</sub> transition, the singlet and triplet reload points are known, we construct three polarizing pulses comprising a S-, a T<sub>+</sub>- and a conditional Spulse<sup>[13]</sup>. For the S  $(T_+)$ -polarizer we first initialize a S  $(T_+)$  state using the respective reload points and then perform a sweep across the ST+-transition, which is typically 100 ns long and  $100 \,\mu\text{V}$  wide. We add a wait time of  $\tau_{\text{fb}}$  at maximum detuning in the (1,1) charge configuration between the reload and ST<sub>+</sub> sweep for the conditional S polarizing pulse that probes the current value of  $\Delta B_z$ . As the pump rate  $d\Delta B_z/dt$  of this pulse is proportional to the triplet return probability  $P(T)^{[13]}$ , every zero crossing with period  $h/g^*\mu_B\tau_{fb}$  is a stable point of the feedback. As the conditional S pump pulse only polarizes in one direction, we interleave the unconditional T<sub>+</sub>-pump pulse to maintain bidirectional pumping. The pump rates of the different pump pulses may vary over time for an unknown reason, hence we typically try different ratios of conditional S- and T<sub>+</sub>pump pulses until a stable gradient is found. Fig. 5.9a shows a typical averaged time trace of  $\Delta B_z$  oscillation at 4 mV detuning with an enhanced coherence time  $T_2^{\star} \approx 165 \text{ ns}$ compared to the unpolarized case with  $T_2^* \approx 10 \, \mathrm{ns}^{[9]}$ . The corresponding distribution of instantaneous  $\Delta B_z$  values is shown in Fig. 5.9b.

## **5.5.10.** Measurement of the exchange interaction $J(\varepsilon)$

Characterization of the dependence of the exchange interaction J on the detuning  $\varepsilon$  is necessary to define, for example, non-trivial high-fidelity gates [90,55] or native  $\pi$ -and  $\pi/2$ -pulses about the  $J(\varepsilon)$ -axis, used to decouple the qubit from the nuclear spin bath fluctuations [15,78]. In order to measure the strength of the exchange interaction we perform Ramsey-type measurements, similar to Refs.9,72.

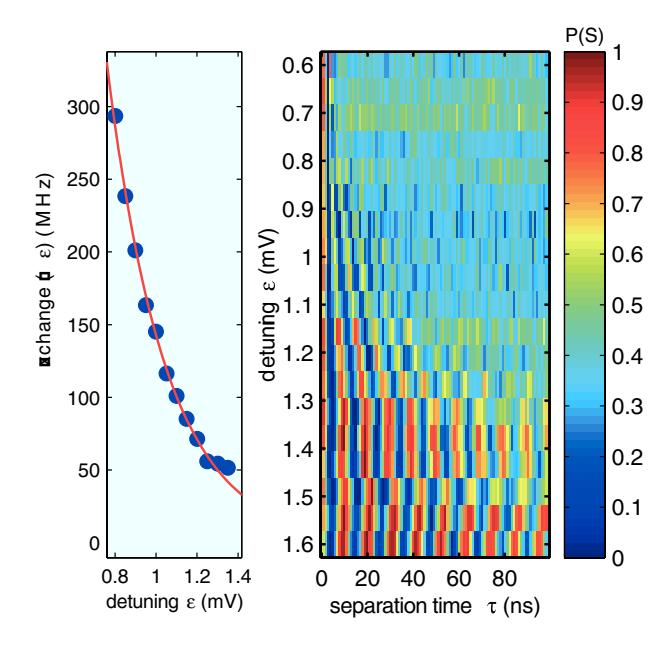


Figure 5.10.: Exchange interaction  $J(\varepsilon)$ . a A phenomenological model  $J = J_0 \exp(\varepsilon/\varepsilon_0)$  is fitted to the extracted values for J as a function of the detuning  $\varepsilon$ . We experimentally find that typically  $\varepsilon_0 \approx 0.3$  mV, independent of the tunnel coupling, whereas the amplitude  $J_0$  depends on the inter-dot coupling. b Normalized Ramsey oscillations as a function of separation time  $\tau$  for different detunings used to extract the values for  $J(\varepsilon)$  in  $\mathbf{a}$ .

To guarantee maximum contrast even in the case where  $J(\varepsilon) \approx \Delta B_z$ , the qubit is first initialized in a S-state, rotated into the  $|\uparrow\downarrow\rangle/|\downarrow\uparrow\rangle$ -plane using a  $\pi/2$ -pulse about the  $\Delta B_z$ -axis (see section 5.5.9) and let it evolve for a variable time at detuning  $\varepsilon$ . The qubit state is read-out after another  $\pi/2$  pulse. The normalized triplet return probability P(T) as a function of separation time  $\tau$  for different detunings  $\varepsilon$  is shown in Fig. 5.10b. Simultaneous recordings of the hyperfine gradient  $\Delta B_z$ , allow to extract the exchange interaction by fitting the oscillations with a damped sine wave. The frequency of this oscillation is given by  $\omega = \sqrt{\Delta B_z^2 + J(\varepsilon)^2}/\hbar$  and shown in Fig. 5.10a. We further fit  $J(\varepsilon)$  to a phenomenological model  $J = J_0 \exp(\varepsilon/\varepsilon_0)$  and find that the  $\varepsilon$  dependence is nearly independent of the inter-dot tunnel coupling with a typical value of  $\varepsilon_0 \approx 0.3$  mV.

### 5.5.11. Setting up an automated detection for charge switching events

Charge noise, whether originating from the heterostructure itself<sup>[21,71,20]</sup> or the electrical setup, is a major challenge in all kinds of semiconductor qubits. While electrical noise from the setup can be mitigated, removing the origin of charge noise from the sample is more complicated. To current understanding, charge traps in the doping layer as well as so-called DX-centers<sup>[21,20]</sup> are believed to be the origin. For ST<sub>0</sub> qubits, charge noise affects the exchange interaction  $J(\varepsilon)$ , being most problematic in regions of high  $dJ/d\varepsilon$ <sup>[72]</sup>. Due to the nonlinearity of  $J(\varepsilon)$ , a small change in detuning results in a big change of J. Hence, coherence is decreased in this region.

Not only does charge noise affect the coherence of the system, but if the charge trap sits in direct vicinity of the quantum dot, it may shift the whole position of the (2,0)-(1,1)-transition in gate space, once an electron tunnels in or out. If such a switching events occurs, the virtual gates may be used to restore the original position, but usually such a retuning takes a long time and is not always deterministic. As some of these charge rearrangements occur at distinct timescales, another alternative is to simply wait for the dot to jump back. In between measurements, we automatically detect switching events by monitoring the position of the  $ST_+$  transition and the conductance level of the sensing dot. If either of these values change too much in between measurements, we conclude that a switching events has occurred and execute the jump detection in an continuous loop until the original values are restored. By monitoring the position of the  $ST_+$  crossing as well as the DC level of the charge sensor the success rate of this detection is very high.

#### 5.6. Conclusion

This paper provides a detailed description of tuning and characterization routines that we use to realize a  $ST_0$  qubit in a GaAs double quantum dot. We describe efficient methods to determine the different inter-dot and lead tunnel couplings and methods how to locate several reload points in the charge stability diagram needed for the qubit itself or the pulsed feedback DNP.

While all relevant, quantitative double dot parameters are already obtained automatically, the decision of how to adjust the gate voltages is currently made by the operator, based on experience. So far, sample stability and resulting frequent charge rearrangements leading to unreliable fits when unsupervised have made a fully automated, gradient-based tune-up procedure too cumbersome to make its development worthwhile. We also find that the effect of the T and N gates on the inter-dot tunnel coupling changes substantially in different regions of gate voltage space or when charge rearrangements in the vicinity of the dot occur, including even sign changes.

This behavior will likely render algorithms to fully automate the tuning that are based on pre-calibrated gradient information ineffective. Nevertheless, we are optimistic that the procedures described here could be used as a starting point for reaching that goal. Improved sample designs<sup>[79]</sup> and lower disorder which make the response to gate voltage changes more predictable would greatly simplify the task. Complementary to that, self-calibrating approaches such as the use of a Kalman<sup>[91]</sup> filter to track the response tensor over the recent tuning history appear promising. Such advances will be indispensable as soon as the number of qubits increases substantially.

# 6. Quadrupolar effects and anisotropy on dephasing in two-electron spin qubits in GaAs

The following chapter is adapted from Ref. 78<sup>1</sup>.

#### 6.1. Abstract

Understanding the decoherence of electron spins in semiconductors due to their interaction with nuclear spins is of fundamental interest as they realize the central spin model and of practical importance for using them as qubits. Interesting effects arise from the quadrupolar interaction of nuclear spins with electric field gradients, which have been shown to suppress diffusive nuclear spin dynamics and might thus enhance electron spin coherence. We show experimentally that for gate-defined GaAs quantum dots, quadrupolar broadening of the nuclear Larmor precession reduces electron spin coherence via faster decorrelation of transverse nuclear fields. However, this effect disappears for appropriate field directions. Furthermore, we observe an additional modulation of coherence attributed to an anisotropic electronic *g*-tensor. These results complete our understanding of dephasing in gated quantum dots and point to mitigation strategies. They may also help to unravel unexplained behaviour in self-assembled quantum dots and III-V nanowires.

#### **6.2.** Introduction

Electron spin qubits in GaAs quantum dots have played a central role in demonstrating the key operations of semiconductor spin qubits  $^{[9,10,11,12]}$ . A prominent and often dominant dephasing mechanism in these devices as well as other semiconductor spin qubits  $^{[92,93]}$  is the interaction of the electron spin with  $10^4 - 10^6$  nuclear spins of the

<sup>&</sup>lt;sup>1</sup>Molecular beam epitaxy growth of the sample was carried out by D. Schuh and D. Bougeard. T.Botzem and R. McNeil set-up the experiment. J.-M. Mol extended the data acquisition protocol. T. Botzem fabricated the sample and conducted the experiment. T.Botzem and H. Bluhm developed the theoretical model, analysed the data and wrote the paper.

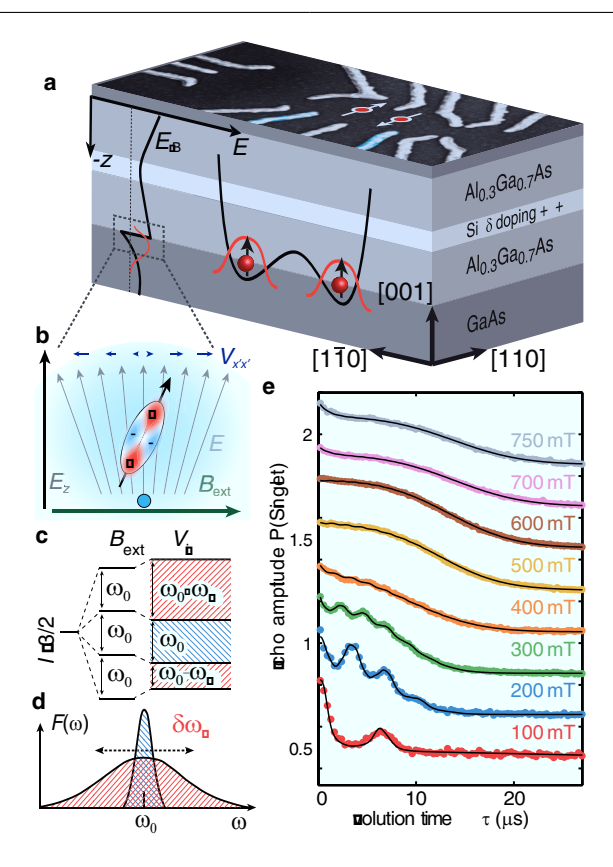


Figure 6.1.: Device Layout and quadrupole broadening. a Gates used for pulsed qubit control are depicted in blue; the energy of the conduction band edge  $E_{CB}$  is shown on the left. b Nuclear spins 3/2 with magnetic moment  $\mu$  in the proximity of the quantum dot experience quadrupolar coupling to electric field gradients  $V_{x'x'}$  induced by crystal distortion due to the electric field of the triangular quantum well. c While the center transition, with splitting  $\omega_0$ , stays unchanged, the satellite transitions, distorted by the electron's own charge, exhibit a quadrupolar shift by  $\omega_Q$ . d The resulting frequency distribution  $F(\omega)$  consists of two Gaussians with different variances, one showing an excess quadrupolar broadening of  $\delta\omega_Q$ . e Echo amplitude for magnetic fields along the [110] axis, showing oscillations with the relative Larmor frequencies of the three nuclear spins. A semi-classical model (solid line) is used to fit the data (dots, offset for clarity).

host lattice. While the fundamentals of this interaction have been studied quite extensively [94,95,40,38,39], and theory and experiments are in reasonable agreement [15,42], theory predicts a potential for much longer dephasing times [96] than observed so far and it remains an open question as to what ultimately limits electron spin coherence. Remarkable progress has also been made in eliminating dephasing from nuclear spins by using Si-based systems [50] that can be isotopically purified, but this route is not open

for III-V semiconductor systems, where all isotopes carry nuclear spin. Nevertheless, the latter remain of practical interest because of their lower effective mass, single conduction band valley and potential for optical coupling.

The role of quadrupolar coupling of nuclear spins to electric field gradients (EFGs) from charged impurities or strain has been investigated, both experimentally and theoretically [97,98,99,100,101,102], mostly in self-assembled quantum dots, which exhibit large quadrupolar splittings due to strain intrinsic to their epitaxial growth. But its influence on electron spin coherence was unclear and it was first thought to enhance coherence due to quadrupolar suppression of nuclear spin flip-flops.

In contrast to this prediction, we find that Hahn echo coherence of our gate-defined quantum dots deteriorates when the magnetic field is rotated to maximize quadrupolar broadening of nuclear levels. This degradation of coherence is similar to very recent findings in self-assembled quantum dots [103,104], although in our case, quadrupolar splittings arise from local electric fields rather than strain and are orders of magnitude weaker. In addition, we find a complex pattern of collapses and revivals of the echo signal unless the magnetic field is aligned with specific crystal axes, which we explain with an anisotropic g-tensor causing a coupling of the nuclear Larmor precession to the electron spin.

#### 6.3. Results

#### **6.3.1.** S-T<sub>0</sub> qubit

The qubit studied here is a two-electron spin qubit  $[^{25,9}]$ , using the  $m_z = 0$  subspace of the spin singlet S and spin triplet  $T_0$  of two electron spins. These electrons are confined in a GaAs double quantum dot formed by electrostatic gating (Fig. 1a) of a two-dimensional electron gas (2DEG). The effects explored in this work apply equally to single electron spins.

A random configuration of the nuclear spins introduces an effective magnetic field of a few mT, the Overhauser field, whose dynamics cause qubit dephasing. Hahn echo measurements that eliminate dephasing from slow fluctuations allow studying these dynamics, as they become the dominant dephasing mechanism.

We follow the experimental procedure from Ref. 15 (see also Methods), implementing the required  $\pi$ -pulse to invert the state of the qubit halfway through the evolution time  $\tau$  using the exchange interaction between the two spins. Fig. 1c shows the spin echo signals as a function of separation time for magnetic fields aligned along the [110] crystal axis. (Note that we experimentally cannot distinguish between the [110] and [110] axes, but refer to the direction parallel to the dot connection line as the [110] axis throughout the paper for ease of reading.) Similar results to Refs. [15,105] are obtained, but with approximately a factor two shorter coherence times (see Supplementary Note

1). At fields below 500 mT, a second order coupling to the oscillating, transverse nuclear field (i.e., its component perpendicular to the external field) leads to periodic collapses and revivals of the echo amplitude [38,39,15,42]. Revivals occur at times corresponding to the periods of the relative Larmor precession of the three species <sup>69</sup>Ga, <sup>71</sup>Ga and <sup>75</sup>As. The overall envelope decay can be modeled by assuming a phenomenological broadening  $\delta B$  of the nuclear Larmor frequencies. Because of this variation of the precession rates, the total transverse hyperfine field of each species decorrelates on the time scale of  $1/\delta B$ . Due to the above mentioned quadratic contribution of the transverse hyperfine field to the electronic Zeeman splitting, these fluctuations contribute to the dephasing of the electrons.

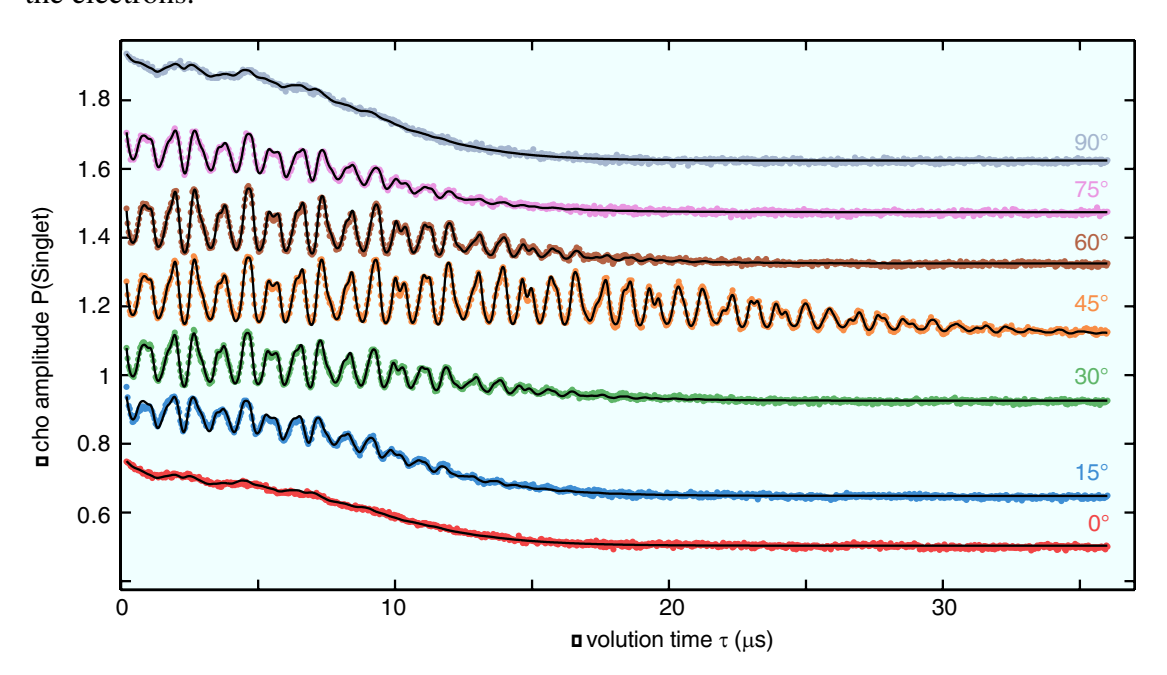


**Figure 6.2.: B-field direction dependence.** Echo amplitude at  $300\,\mathrm{mT}$  as a function of separation time for different in-plane magnetic field directions  $\theta$ , with  $0^\circ$  corresponding to the [110] direction. Curves are offset for clarity. At  $45^\circ$ , parallel to the crystallographic [100] axis, the coherence time is enhanced as quadrupolar couplings are suppressed. When rotating the field a *g*-factor anisotropy leads to oscillations, associated with the three different nuclear Larmor frequencies. A semi-classical model (solid line) is used to fit the data (dots).

#### 6.3.2. Quadrupolar interaction

While such a broadening is expected from dipolar interaction between nuclei, fitting the current and earlier<sup>[15]</sup> data requires a value of  $\delta B = 1.4\,\mathrm{mT}$  and  $\delta B = 0.3\,\mathrm{mT}$  respectively, at least a factor three larger than the intrinsic dipolar nuclear linewidth of 0.1 mT

obtained from nuclear magnetic resonance (NMR) measurements in pure GaAs<sup>[106]</sup>. More direct measurements of the nuclear dynamics based on correlation of rapid single shot measurements<sup>[107]</sup> are consistent with these values.

NMR experiments on GaAs samples with impurities as well as studies in single self-assembled quantum dots [102,108] revealed a similar excess line broadening, which was found to depend on the field direction and explained by quadrupolar effects [106,109]. Strain as well as electric fields from charged impurities or the triangular quantum well, used here to confine electrons (see Fig. 1a), distort the valence orbitals and crystal lattice, thus creating EFGs at nuclear sites (see Fig. 1b). These EFGs couple to the quadrupolar momentum of the nuclei with spin I = 3/2 and (to lowest order) modify the splitting of the  $I_z = \pm 3/2 \leftrightarrow \pm 1/2$  satellite Larmor transitions by [106]

$$\omega_{Q,\alpha} = \frac{eQ_{\alpha}}{2} V_{x'x'},\tag{6.1}$$

where  $Q_{\alpha}$  is the quadrupolar moment of nuclear species  $\alpha$ , e the elementary charge and  $V_{x'x'}$  denotes the component of the electric field gradient tensor in the direction of the external field (Fig 1b). For in-plane fields as considered here, the relevant longitudinal local field gradient induced by an electric field is given by [106] (see also Supplementary Note 2)

$$V_{r'r'} = R_{14,\alpha} E_z \cos(2\theta). \tag{6.2}$$

 $R_{14,\alpha}$  is the species dependent response tensor component relating electric fields to electric field gradients at the nuclear site due to lattice and orbital distortions and  $\theta$  is the angle between the magnetic field and the [110] axis. The angular dependence and the fact that only the z-component of the electric field,  $E_z$ , contributes, arise from the crystal symmetry of the host material. Hence, the local electric field  $E_z$  and its variation across the electronic wave function due to the electron's own charge density introduces a broadening of the precession frequencies. The dependence of  $\omega_{Q,\alpha}$  on  $\theta$ , implies a suppression of the effect for a field along the [100] and [010] axis.

The Hahn echo amplitude as a function of separation time is shown in Fig. 2 for different in-plane field directions  $\theta$  between the [110] and the [1 $\bar{1}$ 0] axes (see Methods). Indeed a factor two longer coherence is seen for  $\theta = 45^{\circ}$ , parallel to the [100] (or [010]) direction. Apart from this enhancement, another oscillatory modulation appears, reaching a maximum at the same angle.

#### 6.3.3. g-factor anisotropy

To further investigate the origin of these oscillations we aligned  $B_{\rm ext}$  along the [100]-axis and varied its magnitude in Fig. 3. With decreasing  $B_{\rm ext}$  the frequency of the modulation decreases, until at 100 mT only a very fast decay of the echo amplitude followed by a revival at  $\tau \approx 13 \,\mu \rm s$  occurs. This envelope modulation can be explained by an electronic g-factor anisotropy, arising from an asymmetric confinement of the electron in the

2DEG and spin-orbit coupling [110,111,112]. The main axes of the *g*-tensor are expected to be the [110] and [110] crystal axis, consistent with the absence of a fast echo modulation with *B* along these directions. For other field directions, the quantization axis of the electron differs from the external field around which the nuclear spins precess. A linear coupling to the transverse nuclear magnetic field  $B_{\text{nuc}}^{\perp}$  thus appears in the effective magnetic field determining the electronic Zeeman splitting (see Fig. 4a, Supplementary Fig. 1 and Supplementary Note 3):

$$B_{\text{eff}} = g_{\parallel} B_{\text{ext}} + g_{\perp} B_{\text{nuc}}^{\perp}(t), \tag{6.3}$$

where  $g_{\parallel}(g_{\perp})$  denotes the (off-)diagonal entries of the *g*-tensor. During the free evolution part of the spin echo, the qubit acquires a phase arising from  $B_{\rm nuc}^{\perp}(t)$ . Due to the dynamics of  $B_{\rm nuc}^{\perp}(t)$  that phase is not eliminated by the echo pulse and hence leads to dephasing. But whenever the evolution time  $\tau/2$  is a multiple of all three Larmor frequencies, the net phase accumulated vanishes and the echo amplitude recovers. Partial recovery occurs if the evolution time only matches a multiple of the Larmor period of two or one species.

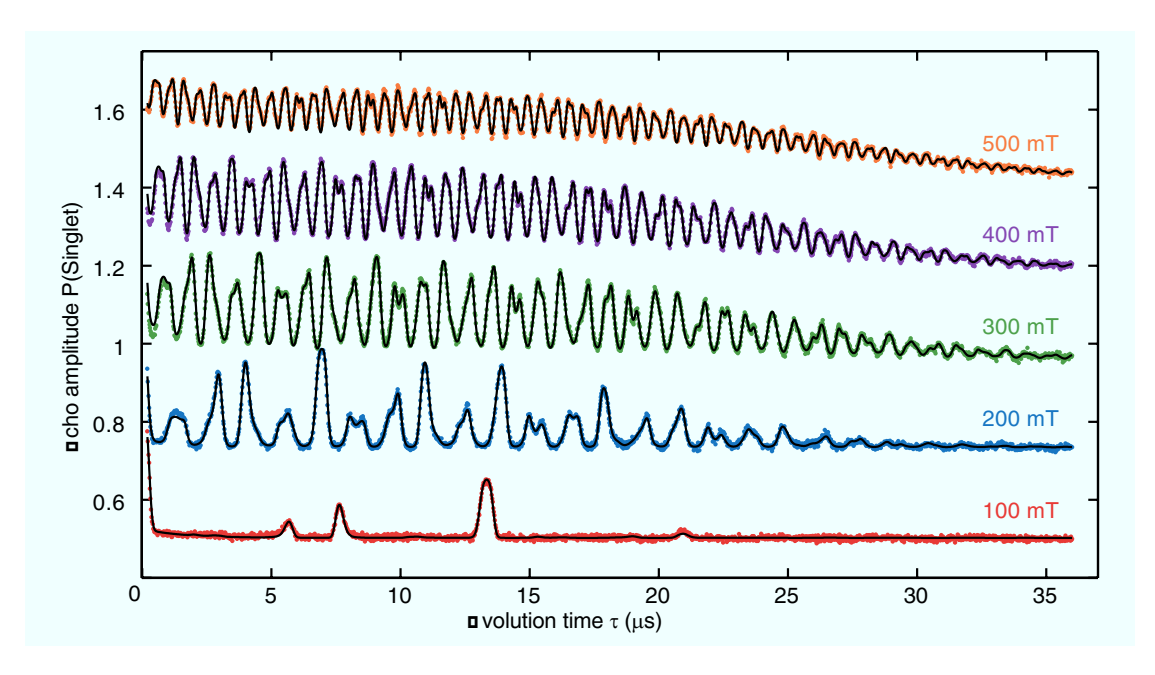


**Figure 6.3.: B-field magnitude dependence.** Echo amplitude for magnetic field magnitudes along the [100] axis. A *g*-factor anisotropy causing different quantization axes for electron and nuclei spins leads to oscillations with the three nuclear Larmor frequencies. For small magnetic fields the echo signal is strongly suppressed in the first hundreds of nanoseconds, but revives at later times. A semi-classical model (solid line) is used to fit the data (dots).

#### **6.3.4.** Semiclassical fit model

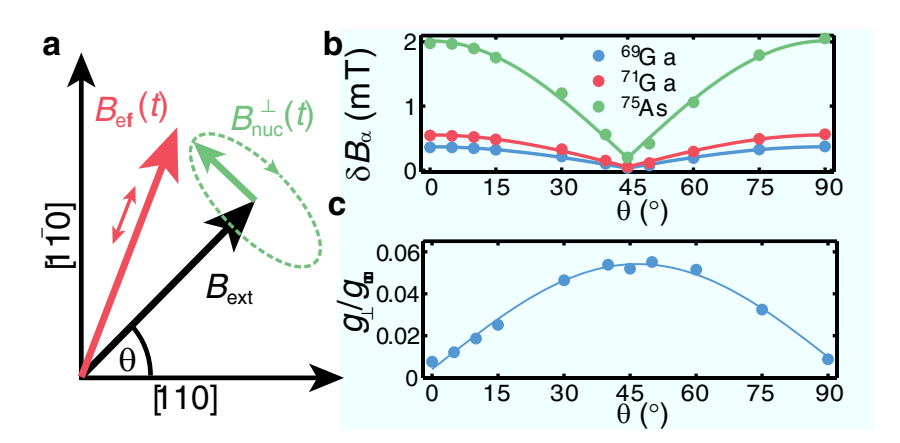


Figure 6.4.: *g*-factor anisotropy and fit parameters. a Due to an anisotropic *g*-tensor electron and nuclear spins have different quantization axes,  $B_{\text{eff}}$  and  $B_{\text{ext}}$ , respectively. This leads to a linear contribution of the transverse Overhauser field to the electronic Zeeman splitting, oscillating with the Larmor frequencies of the nuclear spins. **b**, **c** Fit parameters extracted for different in-plane magnetic field directions  $\theta$ . The quadrupolar contribution to nuclear broadening  $\delta B_{\alpha} = \hbar \delta \omega_{Q,\alpha}/\gamma_{\alpha}$ , expressed in terms of an equivalent line width for the three isotopes using equation (6.1), vanishes at 45° along the [100] direction. At the same angle, the  $\sin(2\theta)$  dependence of the coupling  $g_{\perp}$  to the transverse hyperfine field reaches a maximum.

To obtain a quantitative description of quadrupolar and anisotropy effects, we adapt the semiclassical model of Ref. 15, based on computing the total electronic phase accumulated due to the precessing nuclear spins and averaging [42] over the initial nuclear state. The transverse hyperfine field is modeled as the vector sum of Gaussian distributed contributions arising from the three nuclear species and the spread of quadrupolar shifts. The distribution of nuclear precession frequencies  $F(\omega)$  is chosen such that the correlation function of the transverse field is that obtained from an ensemble of independent nuclear spins 3/2 subjected to a Gaussian distribution of quadrupolar shifts (see Supplementary Note 4).  $F(\omega)$  is taken as the weighted sum of two Gaussians centered on the Larmor frequency, reflecting the contributions from the unperturbed center transition and the quadrupole broadened satellite transitions as schematically depicted in Fig. 1d. The rms-width of the quadrupolar broadened distribution is given by the variation of electric fields via equation (6.1) and (6.2).

Using this model we fit the data (Fig. 1-3) with most free parameters being independent of the magnetic field (see Supplementary Note 4). Most relevant for this work are the quadrupolar broadenings of nuclear transition and the linear coupling to transverse hyperfine fields  $g_{\perp}$  (both depending on field direction only) shown in Fig. 4b and

c. As predicted, the quadrupolar broadening approximately vanishes at  $\theta=45^\circ$  and is maximal at  $\theta=0^\circ$  and  $\theta=90^\circ$ .

The maximum magnitude of  $\delta B_{\alpha}$  is consistent with the electric field variation generated by the electron in the dot (see Supplementary Note 4). The off-diagonal *g*-tensor element  $g_{\perp}$  shows the predicted  $\sin(2\theta)$  dependence, and its maximum anisotropy of 5% is comparable with that found in quantum wells<sup>[111]</sup>.

#### 6.4. Discussion

One of our key results is that quadrupole broadening of nuclear spins can contribute to electronic dephasing by increasing the nuclear linewidth and hence leading to faster decorrelation of the transverse nuclear polarization, which contributes to the electronic Zeeman splitting to second order. While in principle another source of anisotropy with the same angular dependence could explain the observed variation of the coherence time, we are not aware of any other plausible mechanism. Anisotropic diffusion shows a different angular dependence with the longest coherence times along the [110] direction. Our interpretation is further supported by the good quantitative agreement with the model and NMR measurements [106,109]. This result does not contradict the reported suppression of nuclear spin diffusion [101] by quadrupole effects [100] as spin diffusion mostly affects electron coherence via the longitudinal polarization, whereas in our case the transverse coupling is dominant. An isotropic g-factor in combination with an anisotropic hyperfine interaction would lead to the same echo modulation when rotating  $B_{\rm ext}$ , but the anisotropy of the hyperfine interaction is usually assumed to be negligible as the conduction band wavefunction of GaAs is predominantly s-type.

While in the present sample g-factor anisotropy and quadrupolar effects cannot be eliminated simultaneously, symmetric, possibly back-gated quantum wells<sup>[111]</sup> should allow the elimination of any g-factor anisotropy. The back gate could also be used to tune quadrupolar interaction, as it depends on the electric field, thus allowing further studies.

Given that the strain-induced quadrupole broadening in self-assembled dots was found to be 3-4 orders of magnitudes larger<sup>[102,100,108]</sup>, it likely also has pronounced effects on the coherence<sup>[103]</sup> of this type of quantum dot, which is currently less well understood than that of gated dots. In addition to the above-mentioned second order coupling to the transverse Overhauser fields a linear coupling of the parallel field components to the effective spin splitting due to the very large and non-uniformly distributed quadrupole splitting in these systems results in a similar, but more complex echo envelope modulation<sup>[104]</sup>.

Furthermore, the echo modulation due to an anisotropic g-factor may also play an important role in III-V nanowire qubits, where strong g-factor anisotropies and short coherence times have been measured [114,16].

#### 6.5. Methods

#### 6.5.1. Qubit system and experimental setup

The quantum dots used in this work were fabricated on a GaAs/Al<sub>0.69</sub>Ga<sub>0.31</sub>As heterostructure with Si-δ-doping 50 nm below the surface and a spacer thickness of 40 nm, leaving the 2DEG at 90 nm depth, as shown in Fig. 1a.

Using fast voltage pulses provided by a Tektronix AWG5014C to detune the qubit for manipulation requires thoughtful RF-engineering of the experimental setup. To avoid any excess pulse distortion, apart from attenuation and skin-effect of coaxial cables, we abandon bias-Ts and use separate DC-coupled static and control gates. Static voltages of order 1 V are applied to the heavily filtered static gates in order to define and tune the quantum dots. The control-gates are used exclusively to apply the mV-scale signals for qubit manipulation. This separation eliminates the need for bias T's and thus provides a nearly flat frequency response of the control gates from DC to a few hundred MHz (discussed in Supplementary Note 5 and shown in Supplementary Fig. 2). The control gates are DC-coupled to the AWG outputs, although heavily attenuated by  $-33\,\mathrm{dB}$  to reduce thermal noise from room temperature.

#### 6.5.2. Echo sequence

Following the experimental procedure for Hahn spin echo measurements from Ref. 15 we first initialize the qubit system in the spin singlet groundstate S by pulsing both electrons into one dot. Rapidly separating the electrons into both dots lets them evolve in different Zeeman fields arising from the external magnetic field  $B_{\rm ext}$  and the fluctuating local Overhauser field  $B_{L(R)}$  of the left (right) dot for a time  $\tau$ . A gradient  $\Delta B_z = |B_L - B_R|/2$  in the hyperfine field of the two dots leads to coherent rotations between S and  $T_0$  and fluctuations in  $\Delta B_z$  cause dephasing. An exchange splitting between the spin singlet S and triplet state  $T_0$  arises from inter-dot tunnel-coupling. This exchange allows electric control of the qubit by varying the difference in electrostatic potential between the two dots, on the nanosecond time scale with an arbitrary waveform generator. Using this exchange interaction to perform a  $\pi$ -pulse by driving rotations between the eigenstates  $|\uparrow\downarrow\rangle$  and  $|\downarrow\uparrow\rangle$ , we swap the two electrons halfway through the evolution time  $\tau$ . Lastly, we read out the final qubit state by pulsing the electrons into one dot. Using Pauli-spin-blockade we distinguish between singlet and triplet states by measuring the resistance of a nearby sensing dot via RF-reflectometry<sup>[35]</sup>. Such a pulse cycle with varying evolution times is repeated several million times and the average echo amplitude is recorded. Simultaneous histogramming of individual measurement outcomes is used for normalization<sup>[10]</sup> (see Supplementary Figs. 2 and 3 and Supplementary Note 6 for details). The fine tuning of the pulses that was necessary in Ref. 15 to avoid artifacts from shifts of the wave function has been eliminated due to improved

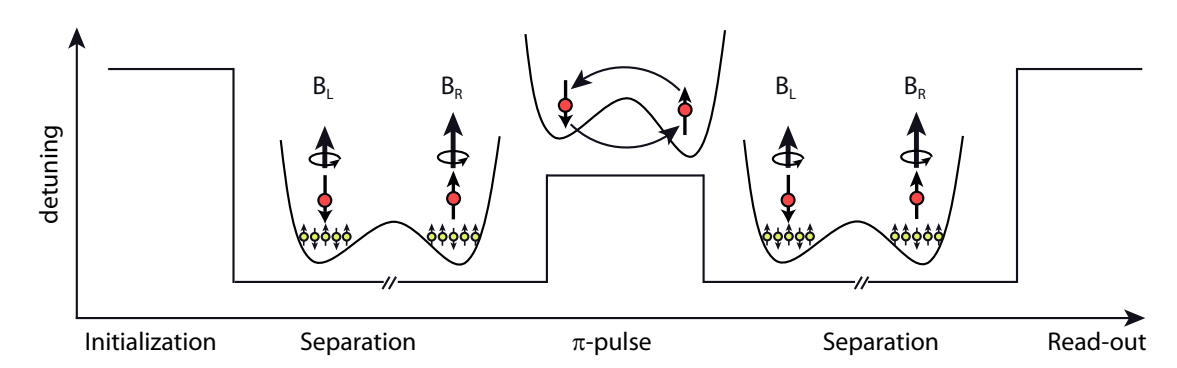


**Figure 6.5.: Pulse sequence for Hahn Echo.** We first initialize the qubit system in the spin singlet S(0,2) ground state by pulsing to a large positive detuning, where both electrons remain in one dot. Pulsing rapidly to large negative detuning separate the electrons in two dots and they evolve for a time  $\tau$  in different Zeeman fields, built up from the external magnetic field  $B_{\rm ext}$  and the individual fluctuating local Overhauser field  $B_{\rm L(R)}$ . A gradient  $\Delta B_z = |B_{\rm L} - B_{\rm R}|/2$  in the hyperfine field of the two dots, leads to coherent rotations between S and  $T_0$  and fluctuations in  $\Delta B_z$  cause dephasing of the latter. Using the exchange interaction driving rotations between the eigenstates  $|\uparrow\downarrow\rangle$  and  $|\downarrow\uparrow\rangle$  of  $\Delta B_z$  at intermediate detuning to perform a  $\pi$ -pulse we swap the two electrons halfway through the evolution time  $\tau$ . We lastly read out the final qubit state by pulsing back to positive detuning.

RF-engineering.

#### 6.6. Supplementary information

This document provides supplementary information to the main text. We first explain the experimental setup, the characterization of the pulse hardware and our approach to data normalization. We continue by deriving the influence of a *g*-factor anisotropy and quadrupolar coupling to the nuclear bath on electron coherence. In the last section we describe the derivation of the semi-classical fit model used to fit all measurements.

#### 6.6.1. Experimental setup

Using fast voltage pulses provided by a Tektronix AWG5014C to detune the qubit for manipulation requires thoughtful RF-engineering of the experimental setup. To avoid any excess pulse distortion, apart from attenuation and skin-effect of coaxial cables, we abandon bias-Ts and use separate DC-coupled static and control gates. Static voltages of order 1 V are applied to the heavily filtered static gates in order to define and tune the quantum dots. The control-gates are used exclusively to apply the mV-scale signals for qubit manipulation. This separation eliminates the need for bias T's and thus provides

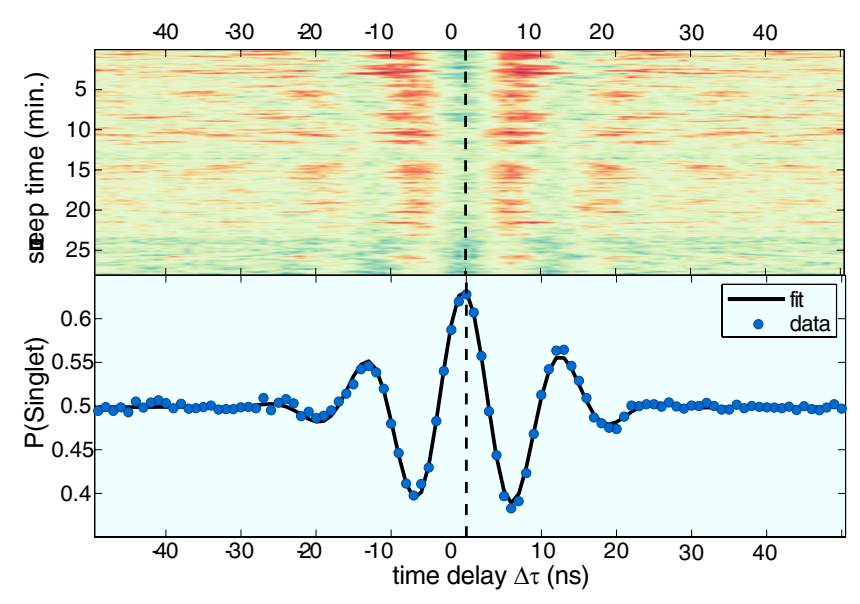


**Figure 6.6.:** Wavefunction shifts. Repetitions of the echo amplitude as a function of a echo pulse time delay  $\Delta \tau$  for total evolution time  $\tau = 10 \mu s$  at 500 mT. Due to improved high-frequency engineering the position of the maximum echo amplitude does not shift over time, even for stabilized magnetic field gradient  $\Delta B_z$ , indicating a stable spatial electronic wavefunction over the pulse cycle (compare Ref. 15).

a nearly flat frequency response of the control gates from DC to a few hundred MHz. The control gates are DC-coupled to the AWG outputs, although heavily attenuated by  $-33 \, \mathrm{dBm}$  to reduce thermal noise from room temperature.

To check for slow drifts in the control pulses, which would lead to spatial shifts of the electronic wavefunction (compare Ref. 15), we shift the  $\pi$ -pulse by a time  $\Delta \tau$  and track the echo amplitude as a function of  $\Delta \tau$  of the  $\pi$ -pulse for the whole measurement time. For  $\Delta \tau = 0$  the evolution time before and after the  $\pi$ -pulse is exactly the same and should yield the best refocusing. A drift of the maximum of the echo amplitude would indicate that the electrons sample different nuclear spins before and after the  $\pi$ -pulse, caused for example by a change in gate voltages. In Fig. 6.6 one can clearly see that the position of the echo amplitude is stable over the whole measurement time, even for intentionally stabilized  $\Delta B_z$  which showed to increase the shift in position [15], reflecting a stable control voltage over the duration of the separation time. Nonetheless we tested the effect of the pulse optimization procedure from Ref. 15 by adding a slope to the detuning once the electrons are separated but are not able to obtain longer coherence times. This test confirms that the pulses already have the optimal shape without further compensation.

#### 6.6.2. Data normalization and stitching

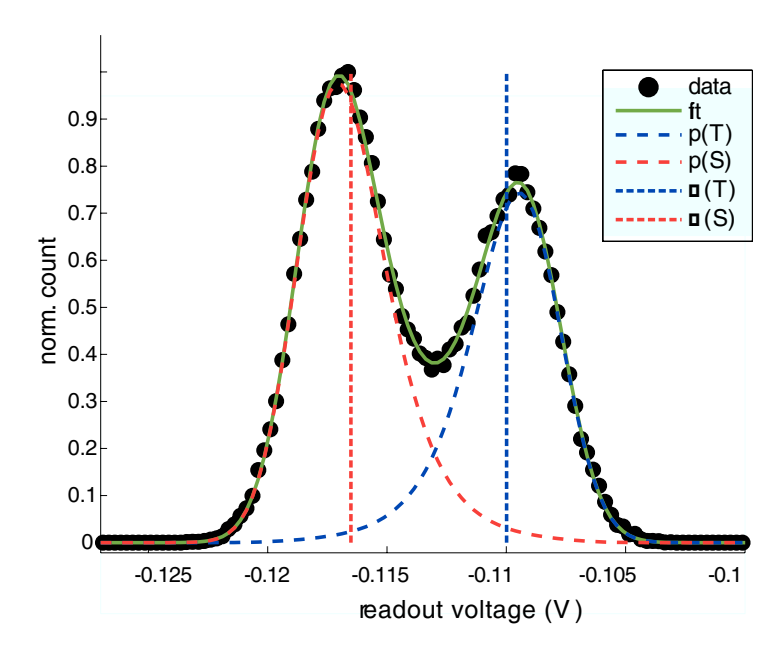


**Figure 6.7.: Single-shot histogram.** Individual measurement outcomes are histogrammed simultaneously with recording the average. By fitting the resulting histogram, we obtain the voltage expectation values E(S) and E(T), representing spin singlet or triplet states. Theses expectation values are used to normalize the averaged measurement data.

In order to link measured RF sensor [35] voltages to the actual qubit states  $|S\rangle$  and  $|T_0\rangle$  we simultaneously record histograms of the single shot readout voltage, averaged over the measurement window after each pulse. As seen in Fig. 6.7 these histograms typically show two Gaussian distributions, corresponding to  $|S\rangle$  and  $|T_0\rangle$ , which are smeared out due to  $T_1$  relaxation from  $|T_0\rangle$  to  $|S\rangle$  and excitation from  $|S\rangle$  to  $|T_0\rangle$ . Using a fit model similar to Ref. 10 and a measured relaxation time of  $\approx 16 \mu s$  for the metastable (1,1) charge configuration, we are able to obtain the distributions for singlet and triplet states. (Note that this relaxation occurs at the measurement point and is different from the relaxation rate of the qubit at its operating point with separated electrons.) We then use the mean voltages E(S) and E(T), corresponding to S and T values, respectively, to normalize our measurement data. While this procedure should largely eliminate readout-related visibility losses,  $\pi$ -pulse errors still contribute to the visibility being less than 0.5. As the relaxation time shows a strong dependence on the magnetic field gradient  $\Delta B_z$ , we restrict our measurements to gradients below 60 MHz by using Dynamic Nuclear Polarization (DNP)<sup>[13]</sup>. Simultaneously recorded values for  $\Delta B_z$  allow for post-selection in case DNP failed (only used for measurements performed at high external magnetic fields along the [110]-axis).

To resolve the fast oscillations of the echo amplitude when rotating the external magnetic field, it is necessary to increase the resolution of the evolution time  $\tau$  to 20 ns, exceeding AWG memory for  $\tau=36\mu s$  if all pulses were uploaded simultaneously. We therefore consecutively record four different time intervals, each overlapping by  $2\mu s$ , and stitch them back together post measurement. Recording individual single shot histograms and normalizing data before stitching allows the removal of slow 1/f-noise and individual time traces fit well, as depicted in Fig. 6.8. Within each interval, a lownoise, high data quality is obtained by recording different evolution times consecutively and then averaging over many repetitions to elude slow drifts in the sensor or gate voltage configuration. For a typical dataset the evolution time was rapidly swept 101 times for a total measurement time of  $101 \times 36\mu s \approx 3.6 \, \text{ms}$  and then averaged over  $> 250 \, \text{repetitions}$ .

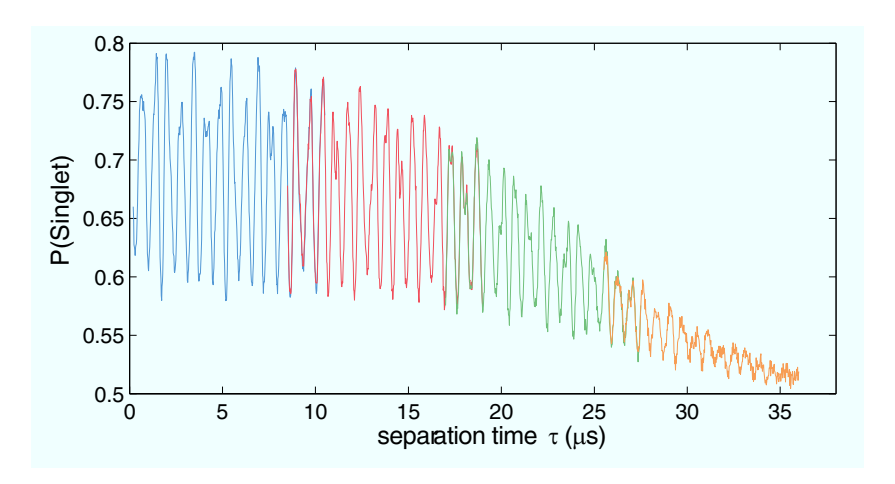


**Figure 6.8.: Data stitching.** Due to limited AWG memory we recorded four individual time traces (different colors) in order to resolve the fast envelope modulation.

#### 6.6.3. g-factor anisotropy in asymmetric GaAs heterostructure

In this section we will show that a *g*-factor anisotropy leads to a linear coupling to the transverse Overhauser-field, as illustrated in Supp. Fig. 6.10, causing additional dephasing (see Sec.6.6.5).

In the main axes coordinate system with  $x \parallel [110]$ ,  $y \parallel [1\overline{1}0]$  and  $z \parallel [001]$ , the electronic *g*-tensor is of diagonal form:

$$\underline{\mathbf{g}} = \begin{pmatrix} g_{xx} & 0 & 0 \\ 0 & g_{yy} & 0 \\ 0 & 0 & g_{zz} \end{pmatrix}. \tag{6.4}$$

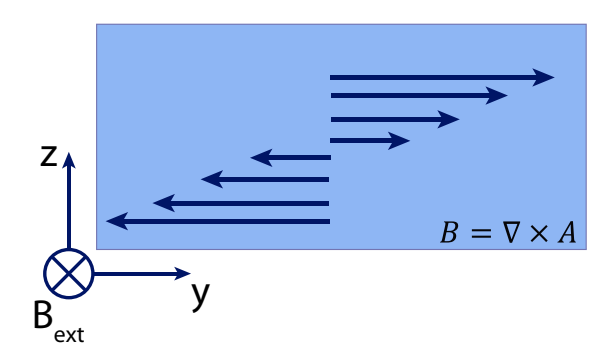


**Figure 6.9.:** *g*-factor anisotropy. An electron captured in an asymmetric quantum well or dot experiences a *g*-factor anisotropy via spin orbit coupling<sup>[115]</sup>. Moving along the *z*-direction in Fig. 6.9 the electron acquires a Lorentz momentum along the *y*-direction  $\delta p_y \propto H_x \cdot \langle z \rangle$ , due to a non-vanishing averaged position probability along *z*, yielding a new quantization axis  $\delta H_{SO}^y \propto p_z \cdot \delta p_y$  via Rashba-Spin-Orbit interaction. On average the effective quantization axis now also shows a component along the *y*-direction of  $\langle \delta H_{SO}^y \rangle \propto H_x \langle p_z \rangle \langle z \rangle$  correspondent to a g-factor anisotropy  $g_{xy}$ . For symmetric quantum wells  $\langle z \rangle = 0$  and hence anisotropy is suppressed in first order.

When rotating the external *B*-field by a rotation angle  $\theta$  about the [001]-axis we define a new coordinate system, such that  $x' \parallel B_{\text{ext}}$ ,  $y' \perp x'$  and z' = z. To calculate the *g*-tensor dependence on the rotation angle, we express the *g*-tensor in the rotated basis using the rotation matrix  $\mathbf{D}_{\theta}$ 

$$\underline{\mathbf{g}}_{\underline{\theta}} = \mathbf{D}_{\underline{\theta}} \underline{\mathbf{g}} \mathbf{D}_{\underline{\theta}}^{\mathsf{T}}, \tag{6.5}$$

For an anisotropic g-factor  $g_{xx} \neq g_{yy}$ , the resulting tensor has both diagonal and off-diagonal components:

$$\frac{g_{\underline{\theta}}}{g_{xx}\cos(\theta)^{2} + g_{yy}\sin(\theta)^{2}} = \frac{\frac{1}{2}\sin(2\theta)(g_{xx} - g_{yy})}{\frac{1}{2}\sin(2\theta)(g_{xx} - g_{yy})} = 0 \\
\begin{pmatrix} \frac{1}{2}\sin(2\theta)(g_{xx} - g_{yy}) & g_{xx}\sin(\theta)^{2} + g_{yy}\cos(\theta)^{2} & 0 \\
0 & 0 & g_{zz} \end{pmatrix} \\
= \begin{pmatrix} g_{\parallel} & g_{\perp} & 0 \\ g_{\perp} & g_{y'y'} & 0 \\ 0 & 0 & g_{zz} \end{pmatrix}.$$
(6.6)

In the last step we have defined the components parallel and perpendicular to  $B_{\text{ext}}$  as

$$g_{\parallel} = g_{x'x'} = g_{xx}\cos(\theta)^2 + g_{yy}\sin(\theta)^2 \approx g_{xx},$$
 (6.7)

$$g_{\perp} = g_{x'y'} = g_{y'x'} = \frac{1}{2}\sin(2\theta)(g_{xx} - g_{yy}),$$
 (6.8)

and find that the perpendicular components show a  $\sin(2\theta)$  dependence. With this g-

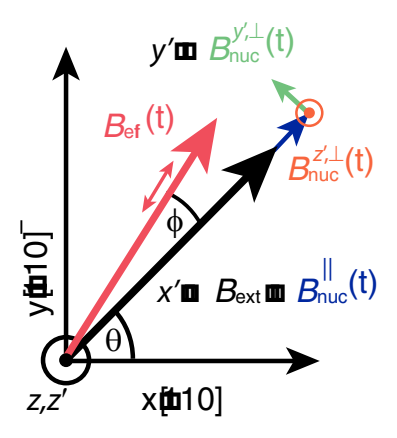


Figure 6.10.: B-field directions. This figure visualizes the two different coordinate systems, one is fixed and one rotates with  $\mathbf{B}_{\text{ext}}$ , and the nomenclature for the relevant field components.

factor anisotropy the Hamiltonian of the system now states

$$\mathbf{\hat{H}} = \mu_{\rm B} \mathbf{g}_{\underline{\theta}} \mathbf{B}_{\rm ext} \cdot \mathbf{\hat{S}} + \mu_{\rm B} g_{\parallel} \mathbf{B}_{\rm nuc} \cdot \mathbf{\hat{S}}$$
(6.9)

$$= \mu_{\rm B} \left( \underline{\mathbf{g}_{\underline{\boldsymbol{\theta}}}} \mathbf{B}_{\rm ext} \mathbf{O}^{\mathsf{T}} \right) \cdot \mathbf{O} \hat{\mathbf{S}} + \mu_{\rm B} g_{\parallel} \mathbf{B}_{\rm nuc} \cdot \mathbf{O}^{\mathsf{T}} \mathbf{O} \hat{\mathbf{S}}. \tag{6.10}$$

Note that the choice of  $g_{\parallel}$  to convert the hyperfine coupling to an effective magnetic field is a matter of convention. In the second step we have defined

$$\mathbf{O} = \begin{pmatrix} \cos(\phi) & -\sin(\phi) & 0\\ \sin(\phi) & \cos(\phi) & 0\\ 0 & 0 & 1 \end{pmatrix},\tag{6.11}$$

such that the vector  $\underline{\mathbf{g}}_{\underline{\theta}}\mathbf{B}_{\mathrm{ext}}\mathbf{O}^{\mathsf{T}}$  only has one nonzero component along the effective quantization direction of the electron.  $\phi$  is the angle between  $\mathbf{B}_{\mathrm{ext}}$  and the electron quantization axis  $\mathbf{g}_{\theta}\mathbf{B}_{\mathrm{ext}}$  and  $\hat{\mathbf{S}}$  denotes the spin operator. With  $\mathbf{O}\hat{\mathbf{S}} = \tilde{\mathbf{S}} = (\tilde{S}_x, \tilde{S}_y, \tilde{S}_z)$ 

and  $\mathbf{B}_{\mathrm{nuc}}=(B_{\mathrm{nuc}}^{\parallel},B_{\mathrm{nuc}}^{y',\perp},B_{\mathrm{nuc}}^{z',\perp})$  we write, ignoring non-secular terms

$$\hat{H} = \mu_{\rm B} \sqrt{g_{\parallel}^2 + g_{\perp}^2} B_{\rm ext} \tilde{S}_x + \mu_{\rm B} g_{\parallel} \left( B_{\rm nuc}^{\parallel} \cos(\phi) + B_{\rm nuc}^{y',\perp} \sin(\phi) \right) \tilde{S}_x.$$
 (6.12)

We further include the second-order coupling to the hyperfine field component perpendicular to the quantization axis  $\underline{\mathbf{g}}_{\underline{\theta}}\mathbf{B}_{\mathrm{ext}}$ , derived in Refs. [15,42], and obtain for the total Hamiltonian

$$\hat{H} = \mu_{\rm B} \sqrt{g_{\parallel}^2 + g_{\perp}^2} B_{\rm ext} \tilde{S}_x$$

$$+ \mu_{\rm B} g_{\parallel} \left( B_{\rm nuc}^{\parallel} \cos(\phi) - B_{\rm nuc}^{y',\perp} \sin(\phi) \right) \tilde{S}_x$$

$$+ \mu_{\rm B} g_{\parallel} \frac{\left( B_{\rm nuc}^{y',\perp} \cos(\phi) + B_{\rm nuc}^{z',\perp} - B_{\rm nuc}^{\parallel} \sin(\phi) \right)^2}{2B_{\rm ext}} \tilde{S}_x$$

$$\approx \mu_{\rm B} g_{\parallel} \left( B_{\rm ext} + B_{\rm nuc}^{\parallel} - \frac{g_{\perp}}{g_{\parallel}} B_{\rm nuc}^{y',\perp}(t) + \frac{B_{\rm nuc}^{\perp}(t)^2}{2B_{\rm ext}} \right) \tilde{S}_x.$$
(6.13)

In the last step we assumed the anisotropy to be small such that  $\sin \phi \approx \tan \phi = g_{\perp}/g_{\parallel}$  and  $\cos(\phi) \approx 1$ . Furthermore, we have defined  $(B_{\text{nuc}}^{\perp})^2 = (B_{\text{nuc}}^{y',\perp})^2 + (B_{\text{nuc}}^{z',\perp})^2$ . We thus find that an anisotropy in the electronic *g*-factor leads to linear coupling to the transverse hyperfine-field. However, note that an anisotropic hyperfine coupling tensor in the second term of equation (7.11) would lead to the same Hamiltonian and could not be distinguished from a *g*-factor anisotropy based on our data. We interpret our results in terms of the latter as such an anisotropy is known to exist, whereas we are not aware of any known corrections to the isotropic contact hyperfine interaction for the s-type GaAs conduction band.

#### 6.6.4. Quadrupolar interaction

In this subsection we derive the broadening of the Larmor frequencies due to dipolar and quadrupolar interaction of a spin 3/2 particle in the presence of a magnetic field and an electric field gradient (EFG) that shifts the normally equidistant Zeeman levels to create three distinct transition frequencies. A distribution of these quadrupolar broadened frequencies leads to dephasing of the qubit. The quadrupole terms are considered to first order in  $\omega_{Q,\alpha}/\omega_{\alpha}\ll 1$ , where  $\omega_{\alpha}$  is the Zeeman splitting of species  $\alpha$ . Our approach is to first compute the two-point time correlator of the transverse Overhauser field from the Zeeman and quadrupole Hamiltonian. We then construct a frequency distribution for the precession of classical Overhauser field contributions resulting in the same correlator.

Following Ref. 116 the Hamiltonian for a spin 3/2 including quadrupolar interaction is

$$\hat{H}_{Q} = \frac{e^{2}qQ}{4I(2I-1)} \left[ 3I_{z}^{2} - I^{2} + \eta \frac{\mathbf{I}_{+}^{2} + \mathbf{I}_{-}^{2}}{2} \right], \tag{6.14}$$

where Q is the quadrupolar moment, **I** the spin operator and  $\eta = (V_{zz} - V_{y'y'})/V_{x'x'}$  the asymmetry parameter of the electric field gradient tensor **V**, with spatial derivatives  $V_{ij} = \frac{\partial^2 V}{\partial r_i \partial r_y}$ . Neglecting the non-secular terms because of the large Zeeman splitting, the  $m = \pm 3/2 \leftrightarrow m = \pm 1/2$  satellite-transitions frequency shift  $\omega_{Q,\alpha}$  only depends on the local EFG  $V_{x'x'} = eq$  in the direction of the externally applied magnetic field and we obtain for species  $\alpha^{[106]}$ 

$$\omega_{\mathbf{Q},\alpha} = \frac{eQ_{\alpha}}{2} V_{x'x'}. \tag{6.15}$$

In order to relate electric fields E in the sample to EFGs, we use the general tensor relation:

$$V_{ij} = \sum_{k} R_{ij,k} E_k, \tag{6.16}$$

where  $R_{ijk}$  is the third rank response tensor. The secular component of **V** in the x'-direction can be written as

$$V_{x'x'} = \hat{\mathbf{n}} \cdot \mathbf{V} \cdot \hat{\mathbf{n}} = -2R_{14,\alpha} \cdot (n_x n_y E_z)$$
(6.17)

$$=2R_{14,\alpha}\cdot(\cos(\psi)\sin(\psi)E_z)$$

$$=R_{14,\alpha}E_{z}\sin\left(2\psi\right)\tag{6.18}$$

$$=R_{14,\alpha}E_z\cos(2\theta)\tag{6.19}$$

with the species dependent response tensor component  $R_{14,\alpha}$  and  $\hat{\bf n}$  being a unit vector in the direction of  $B_{\rm ext}$ . In the last step the angle  $\psi$ , measured from the [100]-direction, is transformed to the angle  $\theta$ , introduced in the last section. We find that the EFG only depends on the electric fields in z-direction, which predominantly originates from the triangular quantum well potential of the heterostructure. Nuclear spins in the proximity of the electron quantum dot additionally experience a spatial variation of these EFGs due to the electron's own charge density, which translates into a distribution of quadrupolar frequency shifts.

To obtain the frequency spectrum arising from these shifts we start by deriving the quantum-mechanical correlator of the angular momentum operator. Without loss of generality and consistent with the chosen coordinate system, we consider the y'-component of the angular momentum operator of a single spin 3/2

$$\hat{J}_{y'} = \frac{1}{i} \begin{pmatrix} 0 & \sqrt{3} & 0 & 0 \\ -\sqrt{3} & 0 & \sqrt{4} & 0 \\ 0 & -\sqrt{4} & 0 & \sqrt{3} \\ 0 & 0 & -\sqrt{3} & 0 \end{pmatrix}, \tag{6.20}$$

Using the time evolution operator of the system

$$e^{i\hat{H}t} = \begin{pmatrix} e^{\frac{i\omega_1 t}{\hbar}} & 0 & 0 & 0\\ 0 & e^{\frac{i\omega_2 t}{\hbar}} & 0 & 0\\ 0 & 0 & e^{\frac{i\omega_3 t}{\hbar}} & 0\\ 0 & 0 & 0 & e^{\frac{i\omega_4 t}{\hbar}} \end{pmatrix}, \tag{6.21}$$

to transform into the Heisenberg picture, one obtains

$$\hat{J}_{y'}(t) = e^{i\hat{H}t} \hat{J}_{y'} e^{-i\hat{H}t} =$$
 (6.22)

$$\begin{pmatrix} 0 & \sqrt{3}e^{\frac{i\omega_{1}2^{t}}{\hbar}} & 0 & 0\\ 0 & 0 & \sqrt{4}e^{\frac{i\omega_{2}3^{t}}{\hbar}} & 0\\ 0 & 0 & 0 & \sqrt{3}e^{\frac{i\omega_{3}4^{t}}{\hbar}} \\ 0 & 0 & 0 & 0 \end{pmatrix} + \text{h.c.}, \tag{6.23}$$

where we introduced the transition frequencies  $\omega_{ij} = \omega_i - \omega_j$ .

Using the infinite temperature density matrix  $\rho = \frac{1}{4}\mathbb{1}$  for the spin, we obtain for the two-point correlator

$$\langle \hat{J}_{v'}(t)\hat{J}_{v'}(t=0)\rangle = \text{tr}\left(\hat{J}_{v'}(t)\hat{J}_{v'}(t=0)\rho\right)$$
 (6.24)

$$= \frac{3}{8}\cos(\omega_{12}t) + \frac{1}{2}\cos(\omega_{23}t) + \frac{3}{8}\cos(\omega_{34}t). \tag{6.25}$$

We continue by calculating the correlator for the y'-component of the hyperfine magnetic field operator appearing in the nuclear part of the effective Zeeman Hamiltonian  $\hat{H}_{\text{nuc}} = g_{\parallel} \mu_{\text{B}} \hat{\mathbf{B}}_{\text{nuc}} \hat{\mathbf{S}}$ :

$$\hat{B}_{\text{nuc}}^{y',\perp}(t) = \sum_{i} A_{i} \hat{J}_{y'}^{i}(t), \tag{6.26}$$

where i runs over all nuclear spins. Hence

$$\langle \hat{B}_{\text{nuc}}^{y',\perp}(t)\hat{B}_{\text{nuc}}^{y',\perp}(t=0)\rangle$$

$$=\sum_{ij}A_{i}A_{j}\langle \hat{J}_{y'}^{i}(t)\hat{J}_{y'}^{j}(t=0)\rangle$$
(6.27)

$$= \sum_{i} A_{i}^{2} \langle \hat{J}_{y'}^{i}(t) \hat{J}_{y'}^{i}(t=0) \rangle$$
 (6.28)

$$= \sum_{i} A_{i}^{2} \left( \frac{3}{8} \cos(\omega_{12}^{i} t) + \frac{1}{2} \cos(\omega_{23}^{i} t) + \frac{3}{8} \cos(\omega_{34}^{i} t) \right), \tag{6.29}$$

where  $A_i$  is the hyperfine coupling parameter for spin i and we have used that different spins  $i \neq j$  are uncorrelated. The transition frequencies  $\omega_{23}^i = \omega_{\alpha(i)} + \Delta\omega_i$  and  $\omega_{12.34}^i =$ 

 $\omega_{\alpha(i)} + \Delta\omega_i \pm \omega_{Q,i}$  are composed of the species-dependent Larmor frequency  $\omega_{\alpha(i)} = \gamma_{\alpha(i)}B_{\rm ext}$  with  $\gamma_{\alpha}$  being the gyromagnetic ratio of species  $\alpha$ , a site dependent frequency shift  $\Delta\omega_i = \gamma_{\alpha(i)}\Delta B_i$  arising from an effective field variations  $\Delta B_i \approx 0.1$  mT due to interactions between nuclear spins, and the quadrupole shifts  $\omega_{Q,i}$ . The latter depend on the local electric field via equations (6.15) and (6.19) and on the species  $\alpha$  via the quadrupole moment  $Q_{\alpha}$ . In consideration of the large number of spins, we model these variations by species-dependent continuous frequency distributions

$$F_{\alpha}(\omega) = \frac{2}{5} \mathcal{N}_{\mathbf{I}}(\omega) + \frac{3}{5} \mathcal{N}_{\mathbf{Q}}(\omega)$$
 (6.30)

with  $\mathcal{N}_{I}$  and  $\mathcal{N}_{Q}$  being Gaussian distributions representing the interaction broadened center transition and the quadrupole broadened satellite transitions, respectively. Their prefactors follow from the relative weights in equation (6.29).  $\mathcal{N}_{I}$  and  $\mathcal{N}_{Q}$  are both assumed to be centered around  $\omega_{\alpha}$ . The standard deviation of  $\mathcal{N}_{I}$  is chosen to correspond to an interaction strength  $\delta B = 0.1$  mT and that of  $\mathcal{N}_{Q}$  is parametrized in terms of the species independent parameter  $\delta \omega_{Q,\alpha}/(Q_{\alpha}R_{14,\alpha})$ . It determines the rms strength of the distribution of local electric field gradients via equation 6.19, added in quadrature to  $\delta B$ .

To arrive at a classical description of the dynamics of the nuclear ensemble, we introduce giant effective classical spins k whose contributions to  $B_{\text{nuc}}^{\perp}$  are described by uncorrelated Gaussian variables, each representing a narrow range of frequencies of width  $\Delta \omega$ . We thus express the transverse nuclear field as a sum of complex-valued classical fields  $B_{\text{nuc}}^{x',\perp}(t) + iB_{\text{nuc}}^{y',\perp}(t) = \sum_k B_k(t) = \sum_k B_k^x(t) + iB_k^y(t)$ . The complex notation was introduced for convenience so that the time-dependence of the  $B_k(t)$  terms can be written as

$$B_k(t) = B_k(0)e^{i\omega_k t}. (6.31)$$

We further write the initial conditions  $B_k(0) = \bar{B}_k z_k$  for the kth spin in terms of their rms values  $\bar{B}_k$  and random variables  $z_k = x_k + iy_k$  following a Gaussian probability distribution  $p(z,z^*) = \frac{i}{4\pi} \exp\left(-zz^*/2\right)$  with unit variance. The  $\bar{B}_k$  reflect both the number of spins with a corresponding level splitting in one of the three transition as well as the strength of that transition. Hence, one can loosely think of each effective spin as representing a group of nuclei with approximately the same transition frequency  $\omega_{mn}^i$ , with the latter depending on the quadrupolar splitting, the local field arising from dipolar coupling to neighbouring nuclei, and the state of each nucleus determining the available transition.

Equation (6.31) leads to a correlator

$$\langle \hat{B}_{\text{nuc}}^{y',\perp}(t)\hat{B}_{\text{nuc}}^{y',\perp}(t=0)\rangle = \sum_{k} \bar{B}_{k}^{2}\cos(\omega_{k}t). \tag{6.32}$$

For this correlator to approximate that of equation (6.29), the  $\bar{B}_k$  have to be chosen according to

$$\bar{B}_k^2 = \frac{5}{4} \frac{\mathcal{A}_{\alpha(k)}^2 n_{\alpha(k)}}{N} F_{\alpha(k)}(\omega_k) \Delta \omega. \tag{6.33}$$

Here N is the number of unit cells overlapping with the quantum dot,  $n_{\alpha(k)}$  is the number of nuclei of species  $\alpha$  per unit cell and  $\mathcal{A}_{\alpha(k)}$  is the hyperfine coupling strength. We neglect a variation of  $A_i$  depending on the position of the nuclear spin relative to the electronic wave function as this inhomogeneity of the coupling was found to be negligible in Ref. 15, thus setting  $A_i = \mathcal{A}_{\alpha(i)}/N$ . We found that discretizing the frequency distribution of each species into seven equidistant intervals  $\Delta \omega$  was sufficient to suppress any numerical artifacts.

#### 6.6.5. Semiclassical fit model

#### **Derivation**

In this subsection we derive the fitmodel used to fit all data sets in the main text. The model is a generalization of the semi-classical approach used in Refs. 15,42 as it accounts for a linear coupling to the transverse field component via a *g*-factor anisotropy from Sec. 6.6.3 and quadrupolar broadening of the individual Larmor frequencies from Sec. 6.6.4.

Following equation (7.15), the effective Zeeman splitting is given by

$$E_{\rm Z}(t) = g_{\parallel} \mu_{\rm B} \left( B_{\rm ext} + \frac{B_{\rm nuc}^{\perp}(t)^2}{2B_{\rm ext}} + \frac{g_{\perp}}{g_{\parallel}} B_{\rm nuc}^{\perp,y}(t) \right),$$
 (6.34)

including both quadratic and linear coupling to the perpendicular nuclear magnetic fields arising from the three species <sup>69</sup>Ga, <sup>71</sup>Ga and <sup>75</sup>As.

Introducing the giant spin model from equation (6.31), the relative phase pickup  $\Phi$  for a separation time  $\tau$ , given initial conditions  $B_k(0)$  and for one quantum dot for the

Hahn echo 
$$(c(t) = 1 \ (-1) \text{ for } t < \tau/2 \ (t > \tau/2)) \text{ is}$$

$$\Phi(\tau) = \frac{\mu_{\text{B}}}{\hbar} \int_{0}^{\tau} c(t) \left( \frac{g_{\parallel}}{2B_{\text{ext}}} \sum_{k,l} B_{k}(t) B_{l}^{*}(t) + g_{\perp} \sum_{k} \Re \left( B_{k}(t) \right) \right) dt$$

$$= \frac{g_{\parallel} \mu_{\text{B}}}{2\hbar B_{\text{ext}}} \sum_{k,l} \bar{B}_{k} \bar{B}_{l} z_{k} z_{l}^{*} \int_{0}^{\tau} c(t) e^{i\omega_{k} t} dt +$$

$$g_{\perp} \frac{\mu_{\text{B}}}{\hbar} \sum_{k} \bar{B}_{k} x_{k} \int_{0}^{\tau} c(t) \Re \left( e^{i\omega_{k} t} \right) dt \qquad (6.35)$$

$$= \sum_{l} T_{k,l} \frac{z_{k} z_{l}^{*}}{2} + \sum_{l} b_{k} x_{k}. \qquad (6.36)$$

In the second step we replaced the initial conditions by the random numbers  $z_k$  and the rms-values from equation (6.33). Furthermore  $\omega_{kl} = \omega_k - \omega_l$  and  $b_k = g_{\perp} \frac{\mu_B}{\hbar} \bar{B}_k$ . The definition of  $T_{kl}$  follows from the last equality and is consistent with Ref. 15.

To perform the ensemble average  $\langle e^{-i\Phi} \rangle$  we have to integrate over the distribution of initial nuclear fields. This integral is solved for one single electron dot by applying the T-matrix approach, similar to Ref. 15, extended by a linear coupling term  $b_k x_k$ .

$$\langle e^{-i\Phi} \rangle = \int \left( \prod_{j} dz_{j} dz_{j}^{*} p(z_{j}, z_{j}^{*}) \right) \times$$

$$\exp \left( -i \sum_{k,l} T_{kl} \frac{z_{k}^{*} z_{l}}{2} + \sum_{k} b_{k} x_{k} \right)$$

$$= \prod_{j} \int dz_{j} dz_{j}^{*} p(z_{j}, z_{j}^{*}) \cdot \exp \left( -i \lambda_{j} \frac{|z_{j}|^{2}}{2} + \tilde{b}_{j} x_{j} \right)$$

$$= \prod_{j} \frac{1}{1 + i \lambda_{j}} \exp \left( \frac{2\tilde{b}_{j}^{2}}{1 + i \lambda_{j}} \right), \tag{6.38}$$

where  $\lambda_j$  are the eigenvalues from  $T_{k,l} = UD_{k,l}U^{\dagger}$  for group j, with D being the diagonal matrix of eigenvalues  $\lambda_j$ . For  $\tilde{b} = Ub$  the same basis transformation is performed.

As the nuclei sampled by the electron spins in the left and right dot can be assumed to be statistically independent, the total decoherence function for dephasing of the two electron spins in a double dot can be written as the product of two identical dots  $|\langle e^{-i\Phi}\rangle|^2$ . While for an ideal Hahn echo measurement the echo response is given by equation (6.38), we also included a visibility factor  $\mathcal{N}$  and an overall offset o in

our fit model to account for imperfect  $\pi$ -pulses in the refocusing part of the Hahn echo sequence, loss of measurement contrast at higher magnetic fields and possible leakage.

The final fit function of the Hahn echo amplitude states

$$P_{S}(\tau) = \mathcal{N} \prod_{j} \left( \frac{1}{1 + i\lambda_{j}} \exp\left(\frac{2\tilde{b}_{j}^{2}}{1 + i\lambda_{j}}\right) \right)^{2} e^{\left(-\frac{\tau}{T_{SD}}\right)^{-4}} + o + Ae^{-\frac{\tau}{1.5\mu s}}.$$

$$(6.39)$$

Here we also introduced a multiplicative term to account for dephasing due to spectral diffusion, which according to theory [38,39] shows a  $e^{-(\tau/T_{SD})^{-4}}$  dependence (see Sec. 6.6.5). Furthermore, we add an additional exponential decay with a fixed time constant of 1.5  $\mu$ s (see Sec. 6.6.5).

Using this model we perform a global fit of all measurement data (Fig. 1-3 of the main text) with the following free parameters: the number of unit cells N, the spectral diffusion time constant  $\tau_{\rm SD}$  (see Sec. 6.6.5), the species independent parameter  $\delta\omega_{\rm Q,\alpha}/(Q_{\alpha}R_{14,\alpha})$  related to the distribution of EFGs (see Sec. 6.6.4 and 6.6.5), the linear coupling to transverse hyperfine fields  $g_{\perp}$  and the scaling and offset parameter (allowed to vary for each data set). The value for N was kept unchanged for all data sets and the best fit yields a value of  $2.4 \times 10^6$  nuclear spins, with two electrons per unit cell for GaAs.

#### Variance of electric field

Modeling the electron as a two-dimensional  $25 \times 25$  nm charge density we estimate a maximal change of the EFG of  $\delta(\partial E/\partial z) = R_{14,\alpha}e/(\epsilon_0\epsilon_r 25 \text{ nm}^2)$  across the wave function according to the Poisson equation and equation (6.19). Expressing this EFG as equivalent Larmor line width using equation (6.15) and using literature values, we obtain broadenings reaching from 0.34 to 1.86 mT for the different species, in good agreement with the fitted values. Even though we can reproduce the line width quite well, other effects, such as strain, electrical field from charged impurities and the lateral confining gates may also contribute to quadrupolar interaction.

#### Spectral diffusion time constant

The spectral diffusion term introduced in equation (6.39) accounts for additional dephasing from fluctuations of  $B_{\text{nuc}}^{\parallel}$  due to spin diffusion. The multiplicative form can be justified with the assumption that  $B_{\text{nuc}}^{\parallel}$  and  $B_{\text{nuc}}^{i,\perp}$  are uncorrelated, with i being either y' or z'. The value of  $\tau_{\text{SD}}$  is difficult to extract independently without going to very large magnetic fields. We obtain good fits by fixing it at  $\tau_{\text{SD}} = 30\,\mu\text{s}$  for all data sets, consistent with earlier measurements<sup>[15]</sup> and theory. As the resulting decay sets in at

larger times than that seen in the experimental traces, this value corresponds to a very small effect on the fitted curves and indicates that spectral diffusion has a very small contribution compared with dephasing from transverse fields. However, the quality of the fits is not very sensitive to  $\tau_{SD}$  so that the above value is not very reliable.

#### **Deviation of first data points**

Similar to Ref.15 we find that the first data points deviate from our fit model and our best fits show an exponential time dependency with a time constant of  $1.5\,\mu$ s with varying amplitude. This additional decay is most visible for high values of the external magnetic field and also more pronounced with a high Overhauser field  $\Delta B_z$ , i.e. the echo time trace at 750 mT in Fig. 1c of the main text. While the origin of this behaviour is currently not understood, it was phenomenologically added to the fit model to ensure that deviations at short times do not affect the quality of the overall fit.

#### Discussion of lower coherence times

The size of the quantum dot determines the overlap of the electron wavefunction with the nuclear spins in the vicinity and hence has a strong influence on coherence times. Fitting all our data, we find that the number of overlapping nuclei is a factor of two smaller compared with Ref. 15, leading to shorter coherence times, that are more comparable with Ref. 105. Note that a smaller electronic wavefunction directly translates into an increased quadrupolar broadening  $\delta B_{\alpha}$  via equation 6.15 and 6.19, further contributing to lower coherence time. The smaller wavefunction may be caused by the thinner spacer layer of the heterostructure and possibly more disorder in the heterostructure used in this work, compared with the one used in Ref. 15.

#### Loss of visibility

The  $\pi$ -pulse used to invert the qubit state is realized by detuning the electrons for a typical time of 5-7 ns to a finite exchange splitting J, which was adjusted to show maximal contrast before each measurement run. Ideally, the  $\pi$ -pulse should rotate about a Bloch sphere axis perpendicular to that of  $\Delta B_z$ , which is only achieved for  $J \gg \Delta B_z$ . As we cannot set the gradient  $\Delta B_z$  to zero, the two rotation axes are in practice not perfectly orthogonal. We typically used an exchange value of  $J \approx 160\,\mathrm{MHz}$  and limited  $\Delta B_z < 60\,\mathrm{MHz}$ , limiting the typical contrast of the Hahn echo to a value of around 0.3. The gradient  $\Delta B_z$  is induced unintentionally and for unknown reasons by the pulses applied to the qubit. For measurements performed at magnetic fields above 500 mT the induced polarization increased, for an unknown reason so far, further reducing the visibility due to faster relaxation during the readout of the qubit state [86].

# 7. Dephasing of electron spins in InAs nanowires

This chapter is in preparation for publication.

#### 7.1. Abstract

Spin qubits in InAs nanowires allow for very fast single qubit control due to the strong spin-orbit coupling. Albeit, experimental realization of such a qubit system shows short coherence times of approximately 50 ns. The underlying dynamics causing decoherence remain unexplained, although recent measurements of electron dephasing in GaAs two-electron spin qubits may provide new insights. Here, a *g*-factor anisotropy occurring at certain *B*-field directions causes the electron spin and the nuclear spins of the host material GaAs to precess around different quantization axes, leading to an echo envelope modulation. Motivated by experiments that show a strong *g*-factor anisotropy in InAs nanowires, we apply the theory of echo modulation due to an anisotropic *g*-factor to this system and find excellent agreement with Hahn echo measurements. We further show that this dephasing channel can be suppressed by rotating the in-plane external magnetic field parallel to the nanowire axis.

#### 7.2. Introduction

The search for an effective mechanism for driving single spin rotations has motivated the study of strong spin-orbit (SO) materials, such as InAs nanowires. The SO interaction which couples the spin and orbital degrees of freedom of the confined electrons promises efficient all-electrical qubit control and has proven promising for coherent spin rotations in lateral gate defined quantum dots [118]. As the *g*-factor strongly depends on the confinement potential it can be used to selectively address individual electron spins. Strong SO interaction, asymmetric confinement and the wurtzite crystal symmetry give rise to a large *g*-factor anisotropy in these nanowires devices. Controlling the electronic *g*-factor in quantum dots allows for selective control of spins via a modulation of the *g*-tensor [119].

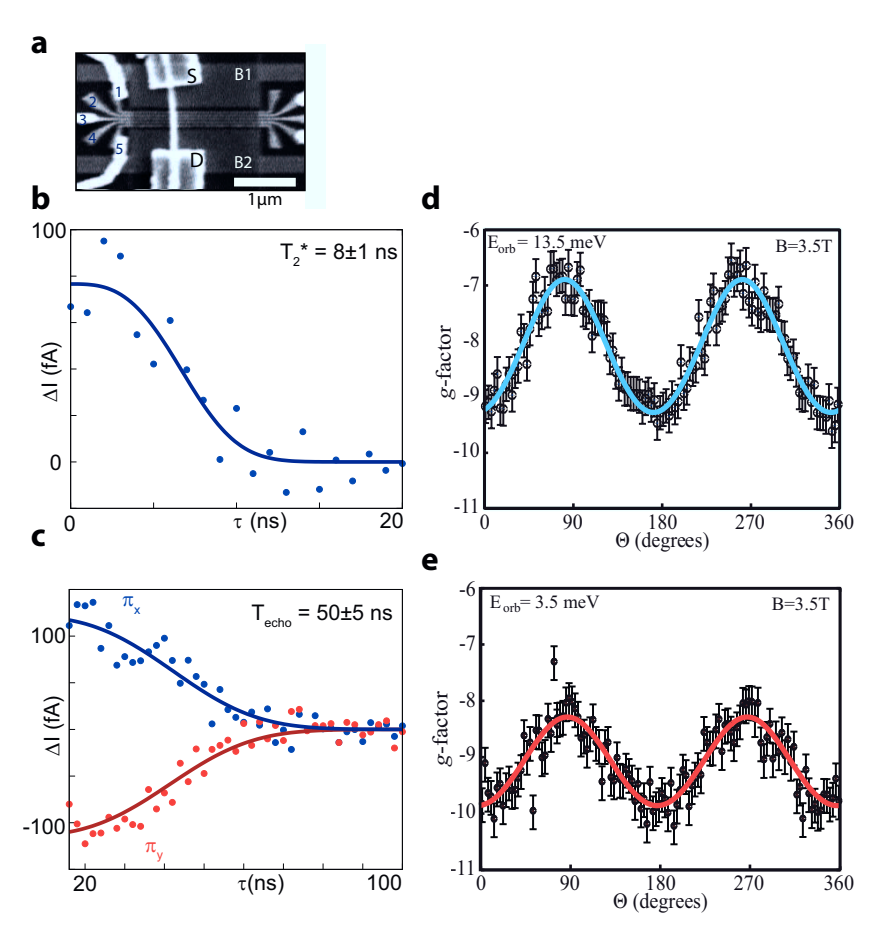


**Figure 7.1.:** Nanowire device and measurements of coherence and *g*-factor. (a) The nanowire is connected to source (S) and drain (D) contacts and is situated on top of five narrow gates (1-5) and two broad gates (B1, B2). (b) Free induction decay of the Ramsey fringe. The dephasing time is on the same order as in GaAs quantum dots. (c) The Hahn echo decay curve reveals relatively short coherence times of 50 ns. This particular measurement is performed at  $B_{\text{ext}} = 102 \, \text{mT}$  at an in-plane angle of 45° with respect to the nanowire. (d,e) The electric *g*-factor of the confined electron in a similar device shows a strong angular dependence. The strength of the *g*-factor anisotropy further depends on the dot size ((d) small dot and (e) large dot). Figures adapted from Refs. 16,117

Ref. 16 demonstrated universal coherent control by electric dipole spin resonance (EDSR) of a spin-orbit quantum bit implemented in an double quantum dot in InAs nanowire. They showed that the two confined electrons had different *g*-factors and that they could be addressed selectively. Surprisingly, the Hahn echo experiment only showed a coherence time of approximately 50 ns that could not be extended much further using more advanced dynamical decoupling techniques. This short coherence time

was unsuspected as it did not fit well with the dephasing mechanisms known at the time for gate defined quantum dot and the origin of this effect was unknown.

From studies of electron coherence in gate defined quantum dot in GaAs, it is known that the coupling to the transverse hyperfine field, built up from the three nuclear isotopes of the host material, plays an important role. In Ref78 which investigated electron coherence as a function of the direction of the external magnetic field, it is shown that coherence is limited by quadrupolar broadening of the nuclear Larmor frequencies and an anisotropic *g*-factor. Broadening of the nuclear Larmor precession reduces electron spin coherence due to faster decorrelation of transverse nuclear fields but can be eliminated for appropriate *B*-field directions. Along these directions an additional modulation of spin coherence that can be attributed to an anisotropic electronic *g*-tensor is observed. If the external magnetic field is not aligned to the a main axis of the *g*-tensor, this *g*-factor anisotropy causes different quantization axes for the electron and the nuclei spins and leads to an additional linear coupling to the transverse nuclear magnetic field. Hence, the Larmor precessions of the three types of nuclei becomes visible as an echo envelope modulation in the Hahn echo decay.

The remainder of this document is structured as follows. In Sec. 7.3 we introduce the qubit system from Ref. 16, and review the experimental setup and the measurements regarding the anisotropic *g*-factor and qubit coherence. The theory of a Hahn echo envelope modulation from Ref. 78 is summarized and adapted for the nanowire system in Sec. 7.4. We fit the data provided in Sec. 7.3 and compare it to measurements of the *g*-factor anisotropy [117]. We continue to investigate different mitigations strategies in Sec. 7.5. Lastly, we conclude our findings in Sec. 7.6

#### 7.3. Qubit system

Fig. 7.1a shows an image of the InAs nanowire device of wurtzite structure used in Refs. 114,16,117. The device is connected to the source and drain contacts, which are used to measure the conductance through the nanowire. By applying a negative voltage to the five closely spaced narrow gates underneath the nanowire, a double well potential for two tunnel-coupled electrons is realized.

Operated in the (1,1)-charge configuration (one electron in the left quantum dot, one electron in the right quantum dot) this device incorporates two so-called spin-orbit qubits. In the presence of strong SO coupling from the host material InAs, neither spin nor orbit are good quantum numbers. The qubit groundstate and first excited state are instead SO doublets,  $\uparrow$  and  $\downarrow$ . Nevertheless, the energy splitting between the two states is still given by the Zeeman energy  $E_Z = g\mu_B B$ , with the Landé g-factor g and Bohr magnetron  $\mu_B$  [16].

Qubit initialization and readout can be achieved by Pauli spin blockade<sup>[3,120]</sup>. A transition is spin-blocked when electron transfer is energetically allowed, but forbid-

den by spin conservation [16]. Current through the double quantum dot transfers one electron from the left to right dot as follow:  $(0,1) \rightarrow (1,1) \rightarrow (0,2) \rightarrow (0,1)$ . The transition  $(1,1) \rightarrow (0,2)$  is spin blocked (energetically allowed, but forbidden by conservation of spin) if the (1,1) state is a triplet and only the singlet (0,2) state is accessible. When in spin blockade, current through the quantum dots is suppressed. The qubit is manipulated by applying a microwave frequency electric field on one of the gates to drive EDSR. The electric field causes an oscillating displacement of the electron and it experiences an additional field related to the SO effect along certain *B*-field directions which can induce resonant transitions between the qubit states. Such transitions are expected for driving frequencies close to the Larmor frequency of the electron  $\omega_L = g\mu_B B/\hbar$ . This so-called Rabi-driving is a standard manipulation technique for single spin qubits and allows for universal control of the qubit.

Fig. 7.1b shows a free induction decay measurement of the Ramsey fringes. The inhomogenous dephasing time is determined to  $T_2^* = 8 \pm 1$  ns, similar to the values found in lateral quantum dots in GaAs<sup>[9]</sup>. This short dephasing time reflects the interaction of the confined electron interacting with approximately  $1.4 \times 10^6$  overlapping nuclear spins (estimated from an EDSR peak width of  $0.66 \, \mathrm{mT}^{[16]}$ ).

Dephasing from slow nuclear spin fluctuations can be recovered by the Hahn echo technique<sup>[41]</sup> (applying a  $\pi$ -pulse halfway through the evolution time). Such a measurement at an external magnetic field of  $B_{\rm ext}=102\,\rm mT$  at a 45° angle with respect to the nanowire [0001] axis is reproduced from Ref. 16 in Fig. 7.1c. Surprisingly, the echo only increases the coherence time to  $T_{\rm echo}=50\,\rm ns$ . Compared to echo times of a few microseconds [78,13,49,105] determined in GaAs devices at comparable fields, this  $T_{\rm echo}$  is two orders of magnitudes shorter. Even more advanced decoupling techniques such as CPMG could not extend the qubit coherence beyond 200 ns [16] and the origin of this fast dephasing was not understood.

In a further study, the dependence of the electronic g-factor on the magnetic field direction is investigated (see Ref. 117 for details). For wurtzite materials which lack inversion symmetry, an anisotropy is expected. These materials are best described by two g-factors along perpendicular crystallographic axes. In the main axes coordinate system with  $x \parallel [0001]$ , y in-plane (plane of the substrate) perpendicular to [0001] and z out-of-plane perpendicular to [0001],  $g_{xx}$  denotes the g-factor along the nanowire axis and  $g_{yy}$  the one perpendicular and in-plane to this direction, with  $g_{xx} < g_{yy}$ . Fig. 7.1d shows the g-factor extracted from measurements of the Zeeman splitting for a full 360 ° rotation of the in-plane magnetic field  $B_{\rm ext}$ . The g-factor shows a strong anisotropy of  $(g_{xx} - g_{yy})/(g_{xx} + g_{yy}) \approx 0.155$  with regard to the field orientation with extrema at around 171° and 81°, respectively. The offset of approximately 10° off the nanowire axis most likely originates from the confinement of the electron as it was shown in Ref. 117 to depend on the gate-tunable confinement potential of the double quantum dots. Nevertheless, the anisotropy of the g-factor is not dominated by theses changes in

confinement potential for the electrons. Similar *g*-factor anisotropies are found in Ref. 121.

## 7.4. Echo envelope modulation due to a *g*-factor anisotropy

Motivated by the similar qualitative situation of a *g*-factor anisotropy, an in-plane magnetic field at 45° and a finding of short coherence times compared to the GaAs system<sup>[78]</sup>, we apply the theory of an echo envelope modulation which was found to successfully describes the experiments to the nanowire system. In this section we review the theory from Ref. 78 and adapt it to the nanowire system. First, we outline hoe a *g*-factor anisotropy causes a linear coupling term to the transverse hyperfine field in the electronic Zeeman splitting. We will then see that this term causes an envelope modulation of the Hahn echo decay which leads to the short coherence times. We continue to fit and reproduce the experimental data<sup>[16]</sup> and will discuss the results.

Following the nomenclature from Sec. 7.2 the electronic *g*-tensor for the InAs nanowire in the main axis coordinate system is of diagonal form:

$$\underline{\underline{g}} = \begin{pmatrix} g_{xx} & 0 & 0 \\ 0 & g_{yy} & 0 \\ 0 & 0 & g_{zz} \end{pmatrix}, \tag{7.1}$$

with  $g_{yy} = g_{zz}$ . When rotating the external *B*-field by a rotation angle  $\theta$  about the *z*-axis, we introduce a new coordinate system, where  $x' \parallel B_{\text{ext}}$ ,  $y' \perp x'$  and z' = z. Anisotropic entries  $g_{xx} \neq g_{yy}$  lead to off-diagonal elements in the *g*-tensor in the new coordinate system (see Appendix for more detail)

$$\underline{\underline{\mathbf{g}}}_{\underline{\underline{\theta}}} = \begin{pmatrix} g_{\parallel} & g_{\perp} & 0 \\ g_{\perp} & g_{y'y'} & 0 \\ 0 & 0 & g_{zz} \end{pmatrix}. \tag{7.2}$$

Here, we have defined the components parallel and perpendicular to  $B_{\text{ext}}$  for small anisotropies as

$$g_{\parallel} \approx g_{xx},$$
 (7.3)

$$g_{\perp} = \frac{1}{2}\sin(2\theta)\left(g_{xx} - g_{yy}\right),\tag{7.4}$$

and find that the perpendicular components show a  $\sin(2\theta)$  dependence.

When calculating the effective Zeeman splitting of the electron along the new quantization axis  $\mathbf{g}_{\theta}\mathbf{B}_{\text{ext}}$  we find that the off-diagonal element  $g_{\perp}$  leads to linear coupling

to the transverse component of the Overhauser field  $\mathbf{B}_{\text{nuc}}$  which is built up from the three spin-carrying isotopes <sup>113</sup>In, <sup>115</sup>In and <sup>75</sup>As. Intuitively speaking, the electron precesses around a slightly tilted quantization axis compared to the nuclei caused by the anisotropic *g*-factor and experiences the transverse nuclear field, which oscillates with the three Larmor frequencies of the nuclei. Including this *g*-factor anisotropy and the second-order coupling <sup>[15,42]</sup> to the perpendicular hyperfine field component, the Hamiltonian of the system states <sup>[78]</sup>

$$\hat{H} = \mu_{\rm B} \mathbf{g}_{\theta} \mathbf{B}_{\rm ext} \cdot \hat{\mathbf{S}} + \mu_{\rm B} g_{\parallel} \mathbf{B}_{\rm nuc} \cdot \hat{\mathbf{S}}$$
(7.5)

$$\approx \mu_{\rm B} g_{\parallel} \left( B_{\rm ext} + B_{\rm nuc}^{\parallel} - \frac{g_{\perp}}{g_{\parallel}} B_{\rm nuc}^{y',\perp}(t) + \frac{B_{\rm nuc}^{\perp}(t)^2}{2B_{\rm ext}} \right) \tilde{S}_x. \tag{7.6}$$

Here,  $\hat{\mathbf{S}}$  denotes the spin operator we have defined  $(B_{\text{nuc}}^{\perp})^2 = (B_{\text{nuc}}^{y',\perp})^2 + (B_{\text{nuc}}^{z',\perp})^2$ . The last term in Eq. 7.6 results from including the contribution of the Overhauser field perpendicular to the electronic quantization axis to second order. The third times results from projecting the component orthogonal to the applied field onto the electronic quantization axis, and arises due to the g-tensor anisotropy. The detailed deduction leading to the second step can be found in App. 7.7.1. The impact on the Hahn echo experiment can be summarized as follows. During the free evolution part of the Hahn echo, the qubit acquires a phase arising from the transverse components. Due to the Larmor precession of these fields, the acquired phase is not eliminated by the echo pulse and causes dephasing. Whenever the evolution time  $\tau/2$  is a multiple of all three Larmor frequencies, the net phase vanishes and the echo amplitude recovers. Partial recovery occurs if the evolution time only matches a multiple of the Larmor period of two or one species. Any broadening of the nuclear Larmor frequencies which is expected for dipolar interaction between nuclei and quadrupolar effects leads to an overall envelope decay. This effect can be modeled by assuming a phenomenological broadening  $\delta B_{\rm nuc}$ of the Larmor frequencies that causes fluctuations and inhomogeneities of the transverse hyperfine field of each species.

To obtain a quantitative description of broadening and anisotropy effects, we adapt the semiclassical model of Ref. 15,78, based on computing the total electronic phase accumulated due to the precessing nuclear spins and averaging over the initial nuclear states (a detailed derivation is given in App. 7.7.2). The transverse hyperfine field is modeled as the vector sum of Gaussian distributed contributions arising from the three nuclear species and the spread of quadrupolar shifts with width. For simplicity, we assume a Gaussian distribution of resulting local nuclear field with width  $\delta B_{\text{nuc}}$  centered on the Larmor frequency, comprising dipolar and quadrupolar broadening.

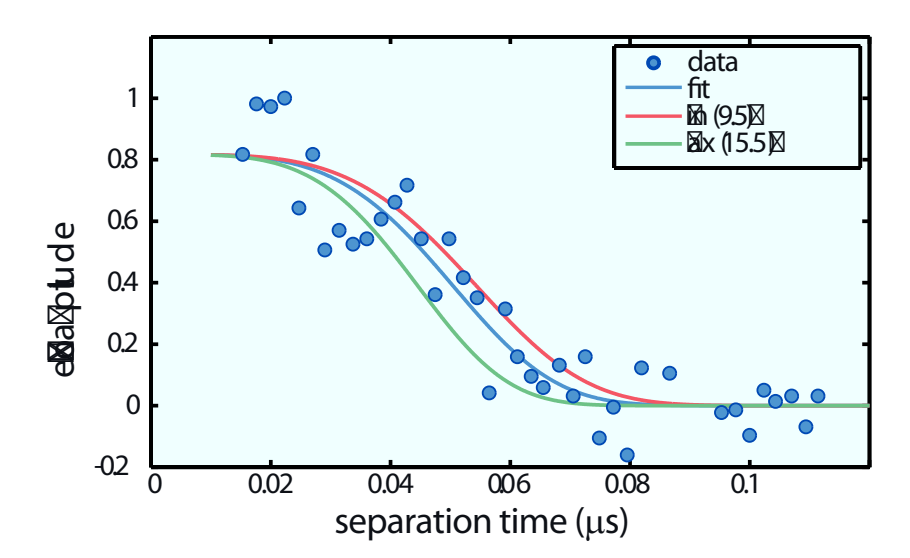


**Figure 7.2.:** Hahn echo decay. Fit and theory prediction for the Hahn echo decay based on the measured g-factor anisotropy to the data from Ref.16, show excellent agreement. Here, the number of unit cells is fixed at  $3.5 \times 10^5$  and the quadrupolar broadening is set to match  $\delta B_{\rm nuc} = 0.1\,\rm mT$ . The fit (blue curve) corresponds to a g-factor anisotropy of 0.11 and lies between the largest and lowest measured values (red and green curve). The theoretical predictions are corrected for an offset in the g-factor anisotropy.

#### 7.4.1. Fit to experimental data

We use the above mentioned model to fit the Hahn echo data provided in Ref. 16. The result is shown in Fig. 7.2. The experimental data was extracted using an online digitizer and normalized. The blue curve corresponds to a fit to the data and results in a g-factor anisotropy of 11 %. The only free parameters for this fit are a visibility factor to account for pulse errors and the g-factor anisotropy. The number of overlapping spins was calculated from the approximate dot size to be  $1.4 \times 10^6$  and the broadening of nuclear Larmor frequencies is set to  $\delta B_{\rm nuc} = 0.1 \,\mathrm{mT}$ . We justify using the lower dipole broadened limit measured in comparable GaAs structures as this value will not have a huge impact on the coherence at short evolution times which is dominated by the anisotropic g-factor (see Sec. 7.5 for more details). To check the extracted value for the g-factor anisotropy we further provide theoretical curves for the minimum and maximum measured anisotropies from Ref. 117 (red and green curve) which have been corrected for the offset angle of the g-factor anisotropy, discussed in the last section. We find excellent agreement between theory and experiment and the fitted value lies between the two extrema. We can therefore reproduce and explain the relatively short coherence time in InAs nanowires by an electronic g-factor anisotropy.

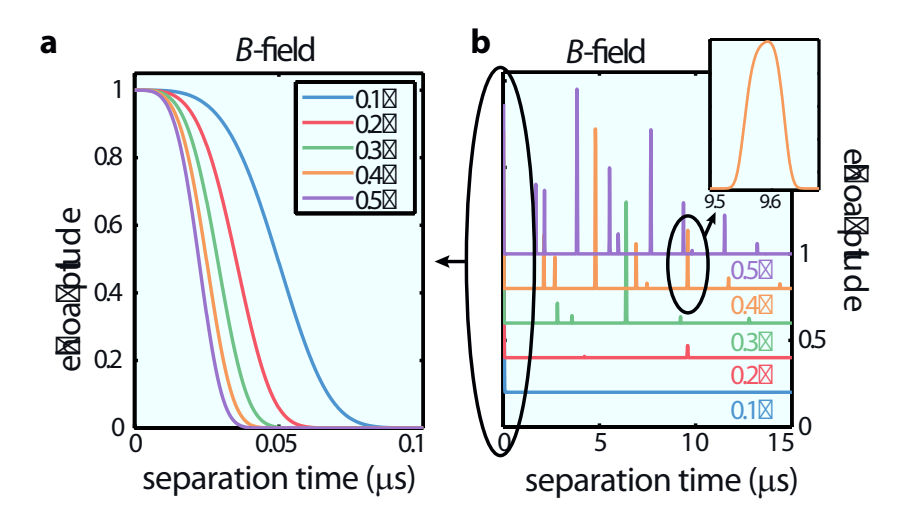


**Figure 7.3.:** Hahn Echo decay for different *B*-fields and nuclear spins. (a) The initial collapse of the Hahn echo amplitude including a *g*-factor anisotropy of 0.11 shifts towards shorter timescales as the Larmor frequency of the nuclei increases with increasing *B*-field. (b) Same plot as (a) over a larger time scale. Later revivals become visible once overall coherence increases with increasing *B*-field demonstrating that the coupling to the transverse Overhauser field components does not lead to an unrecoverable loss of coherence. The insert shows a more detailed picture of one of the revivals at 0.4 T and reveals a structure similar to (a).

#### 7.5. Mitigation strategies

Fig. 7.3a,b investigates the scaling behavior of the Hahn echo amplitude with magnetic field strength at an in-plane angle of 45°. For increasing Larmor frequencies the initial collapse of the echo amplitude shifts towards shorter timescale (Fig. 7.3a). The linear coupling term in Eq. 7.16 only causes an envelope modulation and does not lead to an unrecoverable loss of coherence. Hence, when the overall coherence is increased with increasing  $B_{\rm ext}$  (the quadratic coupling terms scales with  $1/B_{\rm ext}$ ), revivals of the echo amplitude occurring at later timescales become visible. These revivals can be seen as sharp peaks in the echo amplitude in Fig. 7.3b. As Ref. 16 uses transport measurement through the double quantum dot device which require a high repetition rate, these revivals occurring at much later times were not measurable.

In order to suppress decoherence due to an anisotropic g-factor the external magnetic field simply has to be rotated as the perpendicular component of the g-factor shows a  $\sin(2\theta)$  dependence (see Eq. 7.10). Fig. 7.4a shows the Hahn echo decay for various linear coupling strengths  $g_{\perp}/g_{\parallel}$ , corresponding to different B-field directions. A g-factor anisotropy of 0 reflects  $B_{\rm ext}$  parallel or perpendicular to the [0001] axis. Even a small values of the g-factor anisotropy at a rotation angle  $\theta = 0.3^{\circ}$  (red line in Fig. 7.4a) introduces a very strong envelope modulation and quenches the visibility of the Hahn echo

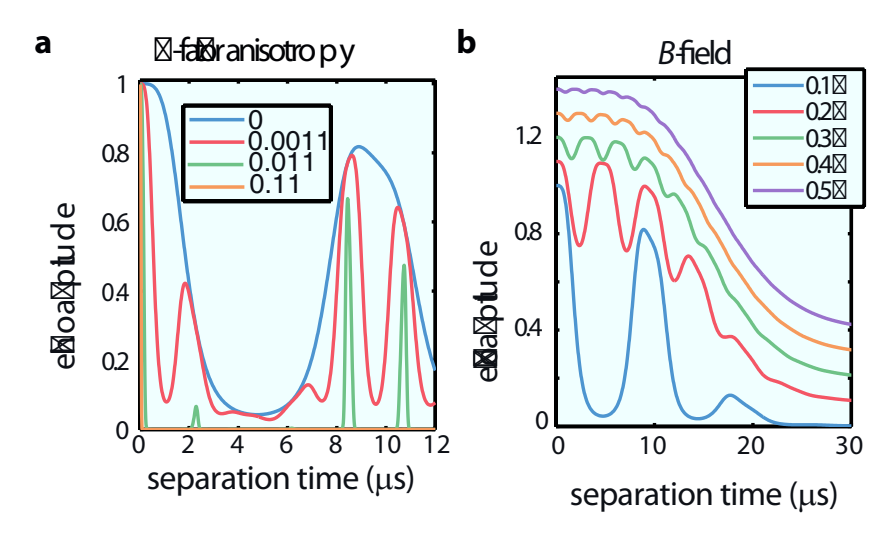


Figure 7.4.: Hahn echo decay for different magnetic field directions. a Hahn echo amplitude plotted for different directions of the externel B-field, representing different coupling strengths  $g_{\perp}/g_{\parallel}$  to the transverse field. Even a very small misalignment of  $\theta=0.3^{\circ}$  leads to a strong modulation of the echo envelope at  $100 \, \mathrm{mT}$ . b Aligning  $B_{\mathrm{ext}}$  parallel to the nanowire suppresses the linear coupling term. The remaining quadratic coupling term scales inversely with  $B_{\mathrm{ext}}$  and shows less influence at higher field. The remaining echo envelope decay is determined by the broadening of  $\delta B_{\mathrm{nuc}}=0.1 \, \mathrm{mT}$ .

amplitude. Once the linear coupling is sufficiently suppressed, collapses and revivals of the echo amplitude at the relative Larmor frequencies of the nuclei originating from the quadratic coupling term in Eq. 7.16 become visible, similar to Refs. 15,78. Note that a potential field-dependence of quadrupolar broadening of the nuclear Larmor frequencies is not taken into account and all curves shown so far correspond to a nuclear broadening of  $\delta B_{\rm nuc} = 0.1 \, {\rm mT}$ . Neglecting this potential additional dephasing channel, coherence times exceeding 1  $\mu$ s for an magnetic field of  $B_{\rm ext} = 102 \, {\rm mT}$  are expected.

Even longer Hahn echo coherence times should be achievable by increasing the magnetic field. Theoretical predictions for the Hahn echo decay are shown in Fig. 7.4b. For an increasing field, the quadratic coupling term in Eq. 7.16 becomes less dominant and adds less to dephasing. Dephasing due to spin diffusion is not taken into account and all dephasing still results from broadening of the Larmor frequencies..

In a last step, we investigate the dependence of the Hahn echo amplitude as a function of quadrupolar broadening for two different external magnetic fields. Electric fields or lattice strain distort the valence orbitals and crystal lattice and result in electric field gradients at nuclear sites [78,106]. These gradients couple to the quadrupolar momentum of the nuclei with spin I > 3/2 and modify the Larmor frequencies. A inhomogeneity of the field gradients introduces an excess broadening of the precession frequencies and

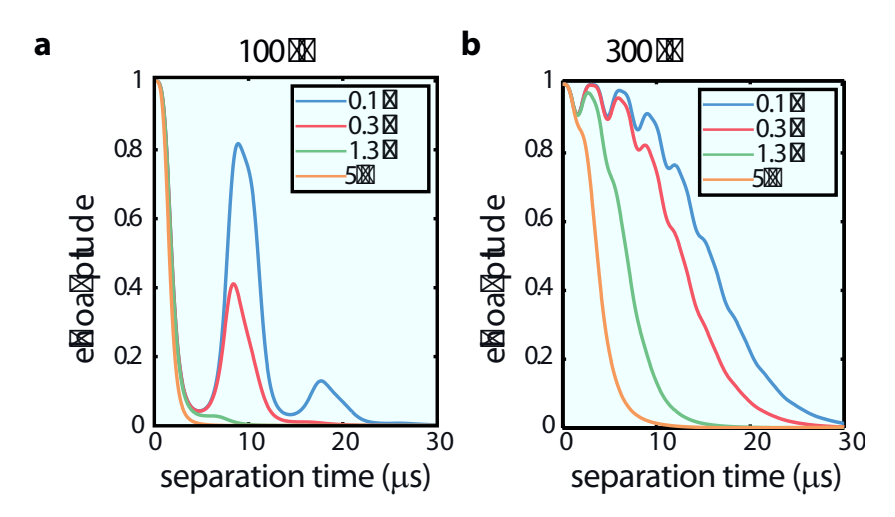


Figure 7.5.: Hahn Echo decay for different quadrupolar broadenings. (a) This graph shows the Hahn echo decay for different broadening of the nuclear Larmor frequencies with values motivates by measurement performed in GaAs structures. The fast, initial decay from Fig. 7.2 can not be reconstructed by this effect. (b) Same as (a) for  $B_{\rm ext} = 300\,\rm mT$ .

leads to additional dephasing that strongly depends on the crystal symmetry and the direction of the external magnetic field. Contrary to Refs. 78,122 who treat quadrupolar broadening in , we only assume an excess broadening of  $\delta B_{\text{nuc}}$  similar to Ref. 15. Due to the comparable wave function size we expect quadrupolar effect of the same order as measured in GaAs samples which could successfully be described by a phenomenological broadening  $\delta B_{\text{nuc}}$ .

Fig. 7.5 shows the Hahn echo decay at 100 and 300 mT for different nuclear broadening. We chose values that represent purely dipolar broadened frequency distributions ( $\delta B_{\rm nuc} = 0.1 \,\mathrm{mT}$ ) and measured values  $\delta B_{\rm nuc} = 0.3 \,\mathrm{mT}$  and  $\delta B_{\rm nuc} = 1.3 \,\mathrm{mT}$  from Refs. 15,78, respectively. To show that the very fast decay within 50 ns shown in Fig. 7.2 can not be caused by quadrupolar interaction alone, we also included a broadening of  $\delta B_{\rm nuc} = 0.5 \,\mathrm{mT}$ , exceeding all measured values in GaAs structures.

#### 7.6. Summary

In this work, we have applied the theory of echo envelope modulation due to an electronic *g*-factor anisotropy, originally developed and validated for gate defined GaAs quantum dots, to Hahn echo measurement in InAs nanowires from Ref.16. We find a *g*-factor anisotropy of 0.11, in excellent agreement with measured values for the *g*-factor anisotropy [117]. We therefore provide an explanation for the relatively short coherence times observed so far in this system. In order to suppress this dephasing mechanism

and prolong coherence, the external magnetic field simply needs to be aligned with one of the main crystallographic axes (perhaps accounting for offset). To reduce anisotropy of the electron's *g*-factor, InAs nanowires with zinc-blende structure can be used<sup>[123]</sup>. However, we find that the alignment needs to be accurate to within a fraction of a degree. Compared to the wurtzite crystal structure used in Ref. 16, zinc-blende shows inversion-symmetry and reduces any anisotropy resulting from the crystal itself. Of course, anisotropy due to electron confinement and SO interaction is still present.

Ultimately, the maximum achievable electron coherence will likely be limited by broadening effects, similar to the findings in GaAs samples. We expect to find that quadrupolar broadening and *g*-factor anisotropy cannot both be minimized at the same time as the optimal axes are different.(checkme)

# 7.7. Appendix

In this section we derive how the *g*-factor anisotropy leads to a linear coupling to the transverse hyperfine field and the impact on qubit coherence. We continue by reviewing the deduction of the semi-classical fit model adapted from Refs. 78,15,42.

# 7.7.1. g-factor anisotropy

Following the nomenclature from Sec. 7.2 the electronic *g*-tensor for the InAs nanowire in the main axis coordinate system is of diagonal form:

$$\underline{\mathbf{g}} = \begin{pmatrix} g_{xx} & 0 & 0 \\ 0 & g_{yy} & 0 \\ 0 & 0 & g_{zz} \end{pmatrix}, \tag{7.7}$$

where typically all *g*-tensor components are different<sup>[121]</sup>. When rotating the external *B*-field by a rotation angle  $\theta$  about the out-of-plane axis, we introduce a new coordinate system, where  $x' \parallel B_{\text{ext}}$ ,  $y' \perp x'$  and z' = z. For anisotropic entries  $g_{xx} \neq g_{yy}$ , the *g*-tensor in this coordinate system can be expressed in terms of the rotation matrix  $\mathbf{D}_{\theta}$ 

$$\underline{g}_{\underline{\theta}} = \mathbf{D}_{\theta} \underline{g} \mathbf{D}_{\theta}^{\mathsf{T}} =$$

$$\begin{pmatrix}
g_{xx} \cos(\theta)^{2} + g_{yy} \sin(\theta)^{2} & \frac{1}{2} \sin(2\theta) (g_{xx} - g_{yy}) & 0 \\
\frac{1}{2} \sin(2\theta) (g_{xx} - g_{yy}) & g_{xx} \sin(\theta)^{2} + g_{yy} \cos(\theta)^{2} & 0 \\
0 & 0 & g_{zz}
\end{pmatrix}$$

$$= \begin{pmatrix}
g_{\parallel} & g_{\perp} & 0 \\
g_{\perp} & g_{y'y'} & 0 \\
0 & 0 & g_{zz}
\end{pmatrix}.$$
(7.8)

Here, we have defined the components parallel and perpendicular to  $B_{\text{ext}}$  as

$$g_{\parallel} = g_{x'x'} = g_{xx}\cos(\theta)^2 + g_{yy}\sin(\theta)^2 \approx g_{xx},$$
 (7.9)

$$g_{\perp} = g_{x'y'} = g_{y'x'} = \frac{1}{2}\sin(2\theta)(g_{xx} - g_{yy}),$$
 (7.10)

and find that the perpendicular components show a  $\sin(2\theta)$  dependence.

Including this g-factor anisotropy, the Hamiltonian of the system now states

$$\mathbf{\hat{H}} = \mu_{\rm B} \mathbf{g}_{\theta} \mathbf{B}_{\rm ext} \cdot \mathbf{\hat{S}} + \mu_{\rm B} g_{\parallel} \mathbf{B}_{\rm nuc} \cdot \mathbf{\hat{S}}$$
 (7.11)

$$= \mu_{\mathrm{B}} \left( \underline{\mathbf{g}}_{\underline{\boldsymbol{\theta}}} \mathbf{B}_{\mathrm{ext}} \mathbf{O}^{\mathsf{T}} \right) \cdot \mathbf{O} \hat{\mathbf{S}} + \mu_{\mathrm{B}} g_{\parallel} \mathbf{B}_{\mathrm{nuc}} \cdot \mathbf{O}^{\mathsf{T}} \mathbf{O} \hat{\mathbf{S}}. \tag{7.12}$$

Here, the Overhauser field  $\mathbf{B}_{nuc}$  is the vector sum of all contributions from the three nuclear species  $^{113}$ In,  $^{115}$ In and  $^{75}$ As, whose properties are summarized in Tab. 7.1.  $\mathbf{\hat{S}}$  denotes the spin operator.

Note that the choice of  $g_{\parallel}$  to convert the hyperfine coupling to an effective magnetic field is a matter of convention. In the second step we have defined

$$\mathbf{O} = \begin{pmatrix} \cos(\phi) & -\sin(\phi) & 0\\ \sin(\phi) & \cos(\phi) & 0\\ 0 & 0 & 1 \end{pmatrix},\tag{7.13}$$

such that the vector  $\underline{\mathbf{g}}_{\underline{\boldsymbol{\theta}}}\mathbf{B}_{\mathrm{ext}}\mathbf{O}^{\mathsf{T}}$  only has one nonzero component along the effective quantization direction of the electron.  $\boldsymbol{\phi}$  is the angle between  $\mathbf{B}_{\mathrm{ext}}$  and the electron quantization axis  $\underline{\mathbf{g}}_{\underline{\boldsymbol{\theta}}}\mathbf{B}_{\mathrm{ext}}$ . With  $\mathbf{O}\hat{\mathbf{S}} = \tilde{\mathbf{S}} = (\tilde{S}_x, \tilde{S}_y, \tilde{S}_z)$  and  $\mathbf{B}_{\mathrm{nuc}} = (B_{\mathrm{nuc}}^{\parallel}, B_{\mathrm{nuc}}^{y', \perp}, B_{\mathrm{nuc}}^{z', \perp})$  we write, ignoring non-secular terms

$$\hat{H} = \mu_{\rm B} \sqrt{g_{\parallel}^2 + g_{\perp}^2} B_{\rm ext} \tilde{S}_x$$

$$+ \mu_{\rm B} g_{\parallel} \left( B_{\rm nuc}^{\parallel} \cos(\phi) + B_{\rm nuc}^{y',\perp} \sin(\phi) \right) \tilde{S}_x. \tag{7.14}$$

We further include the second-order coupling [15,42] to the hyperfine field component

perpendicular to the quantization axis  $g_{\theta}B_{\text{ext}}$  and obtain for the total Hamiltonian

$$\hat{H} = \mu_{\rm B} \sqrt{g_{\parallel}^2 + g_{\perp}^2} B_{\rm ext} \tilde{S}_x$$

$$+ \mu_{\rm B} g_{\parallel} \left( B_{\rm nuc}^{\parallel} \cos(\phi) - B_{\rm nuc}^{y',\perp} \sin(\phi) \right) \tilde{S}_x$$

$$+ \mu_{\rm B} g_{\parallel} \frac{\left( B_{\rm nuc}^{y',\perp} \cos(\phi) + B_{\rm nuc}^{z',\perp} - B_{\rm nuc}^{\parallel} \sin(\phi) \right)^2}{2B_{\rm ext}} \tilde{S}_x$$

$$\approx \mu_{\rm B} g_{\parallel} \left( B_{\rm ext} + B_{\rm nuc}^{\parallel} - \frac{g_{\perp}}{g_{\parallel}} B_{\rm nuc}^{y',\perp}(t) + \frac{B_{\rm nuc}^{\perp}(t)^2}{2B_{\rm ext}} \right) \tilde{S}_x.$$
(7.15)

In the last step we assumed the anisotropy to be small such that  $\sin \phi \approx \tan \phi = g_{\perp}/g_{\parallel}$  and  $\cos(\phi) \approx 1$ . Furthermore, we have defined  $(B_{\text{nuc}}^{\perp})^2 = (B_{\text{nuc}}^{y',\perp})^2 + (B_{\text{nuc}}^{z',\perp})^2$ . We thus find that an anisotropy in the electronic *g*-factor leads to linear coupling to the transverse hyperfine-field.

## 7.7.2. Semiclassical fit model

In this section we derive the semi-classical model that will be used to fit and reproduce the experiments from Ref. 16. It accounts for a linear coupling to the transverse field component via a *g*-factor anisotropy from the last section and quadrupolar broadening of the individual Larmor frequencies [78,15,42].

Following equation (7.15), the effective Zeeman splitting is given by

$$E_{\rm Z}(t) = g_{\parallel} \mu_{\rm B} \left( B_{\rm ext} + \frac{B_{\rm nuc}^{\perp}(t)^2}{2B_{\rm ext}} + \frac{g_{\perp}}{g_{\parallel}} B_{\rm nuc}^{\perp,y}(t) \right),$$
 (7.16)

including both quadratic and linear coupling to the perpendicular nuclear magnetic fields arising from the three species <sup>113</sup>In, <sup>115</sup>In and <sup>75</sup>As.

The Larmor frequencies of the nuclei are broadened by nuclear dipole interaction and quadrupolar coupling to electric field gradients in the sample<sup>[78]</sup>. To capture the Larmor precession and statistics of this nuclear ensemble semi-classically, we introduce

	I	γ (rad/Ts)	A(μeV)
$^{75}As$	3/2	$4.6 \times 10^{7}$	86
<sup>113</sup> In	9/2	$5.88 \times 10^{7}$	110
<sup>115</sup> In	9/2	$5.9 \times 10^{7}$	110

**Table 7.1.: Properties of InAs isotopes.** Nuclear spins I, gyromagnetic ratios  $\gamma$  and contact hyperfine coupling strengths A. Table adapted from Ref. 117.

giant effective classical spins k. Their contributions to  $B_{\rm nuc}^{\perp}$  are described by uncorrelated Gaussian variables, each representing a narrow range of Larmor frequencies. We thus express the transverse nuclear field as a sum of complex-valued classical fields  $B_{\rm nuc}^{x',\perp}(t)+iB_{\rm nuc}^{y',\perp}(t)=\sum_k B_k(t)=\sum_k B_k^x(t)+iB_k^y(t)$ . The complex notation was introduced for convenience so that the time-dependence of the  $B_k(t)$  terms can be written as

$$B_k(t) = B_k(0)e^{i\omega_k t}. (7.17)$$

Here,  $\omega_k = \omega_{L,k} + \delta \omega_k$  describes the time evolution of the nuclear field given by the species dependent Larmor frequency  $\omega_{L,k} = \gamma_{\alpha(k)} B_{\rm ext}$ , where  $\gamma_{\alpha}(k)$  is the gyromagnetic ratio of species  $\alpha(k)$ , and a change in frequency  $\delta \omega_k$  due to dipolar or quadrupolar interaction.

We further write the initial conditions  $B_k(0) = \bar{B}_k z_k$  for the kth spin in terms of their rms values  $\bar{B}_k^2 = \frac{5}{4} \mathcal{A}_{\alpha(k)}^2 n_{\alpha(k)}/N$  and random variables  $z_k = x_k + iy_k$ . We assume a Gaussian probability distribution  $p(z,z^*) = \frac{i}{4\pi} \exp\left(-zz^*/2\right)$  with unit variance for these random variables. The  $\bar{B}_k$  reflect both the number of spins with a corresponding level splitting in one of the three transition as well as the strength of that transition.

During the Hahn echo experiment, the relative phase pickup  $\Phi$  for a separation time  $\tau$ , given initial conditions  $B_k(0)$  and for one quantum dot for the Hahn echo  $(c(t) = 1 \ (-1))$  for  $t < \tau/2 \ (t > \tau/2)$  using Eq. 7.15 is

$$\Psi(\tau) = \frac{\mu_{\rm B}}{\hbar} \int_{0}^{\tau} c(t) \left( \frac{g_{\parallel}}{2B_{\rm ext}} \sum_{k,l} B_{k}(t) B_{l}^{*}(t) + g_{\perp} \sum_{k} \Re(B_{k}(t)) \right) dt$$

$$= \frac{g_{\parallel} \mu_{\rm B}}{2\hbar B_{\rm ext}} \sum_{k,l} \bar{B}_{k} \bar{B}_{l} z_{k} z_{l}^{*} \int_{0}^{\tau} c(t) e^{i\omega_{kl}t} dt + g_{\perp} \frac{\mu_{\rm B}}{\hbar} \sum_{k} \bar{B}_{k} x_{k} \int_{0}^{\tau} c(t) \Re(e^{i\omega_{k}t}) dt \qquad (7.18)$$

$$= \sum_{k,l} T_{k,l} \frac{z_{k} z_{l}^{*}}{2} + \sum_{k} b_{k} x_{k}. \qquad (7.19)$$

Here, N is the number of unit cells overlapping with the quantum dot,  $n_{\alpha(k)}$  is the number of nuclei of species  $\alpha$  per unit cell and  $\mathcal{A}_{\alpha(k)}$  is the hyperfine coupling strength. Furthermore, we introduced  $\omega_{kl} = \omega_k - \omega_l$  and  $b_k = g_{\perp} \frac{\mu_B}{\hbar} \bar{B}_k$ . The definition of  $T_{kl}$  follows from the last equality and is consistent with Refs. 78,15.

To perform the ensemble average  $\langle e^{-i\Phi} \rangle$  we have to integrate over the distribution of initial nuclear fields. This integral is solved for one single electron dot by applying the

T-matrix approach, similar to Ref. 15, extended by a linear coupling term  $b_k x_k$ .

$$\langle e^{-i\Phi} \rangle = \int \left( \prod_{j} dz_{j} dz_{j}^{*} p(z_{j}, z_{j}^{*}) \right) \times$$

$$\exp \left( -i \sum_{k,l} T_{kl} \frac{z_{k}^{*} z_{l}}{2} + \sum_{k} b_{k} x_{k} \right)$$

$$= \prod_{j} \int dz_{j} dz_{j}^{*} p(z_{j}, z_{j}^{*}) \cdot \exp \left( -i \lambda_{j} \frac{|z_{j}|^{2}}{2} + \tilde{b}_{j} x_{j} \right)$$

$$= \prod_{j} \frac{1}{1 + i \lambda_{j}} \exp \left( \frac{2\tilde{b}_{j}^{2}}{1 + i \lambda_{j}} \right), \qquad (7.21)$$

where  $\lambda_j$  are the eigenvalues from  $T_{k,l} = UD_{k,l}U^{\dagger}$  for group j, with D being the diagonal matrix of eigenvalues  $\lambda_j$ . For  $\tilde{b} = Ub$  the same basis transformation is performed.

As the nuclei sampled by the electron spins in the left and right dot can be assumed to be statistically independent, the total decoherence function for dephasing of the two electron spins in a double dot can be written as the product of two identical dots  $|\langle e^{-i\Phi}\rangle|^2$ . While for an ideal Hahn echo measurement the echo response is given by Eq. 7.21, we also included a visibility factor  $\mathcal N$  to account for imperfect  $\pi$ -pulses in the refocusing part of the Hahn echo sequence, loss of measurement contrast at higher magnetic fields and possible leakage.

The final fit function of the Hahn echo amplitude states

$$P_{S}(\tau) = \mathcal{N} \prod_{j} \left( \frac{1}{1 + i\lambda_{j}} \exp\left(\frac{2\tilde{b}_{j}^{2}}{1 + i\lambda_{j}}\right) \right)^{2}. \tag{7.22}$$

Note that we neglect dephasing due to spectral diffusion, which according to theory in GaAs<sup>[38,39]</sup> would lead to a much longer coherence time.

# 8. Feedback-tuned high-fidelity gates for encoded spin qubits

The following chapter is adapted from Ref.55<sup>1</sup>.

# 8.1. Abstract

Two level quantum mechanical systems like spin 1/2 particles lend themselves as a natural qubit implementation [24]. However, encoding a single qubit in several spins reduces the resources necessary for qubit control and can protect from decoherence channels [25]. While several varieties of such encoded spin qubits have been implemented, accurate control remains challenging, and leakage out of the subspace of valid qubit states is a potential issue. Here, we realize high-fidelity single qubit operations for a qubit encoded in two electron spins in GaAs quantum dots by iterative tuning of the all-electrical control pulses. Using randomized benchmarking [124], we find an average gate fidelity of  $\mathcal{F} = (98.5 \pm 0.1)$ % and determine the sum of gate leakage out of and back into the computational subspace to  $\mathcal{L} = (0.4 \pm 0.1)$ % [125,126]. These results also demonstrate that high fidelity gates can be realized even in the presence of nuclear spins as in III-V semiconductors.

# 8.2. Introduction

Spins captured in semiconductor nanostructures provide a solid-state approach to quantum computation which leverages current semiconductor production technology for device fabrication. While the two spin states of an isolated electron form a natural qubit, the microwave signals required for manipulation impose certain drawbacks. Hence, all electrical control is an attractive alternative that can be achieved by encoding a qubit in multi-electron states. Most of the basic operations required for quantum computation

<sup>&</sup>lt;sup>1</sup>D.Schuh and D. Bougeard carried out molecular-beam-epitaxy growth of the sample used in this work. T. Botzem fabricated the sample and set-up the experiment. S. Humpohl developed the driver for the digitizer hardware used for data acquisition. T. Botzem and P. Cerfontaine developed the feedback software and conducted the experiment. H. Bluhm, T. Botzem and P. Cerfontaine analyzed the data and co-wrote the paper. H. Bluhm and P. Cerfontaine developed the theoretical models.

have already been demonstrated experimentally for qubits using one [80,118], two [9,11,12] and three spins [127,128,129].

A key requirement for quantum computation is that qubit manipulations, so-called gates, are highly accurate. Corresponding figures of merit are the gate error rate r or the gate fidelity  $\mathcal{F} \propto 1 - r$ . Fidelities well above 99% are expected to be needed for scalable quantum computing [14].

Recent works have demonstrated 99 %  $^{[130]}$ , 99.6 %  $^{[62]}$  and in one case 99.95 %  $^{[58]}$  using AC-controlled single-spin qubits in Si-based systems. Furthermore, fidelities of 93 – 96% have been demonstrated for a spin-charge hybrid qubit in Si  $^{[129]}$  and about 96% for a single spin in GaAs  $^{[131]}$ .

However, for purely spin-encoded multi-electron qubits recent theoretical gate constructions<sup>[132,133]</sup> have not yet been complemented by a systematic experimental effort to achieve high fidelities. Doing so entails a number of difficulties: The large pulse amplitudes required for fast control are prone to systematic errors and render standard Rabi driving inappropriate. Furthermore, nonlinearities in the electric control and a dependence of the noise sensitivity on the qubit control signal make optimal gate constructions nontrivial. In addition to charge noise present in all spin qubit variants<sup>[72]</sup>, magnetic field fluctuations from nuclear spins are a major challenge in GaAs<sup>[134]</sup>.

In this work, we develop high-fidelity baseband control for a two-spin qubit in a gate-defined GaAs double quantum dot encoded in the subspace with zero net spin ( $s_z = 0$ ). We address the aforementioned difficulties by numerically tailoring control pulses to our experiment [90]. Remaining inaccuracies in these pulses are removed by a control loop termed GAMBIT (Gate Adjustment by Iterative Tomography) which allows the iterative tune-up of gates using feedback [90]. In contrast to control loops based on randomized benchmarking (RB) [124], which have already been applied to superconducting qubits [135,136], GAMBIT extracts tomographic information to improve convergence. Additionally, we optimize about half an order of magnitude more parameters than related work on superconducting qubits [136] to fully leverage the degrees of freedom provided by our hardware.

Using RB, we demonstrate fidelities of 98.5 %. We find the fidelity to be limited more by charge noise than by nuclear spin fluctuations, which are often considered a major hurdle for GaAs qubits. The relatively weak effect of nuclear spins is due to a noise-canceling character of our optimized gates. In addition, we use RB to characterize leakage [125,126] out of and back into the  $s_z = 0$  subspace, an important figure of merit for the performance of any encoded qubit.

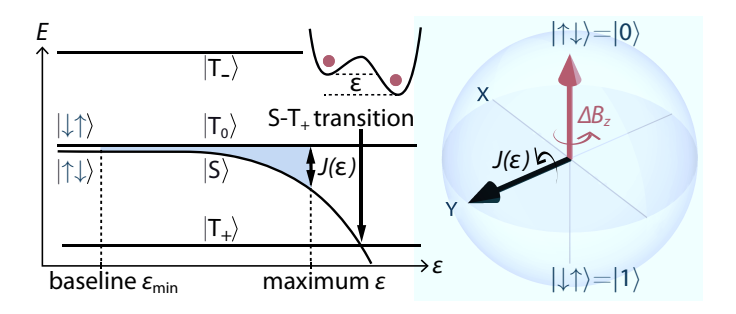


Figure 8.1.:  $S-T_0$  qubit energy diagram and Bloch sphere. The eigenenergies change as a function of detuning  $\varepsilon$ , which is used to control the exchange coupling  $J(\varepsilon)$ . The  $\varepsilon$  pulses presented in this work start and finish at a baseline and pulse to higher amplitudes for short periods. The maximum amplitude is constrained to below the  $S-T_+$  anticrossing at large  $\varepsilon$ . For ease of understanding we choose the convention that  $J(\varepsilon)$  points along the y-axis of the Bloch sphere (see supplementary information). For low  $\varepsilon$  amplitudes, the qubit rotates about  $\Delta B_z$ , the z-axis of the Bloch sphere. Large amplitude  $\varepsilon$  pulses rotate the qubit about the y-axis and thus enable arbitrary single-qubit gates.

# 8.3. Results

# **8.3.1.** S- $T_0$ Qubit

Our S-T<sub>0</sub> spin qubit<sup>[25]</sup> (see methods and Fig. 8.2b) can be described by the Hamiltonian  $H = \frac{\hbar J(\varepsilon)}{2} \sigma_x + \frac{\hbar \Delta B_z}{2} \sigma_z$  in the  $\{|\uparrow\downarrow\rangle = |0\rangle, |\downarrow\uparrow\rangle = |1\rangle\}$  basis, where arrows denote electron spin up and down states.  $J(\varepsilon)$  denotes the exchange splitting between the singlet  $|S\rangle = (|\uparrow\downarrow\rangle - |\downarrow\uparrow\rangle)/\sqrt{2}$  and  $s_z = 0$  triplet state  $|T_0\rangle = (|\uparrow\downarrow\rangle + |\downarrow\uparrow\rangle)/\sqrt{2}$ , while  $\Delta B_z$  is the magnetic field gradient across both dots from different nuclear spin polarizations [9]. The remaining triplet states,  $|T_{+}\rangle = |\uparrow\uparrow\rangle$  and  $|T_{-}\rangle = |\downarrow\downarrow\rangle$ , represent undesirable leakage states.  $J(\varepsilon)$  is manipulated by the detuning  $\varepsilon$ , the potential difference between both dots. We use standard state initialization and readout (see methods). For single qubit operations, ε is pulsed on a nanosecond timescale using an arbitrary waveform generator (AWG) whereas  $\Delta B_z$  is typically stabilized at  $2\pi \cdot 61.6(25)$  MHz by dynamic nuclear polarization<sup>[13]</sup>. The resulting dynamics are illustrated in Fig. 8.1, using the convention that  $J(\varepsilon)$  points along the Bloch sphere's y-axis for ease of understanding (see supplementary information). A perfect gate implementation is hindered by decoherence due to fluctuations in both  $\Delta B_z$  and  $\varepsilon$ . Moreover, an imperfectly known nonlinear transfer function  $J(\varepsilon)$  and finite bandwidth of the voltage pulses can be the source of systematic errors whose elimination requires careful calibration. In our simulations we use the experimentally motivated model  $J(\varepsilon) = J_0 \exp(\varepsilon/\varepsilon_0)^{[72]}$ .

# **8.3.2. GAMBIT**

To experimentally implement accurate single qubit  $\pi/2$  rotations around the x- and y-axis (denoted by  $\pi/2_x$  and  $\pi/2_y$ ), we use a control loop adapted from Ref.90 (Fig. 8.2a-b). To obtain a reasonably accurate system model, we measure the step response of our electrical setup,  $J_0$ ,  $\varepsilon_0$  and  $\Delta B_z$  as well as the coherence properties of the qubit (see supplementary information). We then use this model to numerically optimize pulses consisting of  $N_{\text{seg}}$  piece-wise constant nominal detuning values  $\varepsilon_j$ ,  $j=1...N_{\text{seg}}$  to be programmed into the AWG with a segment duration of 1 ns. The last four to five segments are set to the same baseline level  $\varepsilon_{\text{min}}$  for all gates to minimize errors arising from pulse transients of previous pulses. We choose  $\varepsilon_{\text{min}}$  such that  $J(\varepsilon_{\text{min}}) \ll \Delta B_z$ . Typical optimized pulse profiles  $\varepsilon_j^g$ ,  $j=1...N_{\text{seg}}$  for two gates  $g=\pi/2_x$  and  $g=\pi/2_y$  are shown in Fig. 8.2a.

Since our control model does not capture all effects to sufficient accuracy, these pulses need to be refined using experimental feedback. Hence, error information about the gate set is extracted in every iteration of our control loop. Standard quantum process tomography cannot be applied to extract this information as it requires well-calibrated gates, which are not available before completion of the control loop. We solve this bootstrap problem with a self-consistent method that extracts 8 error syndromes  $S_i$ , i = 1...8 in each iteration [90].  $S_i$ , i = 1...6 is primarily related to over-rotation and off-axis errors while  $S_i$ ,  $i \in \{7,8\}$  are proxies for decoherence. A syndrome  $S_i$  is measured by preparing  $|0\rangle$ , applying the corresponding sequence  $U_i$  of gates from Tab. 8.1, and determining the probability  $p(|0\rangle)$  of obtaining the state  $|0\rangle$  by measuring the sequence  $10^3...10^4$ times. For perfect gates, the first six syndromes [137] should yield  $p(|0\rangle) = 0.5$ , corresponding to  $S_i = \langle \sigma_z \rangle = 0$ . The last two syndromes should yield  $p(|0\rangle) = 0$  ( $S_i = -1$ ). Deviations of  $S_i$  from expectation indicate decoherence and systematic errors in the gate set. To make our method insensitive to state preparation and measurement (SPAM) errors, we also prepare and read out a completely mixed state with measurement result  $S_{\rm M}$ , and a triple state  $|T_0\rangle$ , which yields the measurement result  $S_{\rm T}$  after correcting for the approximate contrast loss of the triplet preparation (see supplementary information). GAMBIT then minimizes the modified error syndromes  $\tilde{S}_i = |S_i - S_{\mathbf{M}}|$  for  $i = 1 \dots 6$  and  $\tilde{S}_i = |S_i - S_T| \text{ for } i \in \{7, 8\}.$ 

For swift convergence, we start the control loop with pulses  $\varepsilon_j^g$  which theoretically implement the desired operations perfectly with minimal decoherence. First, GAMBIT scales these pulses by  $\pm 20\%$  in 4% increments and measures which scaling achieves the lowest  $\tilde{S}_i$ . GAMBIT then optimizes the best pulses by minimizing  $\tilde{S}_i$  with the Levenberg-Marquardt algorithm (LMA). In each LMA iteration, we use finite differences to experimentally estimate derivatives  $d\tilde{S}_i/d\varepsilon_j^g$ , which are subsequently used to calculate updated pulse amplitudes  $\varepsilon_i^g$ .

Pulses with  $N_{\text{seg}} \ge 24$  lead to reliable convergence, typically within 5 iterations (Fig. 8.2e). To demonstrate that our approach is reproducible for different initial gates,

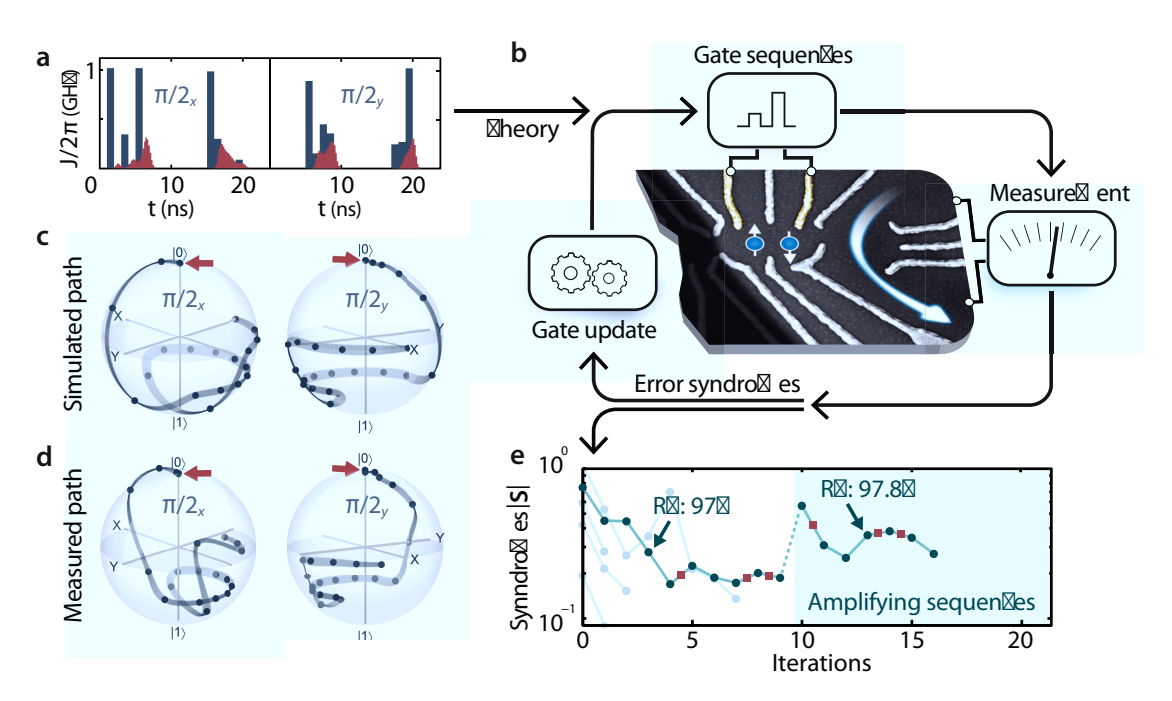


Figure 8.2.: Gate adjustment by iterative tomography. a Numerical pulse optimization based on a realistic but inaccurate qubit model provides initial optimal control pulses (blue) for  $\pi/2_x$  and  $\pi/2_y$  gates (24 ns long gates shown here). According to the model, the pulses shown in red are actually seen by the qubit. b Next, these pulses are optimized on the experiment using GAMBIT. 8 error syndromes  $\tilde{S}_i$  are extracted in each iteration by applying the gate sequences from Tab. 8.1. In order to remove gate errors, the  $\tilde{S}_i$  are minimized by adjusting the pulse segments' amplitudes  $\varepsilon_i^g$ . After a few iterations, the predicted Bloch sphere trajectories c can be reproduced in the experiment **d** as confirmed by self-consistent state tomography<sup>[29]</sup>. A major portion of the remaining deviation can be attributed to concatenation errors with the measurement pulses, specifically when the states following large J pulses are determined. e Typically, GAMBIT converges within 5 iterations and can recover from charge rearrangements in the quantum dot (indicated by red squares, see supplementary information). For a given noise level, better gates can be achieved by using modified gate sequences which amplify gate errors and lead to larger  $\tilde{S}_i$  for the same errors. In this specific run, randomized benchmarking [124] (RB) confirms that  $\mathcal{F}$  of the gate set was first improved to 97 % and then to 97.8 % by using amplifying gate sequences. Other optimization runs are shown in light blue for comparison.

24 ns gates were used in Fig. 8.2 while the experiments in Fig. 8.3 were performed using 30 ns gates. GAMBIT usually only adjusts those segments  $\varepsilon_j^g$  which are not at the baseline, resulting in 14 (24) free parameters for the 30 ns  $\pi/2_x$  ( $\pi/2_y$ ) gate shown in Fig. 8.3. When convergence eventually slows, we apply the sequences from Tab. 8.1

multiple times to amplify certain systematic gate errors (see supplementary information). Thus, further improvement (shaded region in Fig. 8.2e) is possible without increasing the averaging time per iteration.

Unfortunately, frequent charge rearrangements in our sample lead to a deterioration of optimized gates within minutes to hours. As a remedy we run GAMBIT again, resulting in slightly different gates than before. For this reason, the experiments in Fig. 8.3a and Fig. 8.3b were performed with gates from different GAMBIT runs.

# 8.3.3. Tomography and randomized benchmarking

To visualize the experimental gates, we perform self-consistent quantum state tomography  $(QST)^{[29]}$  and extract state information after each segment  $\varepsilon_j^g$ . As seen in Fig. 8.2c-d, the qubit state trajectories for model and experiment closely resemble each other, indicating that the GAMBIT-tuned pulses remain close to the optimum found in simulations.

In order to rigorously determine  $\mathcal{F}$ , we apply RB after completion of GAMBIT. In RB,  $\mathcal{F}$  is obtained by applying sequences of randomly chosen Clifford gates, composed of  $\pi/2_x$  and  $\pi/2_y$  gates, to the initial state  $|0\rangle$ . The last Clifford operation of each sequence is chosen such that  $|0\rangle$  would be recovered if the gates were perfect [124]. For imperfect gates, the return probability  $p(|0\rangle)$  decays as a function of sequence length and the decay rate indicates the average error per gate.

We find that the measured decay curve shown in red in Fig. 8.3 is best fitted by a double exponential, with the slow time constant describing the decay beyond  $\sim 100$  gates. In some cases, such a deviation from a single exponential decay can arise from non-Markovian noise<sup>[62]</sup> or inhomogeneous broadening of the control<sup>[138]</sup>. In our case, we attribute the second decay rate to gate leakage out of the computational subspace<sup>[125]</sup>

Sequences $U_i$ (right to left)	Parametrization		$S_i$
$\pi/2_x$	-2¢	=	$S_1$
$\pi/2_y$	$-2\chi$	=	$S_2$
$\pi/2_y \circ \pi/2_x$	$-n_y-n_z-v_x-v_z$	=	$S_3$
$\pi/2_x \circ \pi/2_y$	$-n_y + n_z - v_x + v_z$	=	$S_4$
$\pi/2_x \circ \pi/2_x \circ \pi/2_x \circ \pi/2_y$	$n_y + n_z + v_x - v_z$	=	$S_5$
$\pi/2_x \circ \pi/2_y \circ \pi/2_y \circ \pi/2_y$	$n_y - n_z + v_x + v_z$	=	$S_6$
$\pi/2_x \circ \pi/2_x$	$d_{\scriptscriptstyle X}$	=	$S_7$
$\pi/2_y \circ \pi/2_y$	$d_{\mathrm{y}}$	=	$S_8$

**Table 8.1.: Tomographic gate sequences.** To first order, the outcome of the measurement  ${\rm Tr}(\sigma_z U_i | 0 \rangle \langle 0 | U_i^\dagger) = S_i$  depends linearly on the gates' rotation-angle errors  $2\phi$  ( $2\chi$ ), the axis-errors  $n_y, n_z$  ( $v_x, v_z$ ) and decoherence  $d_x$  ( $d_y$ ) of the  $\pi/2_x$ -gate ( $\pi/2_y$ -gate). Parametrization defined as in Refs. 90 and 137 (see supplementary information).

into  $|T_{+}\rangle = |\uparrow\uparrow\rangle$ .

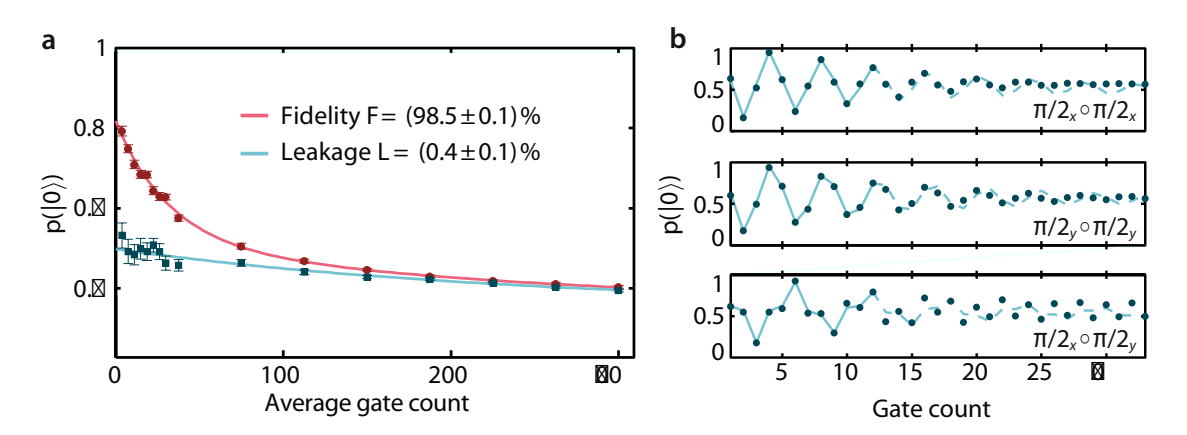


Figure 8.3.: Characterization of optimized gate sets. a The overall fidelity of a gate set consisting of 30 ns long  $\pi/2_x$  and  $\pi/2_y$  gates is determined using RB (red). Each red data point is an average over 50 randomly chosen sequences of the respective length. In order to determine gate leakage we supplement the standard protocol (red) by a variant which omits the last inversion pulse (blue)<sup>[126]</sup>. Fitting both curves simultaneously with a double (red)<sup>[125]</sup> and a single exponential (blue) yields  $\mathcal{F} = 98.5(1)\%$  and a leakage rate  $\mathcal{L} = 0.4(1)\%$ . b In order to determine systematic errors, we measure multiple repetitions of  $\pi/2_x$ ,  $\pi/2_y$  and  $\pi/2_x \circ \pi/2_y$ , using gates obtained in another GAMBIT run. The fit shown in blue estimates systematic errors of 0.7 %. Since we use a depolarizing channel for a simplified decoherence model, we only fit the first 12 data points. Afterwards other decoherence processes like  $T_2^*$  effects become dominant.

To confirm this hypothesis, we apply an extended RB protocol which omits the last Clifford from each RB sequence  $[^{126]}$ . Without leakage, averaging over many randomly chosen sequences should yield  $p(|0\rangle)=50\,\%$ . However, for nonzero leakage we expect a single exponential decay of  $p(|0\rangle)$  as a function of increasing sequence length since the additional leakage states have the same readout signature as  $|1\rangle$  (see methods). We indeed find such a decay law, indicated in blue in Fig. 8.3a. A joint fit of the standard (red) and leakage detection (blue) RB data yields  $\mathcal{F}=98.5(1)\,\%$  and a gate leakage rate  $\mathcal{L}=0.4(1)\,\%$  (the sum of leakage out of and back into the computational subspace  $^{[126]}$ ). Both fitted decay curves asymptotically approach  $p(|0\rangle)=0.36$  for long gate sequences, close to  $\frac{1}{3}$  as expected for a single leakage state  $^{[125,126]}$ . Since our pulses operate close to the  $S-T_+$  transition while  $|T_-\rangle$  is far away in energy, leakage should predominantly occur into the  $|T_+\rangle$  level.

As RB does not reveal whether our gates are limited by systematic errors or decoherence, we perform an independent test by measuring repetitions of  $\pi/2_x$ ,  $\pi/2_y$  and  $\pi/2_x \circ \pi/2_y$  as shown in Fig. 8.3b. By fitting this data (see supplementary information)

we retrieve  $\mathcal{F}_{\rm sys}=99.3\,\%$ , excluding decoherence. RB yields  $\mathcal{F}=98.1(2)\,\%$  for this gate set, indicating that decoherence and systematic errors contribute roughly equally. Note that even for a bare  $T_2^{\star}$  time of less than 100 ns along either J or  $\Delta B_z$ , the decay time for both gates exceeds 500 ns. This behavior is expected since the numerically optimized gates exhibit a reduced sensitivity to quasistatic noise sources [90], which contribute significantly to decoherence. In addition, the numerical optimization minimizes the use of large J to increase the resilience to slow and fast charge noise.

# 8.4. Discussion

We previously predicted fidelities approaching 99.9 % for GaAs based S-T<sub>0</sub> qubits <sup>[90]</sup> with the best reported noise levels <sup>[72,13]</sup>. To determine why our gates perform worse, we measure  $T_2^*$  and  $T_2^{\text{echo}}$  for both exchange and hyperfine driven oscillations. We find that our sample suffers from much larger charge noise than reported in Ref.72, which shows up as a shorter  $T_2^{\text{echo}} = 183\,\text{ns}$  for exchange oscillations at  $J(\epsilon) = 2\pi \cdot 61\,\text{MHz}$ , compared to  $T_2^{\text{echo}} \approx 7.5\,\mu\text{s}$  at comparable charge noise sensitivity  $dJ/d\epsilon \approx 2\pi \cdot 150\,\text{MHz/mV}^{[72]}$ . Using a noise model based on these measurements, we predict fidelities of 98.6 % and 99.0 % for the numerically optimized gates used as a starting point for GAMBIT (see supplementary information). These are close to the experimental value of 98.5(1)% which supports the validity of our noise model and the predictions of Ref.90 that a substantial improvement is possible with previously measured lower charge noise levels. Enhanced suppression of hyperfine fluctuations <sup>[139]</sup> would enable further improvement. Reducing one noise source, either charge or hyperfine noise, generally also allows making gates less sensitive to the other noise source since optimal gates will exploit tradeoffs between the sensitivity to different types of decohering noise.

Our results also indicate that the unavoidable presence of nuclear spins in GaAs spin qubits, which is often thought of as prohibitive for their technological prospects, actually does not preclude the fidelities required for fault-tolerant quantum computing. This could allow leveraging other strengths of GaAs compared to Si, such as a small effective mass leading to relaxed fabrication requirements, the absence of near-degenerate valleys and a direct band gap potentially enabling optical interfacing. Although driven by the needs of GaAs based S-T<sub>0</sub> qubits, we expect that our approach is equally viable for other encoded spin qubits facing similar difficulties, and can be adapted for implementing exchange-mediated two-qubit gates.

# 8.5. Methods

# **8.5.1.** Qubit system

We work in a dilution refrigerator at an electron temperature of about 130 mK using the same sample as Ref.78. A lateral double quantum dot is defined in the two-dimensional electron gas of a doped, molecular-beam epitaxy-grown GaAs/AlGaAs-heterostructure by applying voltages to metallic surface gates. We use the same gate layout as Ref.12 shown in Fig. 8.2b with two dedicated RF gates (yellow) for controlling the detuning. As we only apply RF pulses to these gates and no DC bias, we can perform all qubit operations without the need for bias tees which reduces pulse distortions.

Quantum gates are performed in the (1,1) charge configuration, where one electron is confined in the left and one in the right quantum dot. In this regime, the computational subspace is defined by the  $s_z = 0$  triplet state  $|T_0\rangle$  and the spin singlet state  $|S\rangle$ . The other  $s_z = \pm 1$  (1,1) triplet states  $|\uparrow\uparrow\rangle$  and  $|\downarrow\downarrow\rangle$  are split off energetically via the Zeeman effect by applying an external magnetic field of 500 mT.

We always readout and initialize the dot in the  $\{|\uparrow\downarrow\rangle, |\downarrow\uparrow\rangle\}$  basis by pulsing slowly from (0,2) to (1,1) and thus adiabatically mapping singlet  $|S\rangle$  and triplet  $|T_0\rangle$  to  $|\uparrow\downarrow\rangle$  and  $|\downarrow\uparrow\rangle$  (see supplementary information).

## 8.5.2. Readout calibration

For measuring the quantum state, we discriminate between singlet and triplet states by Pauli spin blockade. Using spin to charge conversion<sup>[9]</sup>, the resistance of an adjacent sensing dot depends on the spin state and can be determined by RF-reflectometry. In this manner, we obtain different readout voltages for singlet and triplet states but cannot distinguish between  $|T_0\rangle$  and the triplet states  $|T_+\rangle$ .

The measured voltages are processed in two ways. First, binning on the order of  $10^4$  consecutive single shot measurements yields bimodal histograms where the two peak voltages roughly correspond to the singlet and triplet state. Second, the measured voltages are averaged over many repetitions of a pulse to reduce noise.

For self-consistent state tomography, we linearly convert the averaged voltages to probabilities  $p(|0\rangle)$ . The parameters of the linear transformation are obtained by fitting the histograms [10] with a model that takes the decay and excitation of  $|S\rangle$  and  $|T_0\rangle$  during the readout phase into account.

Due to the long gate sequences, the benchmarking experiments in Fig. 8.3 are expected to produce a sizable leakage state population  $|T_+\rangle$ . We have attempted to include  $|T_+\rangle$  explicitly in the histogram fit model but found that this introduces too many additional parameters. In order to achieve an approximate calibration, we prepare and readout a completely mixed state once in about  $10^3$  measurements as an additional reference. We then enforce  $p(|0\rangle) = 0.5$  for the mixed state voltage  $U_{\rm M}$  in the histogram fits.

While we have not quantitatively analyzed the error from this approximate procedure, we suspect that the suboptimal contrast in Fig. 8.3 might be related.

For GAMBIT, the averaged voltages  $U_i$  corresponding to the error syndromes  $S_i$  do not need to be explicitly converted to probabilities  $p(|0\rangle)$ . Since mixed and triplet state reference voltages  $U_{\rm M}$  and  $U_{\rm T}$  are measured alongside the error syndromes, it is attractive to directly minimize  $\tilde{U}_i = |U_i - U_{\rm M}|$  for  $i = 1 \dots 6$  and  $\tilde{U}_i = |U_i - U_{\rm T}|$  for  $i \in \{7, 8\}$ . Adjusting the contrast of  $\tilde{U}_i$  with the aid of histograms can improve convergence and yields the expressions for  $\tilde{S}_i$  from the main text.

Note that GAMBIT, RB and all other fits used in this work are insensitive to state preparation and measurement (SPAM) errors. Therefore, our readout calibration does not need to be especially accurate or precise. The only figure which is sensitive to SPAM errors is the singlet probability of the asymptote in Fig. 8.3a. However, the measured value  $p(|0\rangle) = 0.36$  deviates significantly from 0.5 so that leakage is the most plausible explanation for the observed second decay rate, irrespective of SPAM errors.

Further information regarding readout can be found in the supplementary information.

# **8.6.** Supplementary Information

# 8.6.1. Experimental setup

Our sample and electrical setup are the same as in Ref.78.

Hence, the S-T<sub>0</sub> qubit is defined in a  $GaAs/Al_{0.69}Ga_{0.31}As$  heterostructure with Si- $\delta$ -doping 50 nm below the surface. Since a spacer layer of 40 nm is added on top, the 2DEG is located 90 nm below the surface. The gate layout (Fig. 8.2b) is the same as in Ref. 12 with two dedicated RF gates for high-frequency qubit operations like initialization, readout and gate operations while DC gates are used for static tuning of the qubits.

In our electrical setup, we use separate DC and RF control gates to avoid pulse distortions from bias tees, resulting in a nearly flat frequency response of the RF gates from DC to beyond 100 MHz. The qubit is defined and tuned by applying static voltages on the order of 1 V to the DC gates, while we use RF pulses from a Tektronix AWG5014C arbitrary waveform generator (AWG) on the order of 1 mV (after attenuation) for qubit manipulation. The RF gates are DC-coupled to the AWG with 43 dB attenuation.

# 8.6.2. System characterization

# **Exchange pulses**

For system characterization we measure the AWG response through coaxial cables and attenuators. We use the AWG to apply a long, nominally rectangular pulse to the RF

lines, and measure the signal that arrives just before the printed circuit board (PCB), where the sample is mounted. The measured step response includes the effect of attenuators and coaxial cables but no signal distortions due to the PCB and the sample itself. From the step response we obtain a filter describing the behavior of our system. Applying this filter to arbitrary piece-wise constant pulses reproduces the actual signal very accurately as shown in Fig. 8.4.

Parameters for the experimentally motivated model  $J(\varepsilon) = J_0 \exp(\varepsilon/\varepsilon_0)$  from Ref.72 are fitted from the oscillation frequencies of free induction decay (FID) experiments at different  $\varepsilon$  as in Ref.72, where  $\varepsilon$  describes the voltage change on each RF gate. We fix  $J_0 = 2\pi \cdot 159 \, \text{MHz}$  so that  $\varepsilon = 0$  is always defined as the point where  $J(\varepsilon) = 2\pi \cdot 159 \, \text{MHz}$ . This is convenient for describing gate operations as these depend primarily on the magnitude of J, but the exact gate voltages where J has a certain value can vary with dot tuning.

To describe this variation, we define a second frame of reference  $\delta = \varepsilon_{\rm M} - \varepsilon$ . Here,  $\varepsilon_{\rm M}$  is the position of the measurement point in the (2,0) charge configuration as shown in Fig. 8.5 and corresponds to  $\delta = 0$ . Even if the distance of the measurement point from the (2,0)-(1,1) charge transition remains the same, typically around 0.25 mV, the exact value of  $\varepsilon_{\rm M}$  depends on dot tuning since  $\varepsilon = 0$  is defined as the point where  $J(\varepsilon) = 2\pi \cdot 159\,{\rm MHz}$ . This leads to shifts of the  $\varepsilon$  coordinate system when the point where  $J = 2\pi \cdot 159\,{\rm MHz}$  moves. We find that  $\varepsilon_{\rm M}$  varies between 0.7 mV and 1.1 mV. Likewise,  $\varepsilon_0$  can take on values between 0.2 mV and 0.5 mV.

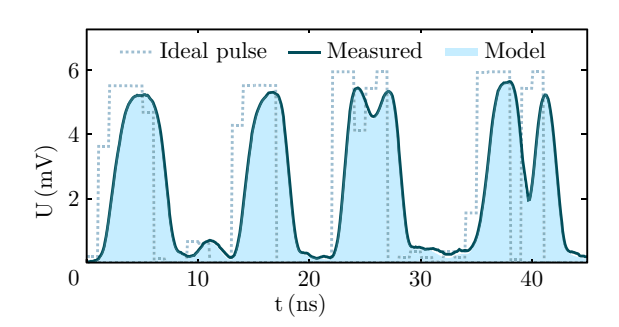


**Figure 8.4.: Pulse model.** A filter based on the step response of our system is applied to nominally piece-wise constant pulses (dashed line) to predict the actual signal arriving at the PCB where the GaAs sample is mounted. Except for long-time transients (not shown) the actual signal (solid line) is accurately reproduced by the model (shaded area).

#### **Noise**

In addition to the characterization of  $J(\varepsilon)$  and the step response of our setup, we extract approximate hyperfine and charge noise levels from free induction decay (FID) and spin

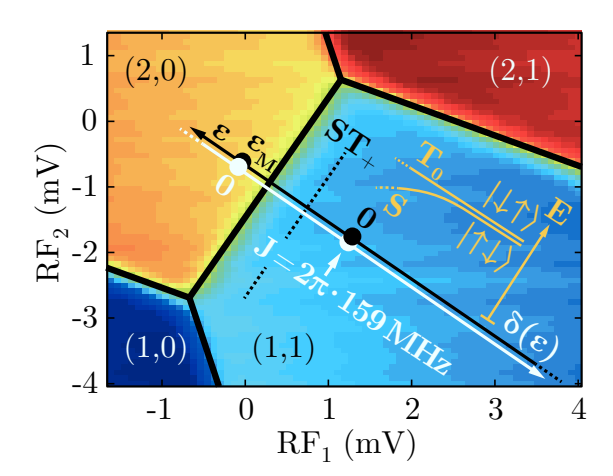


Figure 8.5.: Charge stability diagram. Different charge occupations are indicated as a function of both RF gate voltages by (n,m) with n (m) electrons in the left (right) dot.  $\delta = \varepsilon_{\rm M} - \varepsilon$  (white) denotes the distance between the measurement point at  $\varepsilon_{\rm M}$  and the point given by the detuning  $\varepsilon$  (black).  $\varepsilon = 0$  is defined as the point where  $J(\varepsilon) = 2\pi \cdot 159\,{\rm MHz}$ . For large  $\varepsilon$  (low  $\delta$ ) the exchange interaction is turned on, as indicated in the orange energy diagram. The approximate position of the S-T<sub>+</sub> transition is indicated by a dashed line.

echo (SE) experiments. For hyperfine noise, we find  $T_2^* = 80\,\mathrm{ns}$  and  $T_2^{\mathrm{echo}} = 13\,\mu\mathrm{s}$  as in Ref.78, with  $\Delta B_z$  stabilized at  $2\pi \cdot 61.6\,\mathrm{MHz}$  by dynamic nuclear polarization [13]. These values are smaller than  $T_2^* = 94\,\mathrm{ns}$  and  $T_2^{\mathrm{echo}} = 30\,\mu\mathrm{s}$  reported in Ref. 13. Instead of measuring  $T_2^*$ , we can also measure the fluctuations in  $\Delta B_z$  directly. For a variety of dot tunings, which affect the effectiveness of the dynamic nuclear polarization pulses [13], we find standard deviations between  $\sigma_{\Delta B_z} = 2\pi \cdot 2.2\,\mathrm{MHz}$  and  $\sigma_{\Delta B_z} = 2\pi \cdot 3.4\,\mathrm{MHz}$  (after removing jumps away from the set point of  $\Delta B_z$ ). In consideration of  $T_2^{\mathrm{echo}} \gg T_2^*$  and the slow initial decay of the Hahn echo coherence, we treat hyperfine noise as quasistatic [134] throughout this work.

For charge noise, we similarly perform FID and SE experiments at  $J(\epsilon) = 2\pi \cdot 61 \, \text{MHz}$ , yielding  $T_2^* = 90 \, \text{ns}$  and  $T_2^{\text{echo}} = 183 \, \text{ns}$ . For these FID and SE experiments we also determined  $\epsilon_0 = 0.4 \, \text{mV}$  and  $\epsilon_{\text{M}} = 1.0 \, \text{mV}$  so that we can approximately calculate the charge noise sensitivity in our device at  $J(\epsilon) = 2\pi \cdot 61 \, \text{MHz}$  to  $dJ/d\epsilon = 2\pi \cdot 151 \, \text{MHz/mV}$ . Based on these measurements we estimate that our sample suffers from much larger charge noise compared to Ref.72, where  $T_2^* \approx 100 \, \text{ns}$  and  $T_2^{\text{echo}} \approx 7.5 \, \mu \text{s}$  were measured for  $J \approx 2\pi \cdot 85 \, \text{MHz}$ , which corresponds to a similar charge noise sensitivity  $dJ/d\epsilon \approx 2\pi \cdot 150 \, \text{MHz/mV}$ .

We use the relation

$$T_2^* = \frac{\sqrt{2}}{\sigma_{\varepsilon} dJ/d\varepsilon} \tag{8.1}$$

given in Ref. 140 to calculate our sample's charge noise standard deviation to  $\sigma_{\varepsilon} = 1.66 \times 10^{-5} \,\mathrm{V}$ . To deduce the amplitude  $S_{\varepsilon}^0$  of the high-frequency noise spectrum from  $T_2^{\mathrm{echo}}$ , we assume that the noise spectrum can be described by  $S_{\varepsilon}(f) = S_{\varepsilon}^0/f^{\beta}$  with  $\beta = 0.7$  as measured in Ref. 72 for frequencies  $50 \,\mathrm{kHz} \le f \le 1 \,\mathrm{MHz}$ . For the purpose of calculating gate fidelities in Sec. 8.6.3, we extrapolate the spectrum to follow the same power law for  $f > 1 \,\mathrm{MHz}$ . Due to the proportionality

$$T_2^{\text{echo}} \propto \left(\frac{dJ}{d\varepsilon}\right)^{-2/(\beta+1)}$$
 (8.2)

given in Ref. 140, we can estimate the amplitude of the high-frequency charge noise spectrum by relating our measurements of  $T_2^{\rm echo}$  and  $dJ/d\varepsilon$  to those from Ref. 72, which were given as  $T_2^{\rm echo} \approx 7.5\,\mu s$ ,  $dJ/d\varepsilon \approx 2\pi \cdot 150\,\mathrm{MHz/mV}$  and  $\sqrt{S_\varepsilon^0} = 2.8 \times 10^{-8}\,\mathrm{V/\sqrt{Hz}}$ . For our sample, we then find  $\sqrt{S_\varepsilon^0} = 6.6 \times 10^{-7}\,\mathrm{V/\sqrt{Hz}}$ .

These noise estimates are used in Sec. 8.6.3 to calculate the gate fidelities we expect to reach theoretically, which we then compare to our experimental results.

# 8.6.3. Optimal pulses

### **Bloch sphere convention**

Throughout this work, we use the convention that  $J(\varepsilon)$  coincides with the Bloch sphere's y-axis and  $\Delta B_z$  with the z-axis.

If  $J(\varepsilon)$  would point along the x-axis of the Bloch sphere, our  $\pi/2_x$  ( $\pi/2_y$ ) gate would actually correspond to a  $\pi/2$  rotation around the negative y-axis (positive x-axis). For ease of understanding, we thus apply a coordinate system transformation so that that  $J(\varepsilon)$  points along the y-axis. In this frame, the  $\pi/2_x$  ( $\pi/2_y$ ) gate rotates around the x-axis (y-axis) as expected.

## Numerical pulse optimization

The pulse optimization we perform for this work is similar to the one in Ref. 90. For completeness, we now provide a short summary and highlight any differences.

First, we characterize the step response of our electrical setup and measure  $J_0$ ,  $\varepsilon_0$  and  $\Delta B_z$  as described in Sec. 8.6.2. We also determine the coherence of our qubit as described in Sec. 8.6.2. Consequently, we use this information as a model for the numerical pulse optimization of piece-wise constant detuning pulses with  $N_{\text{seg}}$  segments. Each pulse segment is 1 ns long, corresponding to the sampling rate of our AWG. In the following,  $\varepsilon_j$  with  $j=1...N_{\text{seg}}$  denotes the detuning in the  $j^{\text{th}}$  segment. The actual control pulse arriving at the qubit is determined by applying a filter to the piece-wise constant pulse  $\varepsilon_j$  (see Sec. 8.6.2). This is even more realistic than the procedure outlined in Ref.90 where a purely exponential model was used to account for finite rise times.

We also choose slightly different bounds than Ref. 90 and constrain the detuning to  $0.26\,\mathrm{mV} \le \delta \le 4.00\,\mathrm{mV}$ . The upper bound of  $\delta$  corresponds to the (1,1) charge regime with separated electrons. At this point  $J \ll \Delta B_z$  is essentially turned off and  $\epsilon$  is at the baseline  $\epsilon_{\min}$  mentioned in the main text. The lower bound was chosen to avoid the anticrossing of the singlet state with the  $|T_+\rangle$  state during gate operation. This anticrossing occurs at large detunings  $\epsilon$ , typically at a distance  $\delta \approx 0.22\,\mathrm{mV}$  from the measurement point M. The crossing is also indicated in Fig. 8.1 and Fig. 8.5. We avoid pulsing across this anticrossing as it would lead to a significant portion of the singlet state being converted to  $|T_+\rangle$  and as such increase the gate leakage rate. For future experiments, it would be helpful to further examine the process driving leakage so that it can be captured and minimized directly in the numerical pulse optimization.

Furthermore the last 4 ns (5 ns) of each gate were set to  $\varepsilon_{min}$  (which corresponds to  $\delta = 4.00\,\text{mV}$ ) for the 24 ns long gates in Fig. 8.2 (30 ns long gates in Fig. 8.3) to ensure that the pulse has decayed to  $\varepsilon_{min}$  before another gate is applied. If the decay is not perfect, transients from the previous gate will affect the next gate. Since such gate bleedthrough [136] causes additional errors which depend on the sequence of gates and not just the gates themselves, it is harder to detect and correct than purely gate-dependent errors. Thus, it is best to minimize gate transients whenever possible.

For the pulse optimization, explicitly time-dependent Hamiltonians  $H(J(\epsilon(t)), \Delta B_z) = \frac{\hbar J(\epsilon(t))}{2} \sigma_x + \frac{\hbar \Delta B_z}{2} \sigma_z$  are approximated as piecewise constant on 0.2 ns intervals. This discretization greatly simplifies the calculation of  $U(t,t_0) = \mathcal{T} \exp\left(-\frac{i}{\hbar} \int_{t_0}^t H(t') \, dt'\right)$  and incurs only small systematic errors on the order of  $10^{-3}$  (in fidelity). These can be calibrated in experiments by using GAMBIT (Gate Adjustment by Iterative Tomography). Using this approximation, we can also calculate the effect of quasistatic noise in  $\epsilon$  and  $\Delta B_z$ . All we have to do is to repeat the calculation several times using  $H(J(\epsilon(t)+d\epsilon),\Delta B_z+d\Delta B_z)$ , where  $d\epsilon$   $(d\Delta B_z)$  is sampled discretely from a Gaussian distribution with standard deviation  $\sigma_\epsilon$   $(\sigma_{\Delta B_z})$ . It is a little bit more involved to include fast noise with an arbitrary noise spectral density in a computationally efficient manner. We choose to use a first-order perturbative approach based on filter functions [141] which is fast enough for numerical optimization.

We then combine these methods with the Levenberg-Marquardt algorithm (LMA) to search for  $\pi/2_x$  and  $\pi/2_y$  pulses with maximal fidelity  $\mathcal{F}$ , taking systematic errors and the major decoherence sources into account. Further details regarding the exact implementation of the optimization are given in Ref. 90. An example of the resulting pulses  $\varepsilon_j^g$ ,  $j=1\ldots N_{\text{seg}}$  for two gates  $g=\pi/2_x$  and  $g=\pi/2_y$  can be found in Fig. 8.2a.

#### **Fidelity estimation**

Using the noise model described in Sec. 8.6.2, we use Monte Carlo simulations as in Ref.90 to determine the average gate fidelity of the gate set used in Fig. 8.3a. For hyper-

fine noise we use  $\sigma_{\Delta B_{\tau}} = 2\pi \cdot 2.5 \,\text{MHz}$ . We find an average gate fidelity of 98.8 % which is in good agreement with the fidelity of 98.5(1) % from randomized benchmarking, given that the charge noise model for the high frequencies relevant for nanosecond gates is not known and was extrapolated. The noise contributions to the infidelity  $I = 1 - \mathcal{F}$ listed in Tab. 8.2 indicate that charge noise is the dominant factor for decoherence.

To assess the potential for further improvement with the same noise characteristics, it is instructive to consider the effect of stretching or compressing one of our numerically optimized pulses in time. Doing so results in distinct scaling laws of the contributions to I from different noise types. For fast charge noise, the scaling law also depends on the spectral noise density  $S_{\varepsilon}(f) \propto 1/f^{\beta}$ . When we change the total duration T of a pulse and accordingly adjust  $J(\varepsilon)$  and  $\Delta B_z$  so that the same unitary is still realized, we find

$$I_{\epsilon, \mathrm{fast}} \propto T^{\beta-1},$$
 (8.3)  
 $I_{\epsilon, \mathrm{slow}} \sim \mathrm{const},$  (8.4)  
 $I_{\Delta B_z} \propto T^2,$  (8.5)

$$I_{\text{\epsilon.slow}} \sim \text{const},$$
 (8.4)

$$I_{\Delta B_z} \propto T^2,$$
 (8.5)

assuming  $I \ll 1$ .  $I_{\Delta B_z}$  increases with T since  $\Delta B_z$  decreases with T while the standard deviation of  $\Delta B_z$  remains the same. Thus, the error of the phase acquired due to  $\Delta B_z$  increases with T. For slow charge noise we need to additionally consider  $dJ/d\varepsilon$ which decreases with J. Consequently, the standard deviation of  $J(\varepsilon)$  decreases with T and  $I_{\text{E,slow}}$  is approximately constant. For high-frequency charge noise the form of the noise spectrum given by the exponent  $\beta$  needs to be taken into account since the frequency range most relevant for the gate changes with 1/T. Using the filter function formalism<sup>[141]</sup>,  $I_{\epsilon,\text{fast}} \propto T^{\beta-1}$  can be derived.

Combining the noise contributions in Tab. 8.2 with Eqs. (8.3-8.5) allows us to calculate which duration T is optimal for our  $\pi/2_x$  and  $\pi/2_y$  gate. We find that the  $\pi/2_x$  and  $\pi/2_{\rm v}$  gate could be improved by decreasing T by 20 % and 30 %, respectively. However, doing so would only increase the gate fidelity by about  $1 \times 10^{-4}$  (3 × 10<sup>-4</sup>). Thus, the original gates are already close to optimal and no further modification is needed.

## 8.6.4. Readout and initialization

#### **Pulses**

The FID and SE experiments used for measuring hyperfine noise (see Sec. 8.6.2) are performed with singlet initialization and readout.

For all other experiments, we prepare the state  $|\uparrow\downarrow\rangle$  adiabatically. To this end, we first decrease ε quickly and diabatically jump over the S-T<sub>+</sub> transition to avoid mixing with the  $|T_+\rangle$  level. Then, we slowly ramp  $\varepsilon$  down to  $\varepsilon_{\min}$ . In this way,  $J(\varepsilon)$  is turned off adiabatically since  $J(\varepsilon_{\min}) \ll \Delta B_z$ . For readout, we slowly sweep  $\varepsilon$  from  $\varepsilon_{\min}$  up to a point before the S-T<sub>+</sub> transition. Then, we jump directly to the measurement point  $\varepsilon_M$ .

	$\pi/2_x$	$\pi/2_y$
$I_{\epsilon, \mathrm{fast}}$	$6.4 \times 10^{-3}$	$5.1 \times 10^{-3}$
$I_{ m \epsilon,slow}$	$5.3 \times 10^{-3}$	$3.9 \times 10^{-3}$
$I_{\Delta B_z}$	$1.6 \times 10^{-3}$	$1.8\times10^{-3}$
$I_U$	$6.3 \times 10^{-10}$	$0.5 \times 10^{-10}$
I	$1.4 \times 10^{-2}$	$1.0 \times 10^{-2}$

Table 8.2.: Theoretical infidelity contributions. The different noise contributions to  $I=1-\mathcal{F}$  are obtained using Monte Carlo simulations (1000 time traces)<sup>[90]</sup> for the gates used in Fig. 8.3a. All charge noise below 1 MHz is included in  $I_{\epsilon,\text{slow}}$ , using noise strengths from Sec. 8.6.2. Faster charge noise is taken into account in  $I_{\epsilon,\text{fast}}$ . The infidelity due to hyperfine noise,  $I_{\Delta B_z}$ , is much smaller than the charge noise contributions. In the simulation, the gate was implemented perfectly as indicated by the low unitary infidelity,  $I_U$ .

Since we cross the S-T<sub>+</sub> transition diabatically we avoid mixing with the  $|T_+\rangle$  level. Since  $J(\varepsilon)$  is turned back on adiabatically we measure in the basis  $\{|\uparrow\downarrow\rangle, |\downarrow\uparrow\rangle\}$ .

# **Data acquisition**

Data is acquired in buffers with a duration of approximately 100 ms. Each buffer contains  $\sim$  20 repetitions of  $N\sim$  1000 pulse sequences, and we typically measure between 10 to 1000 buffers in order to ensure good averaging over the slowly decorrelating  $\Delta B_z$ . Every pulse sequence consists of an adiabatic initialization pulse to prepare  $|\uparrow\downarrow\rangle$ , qubit manipulation pulses and adiabatic readout, which maps singlet and triplet probabilities to  $|\uparrow\downarrow\rangle$  and  $|\downarrow\uparrow\rangle$  probabilities. In the following we refer to singlet probabilities  $p(|0\rangle)$  whenever we mean the probability of measuring  $|\uparrow\downarrow\rangle$ .

After each buffer, polarization pulses [13] are applied to stabilize the hyperfine gradient  $\Delta B_z$ . Once in about  $10^3$  measurements we also read out a completely mixed state and a triplet state as additional references. While the mixed state is prepared by rotating around various axes with different  $J(\varepsilon)$  for times on the order of a  $\mu$ s, much longer than the coherence time  $T_2^*$  of the qubit, the triplet state is prepared by precession of a singlet state in the stabilized hyperfine field  $\Delta B_z$ .

We discriminate between singlet and triplet states by Pauli spin blockade. Using spin to charge conversion<sup>[9]</sup>, the resistance of an adjacent sensing dot depends on the spin state and can be determined by RF-reflectometry<sup>[35]</sup>. In this manner, we obtain different readout voltages for singlet and triplets states,  $U_{|S\rangle}$  and  $U_{|T_0\rangle}$ , but cannot distinguish between  $|T_0\rangle$  and the triplet states  $|T_\pm\rangle$ .

We only switch the RF readout power on during measurements while leaving it off during manipulation. The timing of this switching is chosen carefully to minimize the influence of transients on the measured voltages.

The voltages measured in a buffer, which contains about 20 repetitions of a sequence of  $N \sim 1000$  pulses, are processed in two ways:

- 1. All measured voltages are binned, irrespective of the pulse sequence or repetition they are associated with, to obtain histograms of the readout values.
- 2. Measured voltages corresponding to repetitions of the same pulse sequence are averaged, yielding *N* averaged voltages *U*.

Since data requirements differ between the various experiments, details about further data processing and our readout calibration are given in separate sections, specifically in Sec. 8.6.5, Sec. 8.6.5 and Sec. 8.6.5.

#### **Data postselection**

For all measurements, we automatically detect switching events due to charge traps and remove the affected data points.

Furthermore we discard data where dynamic nuclear polarization (DNP) was not stable and deviated by more than  $\pm \sigma_{\Delta B_z} \approx \pm 2\pi \cdot 2.5$  MHz from the set point of  $\Delta B_z$  at about  $2\pi \cdot 61.6$  MHz.

While  $\Delta B_z$  postselection is performed to remove datasets with unstable DNP, this procedure might also lead to increased gate fidelities. However, due to the relatively weak influence of hyperfine noise on gate performance (see Tab. 8.2) we do not expect this effect to be significant.

## Mapping state preparation to measurement errors

In this section, we argue that state preparation errors can be mapped to measurement errors. Hence, we only need to consider the latter in following discussions.

By definition, state preparation does not suffer from systematic errors as it defines the computational basis states  $|0\rangle$  and  $|1\rangle$ . However, the purity of the initial state can be finite due to stochastic errors from incomplete relaxation to the ground state <sup>[29]</sup> or from a combination of imperfect adiabaticity and dephasing. As a check, we prepare  $|\uparrow\downarrow\rangle$ , let it evolve for varying times (between 0 ns and 24 ns in 1 ns increments) and read out along different axes than z using diabatic pulses before the adiabatic readout. Since the resulting readout voltages do not show sinusoidal oscillations, we conclude that imperfect adiabaticity is not a problem for our initialization (dephasing should occur on a timescale of  $T_2^* \geq 80 \, \text{ns}$ ).

Since we use the same sweep speed for the adiabatic ramps used for state initialization and readout, our readout should be along the same axis as the state preparation. We check whether this assumption is justified by preparing different initial states than  $|\uparrow\downarrow\rangle$ 

(using diabatic pulses after the adiabatic initialization) and letting them evolve in the hyperfine field at  $J(\varepsilon_{\min})$  for varying times (between 0 ns and 24 ns in 1 ns increments) before adiabatic readout. The resulting readout voltages do not show sinusoidal oscillations. Thus, we can deduce that readout and initialization axes coincide with the rotation axis at  $J(\varepsilon_{\min})$  since in neither case oscillations could be observed. Thus, readout and initialization are performed along the same axis (up to measurement noise, which could have been larger than a small sinusoidal signal). Note that readout and initialization can still suffer from different stochastic errors.

Since it is impossible to discriminate stochastic state preparation errors from readout errors, the state preparation can be treated as perfect and all state preparation errors can be mapped to our adiabatic measurement [29]. Adiabatic state preparation and adiabatic measurement are performed along the same axis as explained above.

## 8.6.5. Readout calibration

In this section, we discuss how readout signals are processed for the different type of data sets presented.

# **Self-consistent state tomography**

For self-consistent state tomography (see Sec. 8.6.7 and Fig. 8.2d), we convert measured voltages to singlet probabilities  $p(|0\rangle)$  by fitting the bimodal histogram<sup>[10]</sup> obtained from binning the measurement data (see Sec. 8.6.4).

In contrast to Ref. 10, we observe excitation from  $|S\rangle$  to  $|T_0\rangle$  as well as relaxation from  $|T_0\rangle$  to  $|S\rangle$ . Since the standard model<sup>[10]</sup> does not fit our data well, we extend it by including an excitation rate e from  $|S\rangle$  to  $|T_0\rangle$  in addition to the relaxation rate r. In separate experiments we measure  $T_1$  decays in the (2,0) charge region where readout is performed. From this data, we determine  $T_1$  and the steady state voltage  $V_{SS}$  to which states decay after long times in the (2,0) charge region.  $T_1$  and  $V_{SS}$  are then used as additional fixed parameters in the fit of the histograms. The resulting fits typically look like the one in Fig. 8.6.  $U_{|S\rangle}$  and  $U_{|T_0\rangle}$  can then be calculated from the fit parameters and correspond to singlet probabilities of  $p(|0\rangle) = 1$  and  $p(|0\rangle) = 0$ .

We can now convert the averaged voltages to singlet probabilities  $p(|0\rangle) \in [0,1]$  using a linear transformation  $p(|0\rangle) = \frac{1}{2} \langle \sigma_z \rangle + \frac{1}{2} = \frac{c}{2} (U+s) + \frac{1}{2}$  with coefficients c and s obtained from the fit. Inaccuracies from fitting of the single shot histogram do not affect the tomography results as self-consistent state tomography is insensitive to state preparation and measurement (SPAM) errors.

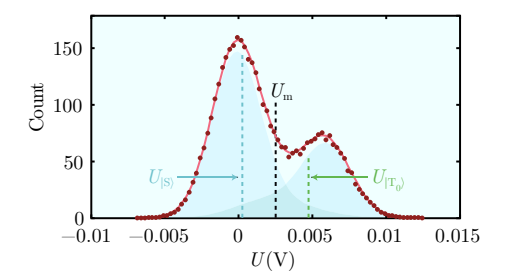


**Figure 8.6.:** Readout calibration. We fit a readout model (light red)<sup>[10]</sup> to the binned readout voltages of an entire buffer (dark red). The fitted underlying distributions of singlet and triplet voltages are shown in blue and green, respectively. The 50th percentile of each distribution is indicated by a dashed line. Extending previous work<sup>[10]</sup>, relaxation (from triplet to singlet) and excitation (from singlet to triplet) are taken into account. The voltages corresponding to singlet  $U_{|S\rangle}$ , triplet  $U_{|T_0\rangle}$  and the completely mixed state  $U_{\rm M}$  are indicated.

#### Benchmarking

For our benchmarking experiments (see Sec. 8.6.7 and Fig. 8.3) we perform a similar calibration as described in the previous section for self-consistent state tomography (Sec. 8.6.5).

In addition, we now consider that long gate sequences create a significant  $|T_+\rangle$  population. For the readout calibration we have so far neglected that other states than  $|T_0\rangle$  and  $|S\rangle$  might be populated. We have attempted to include  $|T_+\rangle$  explicitly in the fit model but found that this introduces too many additional parameters. To circumvent systematic shifts of the fitted  $U_{|S\rangle}$  and  $U_{|T_0\rangle}$  and achieve an approximate calibration, we include an additional constraint in the histogram fit which enforces that the mixed state reference voltage  $U_{\rm M}$  always corresponds to  $p(|0\rangle) = 0.5$ . While we have not quantitatively analyzed the error from this approximate procedure, we suspect that the suboptimal contrast in Fig. 8.3 might be related.

As RB and all other benchmarking experiments performed in this work are insensitive to SPAM errors, our readout calibration does not need to be especially accurate or precise. Specifically, the suboptimal contrast does not affect any figures of merit reported in this work.

#### **GAMBIT**

For optimization with GAMBIT, the averaged voltages  $U_i$  corresponding to the error syndromes  $S_i$  (as defined in Tab. 8.1) do not need to be explicitly converted to singlet probabilities  $p(|0\rangle)$  or  $\langle \sigma_z \rangle$  as in the previous two sections (Sec. 8.6.5 and Sec. 8.6.5). Instead,  $\tilde{U}_i = |U_i - U_{\text{M/T}}|$  can be optimized without further calibration. In this expression  $U_{\text{M/T}}$  corresponds to  $U_{\text{M}}$  if i = 1...6, otherwise the voltage  $U_{\text{T}}$  of the reference

 $|T_0\rangle$  state is used. The reference triplet state  $|T_0\rangle$  is subject to decoherence because it is prepared by letting  $|S\rangle$  evolve in the hyperfine field at  $J(\epsilon_{min}) \ll \Delta B_z$ .  $U_T$  is obtained by correcting the actual measurement result  $U_T'$  for the approximate loss in contrast of the triplet preparation using the transformation  $U_T = U_T' + b(U_T' - U_M)$  with  $b \sim 10^{-2}$  chosen according to  $T_2^*$  measurements. The exact choice of b is not crucially important as long as reductions in the decoherence of the gate set result in a reduction of  $S_7$  and  $S_8$ . Furthermore,  $S_7$  and  $S_8$  should be of comparable magnitude as the other syndromes for optimal convergence. This can be achieved by choosing appropriate weights  $w_7$  and  $w_8$  in Eq. (8.15).

It is helpful to compensate fluctuations of the measurement contrast with the aid of histograms to speed up convergence. With c and s defined as in Sec. 8.6.5 this yields

$$\tilde{S}_i = c\tilde{U}_i \tag{8.6}$$

$$= |c(U_i + s) - c(U_{M/T} + s)| (8.7)$$

$$= |S_i - S_{\mathrm{M/T}}|, \tag{8.8}$$

which is the same relation as given in the main text.

# **8.6.6. GAMBIT**

## **Error syndromes**

The gate sequences from Tab. 8.1 used to extract the error syndromes are modified versions of the previously published bootstrap tomography [137]. GAMBIT uses the information obtained from the error syndromes in a specific manner explained in Sec. 8.6.6. As described in the methods section of the paper and in Sec. 8.6.4, we adiabatically prepare  $|\uparrow\downarrow\rangle$  before applying any of the gate sequences from Tab. 8.1 or Tab. 8.3. At the end of each gate sequence, we read out adiabatically, allowing us to discriminate between  $|\uparrow\downarrow\rangle$  and  $|\downarrow\uparrow\rangle$ .

Possible errors include decoherence and systematic errors, which can be categorized as over-rotation and off-axis errors. We use the same parameterization for systematic errors as in supplementary Refs. 90 and 137 and denote the rotation-angle error of the  $\pi/2_x$  ( $\pi/2_y$ ) gate by  $2\phi$  ( $2\chi$ ) while axis-errors are described by  $n_y$ ,  $n_z$  ( $v_x$ ,  $v_z$ ). Using this notation, the unitary operator of the erroneous  $\pi/2_x$  gate can be written as

$$U_x = \exp\left[-i(\mathbf{n}\cdot\mathbf{\sigma})(\pi/2+2\phi)/2\right] \tag{8.9}$$

with 
$$\mathbf{n} = \left(\sqrt{1 - n_y^2 - n_z^2}, n_y, n_z\right)^{\top}$$
. (8.10)

Likewise, the unitary operator of the erroneous  $\pi/2_v$  gate is given by

$$U_{y} = \exp\left[-i(\boldsymbol{\nu}\cdot\boldsymbol{\sigma})(\pi/2+2\chi)/2\right] \tag{8.11}$$

with 
$$\mathbf{v} = \left(v_x, \sqrt{1 - v_x^2 - v_z^2}, v_z\right)^{\top}$$
. (8.12)

The first six sequences are sufficient to extract all systematic errors, and we introduce two additional sequences to explicitly probe for decoherence. When the systematic errors of the gate set are small, the amplification sequences in Tab. 8.3 are used instead of Tab. 8.1, resulting in three-fold amplification of the rotation-angle errors  $2\phi$  and  $2\chi$  and the axis-errors  $n_y$  and  $v_x$ . It is possible to achieve higher amplification by repeating the gate sequences multiple times but this also increases the overall decoherence. Since decoherence can lead to systematic shifts of the syndromes, the extracted error signature becomes less reliable for long gate sequences.

Sequences $U_i$		Parametrization		$S_i$
	$(\pi/2_x)^3$	6ф	=	$S_1$
	$(\pi/2_{y})^{3}$	6χ	=	$S_2$
$(\pi/2_y)$	$\pi/2_x)^4$	$-2\chi - 3n_y - n_z - 2\phi - 3v_x - v_z$	=	$S_3$
$(\pi/2_x)$ o	$(\pi/2_y)$	$-n_y + n_z - v_x + v_z$	=	$S_4$
$(\pi/2_x)^3$ or	$(\pi/2_y)$	$n_y + n_z + v_x - v_z$	=	$S_5$
$(\pi/2_x)$ o	$(\pi/2_y)^3$	$n_y - n_z + v_x + v_z$	=	$S_6$
	$(\pi/2_x)^2$	$d_x$	=	$S_7$
	$(\pi/2_{y})^{2}$	$d_{y}$	=	$S_8$

**Table 8.3.: Amplifying gate sequences.** To first order, the outcome of the measurement  ${\rm Tr}(\sigma_z U_i | 0 \rangle \langle 0 | U_i^\dagger) = S_i$  depends linearly on the gates' rotation-angle errors  $2\phi$  ( $2\chi$ ), the axis-errors  $n_y, n_z$  ( $v_x, v_z$ ) and decoherence  $d_x$  ( $d_y$ ) of the  $\pi/2_x$ -gate ( $\pi/2_y$ -gate). Parametrization defined in the text and in supplementary Refs. 90 and 137. Here, the amplification sequences used for GAMBIT are shown.

## Insensitivity to measurement errors

In this section we discuss GAMBIT's insensitivity to SPAM errors. As pointed out in Sec. 8.6.4, all adiabatic state preparation errors can be mapped to the adiabatic measurement. Thus, we can focus solely on measurement errors in this section. Furthermore, we have discussed in Sec. 8.6.4 that the state preparation axis and measurement axis align in our system. Since GAMBIT works with only one readout axis and does not require precalibrated gates, the relevant readout errors can be captured by a reduction in contrast  $\delta_c$  ( $0 \le \delta_c \le 1$ ) and a shift  $\delta_s$  ( $-1 \le \delta_s \le 1$ ) of the measurement results.

These parameters capture that measuring the error syndrome  $S_i$  will generally not result in the correct voltage  $U_i$  but instead yield  $U_i' = \delta_c(U_i + \delta_s)$ . Note that some further constraints on  $\delta_c$  and  $\delta_s$  are needed to ensure that the measurement stays physical. As described in Sec. 8.6.5, GAMBIT optimizes

$$\tilde{S}_i = |c(\delta_c U_i + \delta_c \delta_s + s) - c(\delta_c U_M + \delta_c \delta_s + s)|$$
(8.13)

$$= |c\delta_c(U_i - U_{\mathbf{M}})| \tag{8.14}$$

so that shifts  $\delta_s$  are of no consequence.

Changes in the measurement contrast  $\delta_c$  will lead to slower convergence as discussed in Sec. 8.6.6. However, the feedback loop should still converge to the same target as  $|c\delta_c(U_i-U_{\rm M})|$  is always zero for a perfect gate set, irrespective of  $\delta_c$ . As pointed out in Sec. 8.6.5, histograms of the measured voltages can be used to determine c so that  $c\delta_c$  is approximately constant. Hence, GAMBIT can be made insensitive to fluctuations  $\delta_c$  as long as  $c\delta_c$  does not change significantly between GAMBIT iterations.

# Feedback loop

Before the feedback loop is started, we perform a scaling analysis to compensate shifts in  $J(\varepsilon)$ . To this end, we independently scale the  $\varepsilon$  pulses of both gates. Specifically, we scale the amplitude minus the baseline,  $\varepsilon_j^g - \varepsilon_{\min}$ , by  $\pm 20\%$  in increments of 4% and measure all 8 error syndromes for each scale factor. We start the iteration with the best scale factor chosen separately for each gate.

For the iterative control loop we use the Levenberg-Marquardt Algorithm (LMA), which requires derivatives of the objective function to compute an update. Throughout this work, the LMA iteratively solves the problem

$$\min_{\boldsymbol{\varepsilon}_{j}^{g}} \left| \left( \tilde{\mathbf{S}}_{1-6}(\boldsymbol{\varepsilon}_{j}^{g}), \quad w_{7}\tilde{S}_{7}(\boldsymbol{\varepsilon}_{j}^{g}), \quad w_{8}\tilde{S}_{8}(\boldsymbol{\varepsilon}_{j}^{g}) \right) \right|^{2}, \tag{8.15}$$

where  $\tilde{\mathbf{S}}_{1-6}$  is a six-component row vector consisting of the first six error syndromes  $\tilde{S}_i, i=1...6$  (see Tab. 8.1 and Sec. 8.6.5). This minimization problem is a slightly modified version of Eq. (2) from Ref. 90. The weights  $w_7$  and  $w_8$  should be chosen such that the vector components do not differ by orders of magnitude. Here, they were chosen heuristically as 0.5 so that the last two vector components are approximately proportional to the decoherence of a single gate ( $\tilde{S}_7$  and  $\tilde{S}_8$  are obtained by applying  $\pi/2_x$  and  $\pi/2_y$  twice, respectively).

We use the LMA because we found in simulations that derivative free methods such as the Nelder-Mead algorithm (NMA) typically take at least an order of magnitude more iterations than the LMA to converge well. This of course only holds true as long as derivatives can be reliably measured. Minimizing the number of iterations is important as pulse updates on our arbitrary waveform generator (AWG) and reference measurements take about 2 min during which we cannot acquire new data. On the other hand we can perform on the order of 10<sup>5</sup> measurements per second once pulses have been uploaded to the AWG. Consequently, we would like to minimize the number of iterations rather than the number of measurements.

We estimate the derivatives required for the LMA from measurement data using forward finite differences with a fixed step size. It is important to choose a finite difference step size which is large enough so that the numerical derivatives are not dominated by

measurement noise. However, the estimation error becomes larger for large step sizes. The optimum step size depends on the curvature and magnitude of the objective function. Since curvature and magnitude depend on the point in parameter space and are not generally known, we simulate GAMBIT, and find a step size  $h = 0.2\varepsilon_0...0.3\varepsilon_0$  to be optimal for a noise level of  $1 \times 10^{-2}$  of the measured singlet probability  $p(|0\rangle)$ . These values also work well in our experimental setup.

Overall, one iteration takes about 10 min. This includes the time needed for measuring the finite differences, pulse updates on the AWG and post-processing of the data on a standard desktop computer.

## Convergence

Not considering large charge rearrangements, the speed of convergence is similar to what we expect from simulations [90], where SPAM errors were completely disregarded. As mentioned in Sec. 8.6.6, GAMBIT should be insensitive to slow shifts of the readout voltages. But slow changes in the measurement contrast  $\delta_c$  will affect  $\tilde{S}_i = |c\delta_c(U_i - U_{\rm M})|$  if not compensated by a different choice of c so that  $c\delta_c$  remains approximately constant. If this is the case, derivatives  $d\tilde{S}_i/d\epsilon_j^g$  cannot be reliably measured and suboptimal updates of the pulse parameters  $\epsilon_j^g$  will be performed. Since the speed of convergence is similar to the simulations, choosing c from histogram fits seems to work well.

As in the simulations<sup>[90]</sup>, convergence stops when the noise floor has been reached. For our experiments, we measured enough data points for each different gate sequence so that a noise level of approximately  $10^{-2}$  of  $\langle \sigma_z \rangle = 2p(|0\rangle) - 1$  is obtained. With this noise level we find that convergence typically stops when the signals  $\tilde{S}_i$  are on the order of  $10^{-1}$ . However, the simulations converge to lower syndromes  $\tilde{S}_i \approx 3 \times 10^{-2}$  for the same noise level<sup>[90]</sup>. This discrepancy could arise from specific forms of gate related decoherence which affects  $\tilde{S}_i$ . Additionally, charge drifts in our noisy sample could lead to changes in the detuning  $\varepsilon$  (which is equivalent to a change in  $J_0$ ) and hence slowly shift the target during the optimization.

Furthermore, relatively frequent charge rearrangements complicate matters. These typically lead to large changes in  $J(\varepsilon)$  and dramatically affect which pulse parameters  $\varepsilon_j^g$  are optimal. If charge rearrangements occur within an optimization run, we proceed as follows: Initially, we wait for the dot to return to the previous configuration and discard the data recorded in the wrong dot configuration. While there seem to be less than 10 different dot configurations which can be explained by several nearby charge traps, it can take a long time (up to days) for the dot to return. Thus, we manually tune the dot back to a working configuration if the original configuration has not been restored after a short while ( $\sim$  hours). As gate performance is very sensitive to the exact functional form of  $J(\varepsilon)$ , manual tuning of the dot typically leads to a deterioration of gate fidelity. Depending on the amount of tuning required, we can either continue with

the optimization (see for example Fig. 8.2e) or need to start from the beginning.

# 8.6.7. Gate benchmarks

## **Self-consistent state tomography**

Following Ref. 29, we calibrate the self-consistent state tomography using five FID experiments for five different initial states with the exchange interaction switched off  $(\varepsilon = \varepsilon_{min})$ . For each free evolution, multiple points are read out along six different measurement axes. This overcomplete set allows us to determine the five initial states and six measurement operators from a self-consistent fit. Following the argument in Sec. 8.6.4, we assume for the fit that the axes of adiabatic state preparation and measurement align, and that all initialization errors can be mapped to the measurement.

Any unknown state is consequently read out using the six measurement operators known from the calibration. Since this again results in overcomplete information as only three linearly independent measurement operators would be needed, the unknown state is determined as the best fit (in the least-squares sense) to the overcomplete information. The states for different evolution times of FID experiments reconstructed in this way are shown in Fig. 8.7, showing good agreement with the expected trajectories.

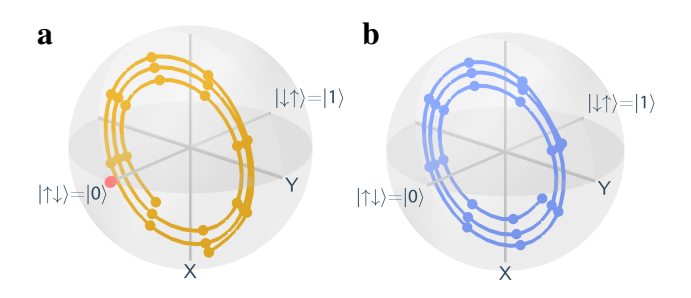


**Figure 8.7.: Self-consistent state tomography.** FID experiments at J=0. The states indicated by dots are reconstructed from an overcomplete set of information, using six different measurements. **a** The state  $|0\rangle$  shown by the red dots is an eigenstate and does not evolve. This is different for the initial state of the other FID experiment and the state shown in blue in panel **b**.

The gate trajectories in Fig. 8.2d are obtained in the same way. The gate operation is stopped in increments of 1 ns and the resulting final state read out. There is a small caveat however. The state tomography was calibrated for readout pulses which start at  $\varepsilon = \varepsilon_{min}$ . While the gate operation returns to  $\varepsilon_{min}$  in the end, intermediate points may be at  $\varepsilon > \varepsilon_{min}$ . Due to finite bandwidth effects, the measurement operator will then vary with  $\varepsilon$  and might be different than in the calibration. Thus, readout is only reliable if the previous operation has already reached  $\varepsilon_{min}$  before the state is read out (including

finite rise times). Such concatenation errors contribute to the deviations between the trajectories shown in Fig. 8.2c and Fig. 8.2d when the exchange interaction is switched on.

# Randomized benchmarking and leakage

For randomized benchmarking (RB), we compose Clifford operations from the primitive gate set according to Tab. 8.4, resulting in an average of 3.75 primitive gates per Clifford. This procedure is commonly used in other works which use RB for gate characterization, e.g. by Ref. 142. In addition to the benchmarking experiments mentioned in the main text, we also apply standard randomized benchmarking (RB) without taking leakage into account.

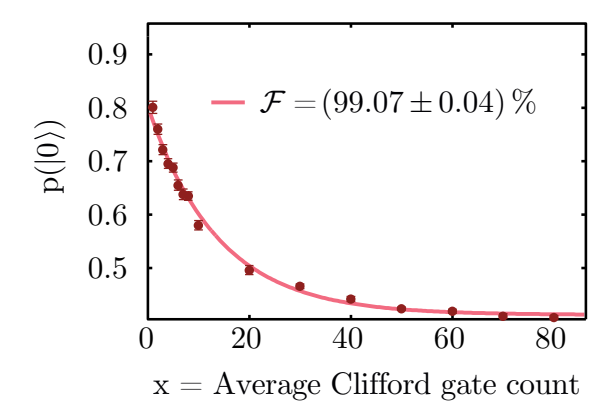


**Figure 8.8.: Standard randomized benchmarking.** The data points shown in dark red are the same as in Fig. 8.3a. The light red curve shows a standard randomized benchmarking fit which yields a gate fidelity of 99.07(4) %. When leakage is taken into account, a lower gate fidelity of 98.5(1) % is extracted (see Fig. 8.3a).

Fig. 8.8 shows a fit applied to the data shown in red in Fig. 8.3a, yielding a gate fidelity of 99.07(4) %. The standard fit model<sup>[27]</sup> with x denoting the number of applied Clifford gates (without the inversion gate)

$$p_{\text{RB}}(|0\rangle)(x) = A \cdot (1 - 2r)^x + B$$
 (8.16)

yields the fit coefficients shown in the first column of Tab. 8.5.

Since this fit model does not explain why the signal decays below  $p(|0\rangle) = 0.5$ , we combine it with a recently developed modified leakage randomized benchmarking (LRB) protocol<sup>[126]</sup> which omits the last Clifford gate from each RB sequence, resulting in the data shown in blue in Fig. 8.3a. We then simultaneously fit the equations

$$p_{\text{RB}}(|0\rangle)(x) = A \cdot (1 - 2r)^x + B \cdot (1 - l)^x + C$$
 (8.17)

$$p_{\text{LRB}}(|0\rangle)(x) = D \cdot (1-l)^{x-1} + E$$
 (8.18)

to the red and blue data set, respectively. This yields the fit coefficients shown in the second column of Tab. 8.5 from which the average fidelity  $(98.5\pm0.1)$ % and leakage rate  $(0.4\pm0.1)$ % for the primitive gate set from Fig. 8.3a are extracted. The leakage rate l reported here is the sum  $l = l^{c \to l} + l^{l \to c}$ , where  $l^{c \to l}$  denotes leakage out of the computational subspace into the leakage subspace and  $l^{l \to c}$  leakage from the leakage subspace to the computational subspace [126]. While the origin of leakage is not absolutely clear, we conjecture that leakage occurs into  $|T_+\rangle$  since our gate pulses get closer to the S-T<sub>+</sub> transition than assumed in previous simulations [90]. The presence of a single leakage level is supported by the fact that  $p(|0\rangle)$  roughly approaches 1/3 (C = 0.3557). Since  $p(|0\rangle)$  corresponds to a singlet probability  $p(|S\rangle)$  due to the adia-

Primitive gates				C	liffo	rd gates
	$(\pi/2_{y})^{4}$					(1)
	$(\pi/2_x)^2$					$(\pi_x)$
	$(\pi/2_{y})^{2}$					$(\pi_y)$
$(\pi/2_x)^2$ o	$(\pi/2_{y})^{2}$					$(\pi_z)$
$(\pi/2_y)$ $\circ$	$(\pi/2_x)$			$(\pi/2_y)$	0	$(\pi/2_x)$
$(\pi/2_y)^3$ o	$(\pi/2_x)$			$(\pi/2_{\bar{y}})$	0	$(\pi/2_x)$
$(\pi/2_y)$ $\circ$	$(\pi/2_x)^3$			$(\pi/2_y)$	0	$(\pi/2_{\bar{x}})$
$(\pi/2_y)^3$ o	$(\pi/2_x)^3$			$(\pi/2_{\bar{y}})$	0	$(\pi/2_{\bar{x}})$
$(\pi/2_x)$ $\circ$	$(\pi/2_y)$			$(\pi/2_x)$	0	$(\pi/2_y)$
$(\pi/2_x)^3$ o	$(\pi/2_y)$			$(\pi/2_{\bar{x}})$	0	$(\pi/2_y)$
$(\pi/2_x)$ o	$(\pi/2_y)^3$			$(\pi/2_{\bar{y}})$	0	$(\pi/2_x)$
$(\pi/2_x)^3$ o	$(\pi/2_y)^3$			$(\pi/2_{\bar{x}})$	0	$(\pi/2_{\bar{y}})$
	$(\pi/2_x)$					$(\pi/2_x)$
	$(\pi/2_x)^3$					$(\pi/2_{\bar{x}})$
	$(\pi/2_y)$					$(\pi/2_y)$
	$(\pi/2_y)^3$					$(\pi/2_{\bar{y}})$
$(\pi/2_x)^3 \circ (\pi/2_y)^3 \circ$	$(\pi/2_x)$					$(\pi/2_z)$
$(\pi/2_x)$ $\circ$ $(\pi/2_y)^3$ $\circ$	$(\pi/2_x)^3$					$(\pi/2_{\bar{z}})$
$(\pi/2_y)$ $\circ$	$(\pi/2_x)^2$			$(\pi/2_y)$	0	$(\pi_x)$
$(\pi/2_y)^3$ o	$(\pi/2_x)^2$			$(\pi/2_{\bar{y}})$	0	$(\pi_x)$
$(\pi/2_x)$ o	$(\pi/2_{y})^{2}$			$(\pi/2_x)$	0	$(\pi_y)$
$(\pi/2_x)^3$ o	$(\pi/2_y)^2$			$(\pi/2_{\bar{x}})$	0	$(\pi_y)$
$(\pi/2_x)$ $\circ$ $(\pi/2_y)$ $\circ$	$(\pi/2_x)$	$(\pi/2_x)$	0	$(\pi/2_y)$	0	$(\pi/2_x)$
$(\pi/2_x)$ $\circ$ $(\pi/2_y)^3$ $\circ$	$(\pi/2_x)$	$(\pi/2_x)$	0	$(\pi/2_{\bar{y}})$	0	$(\pi/2_x)$

**Table 8.4.: Clifford operations**. Sequences of primitive gates used to perform Clifford operations.

	Eq. (8.16)	Eq. (8.17-8.18)
l		$0.0154 \pm 0.0045$
r	$0.0349 \pm 0.0015$	$0.0559 \pm 0.0052$
$\boldsymbol{A}$	$0.3902 \pm 0.0065$	$0.2983 \pm 0.0182$
B	$0.4125 \pm 0.0023$	$0.1634 \pm 0.0179$
C		$0.3557 \pm 0.0199$
D		$0.1408 \pm 0.0169$
E		$0.3553 \pm 0.0208$
$\chi^2/dof$	2.2	0.9
${\mathcal F}$	$0.9907 \pm 0.0004$	$0.9851 \pm 0.0014$
L		$0.0041 \pm 0.0012$

**Table 8.5.: Randomized benchmarking fits.** Fit coefficients (with statistical errors) of different models fitted to our randomized benchmarking experiments.

batic readout (see Sec. 8.6.4), the asymptote is consistent with  $|S\rangle$ ,  $|T_0\rangle$  and  $|T_+\rangle$  being occupied with the same probability when  $x \to \infty$ . While C is sensitive to SPAM errors, it clearly deviates from 0.5. Thus, leakage represents the most plausible explanation for the observed second decay rate, irrespective of SPAM errors.

In addition to leakage, another caveat in RB are gate-dependent errors which are likely to be present here since the Clifford operations are generated from a limited primitive gate set. If we add a term for gate-dependent errors of the form  $F(x-1)(1-2r)^{x-2}$  in Eq.  $(8.17)^{[27,143]}$ , the other fit coefficients change only slightly while F turns out to be insignificantly different from zero. However, the errors on r, A and F are rather large (on the order of 10). This indicates that the fit cannot distinguish between the added term and  $A \cdot (1-2r)^x$ . The fit is therefore not conclusive. However, numerical simulations suggest that even in the case of gate-dependent errors or 1/f-noise, benchmarking provides a "better than a factor-of-2 estimate of the average error rate" (p.11 of Ref. 125). Thus, gate-dependent errors should not significantly influence our fidelity estimate.

Similar to RB, the derivation of the fit model for the leakage protocol assumes gate-independent noise. However, numerical simulations suggest that the protocol is robust even if gate-dependent noise is present<sup>[126]</sup>. Furthermore, the gate operations are required to form a unitary 1-design on the leakage space together with random  $\pm$  phases between leakage and code level<sup>[126]</sup>. Since we do not have control over the leakage space and cannot read it out separately, this is hard to check for our nontrivial gate operations.

While we cannot check whether all formal prerequisites of the leakage protocol are satisfied, the exponential model fits the data well in the limit of long gate sequences so that the extracted rate itself is reliable. Furthermore, decoherence in the code space is

nearly complete for gate counts greater than 200 so that leakage is the only physical process driving the slow decay. Since the omitted correction gate corresponds on average to an intentional inversion and only leaked states would not be driven to  $p(|0\rangle) = 0.5$ , it seems plausible that this rate is proportional to the actual leakage rate. We conclude that the fitted rate should therefore give a good indication of the actual leakage rate.

### **Error amplification**

To separate systematic errors from decoherence, we measure repetitions of  $\pi/2_x$ ,  $\pi/2_y$  and  $\pi/2_x \circ \pi/2_y$ . These sequences amplify over-rotation and axis errors, and typically result in data as shown in Fig. 8.3b. We fit this data using the parameters of two unitary operations given by rotation axis times rotation angle  $\theta \cdot \vec{n}$ , the probabilities  $p_{\text{depol}}$  of an added depolarizing channel, and separate leakage rates  $\mathcal{L}$  for each of the two gates. We do not model the whole leakage space, but rather include leakage phenomenologically by subtracting a fraction  $p(|0\rangle) \rightarrow (1-\mathcal{L})p(|0\rangle)$  with each applied gate since we are more interested in systematic effects rather than extracting a meaningful leakage rate. Thus, this approach should be sufficient to capture most of the effect of leakage, which will be small in the limit of short gate sequences anyway. All fit parameters are given in Tab. 8.6. The systematic fidelity  $\mathcal{F}_{\text{sys}}$  is calculated by removing the depolarizing channel and leakage from the gates so that only systematic errors remain.

Since our simplified decoherence model does not explain the observed behavior for a gate count larger than 12, and we are mainly interested in systematic errors, only the first 12 data points are fitted (solid light blue line in Fig. 8.3b). Fitting only data points not severely affected by decoherence should allow for a more reliable determination of the systematic errors because specific forms of decoherence can produce a behavior similar to systematic errors in these experiments. We are able to fit several periods of the oscillatory signal in the upper two panels of Fig. 8.3b and thus expect that the extracted rotation angles are accurate. Since the first 12 data points in the lower panel correspond only to about 1.5 periods, the extracted axes should be less accurate than the rotation angles.

The fit yields over-rotation errors of  $1.5^{\circ}$  and  $-3.5^{\circ}$  and an angle between both rotation axes of  $85.4^{\circ}$ . The non-amplifyable angles with the z-axis are determined to be  $98.4^{\circ}$  and  $83.9^{\circ}$ . Overall, these deviations correspond to  $\mathcal{F}_{\rm sys} = 99.3\,\%$ , excluding decoherence. As RB yields  $\mathcal{F} = (98.1 \pm 0.2)\,\%$  for this gate set, we conclude that decoherence and systematic errors contribute roughly equally. It is noticeable that while the leakage rate matches the one extracted in Fig. 8.3a for different gates,  $\mathcal{F}$  differs from the RB result by about 2 percentage points. This is likely due to the simplified decoherence model, as otherwise the data points at higher gate counts would also be fitted well. In reality, decoherence can not be explained by a simple depolarizing channel due to the significant amounts of slow noise present. While Markovian depolarization would produce exponential  $(T_2$ -like) decay laws, non-Markovian errors will lead to a

	$\pi/2_x$	$\pi/2_y$
$\theta \cdot n_{x}$	1.5359	0.1461
$\theta \cdot n_y$	0	1.4934
$\theta \cdot n_z$	-0.2281	0.1614
$p_{\rm depol}$	0.0624	0.0647
$\mathcal{L}$	0.0051	0.0021
$\mathcal{F}_{ ext{sys}}$	0.9928	0.9926
$\mathcal{F}$	0.9620	0.9608

**Table 8.6.: Systematic errors**. Fit parameters of the fit in Fig. 8.3b which is used primarily to extract systematic errors of the gate set.

quadratic ( $T_2^*$ -like) decay arising from constructive interference or repeated errors. In the non-Markovian case, the infidelity corresponds to the initial decay so that fitting a Markovian model, as we do here, would overestimate the infidelity.

# 9. Dynamical nuclear polarization by hyperfine mediated electric dipole spin resonance

#### 9.1. Introduction

We experimentally investigate the potential of a feedback mechanism that relies on electric dipole spin resonance (EDSR) for narrowing nuclear Overhauser fields and its effectiveness for extending qubit coherence time. Compared to the previously developed feedback mechanism<sup>[13]</sup> used in experiments throughout this thesis (cf. Ch. 5), this polarization scheme promises higher and more stable pump rates (as it does not rely on time-consuming adiabatic Landau-Zener sweeps across the ST<sub>+</sub>-transition) and the ability to set local magnetic fields in each half of a double quantum dot instead of stabilizing only a gradient between dots.

The functionality of this scheme is discussed theoretically in great detail in Ref. 139 and relies on the application of two AC-electrical fields, slightly detuned from the desired Larmor frequencies of the electrons in each individual dot. To set and stabilize for example the Overhauser-field of the left electron, we first initialize the qubit in an  $|\uparrow\downarrow\rangle$  state (left spin is pointing up) and apply an electric microwave signals with a frequency  $f_1 = f_0 - \delta f$ , slightly offset from resonance of  $|\uparrow\downarrow\rangle$  and  $|\downarrow\downarrow\rangle$  at the desired hyperfine field. By shaking the electrons relative to the lattice, the AC-electric field is transformed to an AC-magnetic field by a spatial variation of the transverse Overhauser field, providing the perpendicular component to the external magnetic field required for driving EDSR transitions of the left electron from  $|\uparrow\rangle$  to  $|\downarrow\rangle$ . Subsequently, we initialize a  $\downarrow\downarrow\uparrow\rangle$  state and apply a microwave pulse with a frequency offset in the other direction  $f_2 = f_0 + \delta f$ . Starting in a well defined state, spin transfer occurs in opposing direction at different frequencies, with a maximum in the spin transfer function at resonance. The resulting pump curve is schematically depicted in Fig. 9.1a and shows a fixed stable point at the zero-crossing of the combined pump curve. This scheme alone allows to set and stabilize the Overhauser-field of the left dot. Applying the same scheme at a different fixed frequency for the right dot further allows to set and stabilize a gradient between the dots.

With a spin transfer rate of one spin per 100 ns<sup>[144]</sup>, an increase of about two orders

of magnitude, this EDSR based DNP scheme promises to out-perform DNP based on Landau-Zener sweeps across the  $ST_+$ -crossing. The higher pump rate directly translates to a larger feedback effect and thus a better stabilization of the nuclei and resulting coherence time up to a few microseconds <sup>[139]</sup> can be expected (compared to  $T_2^{\star} \approx 150 \, \text{ns}$  using the pulsed DNP scheme).

#### 9.1.1. Experimental setup

The system studied in this chapter is identical to the setup used in Ch. 5-8 with the addition of an RF-source connected to one of the RF-gates via a directional coupler (see Ch. 4.2.2 for further details).

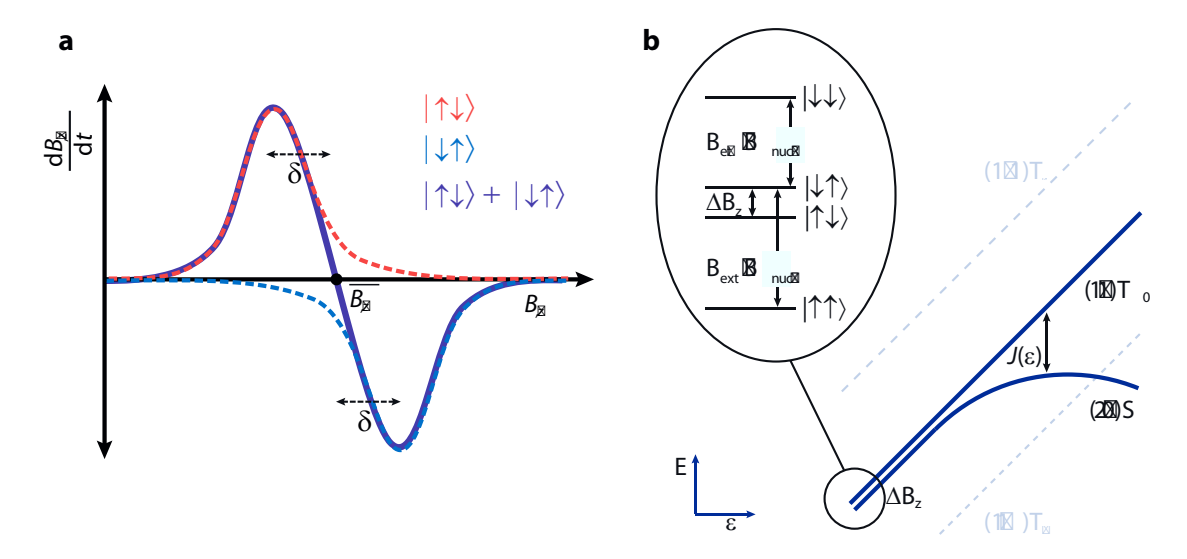
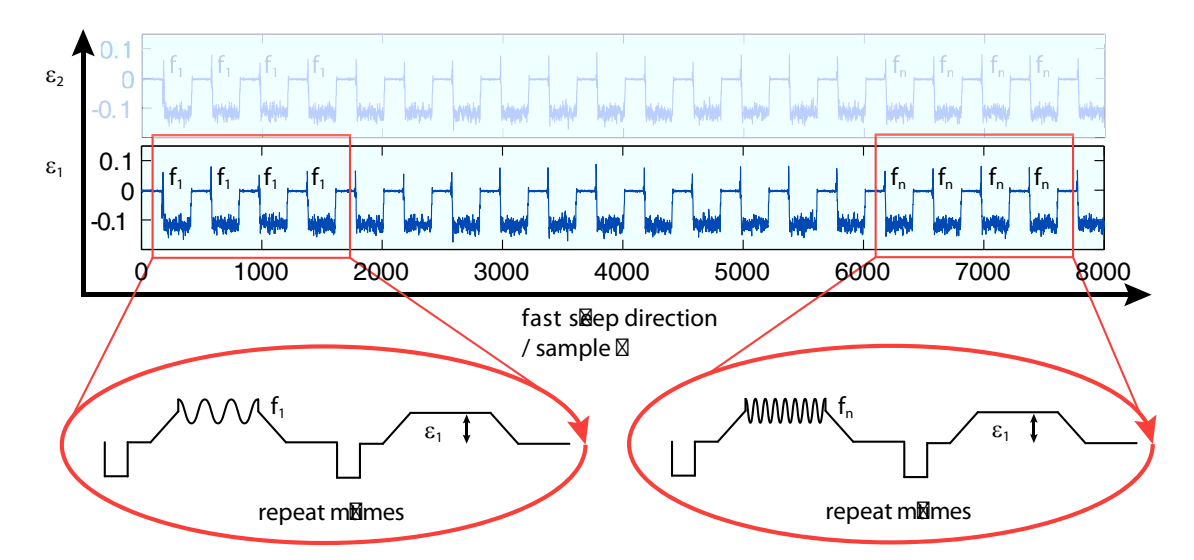


Figure 9.1.: Pump curve and energy diagram for two separated electrons. a Alternating between the two pump pulses  $|\uparrow\downarrow\rangle$  and  $|\downarrow\uparrow\rangle$  with slightly detuned frequencies results in a feedback pump curve (purple) that stabilizes the hyperfine field at  $\overline{B_{L,z}}$  for the left electron. **b** The degeneracy of two tunnel-coupled but well separated electrons is lifted by a magnetic field gradient  $\Delta B_z = (B_{\rm nuc,L} + B_{\rm nuc,R})/2$ . Initialized in the  $|\uparrow\downarrow\rangle$  state, two EDSR transitions to  $T_\pm$  should be visible, depending on which electron is flipped.

#### 9.2. Results

In the following chapters, I will discuss first experiments that locate and identify the two EDSR transitions of the two separated electrons in the two dots. I further discuss experiments that investigate to what extent driving these transitions affects the surrounding nuclear bath and will address open questions.



**Figure 9.2.: Data acquisition.** In order to resolve the EDSR transition of two separated electrons, the data acquisition was slightly changed compared to Ch. 4.6. Limited by the maximum hardware sweep rate of 5 ms/frequency step, we average over 1000 EDSR pulses per frequency with a typical experiment length of  $5 \mu s$ . In each pulse the qubit is first initialized in a S(2,0) state and then adiabatically ramped to a more negative detuning, staying in the ground state  $|\uparrow\downarrow\rangle$ . Once detuned, a  $1.5 \mu s$  long microwave pulse is applied, followed by an adiabatic detuning back into (2,0) for readout. To counteract slow 1/f-noise between different frequency steps, we employ a lock-in technique and alternate between pulses, applying RF-signal and pulses where the RF-burst is switched off. Only measuring the difference between these pulses allows for high quality data acquisition, investigating only the effect of the applied RF-radiation.

#### 9.2.1. Locating the EDSR transitions

In order to locate the two EDSR transitions, we perform electron spin spectroscopy using fast frequency sweeps as a function of the detuning  $\varepsilon$  between the two dot, as depicted in Fig. 9.2. We first initialize the two-electron qubit in the S(2,0) state and adiabatically separate the electrons into the two dots staying in the  $|\uparrow\downarrow\rangle$ -state. Note, we quickly move across the ST<sub>+</sub>-transition to avoid unintentional spin-flips of the electron spin. Once separated, we apply a high frequency burst, typically 1.5  $\mu$ s long, and adiabatically ramp back to the (2,0) charge configuration to measure the singlet return probability  $P_S$ .

Initially an Agilent N5183A RF-source was used to perform the fast frequency sweep. The Agilent RF-source experimentally limits the maximum accurate sweep rate to 5 ms/frequency step. Given that a typical measurement cycle, as described above, lasts  $5 \mu s$ , this allows to average over 1000 measurements per frequency (see Fig. 9.2). In or-

der to counteract slow noise pick up due to the slow repetition rate, we exploit a lock-in measurement technique, only applying the RF-burst to every second pulse sequence and recording the difference between two subsequent measurements.

In a first, coarse overview scan of the spectrum (Fig. 9.3a) two resonances are visible which can be identified as the  $ST_+$  and  $ST_-$  transitions. Note, as the exchange interaction  $J(\varepsilon)$  vanishes for large detuning, these resonances appear at nearly the same frequency and are independent of the detuning  $\varepsilon$ . For this reason, fast frequency sweeps are indispensable to locate these transitions. For two separated electrons (large  $\varepsilon$ ), the energy degeneracy of  $|\uparrow\downarrow\rangle$  and  $|\downarrow\uparrow\rangle$  is lifted by a hyperfine gradient  $\Delta B_z$  that fluctuates with an rms-value of  $\approx 10 \, \text{MHz}$  (see Fig. 9.1b). In order to measure the EDSR resonances, the frequency resolution is increased to 1 MHz in a subsequent measurement, shown in Fig. 9.3b. Indeed, a single resonance becomes visible for detunings above 1.5 mV which shows the characteristic fluctuation of an Overhauser field in GaAs.

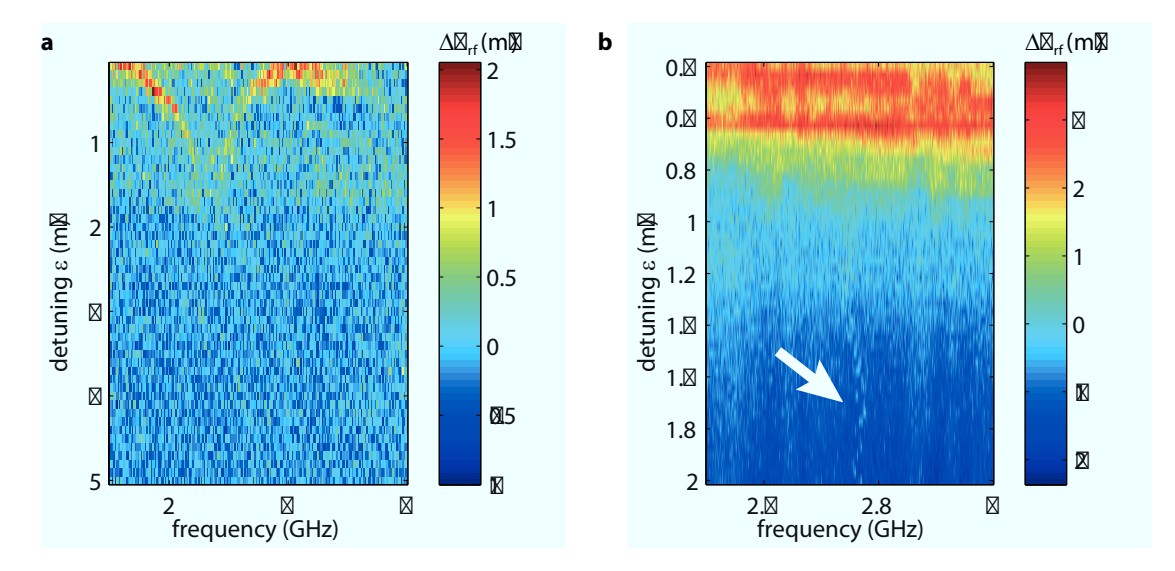
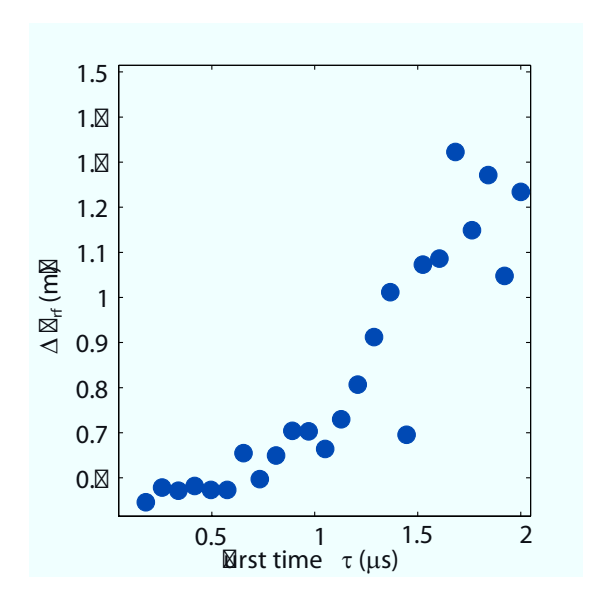


Figure 9.3.: Locating the EDSR transition. a Fast frequency scans as a function of qubit detuning  $\varepsilon$  reveal two transitions  $(1,1)S \rightarrow (1,1)T_{\pm}$ , indicated by a higher triplet return probability (more positive  $V_{rf}$ ). When separating the two electrons, these lines fade until they are no longer visible at high detunings. **b** Increasing RF-power and resolution of the scan ( $\approx$  1 MHz/step) uncovers the hardly-visible transition between  $|\uparrow\downarrow\rangle\rightarrow|\downarrow\downarrow\rangle$ . As the RF-power is applied to the left RF-gate, it is more likely to flip the left electron spin than driving the  $|\uparrow\downarrow\rangle\rightarrow|\uparrow\uparrow\rangle$  transition. The transition frequency fluctuates around the Larmor frequency of 2.7 GHz with an rms-value of approximately 10 MHz, characteristic for spin diffusion of the Overhauser-field.

The output power of the rf-source was set to  $+4 \, dBm$  which translates to an estimated power of  $-45 \, dBm$  at the sample (an voltage of around  $4 \, mV$  peak-to-peak). For higher powers, strange resonances occur, probably associated with crossing the  $ST_+$ -transition

or the inter-dot transition.

For a yet not fully understood reason, the visibility of the EDSR transition of 1.5 mV is rather low compared to the regular singlet-triplet contrast of 6 mV (see for example Figs. 6.7 and 8.6). To ensure that a burst time of 1.5  $\mu$ s is sufficiently long to create a 50:50 mixture of S and  $T_{\pm}$ , we perform a measurement varying the length of the applied RF-burst. Because the EDSR transition is not visible in each scan line, we repeat each burst time five times and only take the maximum contrast into account. From the results, depicted in Fig. 9.4, we find that visibility stalls once 1.5  $\mu$ s long RF-bursts are reached, similar to the findings in Ref.144. Experiments extending the burst times to > 5  $\mu$ s (not shown) do not show higher visibilities.



**Figure 9.4.: Burst time.** The read-out voltage  $V_{rf}$  proportional to the triplet return probability as a function of the time  $\tau$  of the RF-burst. As the visibility of the transition is rather low, each point was taken as the maximum visibility of five scan lines at the same burst length. For burst times longer than the Rabi-period,  $\tau > 1/\Omega_R$ , the triplet probability levels off at 50% when repeatedly probing the Gaussian distributed frequencies  $\Omega_R$ . For a Rabi frequency of  $\Omega_R \approx 1.8\,\text{MHz}^{[144]}$ , burst times  $\tau > 1.5\,\mu\text{s}$  show the highest visibilities.

As already explored in several other works<sup>[144,145,146]</sup>, the width of the EDSR resonance depends on the sweep direction. A comparison between sweeps performed from lower to higher frequencies and vice versa is shown in Fig. 9.5a,b. Sweeps using increasing frequencies reveal a dragging effect of the EDSR resonance towards higher frequencies, while sweeping downwards only shows one sharp resonance. For hyperfine mediated EDSR driving, flipping the electron spin causes a nuclear spin flop which increases the local Overhauser field. Hence, when sweeping from low to high frequen-

cies, the EDSR resonance is locked to the external driving, with a pump rate given by the sweep speed ( $\approx 20\,\text{MHz}$  in our case). Inverting the frequency direction brings the transition out of resonance with the external driving and only a sharp peak is detectable. Performing downward sweeps, a second EDSR transition, corresponding to the second electron in the other dot becomes visible (see Fig. 9.5b). As we only apply the RF-pulses to the left dot, the visibility of the second resonance is even lower and we assume that this transition can only be detected when sweeping in the direction locking the Overhauser field to the external driving (which corresponds to the opposite, non-locking sweep direction for the first resonance in Fig. 9.5b).

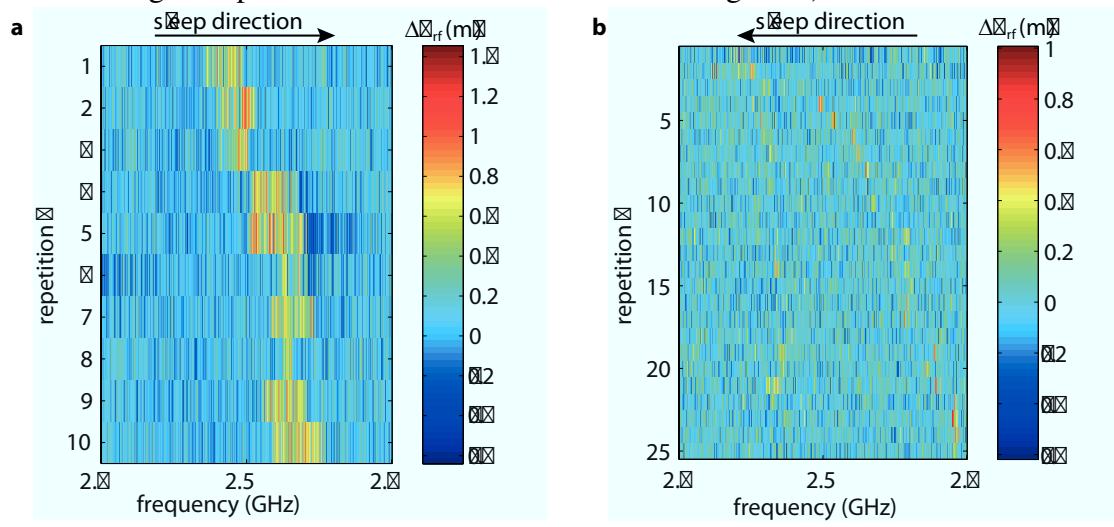


**Figure 9.5.:** Dependence on the sweep direction. a Repeatedly tracking the EDSR transition by sweeping from low to high frequencies reveals a dragging effect. Hitting the resonance condition increases the local nuclear field and hence the nuclear spins get locked to the microwave burst. The maximum pump rate is equivalent to the sweep rate of 20 MHz/s in this case. **b** When reversing the sweep direction, the resonance condition is only fulfilled for a small frequency range and the dragging effect vanishes. When sweeping from high to low frequencies, a second EDSR transition becomes visible (that now shows the aforementioned dragging effect), originating from the second electron in the adjacent dot.

To unambiguously identify the two resonances, we keep track of both transitions by performing downward sweeps while changing  $\Delta B_z$  using pulsed DNP between different scan lines. When changing  $\Delta B_z$ , the distance between the two peaks varies, as can be seen in Fig. 9.6a, indicating that the two peaks indeed represent the two EDSR resonances of the two electrons. Simultaneous recordings of  $\Delta B_z$  by means of free induction decays (see Fig. 9.6b) allow to plot the two EDSR frequencies as a function of  $\Delta B_z$ . The peak position was extracted manually in each scan line and when a broad resonance occurred the lower frequency edge was chosen. Although the extracted peak frequencies  $f_1$  and  $f_2$  scatter a lot,  $f_1$  shows a decreasing trend with increasing  $\Delta B_z$  whereas  $f_2$  is

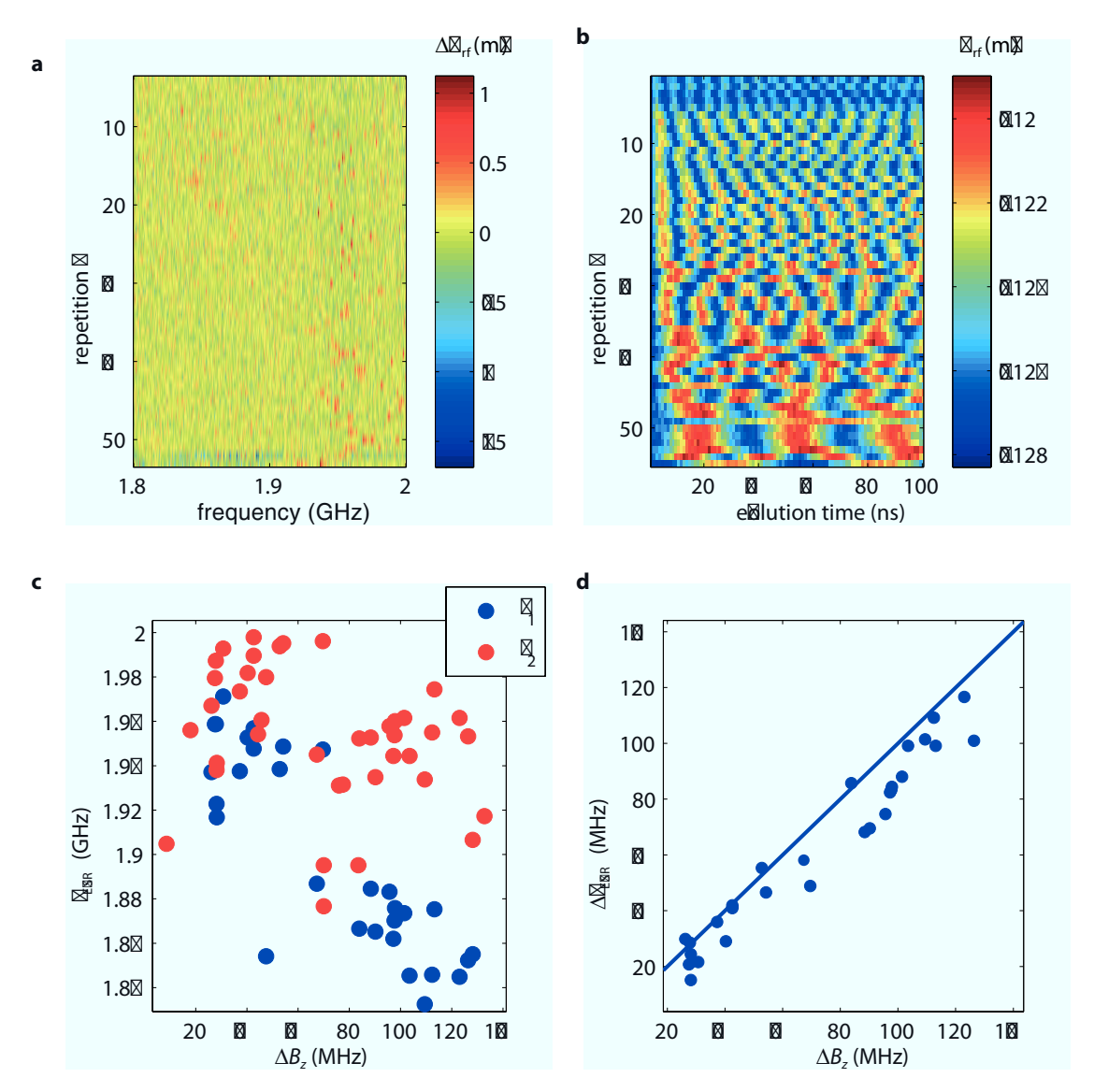


Figure 9.6.: Extracting the hyperfine field gradient  $\Delta B_z$ . a Performing fast frequency sweeps for completely separated electrons, sweeping from high to low frequencies, reveals the EDSR transitions for the left and the right electron. As pulsed DNP is used to vary  $\Delta B_z$  between scan lines, the EDSR resonance frequency varies over time. **b** Interleaving experiments performing free induction decays about  $\Delta B_z$  allows independent and simultaneous measurements of the field gradient. We use regular  $T_+$ -pumping to decrease  $\Delta B_z$  between scanlines. c Manually extracted peak positions for the to EDSR transitions  $f_1$  and  $f_2$  plotted against  $\Delta Bz$  (Only scanlines with two resonances are included). As suspected, DNP based on Landau-Zener sweeps across the ST<sub>+</sub> transition mainly influences the Overhauser field of one dot. **d** We can identify the two resonances with the respective Overhauser field of the left and right dot by plotting the frequency difference  $\Delta f_{\rm EDSR}$  against the independently determined values for  $\Delta B_z$ , which show a strong correlation. Deviations from perfect correlation (solid line) occur by dragging of one of the EDSR transition due to polarizing effects and because both measurements are not performed simultaneously 141 (different scan lines are taken  $\approx 2$  s apart).

mostly constant (see Fig. 9.6c). This effect indicates that polarization predominantly takes place in one dot, as expected for pulsed DNP. Of course, we cannot exclude any polarization effect by the EDSR pulse itself, which also should only polarize one Overhauser field.

Plotting the difference between the two peak positions  $\Delta f_{\rm EDSR} = f_2 - f_1$  as a function of  $\Delta B_z$  reveals a strong correlation between the two values, indicating that the two resonances can indeed be identified as the two EDSR transitions of the two electrons in the double quantum dot.

#### 9.2.2. Pumping the nuclear bath

In order to explore the effect of EDSR driving on the local hyperfine field, we repeatedly track one of the EDSR transitions using downward frequency sweeps and apply additional frequency sweeps between different scan lines in order to polarize the Overhauser field. The initialization state  $(|\uparrow\downarrow\rangle, |\downarrow\uparrow\rangle \text{ or } |\uparrow\uparrow\rangle)$ , frequency range, set point, sweep speed and direction is manually set for each polarizing sweep using a graphical user interface during the actual measurement.

In Fig. 9.7 we perform an experiment alternating between  $|\uparrow\downarrow\rangle$  and  $|\downarrow\uparrow\rangle$  polarizing pulses, shifting the EDSR resonance back and forth inside the measurement window. Starting with  $|\downarrow\uparrow\rangle$  polarization and a downward sweep direction (from higher to lower frequencies) on the first eight scan lines, we notice a decreasing EDSR resonance frequency indicating a lowering of the local Overhauser field. The frequency range of the polarizing sweep was in the order of 50-100 MHz centered around the resonance condition, adjusted manually during the experiment. We then switch to  $|\uparrow\downarrow\rangle$  pumping and an upward sweep direction. Pumping in opposite direction increases the Overhauser field and hence the EDSR resonance frequency. Alternating between the two polarization schemes shows a sawtooth-like pattern, as can be seen in Fig. 9.7a.

In a next step, we combine the two polarizing pulses by first initializing in a  $|\uparrow\downarrow\rangle$  and upwards frequency sweep with a bandwidth of 50 MHz and then immediately polarize in opposite direction by initializing a  $|\downarrow\uparrow\rangle$  and sweeping downwards. The center frequency and the bandwidth of the polarizing frequency sweeps are manually adjusted between different scan lines and aim to stabilize  $\Delta B_z$  at around 2.5 GHz. The result of this experiment is shown in Fig. 9.7b. Indeed, applying the EDSR pump scheme seems to prevent a drifting of the Overhauser field for the whole measurement time and the EDSR resonance can always be found close to the stable point at 2.5 GHz. However, the exact position of the resonance is still subject to a lot of fluctuation, indicating insufficient pump rates of the pump pulses or broad pump sweeps. Especially the effect of the  $|\downarrow\uparrow\rangle$ -pumping is questionable, as its efficiency is rather low and relaxation of polarization would also reduce the Overhauser field. Furthermore, repeating the same experiment, also at different stable points, does not show a high success rate.

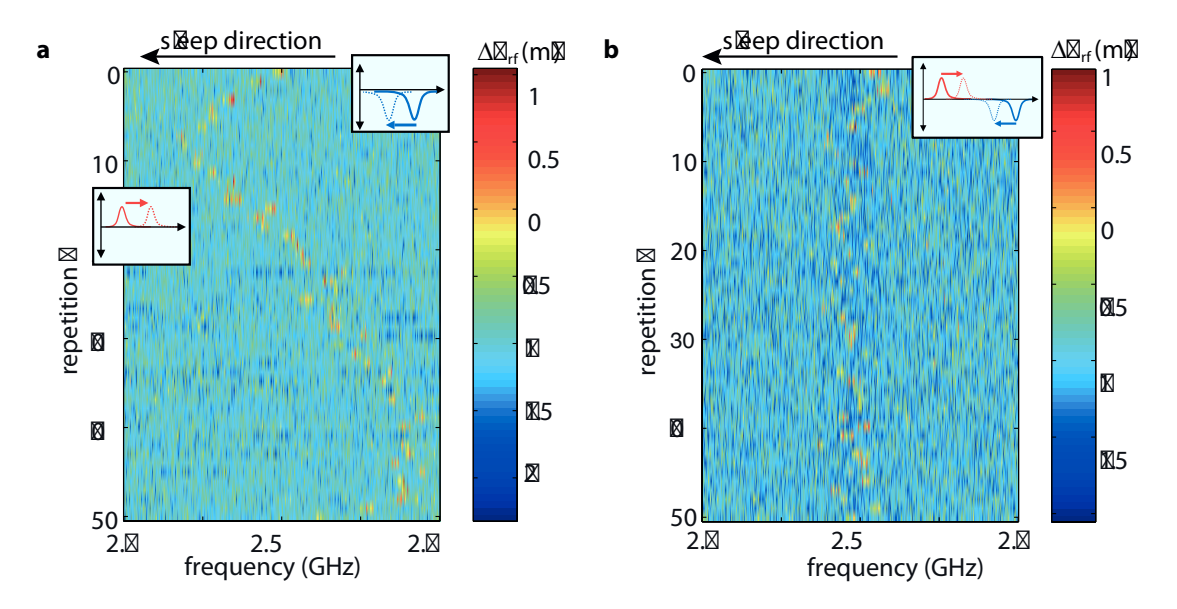


**Figure 9.7.: Pumping the nuclear bath. a** Repeatedly tracking the EDSR transition sweeping from high to low frequencies in order to minimize unintentional pumping. In between scan lines, pump pulses consisting of frequency sweeps across the EDSR transition with manually adjusted bandwidth, are applied to the qubit. In the first couple of scan lines these pulses comprise an  $|\downarrow\uparrow\rangle$  initialization and a upward frequency sweep, intended to lower the local Overhauser field. Indeed the EDSR peak is slowly shifted to lower frequencies. Starting from scan line eight we switch to  $|\uparrow\downarrow\rangle$  pump pulses and reverse the sweep direction. The local Overhauser field is increased and the EDSR peak position shifts to higher frequencies. **b** Applying the EDSR pump scheme between scan lines prevents drifting of the Overhauser field. It still fluctuates and the effectiveness of the pumping, especially the  $|\downarrow\uparrow\rangle$ , is questionable.

#### **B-field dependence**

In the last section we have concluded that low pump rates limit the efficiency of the introduced pumping scheme which relies on hyperfine mediated EDSR. A competing mechanism that is also able to drive EDSR transition, is spin orbit interaction (SOI) which couples the spin of the electron to its momentum. As introduced in Chapter 2.5, the electron then additionally experiences a SOI-field whose direction depend on the direction of electron displacement. In case the SOI-field is perpendicular to the external magnetic field, SOI predominantly drives the EDSR transition. In previous experiments using the "legacy" device layout that included big plunger gates on the sides of the quantum dots, the direction of the electron displacement was obvious and parallel to the dot

<sup>&</sup>lt;sup>1</sup>an additional classical magnetic field

combining axis. By choosing  $B_{\rm ext}$  either parallel or perpendicular to this direction, SOI could be switched on [118] or off [144]. Ref.45 concluded that even a slight misalignment of 5° leads to a quenching of hyperfine mediated DNP. Determining the direction in which the electron moves when applying AC voltage to the RF-gates in the device layout used in this work, is non-trivial, as it depends on the exact location and potential of the electrons, and changes with different dot tunings. As it is not possible to minimize SOI by choosing the direction of  $B_{\rm ext}$  in advance, we conducted an experiment rotating the in-plane external magnetic field in steps of 5 mT about 180°. Although this procedure should reveal the direction of minimal SOI in principle, conducting the experiment was somewhat cumbersome as for each B-field direction the resonance needed to first be located and then the pumping rate had to be extracted manually. Determining the latter was additionally complicated as no standardized extraction method for the rate was yet established.

With no data to show<sup>2</sup>, we want to point out that the following B-field directions showed interesting characteristics and need further investigations. First, at +40° (with +90° pointing perpendicular to the line connecting the two quantum dots) an effect occurs that seems to stabilize  $\Delta B_z$  at 0 mT, also known as the Zamboni-effect. This phenomenon will be further discussed in Ch. 9.2.2. Note that this effect also occurs at different magnetic field directions, but more frequently at +40°. A second interesting B-field direction would be -85° as the EDSR transition here barely showed any movement at all, indicating a very strong SOI. Hence, perpendicular to this direction one might find a vanishing impact of SOI on the EDSR signal.

#### Zamboni effect

An early experiment<sup>[147]</sup> in GaAs double quantum dots found a factor 70 suppression of qubit dephasing when applying the regular S-pumping cycle. This effect was later termed Zamboni-effect in Ref.148 for smoothing the fluctuating Overhauser field similar to a Zamboni ice resurfacer. Even though this effect could be attributed to a visibility loss at high nuclear polarization in a later publication<sup>[86]</sup>, the term Zamboni for stabilizing the fluctuating nuclear hyperfine field was established.

In our case, we sometimes experience a phenomenon that seems to stabilize the hyperfine gradient  $\Delta B_z$  at 0 MHz. In the absence of a gradient,  $|\uparrow\downarrow\rangle$  and  $|\downarrow\uparrow\rangle$  become degenerate resulting in an unpredictable initialization and readout. Hence, whenever  $\Delta B_z$  approaches 0 MHz the lock-in-type measurement outcome of a frequency sweep looks like jitter or noisy zig-zag patterns. This behavior is clearly visible in later scan lines of Fig. 9.8a, but also occasionally visible in other spectra throughout this chapter. When performing a frequency sweep from low to high frequencies, that usually increases the Overhauser field, this behavior sometimes continues through a whole scan

<sup>&</sup>lt;sup>2</sup>This experiment was performed before the two EDSR transitions were identified.

line, indicating a stabilization of  $\Delta B_z$  at 0 mT for the whole measurement time of 2 s. As can be seen in Fig. 9.8, this effect can be triggered by using regular LZ-pumping to adjust  $\Delta B_z \approx 0$  mT. Almost simultaneous recordings of  $\Delta B_z$  by means of FID support the hypotheses of a vanishing gradient. For the first couple of 100 ms, the temporal evolution of the qubit is nearly flat and oscillations only occur at later timescales. The stabilization at zero magnetic field is self-driven and the underlying mechanism is not completely understood yet. We suspect a sign change of the pumping rate once the zero crossing of the field gradient is reached to play an important factor.

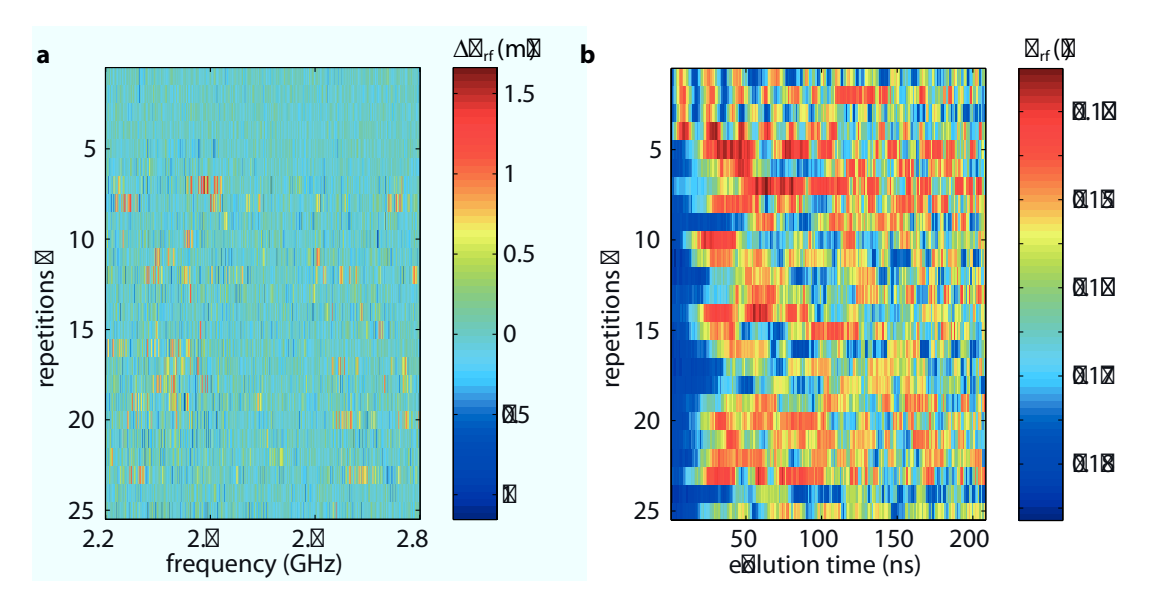


**Figure 9.8.: Zamboni effect.** As  $\Delta B_z$  approaches 0 MHz,  $|\uparrow\downarrow\rangle$  and  $|\downarrow\uparrow\rangle$  become degenerate. Hence,  $|\uparrow\downarrow\rangle$  initialization and readout are undefined and lead to noise-like zig-zag signals as can be seen in scan line 7 and higher.

#### $|\uparrow\uparrow\rangle$ -pumping

Similar to Ref. 144, we investigate the effect of initializing the electrons in the  $|\uparrow\uparrow\rangle$  before applying the EDSR bursts, which in principle should invert the direction of hyperfine polarization. For the following experiment we replace the  $|\uparrow\downarrow\rangle$  initialization from previous polarizing pump pulses (Ch. 9.2.2) with a  $|\uparrow\uparrow\rangle$  initialization, as discussed in more detail in Ch. 5.5.6. We then track the EDSR transition and apply different pump pulses between scan lines to investigate the effect of  $|\uparrow\uparrow\rangle$ -pumping.

The result of a typical experiment is shown in Fig. 9.9. Having located the EDSR transition in the first couple of scan lines, we apply the  $|\uparrow\uparrow\rangle$ -pulse for 1 s around the

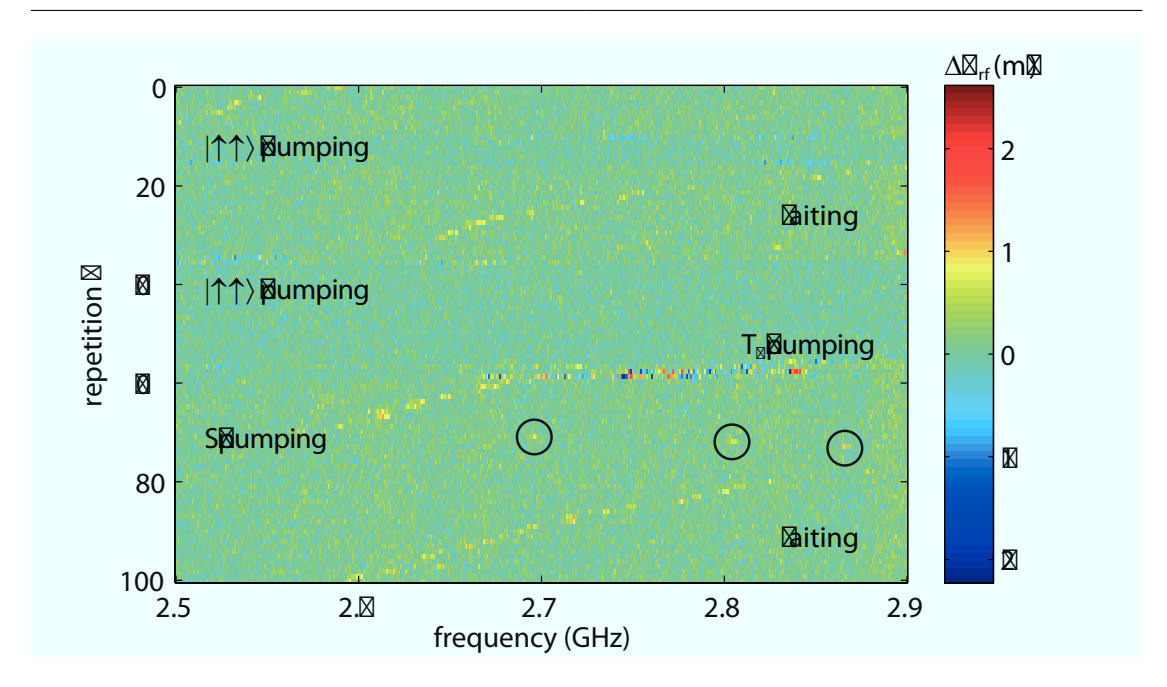


Figure 9.9.: Pumping the nuclear bath II. After locating the EDSR transition in the first couple of scan lines, we apply pump pulses that first initialize a |↑↑⟩ and then apply the EDSR burst. The EDSR peak immediately disappears out of the measurement window and only returns from higher frequencies after waiting for a couple of scan lines, indicating that the pump pulses increase the local Overhauser field. Spumping (around scan line 75) polarizes the Overhauser field in the same direction but it seems to show a smaller pump rate.

resonance condition. The EDSR peak immediately disappears, only to enter the measurement window, coming from higher frequencies, at later scan lines. Repeating this pump pulse at scan line 35 ends in a similar result. Using the regular  $T_+$  pump pulse recovers the EDSR peak inside the measurement window at scan line  $\approx 65$ . Once recovered, applying S-pumping shifts the resonance in the same direction as  $|\uparrow\uparrow\rangle$ -pumping, although the pump rate seems to be lower (see black circles in Fig. 9.9).

From this experiment, one might conclude that  $|\uparrow\uparrow\rangle$ -pumping results in a very strong increase in polarization of the Overhauser field. But this conclusion is inconsistent with the regular Landau-Zener pumping, as  $T_+$ -pumping lowers the local polarization<sup>[13]</sup> (also seen in scan lines 55-70 in Fig. 9.9). Furthermore, the seemingly fast pump rate of the  $|\uparrow\uparrow\rangle$ -pumping contradicts the slower polarization rates of  $|\uparrow\downarrow\rangle$ - or  $|\downarrow\uparrow\rangle$ -pumping from previous chapter at the same *B*-field direction, which were explained in terms of a strong SOI contribution to the EDSR signal. Unfortunately, further investigations were not possible, but it would be very interesting to simultaneously measure  $\Delta B_z$  using regular FID experiments and investigate the influence of  $|\uparrow\uparrow\rangle$ -pumping. As the initialization point for the  $T_+$ -state lies very close to one of the triple points in the charge stabil-

ity diagram (see Fig. 8.5), which are known to cause surprising behavior, measurement artifacts during  $|\uparrow\uparrow\rangle$ -pumping can not be excluded with certainty and require further investigations.

#### 9.2.3. IQ mixer measurements

In order to obtain more direct control of the applied microwave pulses, such as faster sweep speed, more frequency steps and frequency chirping, the setup was equipped with an IQ-mixer. The local oscillator (LO) was supplied by the Agilent N5183A and the I-and Q-frequencies were controlled by a second Tektronik AWG 7082C, with a sampling rate of 8 GHz, as depicted schematically in Fig. 4.2. To suppress any feed-through from LO or undesired sidebands, a calibration of the IQ mixer was performed at a fixed LO frequency of 2.4 GHz<sup>3</sup> using a spectrum analyzer. Whereas adjusting the DC-offset of I and Q allows to minimize LO feed-through, tuning the phase and amplitude of I and Q allows a significant reduction of the unwanted sideband power. After calibration of both frequency sidebands individually, fast frequency sweeps from 1.9 GHz to 2.9 GHz were available, changing the sideband frequency when passing the LO frequency.

As a first test of the IQ mixer setup, experiments reproducing the simple frequency sweeps using only the RF-source were performed<sup>4</sup>. As depicted in Fig. 9.10, repeatedly sweeping the frequency from 2.3 to 2.7 GHz using the same sweep speed as used in previous chapters, locates the EDSR transition(s).

For an unknown reason so far, performing IQ-mixer experiments always showed an increased unintentional hyperfine polarization, such that  $\Delta B_z > 100\,\mathrm{MHz}$  without DNP. This high value complicated locating the EDSR transition and it was only possible using regular DNP to counter the unintentional hyperfine gradient.

#### 9.3. Discussion

Unfortunately, after a two-year cooldown we encountered some complications with the dilution refrigerator and we were forced to warm up the setup before completing all open investigations. For this reason, this chapter is far from being complete and open questions remain, which I will address in this section.

In this chapter we have successfully located the two EDSR transitions of the two electrons in the GaAs double quantum dot. We have identified the EDSR transitions by measuring the difference of the two local Overhauser fields in two separate experiments showing a strong correlation. From investigations of the pump efficiency when driving

<sup>&</sup>lt;sup>3</sup>at a sampling rate of 1 GS/s of the AWG this would yield a bandwidth of 500 MHz, sufficient for useful frequency sweeps

<sup>&</sup>lt;sup>4</sup>Note, when running a Tektronix AWG 7000 and AWG 5014 without the advanced syncing option there is a trigger delay of a couple hundred ns.

# 9. Dynamical nuclear polarization by hyperfine mediated electric dipole spin resonance

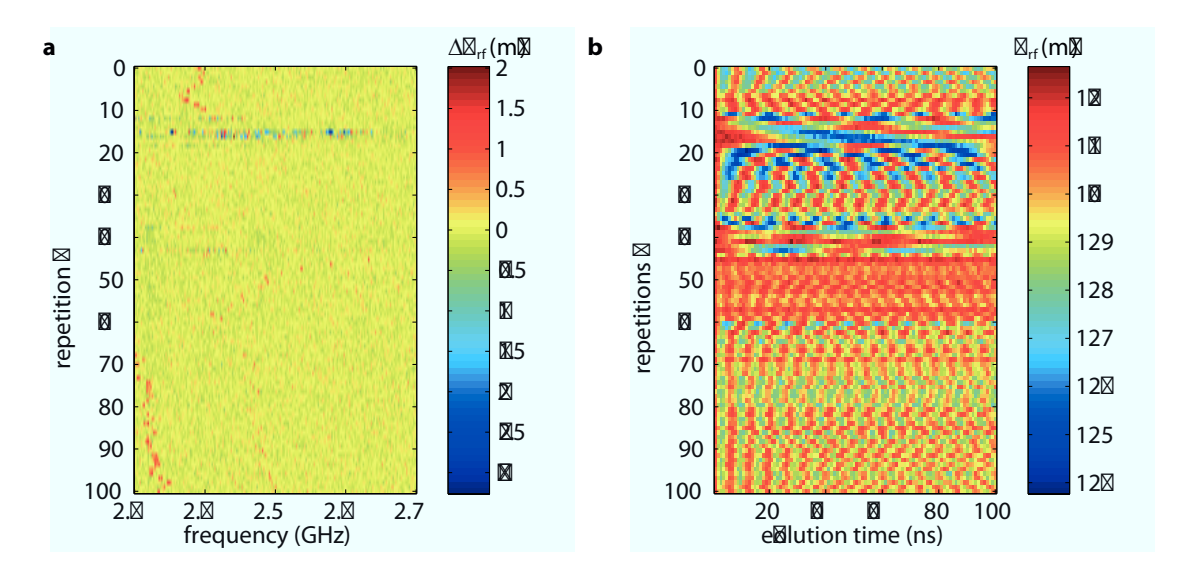


Figure 9.10.: Locating the EDSR transition using an IQ-mixer setup. a,b Fast frequency sweeps using an AWG7082C and an IQ-mixer and simultaneously recorded free induction decays about  $\Delta B_z$ . For an unknown reason,  $\Delta B_z$  was hard to control using regular polarization and always showed a relatively high value of  $\Delta B_z > 100 \, \text{MHz}$  when using the IQ-mixer.

these transitions, we concluded that due to the non-trivial gate structure of our sample design SOI cannot be neglected and presumably quenches hyperfine mediated EDSR and hence limits the pump rates. In principle, SOI can be completely switched off at a particular direction of the external magnetic field. Although a first experiment rotating  $B_{\rm ext}$  was unsuccessful in identifying this direction, the field dependence of pump rates should be investigated further in future experiments. As an alternative to the time-consuming rotation of  $B_{\rm ext}$ , the electrical wiring of the sample has been modified to additionally allow AC-control of the nose and tail gates between the two quantum dots individually (see Appendix A.2). Adjusting the amplitude ratio of the RF-pulses to these gates allows for changing the direction of the electron displacement and thus changing the strength of SOI at a given B-field direction.

# 10. Summary and outlook

In this section I summarize and highlight the experiments performed during my PhD and place them into context of the general experimental progress made towards realizing a semiconductor spin based quantum computer. Furthermore, I will point out interesting new experiments enabled by the findings in this thesis, future challenges and milestones that need to be achieved.

The preceding chapters discussed recent progress made in the field of two-electron spin qubits in GaAs in our group which indicate high qubit performance and show that even in the presence of nuclear spins, GaAs based qubits can still be competitive with spin qubits realized in a nuclear spin free material, such as SiGe. The results and insight gained in this thesis furthermore point to mitigation strategies by changing the sample layout which allows new, interesting experiments.

In Ch. 8 we have experimentally demonstrated a gate operation fidelity of 98.5 %, setting a new benchmark, not only for GaAs based spin qubits but also for encoded spin qubits in general. Naturally, the next step is to increase the fidelity to well exceed the error correction threshold of approximately 99%. We are confident to achieve this goal with a more electrically stable sample and reduced high frequency charge noise, as in comparable state of the art devices from other groups [77]. We currently tune-up a promising device that uses a wider spread modulation doping layer compared to the  $\delta$ -doped sample from previous study. Distributing donors over a wider area might show less influence on the quantum dot than the high dopant density used in the  $\delta$ -doping approach. Reducing charge noise and improving sample stability would directly decrease the qubit gate operation error rate.

So far, apart from our tuning procedure GAMBIT, we have only used randomized benchmarking (RB) to determine the error rate per gate operation, which is known to be insensitive to certain gate errors and might give a false result concerning fidelity measurements. A more rigorous routine to characterize our quantum gates is Gate Set Tomography (GST)<sup>[28]</sup>. In contrast to regular Quantum Process Tomography (QPT), GST self-consistently and correctly accounts for state preparation and measurement errors. We have already started to implement GST on our experimental setup, but so far were not able to extract meaningful data as we ran into problems with our cryogenic refrigerator. Not only can we use GST for a full characterization of our gate set, but we can also use this routine for tuning-up the gate set itself, presuming fitting the data is fast enough compared to the stability of the qubit [149].

Another next step regarding future development of GAMBIT would be to include

more gates in the gate set, like  $\pi_x$  and  $\pi_y$ . For instance, tuning-up high fidelity  $\pi$ -pulses will be very useful for increasing the contrast of refocusing pulses in any decoupling scheme. Furthermore, the tuned-up pulses can be used to perform high fidelity QPT, which will give new insight into the dephasing and decoherence mechanisms when performed on echo-experiments<sup>[150]</sup>, for example.

In terms of how to further improve GAMBIT itself, I think it would be reasonable to also include the voltage resolution of the arbitrary waveform generator when optimizing the pulse segments. Furthermore, one can think of other parametrization of the pulse segments themselves. Looking at the optimal simulation results in Ref. 90, the pulse sequence shows striking similarities with regular Rabi-driving pulses. Hence, instead of optimizing each individual detuning segment, several of them could be combined and only their amplitude, frequency and duty cycle would be optimized.

In Ch. 8 we revealed that electron coherence is ultimately limited by nuclear quadrupolar interaction and an electron g-factor anisotropy by investigating the echo experiment along different B-field directions. Novel insights point to mitigation strategies minimizing quadrupolar broadenings of nuclear Larmor frequencies and the anisotropy in the electric g-factor simultaneously, which is not possible with our current sample design. We propose to use symmetric quantum wells to confine electrons, which are experimentally feasible by tuning a bottom and top gate, as they prevent any anisotropy in the g-factor. Quadrupolar interaction can then be suppressed by choosing the right external B-field direction. By creating larger quantum dots such that the electron wavefunction will overlap with a huge number N of nuclear spins, nuclear fluctuation will follow a  $1/\sqrt{N}$  law and maximum coherence time of the qubit can be achieved. The top and bottom gate can also be used to further investigate quadrupolar interactions as quadrupolar broadenings depend on the electric field at the nuclear sites.

Furthermore, the findings of this experiment helped understanding the decoherence mechanism in closely related qubit systems. As suspected due to increased lattice strain, quadrupolar broadening of the nuclear Larmor frequencies is found to play an important role in self-assembled InGaAs quantum dot as shown in a recent publication [122]. In Ch. 7 we have seen that the theory of an Hahn echo envelope modulation due to a *g*-factor anisotropy can explain the relatively short coherence times in InAs nanowire systems and point to mitigating strategies.

The sharp resonances in the echo decay curve, originating from the linear coupling to the transverse hyperfine field components due to the *g*-factor anisotropy, can also be used for correlation measurements investigating any quantum back-action between the nuclear bath and the qubit<sup>[151]</sup>. This experiment would answer the question if the nuclear Overhauser field can be treated as a purely classical field or whether it requires a full quantum mechanical description.

In the final chapter, I have presented preliminary results of the endeavor to establish a novel polarization scheme for the nuclear bath using hyperfine mediated electric dipole

spin resonance. We have successfully located the two EDSR transitions of the two electrons in the GaAs double quantum dot. From investigations of the pump efficiency when driving these transitions we concluded that due to the non-trivial gate structure of our sample design, spin orbit interaction cannot be neglected and presumably quenches hyperfine mediated EDSR and hence limits the pump rates. As discussed in more detail in this chapter, experimental work is far from being completed. For this reason I have modified the high frequency wiring of the current sample generation to additionally allow RF-control on the two gates separating the electrons. By varying the phase between these two gates one can control the direction of electron displacement, which in turn should make it easier to find the *B*-field direction of suppressed spin-orbit interaction.

Once the EDSR-based polarization scheme is established and indeed shows an enhancement in the dephasing time  $T_2^*$ , it directly translates into higher gate fidelities. Being able to set the Overhauser field of each quantum dot individually and in parallel, this scheme can also stabilize a hyperfine gradient between two adjacent double quantum dots which is a requirement for perform two-qubit operations [152,48].

All work and results presented in this thesis aim to improve and understand the single-qubit performance. But ultimately, the real benchmark will be the two-qubit performance, charge noise and scalability. In order for two-electron spin qubits in GaAs to present a viable option as a qubit platform, all these challenges have to be overcome. From my point of view, the error rate per two-qubit gate operation will be a strict ultimatum. Reaching the threshold for the surface code, which at this time requires the lowest gate fidelity of  $\approx 99\%$  [14], will determine if a certain qubit platform or realization is indeed a serious competitor to provide the building blocks of a quantum processor, despite other advantages it may have.

As of now, there is no systematic study of a two-qubit gate in  $ST_0$ -qubits in GaAs, although entanglement with a fidelity of 72% has been shown experimentally <sup>[12]</sup>. The low fidelity was a result of low capacitive coupling between the two qubits and current effort aims to increase this coupling using either floating gates <sup>[47]</sup> to increase capacitive coupling or use the exchange interaction <sup>[152,48]</sup> for coupling by placing the two dots in closer proximity. But either way, in order to reach high fidelity two-qubit gate operations an automated tune-up procedure, similar to GAMBIT, has to be implemented that optimizes the base-band pulses by extracting gate error syndromes from experimental data.

Electrical charge noise is a general problem in all types of semiconductor spin qubits. In order to minimize it, novel designs of the heterostructure layer are currently under investigation which try to remove the donor atom layer. This effort is encouraged by experiments indicating that this donor layer is the origin of charge noise [20,21]. Furthermore, this approach is motivated by recent experimental success in the silicon community [50] that showed an increase in sample stability by removing this layer. So far, there has only been a few successful realizations of devices on dopant-free GaAs heterostruc-

tures [66,153] as it turns out that providing ohmic contact is non-trivial. Furthermore, it remains to be seen if the additional top gate electrode needed to induce the two-dimensional electron gas hinders the implementation of RF-read-out by providing too much stray capacitance.

Once high gate fidelities are reached and charge noise is under control, the next challenge of scalability awaits which is not yet just an engineering problem. A lot of fundamental questions, such as nearest-neighbor coupling, mid- and long-range coupling, read-out and, let alone, DC- and AC-control, have to be answered and a proof of principle experimental realization has to be shown first. As there currently is a myriad of promising ideas how to pursue each of these goals, I just want to point out a few of them which I find in particular interesting.

For nearest-neighbor and mid-range coupling, structures that shuttle electrons in a linear array or even in a conveyor have been proposed and even experimentally realized. Inspired by the classical charged-coupled device (CCD), these structures transport one individual electron and its spin information from one place to another. So far, individual electron transport has been shown [56], but a coherent shuffle still needs to be realized.

Exploiting the fact that GaAs is a direct semiconductor, optical coupling between electrons and photons can be used to realize long-range coupling. An interesting idea is to tunnel-couple a self-assembled InGaAs quantum dots to a gate-defined ST<sub>0</sub>-qubit which can be initialized and read-out by optical photons<sup>[154]</sup>. By now, a theoretical transfer protocol that uses excitonic states in the mediating self-assembled quantum dot already exist. But it remains to be seen experimentally whether the modified heterostructure including the additional InGaAs layer is suitable to form gate-defined quantum dots.

Currently about eight gate electrodes (including six DC- and two AC-coupled connections) are needed per qubit which all need to be connected to some kind of electrical conductor, ranging from the mixing chamber of the cryostat to the room-temperature electronics. Obviously, this wiring concept will not scale up to a million qubits. Promising ideas for more efficient electrical connections include cooling down the room-temperature electronics to below  $4\,\mathrm{K}^{[155]}$ , using flip-chip-bonding of the actual quantum dot device to an interposer and using multiplexed charge-locking devices [156]. Especially cooling down existing electronics is non-trivial, as dopant freezing out complicates the use of regular CMOS technologies. Furthermore, cooling power of the cryogenic refrigerator sets an upper limit on the allowed power consumption of these devices. Nevertheless, there are a few recent studies that successfully use room-temperature electronics, such as FPGAs, at liquid helium temperatures [157,158] and one can easily imagine specifically engineered devices that work at these temperatures, like voltage supplies and waveform generators.

An often overlooked or ignored problem once the multi-qubit state is reached, is the tuning-up of the devices. By tuning, I do not only mean locating the right gatevoltage space to isolate single electrons, but also the adjustment of the tunnel-couplings to neighboring dots and leads and characterization of the gate-voltage space in order to initialize, manipulate and measure the quantum state of the electrons. Current tuning schemes are semi-automated at best - although there is recent progress in automatically locating the single electron regime<sup>[79]</sup> - state of the art sample quality has so far hindered a fully automated routine. For example, local inhomogeneities in the electron potential lead to non-deterministic dependence of the inter-dot tunnel-coupling on specific gate electrodes. Relying on previous experience, we conclude that a gradient-based algorithm has problems with this occasional non-determinstic behaviour of current sample quality and stability. A machine-learning-algorithm, based on recognizing recurring patterns, would be a promising approach. For a growing number of gate-defined qubits an automatic tuning protocol is going to be a requirement.

With governments and global companies investing millions of dollars (and euros) into the research and development of quantum computing and closely related technologies and with the increased funding in startups and private companies devoted to building such devices it is not a question if but when the first quantum computers will be built. Up to now, completely open questions comprise what type of qubit and what material system renders itself the most promising. For a semiconductor spin qubit approach charge noise and sample stability will have to be reduced significantly in order to reliably and reproducibly confine single electrons. Although a current trend points to nuclear spin free materials such as Si and SiGe, in the end the material which promises lower charge noise may be more advantageous. But nevertheless, electron spin qubits in GaAs always have and are still playing an important role in the ongoing development of semiconductor qubits. And reflecting on the recent progress in suppressing nuclear spin noise and advance in qubit control will continue to do so in the near future. Even if the choice for a suitable qubit platform does not include GaAs based spin qubits, I am very sure that research in this field will yield many more useful control techniques and interesting physics along the way.

# A. Appendix

#### A.1. Double quantum dot fabrication recipe

This recipe was used to fabricate the double quantum dot devices in the cleanroom facility of the 2nd Institute of Physics at the RWTH Aachen as described in Ch. 3.

#### **Preliminary preparation**

- Cut the wafer with photo resist on it (soft baked for 2 min)
- Clean off the resist

#### Mesa

- Clean the wafer with acetone and IPA
- Spin resist AR-U 4040 30 s @ 6000 rpm
- Bake at 100 °C for 2 min
- Exposure for 10 s
- Develop in AR 300-47 for 30 s and then flush in water and blow dry
- Check under the microscope
- Post-bake for 2 min @ 110 °C
- Plasma asher program 5

#### Mesa etching

- Etching solution: Add successively 100 ml water, 3 ml H<sub>2</sub>O<sub>2</sub> (30%), 3 ml H<sub>2</sub>SO<sub>4</sub>
- Etch for a convenient time (etch rate of 2 nm/s once etching solution is cooled to room temperature) and then flush in water and blow dry
- Wash off the resist with acetone and IPA (5 min warm) and measure the height

#### **Ohmic contacts**

- Clean the wafer in acetone and IPA and blow dry
- Just before spinning the resist take out from the IPA and blow dry
- Spin image reversal AR-U 4040 for 30 s at 6000 rpm
- Bake for 2 min @ 90 °C, let cool
- Expose for 15 s
- Bake for 5 min @ 115 °C and let cool
- Flood expose for 45 s
- Develop in negative developer for 25 s and then flush in water and blow dry
- Plasma asher program 5

#### **Ohmic contact evaporation**

- HCl-dip (HCl:H<sub>2</sub>O 1:1) for 20 s, flush in water and blow dry
- Ni 50 Å (0.06 Å/s), Au 2000 Å (0.3 Å/s), Ge 1000 Å (0.25 Å/s), Ni 750 Å (0.2 Å/s)
- Lift-off in warm acetone
- Annealing: ramp to 460 °C as fast as possible and wait for 50 s

#### E-beam gates

- First layer: 639.04 30s @ 6000 rpm
- Bake @180 °C for 5 min
- Second layer: 679.01 30 s @ 6000 rpm
- Bake @180°C for 5 min
- After e-beam writing develop in AR 600-55 for 75 s and flush in IPA
- Standard recipe for evaporation 5 nm Ti, 20 nm Au
- Lift-off in warm acetone

#### **Optical gates**

- Clean the sample with acetone and IPA
- Spin image reversal AR-U-4040 for 30 s @ 6000 rpm
- Bake for 2 min @ 90 °C and let cool
- Expose for 15 s
- Bake for 5 min @ 115 °C
- Flood expose for 46 s
- Develop in negative developer for 25 s and then flush in water and blow dry
- Plasma asher program 5

#### **Optical gates evaporation**

- HCl-dip (HCl:H<sub>2</sub>O 1:1) for 20 s, flush in water and blow dry
- Evaporation: Ti 250 Å (0.1 Å), Au 2000 Å (0.25-0.35 Å/s)
- Lift-off in warm acetone

Note: The use of plasma etching to remove residual optical resist was omitted for later processing as it might damage the substrate and was substituted by a short HCl-dip if needed.

#### A.2. Bonding scheme

Bonding the double dot sample with its 26 connections is not a completely trivial task, as the current sample holder only allows for 24 DC-lines. Hence some of the ohmic contacts, historically used for transport measurements through the dots, are shorted together (leading to some strange pinch-off curves once forgotten). A later wiring scheme, including additional bias-T for the N and T gates, results in an even more complex bonding scheme, including several 'bonds-around-the-edges' and a lot of inappropriate cursing. Tabular A.1 shows a detailed mapping of the bonding pads (shown in Fig A.1) to the associated gates.

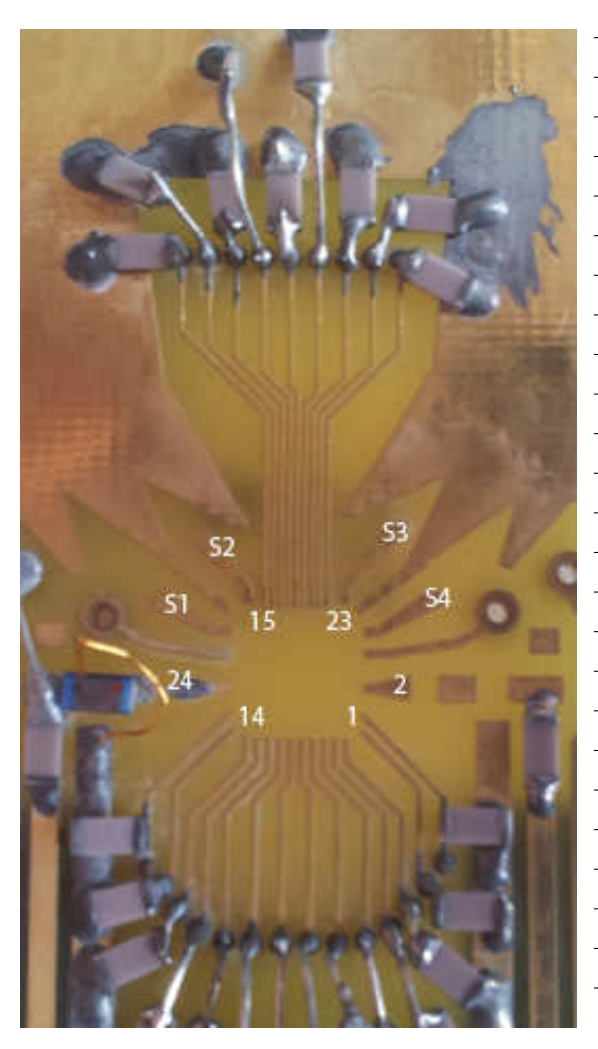


Figure A.1.: Numeration of bonding pads.
Simple numeration of bond pads
on the sample holder PCB from
Harvard University.

Bonding pad	Gate	Gate
	(bias-	(legacy)
	Tee)	
1	SA	SA
2	ORFA2	ORFA2
3	SAB2	SAB2
4	SAP	SAP
5	SAB1	SAB1
6	ORFA1	ORFA1
7	BA	BA
8	NAB	NAB
9	BB	BB
10	SC	SC
11	OA/OC	OA/OC
12	OB/OD	TCD
13	SD	OB/OD
14	SDB1	SD
15	NCD	SDB1
16	SDP	SDP
17	SDB2	SDB2
18	ORFD2	ORFD2
19	BD	BD
20	BC	NCD
21	SB	BC
22	TAB	SB
23	TCD	TAB
24	ORFD1	ORFD1
<b>S</b> 1	RFB/RFD	RFD
S2	NCD	RFC
S3	TCD	RFA
S4	RFA/RFC	RFB

**Table A.1.: Bonding scheme** Mapping of gates and ohmic contacts to bond pads used in this work.

#### A.3. Sample stability

In this section I list all the wafer I tried during my PhD. I was quite lucky that I could use my first sample for nearly two years. It was not a stable or quiet sample in general, as there was a dot jump every couple of hours, but it allowed performing a lot of interesting experiments. Luckily most of the time when a dot jump occurred waiting for the jump back was the solution, indicating the populating and depopulating of a nearby charge trap.

As we encountered some fridge problems and were forced to warm up, we decided to change the sample which is quite a risky decision. As it turns out, the next sample was not suitable for our standards. Although I was able to tune-up a working qubit, the sample itself was unstable and rather noisy. Not only did the number of dot jumps increase, but I could also see that the charge stability diagram during the recording time was unstable depending on certain gate voltage. This behaviour indicates the presence of an ensemble of charge traps, far away from the dot and leaky depletion gates.

The most important properties of the heterostructures used in this thesis are summarized in table A.2.

wafer name	grower	doping layer	bias cooling	dielectric	remark
C120522A	Bougeard	δ-doping	150 mV	no	both slow and fast noise present, but usable (3-5 dot jumps/day)
B14395	Wiek	δ-doping	150 mv	no	both slow and fast noise present, not workable as dot was too jumpy, at certain voltages elec- tric noise could be re- duced but not removed, suspect gate leakage
B14722	Wiek	modulation doping	150 mv	no	stable quantum dot

**Table A.2.:** Wafer table All my noisy samples are listed here. So far the wonder wafer has not been found.

#### A.4. Circuit diagram of roomtemperature filters

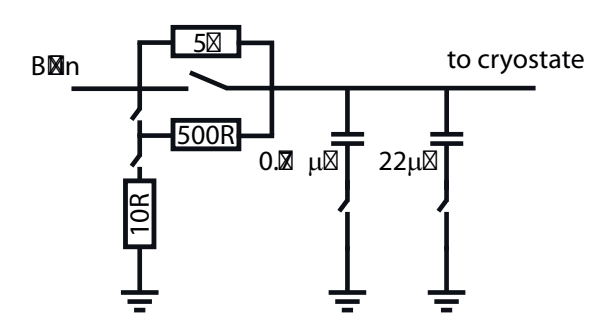


**Figure A.2.: Circuit diagram of roomtemperature filters.** Schematic diagram of the roomtemperature low-pass filters inside the hf-sealed break-out-box. Optionally a 1:11 voltage divider can be used.

#### A.5. Circuit diagram of the cryogenic filter box

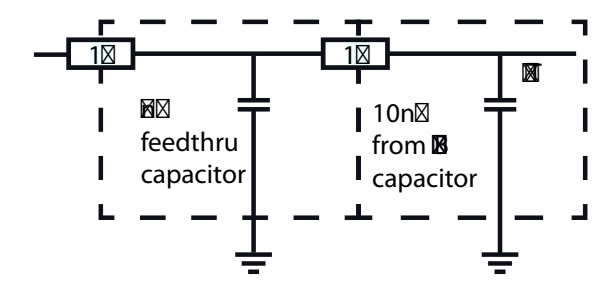


**Figure A.3.: Circuit diagram of the cryogenic filter box.** Schematic diagram of the cryogenic low-pass filters inside a hf-sealed box. Note that the homebuilt feedthru-resistors damps propagation of electrical field between the different stages and thus prevents high frequency resonances of the filter.

#### A.6. Tuning the double quantum dot using tune.m

This document will describe the techniques used to tune our double quantum dot. Although the dots are formed by a lot of electrostatic gates, there are basically only four important values for a working STO qubit:

- The electron number: The dots have to be tuned to either the (2,0)-(1,1) or the (1,1)-(0,2) transition.
- The inter-dot tunnel coupling

• The two tunnel rates to the leads.

Furthermore some other parameters, e.g. the position of the measurement triangle or the position of the ST+ transition, have to be characterized.

#### **Preliminary tasks**

To first define a double quantum take a look at old gate voltages found in one of the logs. Set the voltages accordingly. A wall-wall scan scanGate with SAB1 against SAB2 will tune the readout. The setpoint for the QPC or Sensing Dot (SD) should be located on a very steep coulomb peak. You can also use a 1D scan like scanGateTest for this manner.

Once the readout is working a wall-wall scan with SA against SB will eventually show a double dot characteristic charge stability diagram. I recommend using SA as a stepping channel and sweep SB. Furthermore a QPC compensation should be added allowing larger scan fields in the order of a few ten mV. Shift the center of the scan with smscanpar and follow the leads to find the (2,0)-(1,1) transition. As the honeycombs get wider when reaching smaller the electron numbers, make sure that there are no more transitions by sweeping further negative.

After finding the right transition, center SA and SB around this junction and do a wide charge scan using tune ('chrg wide') using the RF-gates. Rearrange voltages on SA or SB if you do not see the transition. Once the transition is centered in the scan field characterization of the junction can start. As you will probably have to rearrange the voltages on all dot-defining gates it is now useful to switch to virtual gates. The idea behind these virtual gates is that they do not change the dot position while tuning the transitions to the leads and the inter-dot coupling. Any change in SA, TAB, NAB or SB is compensated by BA and BB. Use the virtual gates 'LeadA' and 'LeadB' to tune the tunnelling to the leads and 'T' or 'N' to change the inter-dot coupling. If you have to change the dot position (jumped occured) use 'X' and 'Y' to rearrange the center. To switch to the virtual gates you first have to measure the dot's response to all individual gate changes by using tune ('resp'). Afterwards you have to copy the gradient to tunedata (have a look at virtgates\_startup.m). Now you can use the virtual gates by using the atchg function and start tuning the dot.

#### Tunnel coupling to the leads

For tuning the leads use atch('LeadA') and atch('LeadB'). Be aware that for instance decreasing LeadA still weakly effects the inter-dot coupling. Going in 5-10 mV steps is not a bad idea. To check the tunnel rates to the two leads run tune('lead'). This scan applies square wave pulses to the leads (with a background subtraction) to determine the rates. Aim for fast tunnelrates (bandwidth limit is around 50 ns) for the

A lead and higher ones for the B lead (around 70 ns), as we only need the A lead for reloading. Basically only the A lead needs to be tuned and don't worry too much about the B lead, just make sure it is somehow closed.

#### **Inter-dot tunnel coupling**

Use atch ('T') and atch ('N') to change the inter-dot coupling. Again go in 5-10mV steps. From my experience the N gate behaves counter intuitively. To check the tuning run tune('line') which initiates a line scan at 45 degrees across the junction using RFA and RFB. The lowest value for the inter-dot linewidth was around  $120\,\mu\text{V}$ . As this is temperature limited it gives an estimate of the electron temperatures. For a working dot I recommend values around  $200\,\mu\text{V}$ . With lower tunnel coupling the ST+ is harder to see. But everything between 180 and  $220\,\mu\text{V}$  did work so far. Now that you have tuned the three most important values of the dot and you can continue by characterizing the dot. In order to define a qubit you will first have to find a measurement point to distinguish between singlet and triplet states.

#### Locating the measurement point

In order to locate the measurement point, a point in the charge stability diagram where the T is metastable, run tune ('zoom'). This scan produces a regular charge scan with random reload pulses.

### **B.** Publications

- 1. P. Cerfontaine, T. Botzem, D. P. DiVincenzo, and H. Bluhm. "High-Fidelity Single-Qubit Gates for Two-Electron Spin Qubits in GaAs", *Phys. Rev. Lett.* **113**, 150501, 2014. doi: PhysRevLett.113.150501
- 2. T. Botzem, R. P. G. McNeil, J.-M. Mol, D. Schuh, D. Bougeard and H. Bluhm. "Quadrupolar and anisotropy effects on dephasing in two-electron spin qubits in GaAs", *Nat. Commun.* 7, 11170, 2016. doi: 10.1038/ncomms11170
- 3. P. Cerfontaine, T. Botzem, S. S. Humpohl, D. Schuh, D. Bougeard and H. Bluhm. "Feedback-tuned noise-resilient gates for encoded spin qubits", arXiv:1606.01897, 2016.
- 4. M. Nagel, A. Michalski, T. Botzem, and H. Kurz. "Near-field investigation of THz surface-wave emission from optically excited graphite flakes", *Optics Express* **19**, 4667-4672, 2011. doi: 10.1364/OE.19.004667

#### **Presentations**

- 1. Quadrupolar and Anisotropy Effects on Dephasing in Two-Electron Spin Qubits in GaAs, Contributed Talk, SpinTech VIII, Basel, Switzerland, 2015
- 2. Quadrupolar and Anisotropy Effects on Dephasing in Two-Electron Spin Qubits in GaAs, Contributed Talk, APS March Meeting, San Antonio, USA, 2015
- Quadrupolar and Anisotropy Effects on Dephasing in Two-Electron Spin Qubits in GaAs, Invited Talk, JARA-FIT Science Days, Schleiden, Germany, 2014 High-Fidelity Single-Qubit Gates for Two-Electron Spin Qubits, Poster, Spin Qubits 2, Konstanz, Germany, 2014
- 4. *High-Fidelity Single-Qubit Gates for Two-Electron Spin Qubits*, Contributed Talk, APS March Meeting, Denver, USA, 2014
- 5. Towards High-Fidelity Gates in GaAs S-T<sub>0</sub> Spin Qubits, Poster, International Workshop on Quantum Noise and Measurement, Dresden, Germany, 2012

# **List of Figures**

2.1.	Bloch Sphere
2.2.	Device layout
2.3.	Single quantum dot in the low bias regime
2.4.	Double quantum dot
2.5.	Energy diagram and Bloch sphere of the $ST_0$ qubit
2.6.	Spin-orbit interaction
2.7.	Effective magnetic field
3.1.	Device layout
3.2.	Coarse sample pattern
3.3.	Faulty e-beam-lithography
3.4.	Fine e-beam gates
3.5.	4K gate test
4.1.	ICE Oxford dilution refrigerator
4.2.	Schematic setup
4.3.	Cryogenic filterbox
4.4.	Cold finger
4.5.	PCB control and filter wiring scheme
4.6.	Schematic flow of typical data acquisition
5.1.	Device Layout
5.2.	Tuning of the RF-read-out circuit
5.3.	Charge sensor tuning
5.4.	Charge sensing and transport through a double dot
5.5.	Charge sensing with QPC compensation
5.6.	Charge stability diagram
5.7.	Tuning parameters
5.8.	Measurement triangle
5.9.	Averaged $\Delta B_z$ oscillations 61
5.10.	Exchange interaction $J(\varepsilon)$
6.1.	Device Layout and quadrupole broadening
	<b>B</b> -field direction dependence
6.3.	<b>B</b> -field magnitude dependence

6.4.	g-factor anisotropy and fit parameters
6.5.	Pulse sequence for Hahn Echo
6.6.	Wavefunction shifts
6.7.	Single-shot histogram
6.8.	Data stitching
6.9.	g-factor anisotropy
6.10.	<b>B</b> -field directions
7.1.	Nanowire device and measurements of coherence and <i>g</i> -factor 90
7.2.	Hahn echo decay
7.3.	Hahn Echo decay for different <i>B</i> -fields and nuclear spins 96
7.4.	Hahn echo decay for different magnetic field directions
7.5.	Hahn Echo decay for different quadrupolar broadenings
8.1.	$S-T_0$ qubit energy diagram and Bloch sphere
8.2.	Gate adjustment by iterative tomography
8.3.	Characterization of optimized gate sets
8.4.	Pulse model
8.5.	Charge stability diagram
8.6.	Readout calibration
8.7.	Self-consistent state tomography
8.8.	Standard randomized benchmarking
9.1.	Pump curve and energy diagram for two separated electrons 136
9.2.	Data acquisition
9.3.	Locating the EDSR transition
9.4.	Burst time
9.5.	Dependence on the sweep direction
9.6.	Extracting the hyperfine field gradient $\Delta B_z$
9.7.	Pumping the nuclear bath
9.8.	Zamboni effect
9.9.	Pumping the nuclear bath II
9.10.	Locating the EDSR transition using an IQ-mixer setup
A.1.	Numeration of bonding pads
	Circuit diagram of roomtemperature filters
A.3.	Circuit diagram of the cryogenic filter box

# **Bibliography**

- [1] Quantum Manifesto endorsement QUROPE. URL http://qurope.eu/manifesto.
- [2] Dowling, J. P. & Milburn, G. J. Quantum Technology: The Second Quantum Revolution. *arXiv:quant-ph/0206091* (2002). ArXiv: quant-ph/0206091.
- [3] Hanson, R., Kouwenhoven, L. P., Petta, J. R., Tarucha, S. & Vandersypen, L. M. K. Spins in few-electron quantum dots. *Reviews of Modern Physics* 79, 1217–1265 (2007).
- [4] Clarke, J. & Wilhelm, F. K. Superconducting quantum bits. *Nature* **453**, 1031–1042 (2008).
- [5] Shor, P. Polynomial-Time Algorithms for Prime Factorization and Discrete Logarithms on a Quantum Computer. *SIAM Journal on Computing* **26**, 1484–1509 (1997).
- [6] Reiher, M., Wiebe, N., Svore, K. M., Wecker, D. & Troyer, M. Elucidating Reaction Mechanisms on Quantum Computers. *arXiv:1605.03590 [quant-ph]* (2016). ArXiv: 1605.03590.
- [7] Hoffman, B. M., Lukoyanov, D., Dean, D. R. & Seefeldt, L. C. Nitrogenase: A Draft Mechanism. *Accounts of Chemical Research* **46**, 587–595 (2013).
- [8] Lloyd, S. Universal Quantum Simulators. *Science* **273**, 1073–1078 (1996).
- [9] Petta, J. R. *et al.* Coherent manipulation of coupled electron spins in semiconductor quantum dots. *Science* **309**, 2180–2184 (2005).
- [10] Barthel, C., Reilly, D., Marcus, C., Hanson, M. & Gossard, A. Rapid Single-Shot Measurement of a Singlet-Triplet Qubit. *Physical Review Letters* 103, 160503– 160503 (2009).
- [11] Foletti, S., Bluhm, H., Mahalu, D., Umansky, V. & Yacoby, A. Universal quantum control of two-electron spin quantum bits using dynamic nuclear polarization. *Nature Physics* **5**, 903–908 (2009).

- [12] Shulman, M. D. *et al.* Demonstration of entanglement of electrostatically coupled singlet-triplet qubits. *Science* **336**, 202–205 (2012).
- [13] Bluhm, H., Foletti, S., Mahalu, D., Umansky, V. & Yacoby, A. Enhancing the Coherence of a Spin Qubit by Operating it as a Feedback Loop That Controls its Nuclear Spin Bath. *Physical Review Letters* **105**, 216803 (2010).
- [14] Fowler, A., Stephens, A. & Groszkowski, P. High-threshold universal quantum computation on the surface code. *Physical Review A* **80**, 052312–052312 (2009).
- [15] Bluhm, H. *et al.* Dephasing time of GaAs electron-spin qubits coupled to a nuclear bath exceeding 200 µs. *Nature Physics* **7**, 109–113 (2011).
- [16] Nadj-Perge, S., Frolov, S. M., Bakkers, E. P. a. M. & Kouwenhoven, L. P. Spin-orbit qubit in a semiconductor nanowire. *Nature* **468**, 1084–1087 (2010).
- [17] Stefanie Tenberg. Narrowing of the Overhauser Field Distribution in a GaAs Double Quantum Dot. *Master's Thesis (RWTH Aachen University)* (2014).
- [18] Nielsen, M. A. & Chuang, I. L. Quantum Computation and Quantum Information (Cambridge University Press, Cambridge, UK, 2000), 1st ed. edn. URL http://books.google.de/books/about/Quantum\_Computation\_and\_Quantum\_Informat.html?id=65FqEKQOfP8C&pgis=1.
- [19] T. Ihn. *Electronic Quantum Transport in Mesoscopic Semiconductor Structures* (Springer), 3 edn.
- [20] Pioro-Ladrière, M. *et al.* Origin of switching noise in GaAs/Al<sub>x</sub>GaAs lateral gated devices. *Physical Review B* **72**, 115331 (2005).
- [21] Buizert, C. et al. InSitu Reduction of Charge Noise in  $GaAs/Al_xGa_{1-x}As$  Schottky-Gated Devices. *Physical Review Letters* **101**, 226603 (2008).
- [22] Kilian Floehr. PhD Thesis (2015).
- [23] van der Wiel, W. G. *et al.* Electron transport through double quantum dots. *Reviews of Modern Physics* **75**, 1–22 (2002).
- [24] Loss, D. & DiVincenzo, D. P. Quantum computation with quantum dots. *Physical Review A* 57, 120–126 (1998).
- [25] Levy, J. Universal Quantum Computation with Spin-1/2 Pairs and Heisenberg Exchange. *Physical Review Letters* **89**, 147902–147902 (2002).
- [26] DiVincenzo, D. P., Bacon, D., Kempe, J., Burkard, G. & Whaley, K. B. Universal quantum computation with the exchange interaction. *Nature* **408**, 339–42 (2000).

- [27] Magesan, E., Gambetta, J. M. & Emerson, J. Characterizing quantum gates via randomized benchmarking. *Physical Review A* **85**, 042311–042311 (2012).
- [28] Blume-Kohout, R. *et al.* Robust, self-consistent, closed-form tomography of quantum logic gates on a trapped ion qubit. Preprint at http://arxiv.org/abs/1310.4492 (2013).
- [29] Takahashi, M., Bartlett, S. D. & Doherty, A. C. Tomography of a spin qubit in a double quantum dot. *Physical Review A* **88**, 022120–022120 (2013).
- [30] Braginsky, V. B., Vorontsov, Y. I. & Thorne, K. S. Quantum Nondemolition Measurements. *Science* **209**, 547–557 (1980).
- [31] C. P. Slichter. *Principles of magnetic resonance* (Springer, 1990).
- [32] Shulman, M. D. *et al.* Suppressing qubit dephasing using real-time Hamiltonian estimation. *Nature Communications* **5**, 5156 (2014).
- [33] Johnson, A. C., Petta, J. R., Marcus, C. M., Hanson, M. P. & Gossard, A. C. Singlet-triplet spin blockade and charge sensing in a few-electron double quantum dot. *Physical Review B* **72**, 165308 (2005).
- [34] Koppens, F. H. L. *et al.* Control and Detection of Singlet-Triplet Mixing in a Random Nuclear Field. *Science* **309**, 1346–1350 (2005).
- [35] Reilly, D. J., Marcus, C. M., Hanson, M. P. & Gossard, A. C. Fast single-charge sensing with a rf quantum point contact. *Applied Physics Letters* **91**, 89–92 (2007).
- [36] Ivo Vink. Manipulation and Read-out of Spins in Quantum Dots. *PhD Thesis* (*Delft University of Technology*) (2008).
- [37] Sandra Foletti. PhD Thesis (Harvard University) (2010).
- [38] Witzel, W. M. & Das Sarma, S. Quantum theory for electron spin decoherence induced by nuclear spin dynamics in semiconductor quantum computer architectures: Spectral diffusion of localized electron spins in the nuclear solid-state environment. *Physical Review B* **74**, 035322 (2006).
- [39] Yao, W., Liu, R.-B. & Sham, L. J. Theory of electron spin decoherence by interacting nuclear spins in a quantum dot. *Physical Review B* **74**, 195301 (2006).
- [40] Cywinski, L., Witzel, W. M. & Das Sarma, S. Electron Spin Dephasing due to Hyperfine Interactions with a Nuclear Spin Bath. *Physical Review Letters* **102**, 057601 (2009).

- [41] Hahn, E. Spin echoes. *Physical Review* **297** (1950).
- [42] Neder, I. *et al.* Semiclassical model for the dephasing of a two-electron spin qubit coupled to a coherently evolving nuclear spin bath. *Physical Review B* **84**, 035441–035441 (2011).
- [43] Taylor, J. *et al.* Relaxation, dephasing, and quantum control of electron spins in double quantum dots. *Physical Review B* **76**, 035315–035315 (2007).
- [44] Cywinski, L., Lutchyn, R., Nave, C. & Das Sarma, S. How to enhance dephasing time in superconducting qubits. *Physical Review B* 77, 174509–174509 (2008).
- [45] Nichol, J. M. *et al.* Quenching of dynamic nuclear polarization by spin-orbit coupling in GaAs quantum dots. *Nature Communications* **6**, 7682 (2015).
- [46] Divincenzo, D. P. The Physical Implementation of Quantum Computation. *Fortschritte der Physik* **48**, 771–783 (2000).
- [47] Trifunovic, L. *et al.* Long-Distance Spin-Spin Coupling via Floating Gates. *Physical Review X* **2**, 011006 (2012).
- [48] Wardrop, M. P. & Doherty, A. C. Exchange-based two-qubit gate for singlet-triplet qubits. *Physical Review B* **90**, 045418 (2014).
- [49] Malinowski, F. K. *et al.* Notch filtering the nuclear environment of a spin qubit (2016).
- [50] Zwanenburg, F. a. *et al.* Silicon quantum electronics. *Reviews of Modern Physics* **85**, 961–1019 (2013).
- [51] Braslau, N. Alloyed ohmic contacts to GaAs. *Journal of Vacuum Science & Technology* **19**, 803–807 (1981).
- [52] Barthel, C. *et al.* Fast sensing of double-dot charge arrangement and spin state with a radio-frequency sensor quantum dot. *Physical Review B* **81**, 161308–161308 (2010).
- [53] Schoelkopf, R. J., Wahlgren, P., Kozhevnikov, A. A., Delsing, P. & Prober, D. E. The Radio-Frequency Single-Electron Transistor (RF-SET): A Fast and Ultrasensitive Electrometer. *Science* 280, 1238–1242 (1998).
- [54] Cassidy, M. C. *et al.* Single shot charge detection using a radio-frequency quantum point contact. *Applied Physics Letters* **91**, 222104 (2007).

- [55] Cerfontaine, P. et al. Feedback-tuned noise-resilient gates for encoded spin qubits. arXiv:1606.01897 [cond-mat, physics:quant-ph] (2016). ArXiv: 1606.01897.
- [56] Baart, T. A. et al. Single-spin CCD. Nature Nanotechnology 11, 330–334 (2016).
- [57] Kawakami, E. *et al.* Electrical control of a long-lived spin qubit in a Si/SiGe quantum dot. *Nature Nanotechnology* **9**, 666–670 (2014).
- [58] Muhonen, J. T. *et al.* Quantifying the quantum gate fidelity of single-atom spin qubits in silicon by randomized benchmarking. *Journal of Physics: Condensed Matter* **27**, 154205 (2015).
- [59] Maune, B. M. *et al.* Coherent singlet-triplet oscillations in a silicon-based double quantum dot. *Nature* **481**, 344–7 (2012).
- [60] Takakura, T. *et al.* Single to quadruple quantum dots with tunable tunnel couplings. *Applied Physics Letters* **104**, 113109 (2014).
- [61] Delbecq, M. R. *et al.* Full control of quadruple quantum dot circuit charge states in the single electron regime. *Applied Physics Letters* **104**, 22–25 (2014).
- [62] Veldhorst, M. *et al.* An addressable quantum dot qubit with fault-tolerant control-fidelity. *Nature Nanotechnology* **9**, 981–985 (2014).
- [63] Veldhorst, M. et al. A two-qubit logic gate in silicon. *Nature* **526**, 410–414 (2015).
- [64] MacLeod, S. J. *et al.* Hybrid architecture for shallow accumulation mode Al-GaAs/GaAs heterostructures with epitaxial gates. *Applied Physics Letters* **106**, 012105 (2015).
- [65] Frees, A. et al. Compressed optimization of device architectures 8–8 (2014).
- [66] Mak, W. Y. *et al.* Ultra-shallow quantum dots in an undoped GaAs/AlGaAs two-dimensional electron gas. *Applied Physics Letters* **102**, 103507 (2013).
- [67] McNeil, R. P. G. *et al.* On-demand single-electron transfer between distant quantum dots. *Nature* **477**, 439–442 (2011).
- [68] Trifunovic, L. *et al.* Long-Distance Spin-Spin Coupling via Floating Gates. *Physical Review X* **2**, 011006–011006 (2012).
- [69] Serina, M., Trifunovic, L., Kloeffel, C. & Loss, D. Long-Range Interaction between Charge and Spin Qubits in Quantum Dots 1–7 (2016).

- [70] Fowler, A. G., Mariantoni, M., Martinis, J. M. & Cleland, A. N. Surface codes: Towards practical large-scale quantum computation. *Physical Review A* **86**, 032324 (2012).
- [71] Kuhlmann, A. V. *et al.* Charge noise and spin noise in a semiconductor quantum device. *Nature Physics* **9**, 570–575 (2013).
- [72] Dial, O. E. *et al.* Charge noise spectroscopy using coherent exchange oscillations in a singlet-triplet qubit. *Physical Review Letters* **110**, 146804–146804 (2013).
- [73] Johansson, J. R., Nation, P. D. & Nori, F. QuTiP 2: A Python framework for the dynamics of open quantum systems. *Computer Physics Communications* **184**, 1234–1240 (2013).
- [74] Svore, K. M., Aho, A. V., Cross, A. W., Chuang, I. & Markov, I. L. A Layered Software Architecture for Quantum Computing Design Tools. *Computer* **39**, 74–83 (2006).
- [75] Jones, N. C. *et al.* Layered Architecture for Quantum Computing. *Physical Review X* **2**, 031007 (2012).
- [76] Levy, J. E. *et al.* Implications of electronics constraints for solid-state quantum error correction and quantum circuit failure probability. *New Journal of Physics* **13**, 083021 (2011).
- [77] Dial, O. E. *et al.* Electrometry Using Coherent Exchange Oscillations in a Singlet-Triplet-Qubit. *arXiv:1208.2023v4* (2012).
- [78] Botzem, T. *et al.* Quadrupolar and anisotropy effects on dephasing in twoelectron spin qubits in GaAs. *Nature Communications* **7**, 11170–11170 (2016).
- [79] Baart, T. A., Eendebak, P. T., Reichl, C., Wegscheider, W. & Vandersypen, L. M. K. Computer-automated tuning of semiconductor double quantum dots into the single-electron regime. *Applied Physics Letters* 108, 213104 (2016).
- [80] Elzerman, J. M. *et al.* Single-shot read-out of an individual electron spin in a quantum dot. *Nature* **430**, 431–435 (2004).
- [81] Nowack, K. C. *et al.* Single-shot correlations and two-qubit gate of solid-state spins. *Science (New York, N.Y.)* **333**, 1269–72 (2011).
- [82] DiCarlo, L. *et al.* Differential Charge Sensing and Charge Delocalization in a Tunable Double Quantum Dot. *Physical Review Letters* **92**, 226801 (2004).

- [83] Gorman, S. K. *et al.* Extracting inter-dot tunnel couplings between few donor quantum dots in silicon. *New Journal of Physics* **18**, 053041 (2016). ArXiv: 1606.00851.
- [84] Schreiber, L. R. *et al.* Coupling artificial molecular spin states by photon-assisted tunnelling. *Nature communications* **2**, 556–556 (2011).
- [85] Studenikin, S. A. *et al.* Enhanced charge detection of spin qubit readout via an intermediate state. *Applied Physics Letters* **101**, 233101 (2012).
- [86] Barthel, C. *et al.* Relaxation and readout visibility of a singlet-triplet qubit in an Overhauser field gradient. *Physical Review B* **85**, 035306–035306 (2012).
- [87] Pioro-Ladrière, M. *et al.* Electrically driven single-electron spin resonance in a slanting Zeeman field. *Nature Physics* **4**, 776–779 (2008).
- [88] Forster, F., Mühlbacher, M., Schuh, D., Wegscheider, W. & Ludwig, S. Electric-dipole-induced spin resonance in a lateral double quantum dot incorporating two single-domain nanomagnets. *Physical Review B* **91**, 195417 (2015).
- [89] Wu, X. et al. Two-axis control of a singlet-triplet qubit with an integrated micromagnet. *Proceedings of the National Academy of Sciences* **111**, 11938–11942 (2014).
- [90] Cerfontaine, P., Botzem, T., DiVincenzo, D. P. & Bluhm, H. High-Fidelity Single-Qubit Gates for Two-Electron Spin Qubits in GaAs. *Physical Review Letters* **113**, 150501 (2014).
- [91] Kalman, R. E. A New Approach to Linear Filtering and Prediction Problems. *Journal of Basic Engineering* **82**, 35–45 (1960).
- [92] Press, D. et al. Ultrafast optical spin echo in a single quantum dot. *Nature Photonics* **4**, 367–370 (2010).
- [93] Greilich, A. *et al.* Mode Locking of Electron Spin Coherences in Singly Charged Quantum Dots. *Science* **313**, 341–345 (2006).
- [94] Chen, G., Bergman, D. L. & Balents, L. Semiclassical dynamics and long-time asymptotics of the central-spin problem in a quantum dot. *Physical Review B* **76**, 045312 (2007).
- [95] Cywinski, L., Witzel, W. M. & Das Sarma, S. Pure quantum dephasing of a solid-state electron spin qubit in a large nuclear spin bath coupled by long-range hyperfine-mediated interactions. *Physical Review B* **79**, 245314 (2009).

- [96] Lee, B., Witzel, W. M. & Das Sarma, S. Universal Pulse Sequence to Minimize Spin Dephasing in the Central Spin Decoherence Problem. *Physical Review Letters* **100**, 160505 (2008).
- [97] Welander, E., Chekhovich, E., Tartakovskii, A. & Burkard, G. Influence of Nuclear Quadrupole Moments on Electron Spin Coherence in Semiconductor Quantum Dots. *arXiv:1405.1329 [cond-mat]* (2014). ArXiv: 1405.1329.
- [98] Sinitsyn, N. A., Li, Y., Crooker, S. A., Saxena, A. & Smith, D. L. Role of Nuclear Quadrupole Coupling on Decoherence and Relaxation of Central Spins in Quantum Dots. *Physical Review Letters* **109**, 166605 (2012).
- [99] Munsch, M. *et al.* Manipulation of the nuclear spin ensemble in a quantum dot with chirped magnetic resonance pulses. *Nature Nanotechnology* **9**, 671–675 (2014).
- [100] Chekhovich, E. A., Hopkinson, M., Skolnick, M. S. & Tartakovskii, A. I. Suppression of nuclear spin bath fluctuations in self-assembled quantum dots induced by inhomogeneous strain. *Nature Communications* **6** (2015).
- [101] Maletinsky, P., Badolato, A. & Imamoglu, A. Dynamics of Quantum Dot Nuclear Spin Polarization Controlled by a Single Electron. *Physical Review Letters* **99**, 056804 (2007).
- [102] Chekhovich, E. A. *et al.* Structural analysis of strained quantum dots using nuclear magnetic resonance. *Nature Nanotechnology* **7**, 646–650 (2012).
- [103] Bechtold, A. *et al.* Three-stage decoherence dynamics of an electron spin qubit in an optically active quantum dot. *Nature Physics* **11**, 1005–1008 (2015).
- [104] Stockill, R. *et al.* Intrinsic limit to electron spin coherence in InGaAs quantum dots featuring strain-induced nuclear dispersion. *arXiv:1512.01811* [cond-mat, physics:quant-ph] (2015). ArXiv: 1512.01811.
- [105] Medford, J. et al. Scaling of Dynamical Decoupling for Spin Qubits. *Physical Review Letters* **108**, 086802 (2012).
- [106] Sundfors, R. K. Exchange and Quadrupole Broadening of Nuclear Acoustic Resonance Line Shapes in the III-V Semiconductors. *Physical Review* **185**, 458–472 (1969).
- [107] Dickel, C., Foletti, S., Umansky, V. & Bluhm, H. Characterization of S-T<sub>+</sub> transition dynamics via correlation measurements. *Physical Review B* **92**, 125402 (2015).

- [108] Gammon, D. *et al.* Nuclear Spectroscopy in Single Quantum Dots: Nanoscopic Raman Scattering and Nuclear Magnetic Resonance. *Science* **277**, 85–88 (1997).
- [109] Hester, R. K., Sher, A., Soest, J. F. & Weisz, G. Nuclear-magnetic-resonance detection of charge defects in gallium arsenide. *Physical Review B* **10**, 4262–4273 (1974).
- [110] V. K. Kalevich & V. L. Korenev. Electron *g*-factor anisotropy in asymmetric GaAs/AlGaAs quantum well. *JETP Lett* **57**, 571 (1993).
- [111] Nefyodov, Y. A., Shchepetilnikov, A. V., Kukushkin, I. V., Dietsche, W. & Schmult, S. Electron *g*-factor anisotropy in GaAs/Al<sub>1-x</sub>Ga<sub>x</sub>As quantum wells of different symmetry. *Physical Review B* **84**, 233302 (2011).
- [112] Snelling, M. J. *et al.* Magnetic *g*-factor of electrons in  $GaAs/Al_xGa_{1-x}As$  quantum wells. *Physical Review B* **44**, 11345–11352 (1991).
- [113] Witzel, W. M. & Das Sarma, S. Wavefunction considerations for the central spin decoherence problem in a nuclear spin bath. *Physical Review B* 77, 165319 (2008).
- [114] Nadj-Perge, S. *et al.* Spectroscopy of Spin-Orbit Quantum Bits in Indium Antimonide Nanowires. *Physical Review Letters* **108**, 166801 (2012).
- [115] Ivchenko, E. L. Spin physics in semiconductor nanosystems. *Uspekhi Fizicheskih Nauk* **182**, 869 (2012).
- [116] Suits, B. H. NUCLEAR QUADRUPOLE RESONANCE SPECTROSCOPY. In Vij, D. R. (ed.) *Handbook of Applied Solid State Spectroscopy*, 65–96 (Springer US, 2006). URL http://link.springer.com/chapter/10.1007/0-387-37590-2\_2.
- [117] Stevan Nadj-Perge. PhD thesis (2010).
- [118] Nowack, K. C., Koppens, F. H. L., Nazarov, Y. V. & Vandersypen, L. M. K. Coherent Control of a Single Electron Spin with Electric Fields. *Science* **318**, 1430–1433 (2007).
- [119] Kato, Y. *et al.* Gigahertz Electron Spin Manipulation Using Voltage-Controlled g-Tensor Modulation. *Science* **299**, 1201–1204 (2003).
- [120] Nadj-Perge, S. *et al.* Disentangling the effects of spin-orbit and hyperfine interactions on spin blockade. *Physical Review B* **81**, 201305 (2010).

- [121] Schroer, M. D., Petersson, K. D., Jung, M. & Petta, J. R. Field Tuning the \$g\$ Factor in InAs Nanowire Double Quantum Dots. *Physical Review Letters* **107**, 176811 (2011).
- [122] Stockill, R. *et al.* Quantum dot spin coherence governed by a strained nuclear environment. *Nature Communications* **7**, 12745 (2016).
- [123] Wang, J. *et al.* Measurements of the spin-orbit interaction and Land\'e g factor in a pure-phase InAs nanowire double quantum dot in the Pauli spin-blockade regime. *Applied Physics Letters* **109**, 053106 (2016). ArXiv: 1607.06951.
- [124] Magesan, E., Gambetta, J. M. & Emerson, J. Scalable and Robust Randomized Benchmarking of Quantum Processes. *Physical Review Letters* **106**, 180504–180504 (2011).
- [125] Epstein, J. M., Cross, A. W., Magesan, E. & Gambetta, J. M. Investigating the limits of randomized benchmarking protocols. *Physical Review A* **89**, 062321–062321 (2014).
- [126] Wallman, J. J. & Flammia, S. T. Randomized benchmarking with confidence. *New Journal of Physics* **16**, 103032–103032 (2014).
- [127] Gaudreau, L. *et al.* Coherent control of three-spin states in a triple quantum dot. *Nature Physics* **8**, 54–58 (2011).
- [128] Medford, J. et al. Self-consistent measurement and state tomography of an exchange-only spin qubit. *Nature Nanotechnology* **8**, 654–9 (2013).
- [129] Kim, D. *et al.* High-fidelity resonant gating of a silicon-based quantum dot hybrid qubit. *npj Quantum Information* **1**, 15004–15004 (2015).
- [130] Kawakami, E. *et al.* Gate fidelity and coherence of an electron spin in a Si/SiGe quantum dot with micromagnet. Preprint at http://arxiv.org/abs/1602.08334 (2016) (2016).
- [131] Yoneda, J. *et al.* Fast Electrical Control of Single Electron Spins in Quantum Dots with Vanishing Influence from Nuclear Spins. *Physical Review Letters* **113**, 267601 (2014).
- [132] Wang, X., Bishop, L. S., Barnes, E., Kestner, J. P. & Das Sarma, S. Robust quantum gates for singlet-triplet spin qubits using composite pulses. *Physical Review A* **89**, 022310–022310 (2014).
- [133] Khodjasteh, K., Bluhm, H. & Viola, L. Automated synthesis of dynamically corrected quantum gates. *Physical Review A* **86**, 042329–042329 (2012).

- [134] Reilly, D. J. *et al.* Measurement of Temporal Correlations of the Overhauser Field in a Double Quantum Dot. *Physical Review Letters* **101**, 236803–236803 (2008).
- [135] Egger, D. J. & Wilhelm, F. K. Adaptive Hybrid Optimal Quantum Control for Imprecisely Characterized Systems. *Physical Review Letters* **112**, 240503–240503 (2014).
- [136] Kelly, J. *et al.* Optimal Quantum Control Using Randomized Benchmarking. *Physical Review Letters* **112**, 240504–240504 (2014).
- [137] Dobrovitski, V. V., de Lange, G., Ristè, D. & Hanson, R. Bootstrap Tomography of the Pulses for Quantum Control. *Physical Review Letters* **105**, 077601–077601 (2010).
- [138] Ryan, C. a., Laforest, M. & Laflamme, R. Randomized benchmarking of singleand multi-qubit control in liquid-state NMR quantum information processing. *New Journal of Physics* **11**, 013034–013034 (2009).
- [139] Tenberg, S., McNeil, R. P. G., Rubbert, S. & Bluhm, H. Narrowing of the Overhauser field distribution by feedback-enhanced dynamic nuclear polarization. *Physical Review B* **92**, 195428–195428 (2015).
- [140] Dial, O. E. *et al.* Supplement: Charge noise spectroscopy using coherent exchange oscillations in a singlet-triplet qubit. *Physical Review Letters* **110**, 1–4 (2013).
- [141] Green, T., Uys, H. & Biercuk, M. J. High-order noise filtering in nontrivial quantum logic gates **0**, 1–5 (2012).
- [142] Barends, R. *et al.* Superconducting quantum circuits at the surface code threshold for fault tolerance. *Nature* **508**, 500–503 (2014).
- [143] Magesan, E. *et al.* Efficient Measurement of Quantum Gate Error by Interleaved Randomized Benchmarking. *Physical Review Letters* **109**, 080505–080505 (2012).
- [144] Laird, E. A. *et al.* Hyperfine-Mediated Gate-Driven Electron Spin Resonance. *Physical Review Letters* **99**, 246601 (2007).
- [145] Shafiei, M., Nowack, K. C., Reichl, C., Wegscheider, W. & Vandersypen, L. M. K. Resolving Spin-Orbit- and Hyperfine-Mediated Electric Dipole Spin Resonance in a Quantum Dot. *Physical Review Letters* 110, 107601–107601 (2013).

- [146] Vink, I. T. *et al.* Locking electron spins into magnetic resonance by electron-nuclear feedback. *Nature Physics* **5**, 764–768 (2009).
- [147] Reilly, D. J. *et al.* Suppressing Spin Qubit Dephasing by Nuclear State Preparation. *Science* **321**, 817–821 (2008).
- [148] Ramon, G. & Hu, X. Dynamical nuclear spin polarization and the Zamboni effect in gated double quantum dots. *Physical Review B* **75**, 161301 (2007).
- [149] pyGSTi. URL http://www.pygsti.info/.
- [150] de Lange, G., Wang, Z. H., Ristè, D., Dobrovitski, V. V. & Hanson, R. Universal dynamical decoupling of a single solid-state spin from a spin bath. *Science (New York, N.Y.)* **330**, 60–3 (2010).
- [151] Fink, T. & Bluhm, H. Distinguishing Quantum and Classical Baths via Correlation Measurements. *arXiv:1402.0235 [cond-mat, physics:quant-ph]* (2014). ArXiv: 1402.0235.
- [152] Mehl, S., Bluhm, H. & DiVincenzo, D. P. Two-qubit couplings of singlet-triplet qubits mediated by one quantum state. *Physical Review B* **90**, 045404–045404 (2014).
- [153] Mak, W. Y. *et al.* Distinguishing impurity concentrations in GaAs and AlGaAs using very shallow undoped heterostructures. *Applied Physics Letters* **97**, 242107 (2010).
- [154] Engel, H.-A., Taylor, J. M., Lukin, M. D. & Imamoglu, A. Quantum optical interface for gate-controlled spintronic devices. *arXiv:cond-mat/0612700* (2006). ArXiv: cond-mat/0612700.
- [155] Hornibrook, J. et al. Cryogenic Control Architecture for Large-Scale Quantum Computing. *Physical Review Applied* **3**, 024010 (2015).
- [156] Puddy, R. K. *et al.* Multiplexed charge-locking device for large arrays of quantum devices. *Applied Physics Letters* **107**, 143501 (2015).
- [157] Lamb, I. D. C. *et al.* An FPGA-based instrumentation platform for use at deep cryogenic temperatures. *Review of Scientific Instruments* **87**, 014701 (2016).
- [158] Homulle, H. *et al.* A Reconfigurable Cryogenic Platform for the Classical Control of Scalable Quantum Computers 1–8 (2016).